



THE UNIVERSITY  
ofADELAIDE

Studies of the Interstellar Medium  
Towards Dark TeV Gamma-ray Sources

James Cheuk-Heng Lau  
School of Physical Sciences  
University of Adelaide

A thesis submitted for the degree of  
*Doctor of Philosophy*

October 2017



## Abstract

Recent advances involving ground based observations of the very-high-energy sky have led to the discovery of a growing number of Galactic tera-electron volt (TeV)  $\gamma$ -ray sources. Many of these sources have been associated with other high energy phenomena, such as supernova remnants (SNRs) and pulsar wind nebulae. However, a number of TeV  $\gamma$ -ray sources are ‘dark’, with no strong counterparts seen at other wavelengths.

Astrophysical TeV  $\gamma$ -rays are produced via two channels; leptonic and hadronic. The leptonic process involves the upscattering of background photons by high energy electrons through the inverse-Compton effect. The hadronic process involves the decay of neutral pions produced by interactions between highly accelerated cosmic-rays (CRs) and the ambient interstellar medium (ISM). Dark TeV  $\gamma$ -ray sources may result from CR and ISM interactions, and studying these sources will shed light on the nature of the parent particle accelerators. Some of the sources selected for study in this thesis are considered candidate PeVatrons, an emerging class of extreme accelerators which produce CRs with energies in the peta-electron volt (PeV) range.

A detailed understanding of the ISM towards dark TeV  $\gamma$ -ray sources is vital in order to investigate possible origin scenarios. In addition to providing contextual clues, morphological similarities between TeV  $\gamma$ -rays and the ISM can provide strong evidence of hadronic CR interactions. This may lead to positive associations between TeV sources and other sources observed at different wavelengths.

The work in this thesis primarily involves the use of radio telescopes to investigate the distribution of the ISM towards dark TeV  $\gamma$ -ray sources. The data has been used to constrain the mechanisms behind these objects, and underpins the investigations into their mysterious origins. Five TeV  $\gamma$ -ray sources were studied as part of the work in this thesis.

---

HESS J1640–465 and the PeVatron candidate HESS J1641–463 are a pair of  $\gamma$ -ray sources each coincident with a SNR bridged by bright HII regions. The study of the ISM suggests that the TeV emission from both sources may be hadronic in origin, and provides evidence to support the PeVatron nature of HESS J1641–463.

HESS J1614–518 has no obvious counterparts seen in other wavelengths. The investigation of the ISM reveals an overlapping ring of gas potentially associated with an undiscovered SNR or the stellar cluster Pismis 22, which may power the TeV emission. The nearby TeV source HESS J1616–508 has several potential counterparts, including two SNRs and three pulsars, though there was no evidence in the study of the ISM to support any association. Spatially matching gas, however, is found coincident with the TeV source, suggesting a possible link with an undiscovered accelerator.

HESS J1702–420 is both a dark TeV  $\gamma$ -ray source and a PeVatron candidate. Though a SNR and pulsar are seen near the outskirts of this source, no evidence in the study of the ISM is found to support any association. Morphologically favourable gas overlapping the TeV source, however, suggests possible scenarios involving nearby accelerators, such as stellar winds from massive stars or an undetected SNR.

## **Statement of Originality**

I, James Cheuk-Heng Lau, certify that this work contains no material which has been accepted for the award of any other degree or diploma in my name, in any university or other tertiary institution and, to the best of my knowledge and belief, contains no material previously published or written by another person, except where due reference has been made in the text. In addition, I certify that no part of this work will, in the future, be used in a submission in my name, for any other degree or diploma in any university or other tertiary institution without the prior approval of the University of Adelaide and where applicable, any partner institution responsible for the joint-award of this degree.

I give consent to this copy of my thesis when deposited in the University Library, being made available for loan and photocopying, subject to the provisions of the Copyright Act 1968.

I acknowledge that copyright of published works contained within this thesis resides with the copyright holder(s) of those works.

I also give permission for the digital version of my thesis to be made available on the web, via the University's digital research repository, the Library Search and also through web search engines, unless permission has been granted by the University to restrict access for a period of time.

I acknowledge the support I have received for my research through the provision of an Australian Government Research Training Program Scholarship.

Signature:

Date: *30/10/2017*



## Acknowledgements

This PhD would not have been possible without the support of many people, to whom I am deeply indebted. Here, I'd like to take the time to acknowledge all those who have been a part of my PhD journey; I would not have been able to do it without you.

Firstly, I'd like to thank my supervisor, Gavin Rowell, for his continued guidance over the years. His advice and support allowed for my PhD journey to be a smooth and rewarding experience. I very much appreciate Gavin's feedback he provided on my innumerable drafts, as well as the many unique opportunities that he provided for me to travel both nationally and internationally.

I'm very grateful to the academics of the High Energy Astrophysics Group, who have been excellent mentors throughout my entire time as both an undergraduate and postgraduate student. Special mention goes to Bruce Dawson and Roger Clay who have been there for me since day one. Thanks to Gary Hill for allowing himself to be roped in as my co-supervisor. Many thanks goes to the academics and students outside Adelaide who helped me through my PhD, especially Michael Burton and the members of TeamMopra.

I am thankful to my peers in the Radeladio research group. You have been a amazing group of people, and I am glad that we were able to share an office during my PhD. Many thanks goes to my seniors: Fabien Voisin, Phoebe de Wilt and Rebecca Blackwell. I'd be remiss if I did not say that I learnt an incredible amount from all of you. Thank you for all the time we spent discussing our research, as well as for the (very enjoyable) random tangents we'd inevitably find ourselves on. I'd also like to thank all my juniors: Stephanie Pointon, Luke Bowman, Cameron Snoswell, Andrew Curzons, Kirsty Feijen and Brayden Pullen, as well as all the other students in the High Energy Astrophysics Group. It was a pleasure working (and procrastinating) with you all, and I wish you well on your future endeavours.

Of course, I need to make special mention of the other astrophysics students in my year: Patrick van Bodegom, Phong Nguyen and Simon Blaess. The four of us started together as first year Space Science and Astrophysics students, and have been together through our undergrad, honours and PhDs. Special mention to Alex Chambers, who despite being a theorist, we considered the honanary '5th member' of our group. From working on assignments together (perhaps too closely), to the late

---

nights playing video games, to even just me popping by your office for a chat, many thanks to you guys for keeping my journey an entertaining one.

Thank you to all my friends from my school days for the continued support. It is heart-warming to know that, regardless of the paths we take, we can always find a way to spend time together to laugh and enjoy life. Many thanks to all my friends from Church who have been with me throughout my PhD, and indeed, most of my life. Your wide-eyed wonder (and jokes) at my research certainly encouraged me to the finish line.

While most of my extended family does not live in Australia, I must express my gratitude for the care they have for me. Thank you for your messages of support throughout my studies. I'd like to make a special thanks to my grandparents. Though they passed away before I completed my PhD, the joy they had as they spoke with me about my studies is something I will never forget.

To my parents, Kitty and Quentin, and my brothers Ian and Samuel. You've provided me with the most wonderful of homes to live in. The years of support and love that you have given me have had the most profound impact on my life, and I am deeply grateful for it. Thank you all so much.

Finally, I'd like to thank God for his endless provision in my life, including blessing me with wonderful mentors, peers, friends and family.

# Contents

<b>Abstract</b>	<b>i</b>
<b>Statement of Originality</b>	<b>iii</b>
<b>Acknowledgements</b>	<b>v</b>
<b>1 Cosmic-rays, Gamma-rays and High Energy Astrophysics</b>	<b>1</b>
1.1 Introduction and Motivation . . . . .	1
1.2 Astrophysical Sources of VHE Gamma-rays . . . . .	2
1.2.1 Supernova Remnants . . . . .	3
1.2.2 Pulsars and Pulsar Wind Nebulae . . . . .	4
1.2.3 Binary Systems . . . . .	4
1.2.4 Massive Stellar Clusters . . . . .	5
1.2.5 Diffuse VHE Gamma-ray Emission at the centre of the Galaxy	5
1.2.6 PeVatrons . . . . .	5
1.2.7 Dark and Unidentified Sources . . . . .	6
1.3 Cosmic Rays and Electrons . . . . .	7
1.3.1 The Cosmic-Ray Spectrum . . . . .	8
1.3.2 Cosmic-Ray and Electron Propagation . . . . .	10
1.3.3 Cosmic-Ray and Electron Acceleration . . . . .	11
1.3.3.1 2nd Order Fermi Acceleration . . . . .	12
1.3.3.2 1st Order Fermi Acceleration . . . . .	14
1.4 Production Processes of High-Energy Radiation . . . . .	17
1.4.1 Inverse-Compton Scattering . . . . .	17
1.4.2 Synchrotron Emission . . . . .	18
1.4.3 Bremsstrahlung . . . . .	20
1.4.4 Cosmic-ray and Interstellar Medium Collisions . . . . .	20
1.4.5 Energy-Loss Timescales . . . . .	21
1.5 Ground Based Gamma-ray Astronomy . . . . .	22
1.5.1 Extensive Air-Shower . . . . .	22

## CONTENTS

---

1.5.2	Electromagnetic Extensive Air-Shower	23
1.5.3	Hadronic Extensive Air-Shower	25
1.5.4	Cherenkov Light and its Imaging	27
1.5.5	High Energy Stereoscopic System	28
1.6	TeV gamma-ray sources studied	30
<b>2</b>	<b>Spectral Lines and Radio Astronomy</b>	<b>33</b>
2.1	Basic Radiation Theory	34
2.1.1	Intensity, Flux and Luminosity	34
2.1.2	Thermal Radiation and Brightness Temperature	34
2.1.3	Radiative Transfer	35
2.2	Molecular Line Emission	38
2.2.1	Rotational Molecular Energy Levels	38
2.2.2	Einstein Coefficients	40
2.2.3	Critical Density	42
2.3	Millimetre Radio Astronomy	43
2.3.1	Mopra	43
2.3.2	Source Temperature and Antenna Temperature	44
2.4	Physical parameters from observations	48
2.4.1	Column Density	48
2.4.2	Optical Depth	50
2.4.3	The Doppler Effect	50
2.4.4	Line Profiles	51
2.5	Kinematic Distances and the Rotation of the Galaxy	52
2.6	Tracers of Interstellar Gas	54
2.6.1	Molecular Hydrogen	55
2.6.1.1	Column density and X-factors	55
2.6.1.2	Mass and Density	56
2.6.2	Carbon Monoxide	56
2.6.3	Carbon Monosulfide	58
2.6.4	Silicon Monoxide	58
2.6.5	Methanol and masers	59
2.6.6	Atomic Hydrogen	59
2.6.7	Atomic Carbon	60
<b>3</b>	<b>The ISM towards HESS J1640–465 and HESS J1641–463</b>	<b>63</b>
<b>4</b>	<b>The ISM towards HESS J1614–518 and HESS J1616–508</b>	<b>85</b>

---

## CONTENTS

<b>5 The ISM towards HESS J1702–420</b>	<b>115</b>
<b>6 Conclusions and Future Work</b>	<b>135</b>
<b>A Cosmic-ray Acceleration</b>	<b>139</b>
A.1 2nd Order Fermi Acceleration . . . . .	139
A.2 1st Order Fermi Acceleration . . . . .	141
<b>Bibliography</b>	<b>145</b>

## CONTENTS

# Chapter 1

## Cosmic-rays, Gamma-rays and High Energy Astrophysics

### 1.1 Introduction and Motivation

Since time immemorial, humans have cast their eyes upwards in wonderment at the great expanse of the heavens. Not content with simply admiring the distant lights, we have continued to question their origins, driven by our natural curiosity and desire for knowledge. The field of astronomy has come far, expanding past the light that can be seen by our own eyes to discover a vast universe filled with incredible phenomena at all frequencies of the electromagnetic spectrum.

At the furthermost end of the electromagnetic spectrum are gamma-rays, the most energetic form of light. While thermally generated light constitutes much of the radiation in the universe, physical objects typically do not have temperatures large enough to generate gamma-rays at the highest energies. These astrophysical gamma-rays are instead produced by some of the most extreme and violent ‘non-thermal’ processes that occur in the universe.

Very high energy (VHE) gamma-rays may be generated through the various interactions of highly accelerated charged particles, known as cosmic-rays. The origins of cosmic-rays remains an open question, but are generally thought to be produced by astrophysical particle accelerators. Galactic particle accelerators may include such extreme phenomena as supernova remnants, pulsars and pulsar wind nebulae, binary systems, and the stellar winds of massive stars clusters.

Recent advances and observations with ground based gamma-ray telescopes, such as the High Energy Stereoscopic System (HESS, see HESS website 2017), have revealed numerous Galactic gamma-ray sources in the TeV ( $10^{12}$  eV) energy range. Many of these sources have been associated with high energy particle accelerators. However, a large population of these TeV sources are unidentified, with many being

---

## CHAPTER 1. COSMIC-RAYS, GAMMA-RAYS AND HIGH ENERGY ASTROPHYSICS

---

‘dark’; having no compelling counterparts seen in any other wavelengths. The motivation behind the majority of the work presented in this thesis is the investigation into the nature of these dark TeV gamma-ray sources.

Astrophysical TeV gamma-rays have two main mechanisms of production: the decay of neutral pions produced by the interaction between hadronic cosmic-rays and ambient interstellar medium; and the upscattering of background photons via the inverse-Compton effect by high energy leptons. Identifying the process behind the production of gamma-rays is a key task in investigating any particular TeV source.

An understanding of the distribution of the interstellar medium towards dark TeV gamma-ray sources is paramount in order to constrain the possible gamma-ray production scenarios. Morphological similarities between gamma-ray emission and interstellar gas can provide strong indicators of hadronic cosmic-ray interactions, while additional contextual clues aid to unravel the local environment these sources reside in.

Radio astronomy, targeting molecular gas tracers, is used to study the interstellar medium towards TeV gamma-ray sources. The work presented in this thesis is a dedicated attempt, using data from Earth-based radio telescopes, to investigate the interstellar medium towards Galactic TeV gamma-ray sources in order to gain further understanding into the nature of these incredible astronomical phenomena.

This chapter provides background into the high-energy astrophysics involved in this thesis. A general overview of Galactic TeV gamma-ray sources is first presented (§1.2), followed by a discussion of cosmic-rays (§1.3). Afterwards, an explanation of the production process of high-energy radiation is given (§1.4), followed by a discussion on ground based gamma-ray astronomy (§1.5), before ending with a brief introduction to the TeV sources studied (§1.6).

## 1.2 Astrophysical Sources of VHE Gamma-rays

Beginning with the detection of VHE gamma-rays from the Crab Nebula in 1989 (Weekes et al., 1989), ground based gamma-ray observatories (see §1.5) have revealed the existence of many VHE gamma-ray sources throughout the sky. These sources are divided into Galactic and extra-Galactic sources, with most Galactic sources located along the Galactic plane. Figure 1.1 shows the sky distribution of all currently known VHE gamma-ray sources.

Astrophysical VHE gamma-rays have two main mechanisms of production, as discussed in §1.4. These are the hadronic interaction between highly accelerated cosmic-ray (CR) particles (see §1.3) and ambient interstellar medium, and the leptonic inter-

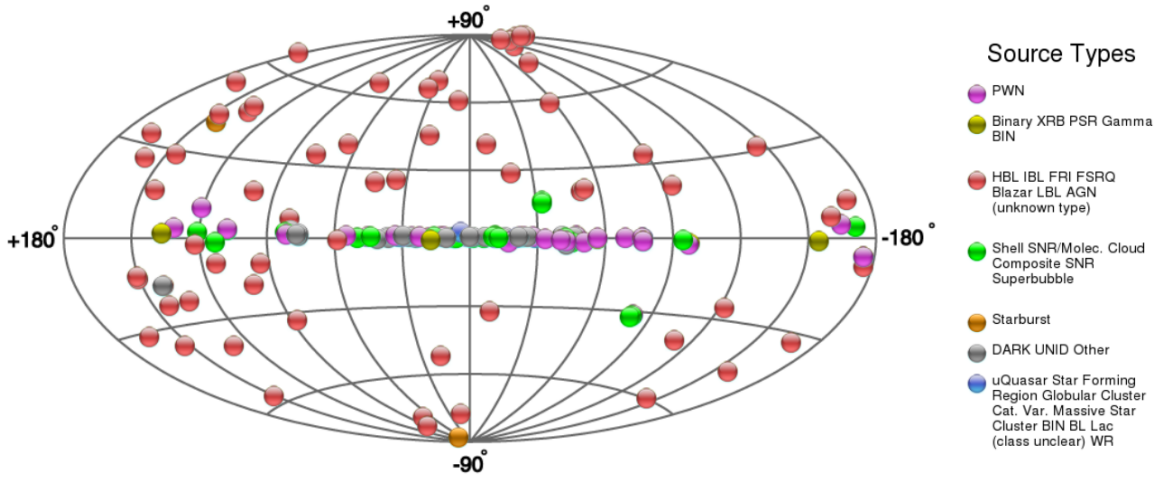


Figure 1.1: The positions and source types of the currently known VHE gamma-ray objects in Galactic coordinates. Image generated using the online source catalogue, TeVCat (Wakely & Horan, 2008).

action of upscattering of background photons via the inverse-Compton effect. Both of these mechanisms require an astrophysical particle accelerator to generate the parent population of energetic particles. Extragalactic sources may include active galactic nuclei, starburst galaxies and gamma-ray bursts, while possible Galactic sources are discussed below. The gamma-ray sources considered in this thesis are all Galactic sources.

### 1.2.1 Supernova Remnants

Supernova remnants (SNR) are thought to be a prime candidate for the acceleration of Galactic cosmic-rays (Baade & Zwicky, 1934; Ginzburg & Syrovatskii, 1964). In a typical supernova explosion, several solar masses worth of material is ejected at high velocities ( $\sim 10^4$  km/s). The rapidly moving ejecta, interacting with the surrounding interstellar medium, produces a radially expanding magnetised shock front with conditions necessary for 1st-order Fermi acceleration to occur (see §1.3.3.2). The canonical amount of kinetic energy that a supernova explosion releases into its ejecta is  $\sim 10^{51}$  erg (1 erg =  $10^{-7}$  Joules). Based on the average rate of supernovae in the galaxy (2-3 per 100 years), only a small fraction ( $\sim 3 - 10\%$ ) of the available kinetic energy is required to go towards accelerating CRs in order for SNRs to provide sufficient power ( $10^{41}$  erg/s) to maintain the level of Galactic CRs up to the knee of the CR spectrum ( $\sim 10^{15}$  eV) (Blandford & Eichler 1987, see §1.3.1).

Accelerated leptons will lose energy dominantly through synchrotron processes in the highly magnetised environment of the shock front (§1.4.2). In young remnants

---

## CHAPTER 1. COSMIC-RAYS, GAMMA-RAYS AND HIGH ENERGY ASTROPHYSICS

---

( $\lesssim 10^3$  yr), X-ray synchrotron radiation is often seen from accelerated high-energy leptons. As the remnant gets older ( $\gtrsim 10^4$  yr), the energy of the local electron population decreases, and synchrotron radiation in the radio band is often observed.

TeV gamma-rays from SNRs may be due to accelerated leptons via the inverse-Compton effect, but competition with the dominant synchrotron energy loss process generally disfavours this scenario. Accelerated CR hadrons, however, may interact with the interstellar medium to produce TeV gamma-rays via p-p interactions and neutral pion decay (§1.4.4). The target material may be located some distance away from the SNR, and CR escape and diffusion become important aspects to consider (Aharonian & Atoyan, 1996). An example of a TeV gamma-ray source identified as the result of CRs accelerated by a SNR interacting with nearby interstellar gas is the W28 SNR (Aharonian et al., 2008).

### 1.2.2 Pulsars and Pulsar Wind Nebulae

Pulsars are rapidly rotating neutron stars produced by the collapse of the progenitor star core in a supernova event. Pulsars have intense magnetic fields which are usually misaligned with their rotation axis. The rotating magnetic fields generate very strong electric fields which accelerate charged particles, primarily leptons, at the surface of the pulsar. Rotational energy from pulsars are transferred into a wind of charged particles which stream radially outwards, forming pulsar wind nebulae (PWN). This outflow of accelerated particles terminate in a shock that may produce synchrotron radiation, and from which acceleration of charged particles may occur. Gamma-rays may be produced from inverse-Compton processes between accelerated leptons and background photons. The Crab Nebula is the most prominent example of a gamma-ray producing PWN (see e.g. Aharonian et al. 2006b).

### 1.2.3 Binary Systems

Binary systems contain two objects; a massive star and a compact object, both of which orbit about a common centre of mass. The compact object is often a neutron star or a black-hole, products of supernova events. Gamma-ray emission from binary systems arise from the interaction between the two objects, either via an accretion powered relativistic jet (microquasar scenario), or via the shock between pulsar and stellar winds (wind scenario).

In the microquasar scenario, particle acceleration occurs at the jets which are powered by the compact object accreting material from the companion massive star. In the wind scenario, particle acceleration may occur in the shocked regions where pulsar and stellar winds interact. The highly accelerated particles can then go on

to produce radiation in a wide energy range, including gamma-ray energies, through processes outlined in §1.4. More detailed reviews of gamma-ray binary systems can be found in, e.g., Rieger et al. (2013) and references within.

### 1.2.4 Massive Stellar Clusters

Massive stellar clusters and star forming regions may be sources of Galactic gamma-rays (e.g. Romero 2008). Stellar clusters may contain a number of energetic stars, each producing strong stellar particle winds. The collisions between stellar winds may produce strong shocks, resulting in particle acceleration to relativistic energies. Additionally, stellar clusters may also contain past supernova explosions, which may help produce super-bubbles and collective shocks leading to further particle acceleration. Locally generated CRs by these processes may interact with the stellar winds or ambient interstellar gas to produce gamma-rays. Examples of massive stellar clusters thought to be involved with the production of TeV gamma-rays are Westerlund 1 (Abramowski et al., 2012) and Westerlund 2 (Aharonian et al., 2007).

### 1.2.5 Diffuse VHE Gamma-ray Emission at the centre of the Galaxy

Diffuse VHE gamma-ray emission was seen by HESS towards the centre of our galaxy, extending over  $1^\circ$  in Galactic longitude (Aharonian et al., 2006a). This gamma-ray emission is spatially coincident with dense interstellar medium that forms the Central Molecular Zone (CMZ). It is likely that CRs accelerated near or at the Galactic centre are interacting with the CMZ to produce the diffuse Galactic ridge of TeV gamma-ray emission. Recent results from HESS on the diffuse VHE gamma-ray emission from the central  $\sim 200$  pc suggest that the inferred CR density follows a gradient, with a maximum towards the inner tens of parsecs (HESS Collaboration, 2016). This gradient is consistent with a scenario in which CRs are accelerated by some steady source at the Galactic centre itself and propagating through the CMZ. The lack of a cut-off seen in the diffuse VHE gamma-ray spectrum indicates that the parent CRs have energies of at least 1 PeV ( $10^{15}$  eV), likely produced by the PeVatron (see §1.2.6) linked with the supermassive black hole at the centre of our Galaxy (HESS Collaboration, 2016).

### 1.2.6 PeVatrons

PeVatrons are a class of particle accelerators thought to be responsible for generating our Galaxy's highest energy PeV CRs. A strong indicator of such an accelerator can be inferred from the observations of gamma-rays at energies up to and beyond 100 TeV.

---

## CHAPTER 1. COSMIC-RAYS, GAMMA-RAYS AND HIGH ENERGY ASTROPHYSICS

---

The is because inverse Compton scattering (see §1.4.1) is severely hampered due to the Klein-Nishina effect in this energy band, and the most likely mechanism capable of producing such gamma-rays is the decay of neutral pions formed by hadronic interactions between the CRs and target interstellar medium (see §1.4.4).

Young SNRs are promising PeVatron candidates (Gabici & Aharonian, 2007), as they are thought to be able to accelerate particles to PeV energies through diffusive shock acceleration (see §1.3.3.2). A nearby molecular cloud may then act as an effective target for the production of TeV gamma-rays. Multi-PeV CRs are only thought to be accelerated during a short period during the SNR lifetime. These CRs will tend to escape the shell earlier and diffuse faster through the ISM compared with lower energy CRs, thus preferentially arriving first at nearby molecular clouds. The multi-PeV CRs interacting with the target molecular clouds may then give rise to the production of gamma-rays with a hard spectrum extending well above several tens of TeV (e.g. Gabici et al. 2009). The time during which such a spectrum may be observed is determined by the propagation time of the CRs to the cloud, rather than the time period in which PeV CRs are able to be accelerated. Hence, the detection of such gamma-ray spectra from molecular clouds may indicate the past PeVatron nature of a nearby SNR (Gabici & Aharonian, 2007).

Several PeVatron candidates have been identified among the known Galactic TeV sources (e.g. Safi-Harb 2017, and references therein), and are included as some of the specific sources studied as part of this thesis (see §1.6).

### 1.2.7 Dark and Unidentified Sources

While many TeV gamma-rays sources have been associated with other astrophysical phenomena, a large population ( $\gtrsim 50\%$ ) of gamma-ray sources remain unidentified (Donath et al., 2017). Figure 1.2 shows the distribution of Galactic TeV gamma-ray source types as seen by the HESS Galactic Plane Survey, and highlights the large fraction of ‘not firmly identified’ and ‘not associated’ sources.

Many of these unidentified sources have several possible counterparts which may be linked to the gamma-ray emission. However, several TeV gamma-ray sources have no promising counterparts seen in any other wavelengths, and have subsequently been referred to as “dark  $\gamma$ -ray sources” (Aharonian et al., 2005a). While the exact mechanisms behind these types of sources are unknown, the lack of emission in lower wavelengths tentatively suggests that the observed gamma-rays are hadronic in origin, as leptonic processes will also generally produce synchrotron radiation (§1.4).

One method to investigate the nature of dark accelerator TeV gamma-ray sources is to study the interstellar medium in the regions where these mysterious sources are

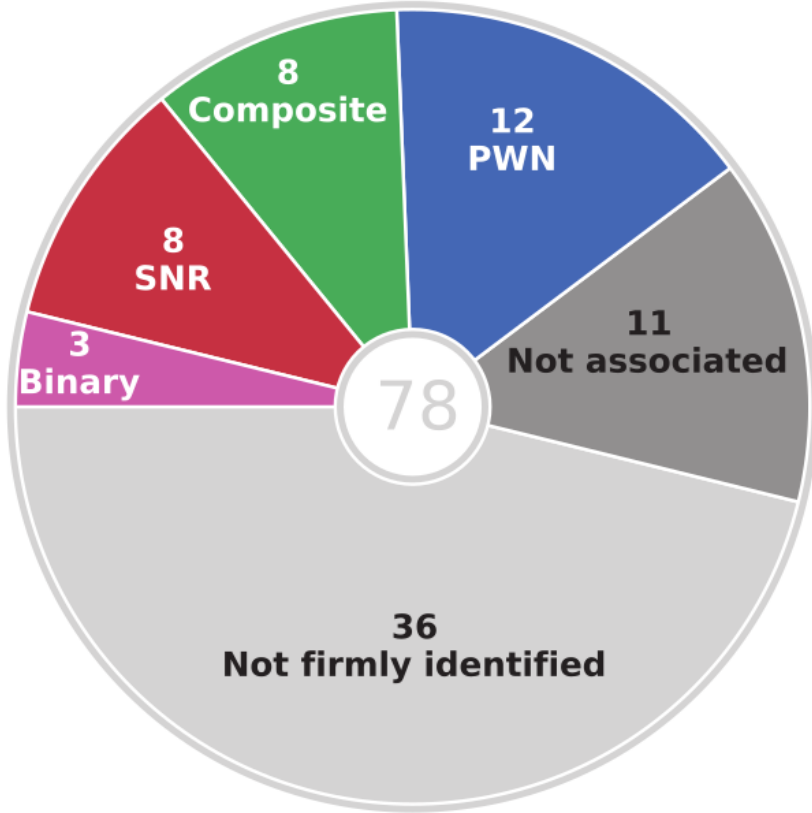


Figure 1.2: Pie chart showing the distribution of Galactic TeV gamma-ray source types in the HESS Galactic Plane Survey. Note that a significant fraction are classified as ‘not firmly identified’ and ‘not associated’. Image is from Donath et al. (2017).

located. In addition to contextual clues which may aid in understanding the local environment in which these sources lie, morphological similarities between gamma-ray emission and interstellar gas can provide strong indicators of hadronic CR interactions. Radio astronomy targeting molecular gas tracers can be used to study the interstellar medium towards unidentified TeV gamma-ray sources, (e.g. Voisin et al. 2016; de Wilt et al. 2017). This is described in detail in Chapter 2.

CRs play an important role in the production of VHE gamma-rays. The following section briefly outlines the current understanding of CRs and how they are produced.

## 1.3 Cosmic Rays and Electrons

Cosmic-rays (CRs) are extremely energetic charged particles of extraterrestrial origin. Consisting primarily of protons and nuclei of heavier elements, CRs travel through the universe with speeds close to that of the speed of light. Over a century ago, Victor

Hess discovered CRs in a series of experiments conducted in a hot air balloon (Hess, 1912), in which he found the atmospheric ionisation rate increased with altitude. Ever since, the nature of CRs has been the subject of intense study by scientists around the world. In this thesis, the term ‘CRs’ will refer to high energy hadrons, while discussion of high energy electrons will be additionally specified.

### 1.3.1 The Cosmic-Ray Spectrum

The Earth is constantly bombarded by CRs with a vast energy spectrum. The energy of these particles range from several GeV ( $10^9$  eV) to in excess of  $10^{20}$  eV (e.g. Abreu et al. 2010), over 10 orders of magnitude. The flux of CRs depends strongly with energy, with CRs in the GeV energies having detected fluxes of  $\sim 1000$  per square metre per second, and CRs with energies  $\sim 10^{20}$  eV having fluxes of  $\sim 1$  per square kilometre per century. The differential energy spectrum of CRs incident on the Earth approximates a power law:

$$\frac{dN}{dE} \propto E^{-\alpha} \quad (1.1)$$

where  $N$  is the number of CRs,  $E$  is the energy and  $\alpha$  is the spectral index. The value of  $\alpha$  varies somewhat with energy, by can generally be approximated to be 2.7 (Protheroe & Clay, 2004). The power law nature of the CR spectrum (Equation 1.1) describes the rapid decrease of the CR flux at higher energies.

Figure 1.3 illustrates the CR spectrum as it is observed from Earth. The figure combines data from many observatories over the vast energy range that CRs appear in. While the general power law form of the spectrum is clearly seen, there are three particular spectral variations that are apparent; the ‘knee’, ‘ankle’, and high energy cutoff. The CR spectral index is seen to be  $\alpha = 2.7$  until the knee region at  $E \sim 10^{15}$  eV, where the spectrum steepens somewhat with a spectral index of  $\alpha \sim 3.3$  (Abraham et al., 2010). Further on, at the ankle region at  $E \sim 10^{18.5}$  eV, the CR spectrum flattens out to a spectral index  $\alpha \sim 2.6$ . At extreme energies,  $E \sim 10^{19.5}$  eV, there is a rapid cutoff in the CR flux.

The shape of the overall CR spectrum, particularly the knee and ankle features, is thought to be the superposition of CRs spectra from more than one source population (see e.g. Blümer et al. 2009). Galactic sources, such as supernova remnants (SNR), pulsar wind nebulae (PWN), binary systems and stellar winds of massive stars (see §1.2 for further discussion and references), may be responsible for CRs in the GeV to TeV energy ranges. Extragalactic sources, such as Active Galactic Nuclei (AGN),

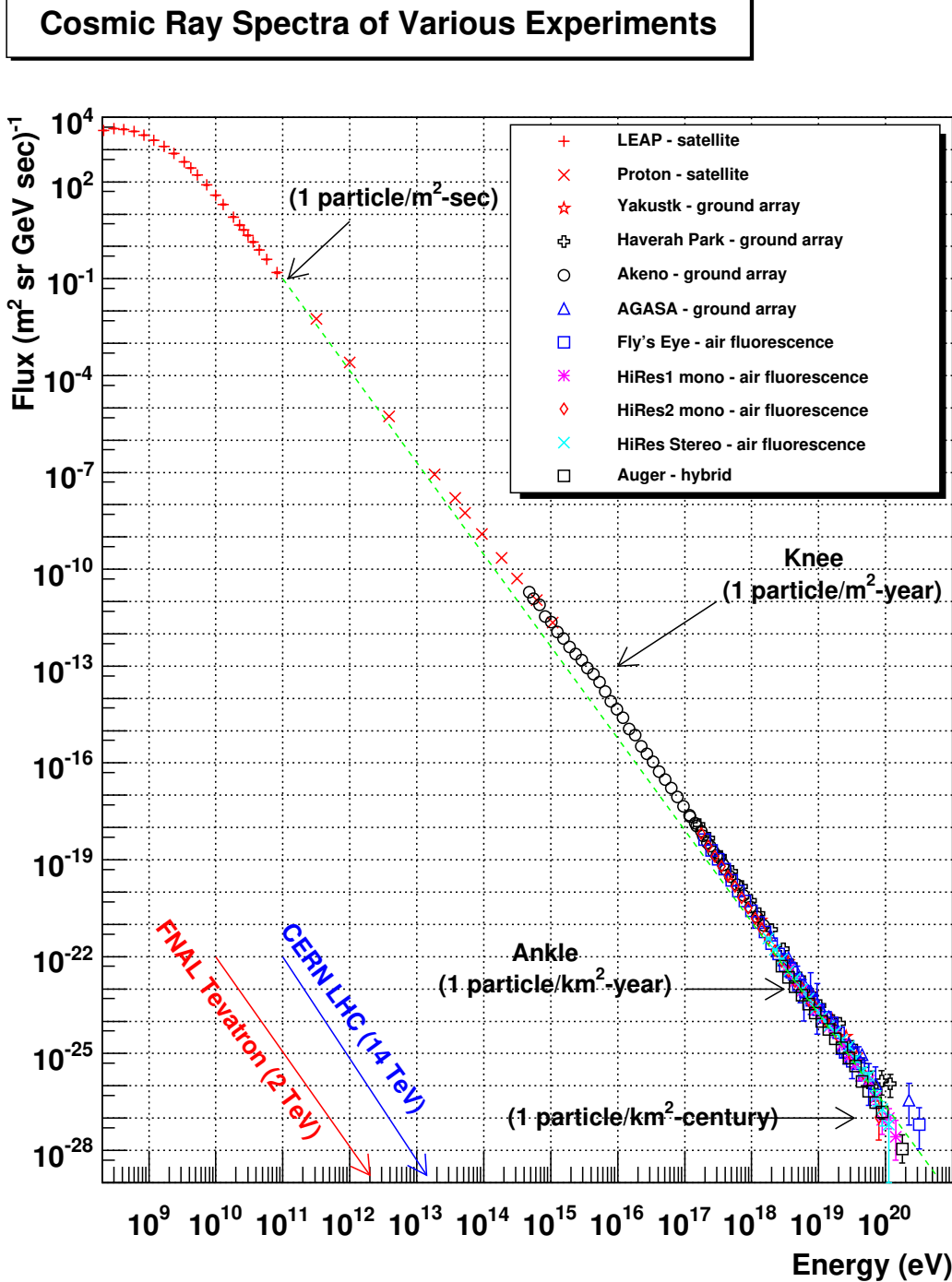


Figure 1.3: The cosmic-ray energy spectrum, as observed by the indicated CR experiments. The highest energy terrestrial particle accelerators are marked on the x-axis for comparison (in rest frame of the lab). Image is taken from <http://www.physics.utah.edu/~whanlon/spectrum1.html>. References to the specific CR experiment results can also be found at the aforementioned site.

starburst galaxies and gamma-ray burst events, would then produce the highest energy CRs. As CRs propagate through space, they interact with Galactic magnetic fields which may also contribute to the resulting CR spectrum observed at Earth. CRs may additionally interact with other particles and photons through a variety of different channels. The cutoff in CRs spectrum above  $E \sim 10^{19.5}$  eV is likely due to one such interaction; Greisen-Zatsepin-Kuzmin (GZK) suppression (Greisen, 1966; Zatsepin & Kuz'min, 1966), in which extremely high-energy CRs collide with cosmic microwave background photons, losing energy through photon-pion production.

### 1.3.2 Cosmic-Ray and Electron Propagation

CRs and electrons are charged particles, and are deflected by Galactic and extra-Galactic magnetic fields. The force they experience is described by the Lorentz equation:

$$\mathbf{F} = q(\mathbf{E} + \mathbf{v} \times \mathbf{B}) \quad (1.2)$$

where  $\mathbf{F}$  is the force vector,  $q$  is the charge of the CR,  $\mathbf{E}$  is the electric field vector,  $\mathbf{v}$  is the CR velocity vector, and  $\mathbf{B}$  is the magnetic field vector. Typically in the interstellar medium, the electric field is negligible, and the dominant contribution of force comes from the magnetic field. Thus we generally ignore the  $\mathbf{E}$  term in Equation 1.2. We consider the maximum deviation a CR will experience travelling through a constant perpendicular magnetic field  $B_\perp$ . This will result in uniform circular motion with some radius  $r_g$ , and we can find an expression for  $r_g$  by considering the equation for centripetal force:

$$\mathbf{F} = \frac{mv^2}{r} \quad (1.3)$$

CRs are relativistic particles and travel close to the speed of light, so we can let  $v \rightarrow c$  and  $m \rightarrow E/c^2$ . Thus, substituting Equation 1.2 into 1.3, and rearranging for  $r$ , it can be shown that:

$$r_g = \frac{(E/1 \text{ Joule})}{qcB_\perp} = \frac{(E/1 \text{ eV})}{ZcB_\perp} \quad (1.4)$$

where  $Z$  is the atomic number of the CR nucleus. The radius  $r_g$  is known as the gyroradius; the radius of the circular path a charged particle will have as it propagates under the influence of a constant and perpendicular magnetic field.

Galactic magnetic fields vary in strength, but are considered to be at and above the order of  $1 \mu\text{G}$  (e.g. Beck 2008). By Equation 1.4 we can see that most CRs, except those at the highest energies, will have gyroradii much less than the scale of the galaxy ( $\sim 30$  kpc). For example, at  $10^{15}$  eV which is typical of CRs at the ‘knee’ of

the CR spectrum, the gyroradius will be  $\sim 1$  pc. Thus, due to deflection by Galactic magnetic fields, CR directional information is lost except at extremely high energies. Except at the highest energies ( $\gtrsim 10^{19}$  eV), the detection of CRs on Earth tells us very little about their position of origin, and we require additional information via other messenger particles to mark CR acceleration sites. Some such messengers are neutrinos and gamma-rays which are produced at CR collisions with ambient matter (see §1.4.4). Gamma-rays are far easier to detect than neutrinos, and instruments such as the High Energy Stereoscopic System (HESS) (§1.5) have made great progress in studying gamma-ray emission towards suspected CR acceleration sites.

### 1.3.3 Cosmic-Ray and Electron Acceleration

The acceleration of CRs to their remarkable energies is still an open question in modern astrophysics. We know, based on the Lorentz equation (Equation 1.2), magnetic fields acting on a CR will not change the total energy of the particle. However, strong electrostatic fields due to large charge separations do not typically exist in space, as free ions are able to move freely to rapidly neutralised any imbalances. In order to find such occurrences of electric fields capable of CR acceleration, we can invoke the Maxwell-Faraday Equation which describes electric fields which are induced by a changing magnetic flux:

$$\oint_S \mathbf{E} \cdot d\mathbf{l} = - \int_S \frac{\partial \mathbf{B}}{\partial t} \cdot d\mathbf{A} \quad (1.5)$$

Here,  $\mathbf{E}$  and  $\mathbf{B}$  are the electric and magnetic fields respectively,  $d\mathbf{l}$  is the infinitesimal vector element of the path which bounds surface  $S$ , and  $d\mathbf{A}$  is the infinitesimal area vector element of  $S$ . In an astrophysical situation, we assume that magnetic fields are frozen into the interstellar medium and are transported together with movement of the gas. The change in the area vector element  $d\mathbf{A}$  can be given by  $d\mathbf{A} = d\mathbf{l} \times \mathbf{v}_{bulk} dt$ , where  $\mathbf{v}_{bulk}$  is the velocity of the expanding surface  $S$  swept up by segment  $d\mathbf{l}$ . Substituting this into Equation 1.5 and using the vector identities  $\mathbf{X} \cdot (\mathbf{Y} \times \mathbf{Z}) = \mathbf{Y} \cdot (\mathbf{Z} \times \mathbf{X})$  and  $\mathbf{X} \times \mathbf{Y} = -\mathbf{Y} \times \mathbf{X}$ , we can rewrite the relation as:

$$\oint_S \mathbf{E} \cdot d\mathbf{l} = \int_S \mathbf{v}_{bulk} \times \mathbf{B} \cdot d\mathbf{l} \quad (1.6)$$

Assuming a constant magnitude for the magnetic field, the induced electric field will be maximised if the magnetic field is moving in a direction that is perpendicular to its orientation. For a fixed magnetic field  $|\mathbf{B}|$  moving with a velocity  $\mathbf{v}_{bulk}$ , the maximum

induced electric field is given by:

$$|\mathbf{E}_{max}| \approx v_{bulk} |\mathbf{B}| \quad (1.7)$$

Charged particles will gain energy as they interact with electric fields. The change in energy of a particle with some velocity  $\mathbf{v}$  and charge  $q$ , due to a constant Lorentz force is given by:

$$\begin{aligned} \frac{dE}{dt} &= \mathbf{v} \cdot \mathbf{F} \\ &= q\mathbf{v} \cdot \mathbf{E} \end{aligned} \quad (1.8)$$

The maximum energy gain rate of a charged particle can be approximated by substituting Equation 1.7 into Equation 1.8, and is given as  $dE/dt \sim qvv_{bulk}|\mathbf{B}|$ . If we let the particle velocity,  $v$ , and the magnetic field carrying gas velocity,  $v_{bulk}$ , be the speed of light,  $c$ , then  $dE/dt < qc^2|\mathbf{B}|$ . By introducing a parameter  $\xi < 1$ , we can write:

$$\left. \frac{dE}{dt} \right|_{acc} = \xi Zec^2 |\mathbf{B}| \quad (1.9)$$

Here, we have taken the charge of the particle  $q$  as  $Ze$ .  $\xi$  is an “acceleration rate parameter” whose value ( $0 < \xi < 1$ ) depends on the acceleration mechanism. Equation 1.9 allows for a basic estimate for the rate at which energy is gained by a charged particle under the influence of an astrophysical magnetic field.

### 1.3.3.1 2nd Order Fermi Acceleration

A method for the acceleration of CR particles via the interaction with magnetic fields in interstellar molecular clouds was first proposed by Fermi (Fermi, 1949). Interstellar molecular clouds have, in addition to regular motion about the galaxy, random local velocities that cause turbulence in their magnetic fields which are ‘frozen in’ to associated ions and plasma (see e.g. Crutcher et al. 2010). Fermi’s original idea was that CR particles entering these clouds would undergo elastic collisions with the associated moving magnetic fields. The change in energy of the CR would depend on the geometry of the collisions; a head on collision with the cloud would impart it with additional energy, while a trailing collision would cause the CR to lose energy.

Consider a charged particle with energy  $E_1$  entering a cloud which has some velocity  $V_{cloud}$  at an incident angle  $\theta_1$  relative to the cloud. This CR undergoes elastic collisions with the turbulent magnetic field inside the cloud, and eventually escapes

the cloud with energy  $E_2$  at an angle  $\theta_2$ . This is illustrated in Figure 1.4. For the relativistic CR particles we are considering, we can use Lorentz transformations to move between the laboratory frame (our frame - unprimed) and the cloud frame (primed).

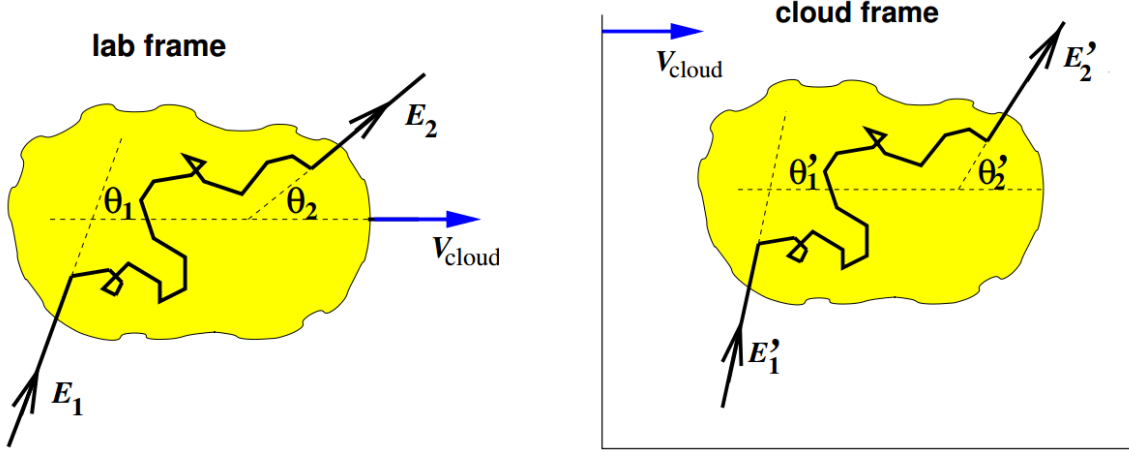


Figure 1.4: *Left:* In the lab frame, a CR with energy  $E_1$  enters an interstellar medium cloud, which has velocity  $V_{\text{cloud}}$ , at some angle  $\theta_1$ . The particle scatters off the magnetic fields inside the cloud and exits with energy  $E_2$  at an angle  $\theta_2$ . *Right:* The situation as seen in the cloud frame. Image is adapted from Protheroe & Clay (2004).

In the cloud frame, the incident energy of the CR particle is given by:

$$E'_1 = \gamma_{\text{cloud}} E_1 (1 - \beta_{\text{cloud}} \cos \theta_1) \quad (1.10)$$

where  $\beta_{\text{cloud}} = V_{\text{cloud}}/c$  and  $\gamma_{\text{cloud}} = 1/\sqrt{1 - \beta_{\text{cloud}}^2}$ . The scattering of the CR off the turbulent magnetic fields is collisionless and elastic, so the energy is unchanged in this frame:

$$\begin{aligned} E'_2 &= E'_1 \\ &= \gamma_{\text{cloud}} E_1 (1 - \beta_{\text{cloud}} \cos \theta_1) \end{aligned} \quad (1.11)$$

In the lab frame, the energy of the exiting CR is given by:

$$\begin{aligned} E_2 &= \gamma_{\text{cloud}} E'_2 (1 + \beta_{\text{cloud}} \cos \theta'_2) \\ \therefore E_2 &= \gamma_{\text{cloud}}^2 E_1 (1 - \beta_{\text{cloud}} \cos \theta_1) (1 + \beta_{\text{cloud}} \cos \theta'_2) \end{aligned} \quad (1.12)$$

We find that there is a change in the energy of the CR between entering and exiting the interstellar medium cloud in the lab frame. The fractional change in energy

is then:

$$\begin{aligned}\frac{\Delta E}{E} &\equiv \frac{E_2 - E_1}{E_1} \\ &= \frac{1 - \beta_{\text{cloud}} \cos \theta_1 + \beta_{\text{cloud}} \cos \theta'_2 - \beta_{\text{cloud}}^2 \cos \theta_1 \cos \theta'_2}{1 - \beta_{\text{cloud}}^2} - 1\end{aligned}\quad (1.13)$$

From here, the average energy change for a large population of charged particles,  $\langle \Delta E / E \rangle$ , can be found by considering the average values of  $\cos \theta_1$  and  $\cos \theta'_2$ . The derivation of these values can be found in §A.1 of Appendix A, and inserting the results into Equation 1.13 yields the expression:

$$\frac{\langle \Delta E \rangle}{E} \approx \frac{4}{3} \beta_{\text{cloud}}^2 \quad (1.14)$$

The average change in energy is positive and a population of CRs will be, on average, accelerated by the process. However, since the process is proportional to  $\beta_{\text{cloud}}^2$ , and  $\beta_{\text{cloud}} \ll 1$ , the average every gain is very small. The reason the energy gain is small is due to there being almost as many head-on collisions (energy gained) as there are overtaking collisions (energy lost) between CRs and the cloud. Due to the proportionality dependent on  $\beta_{\text{cloud}}^2$ , this process is known as ‘2nd order Fermi acceleration’. While the process likely occurs in nature, the small average gain in energy per interaction cannot explain the acceleration of CRs to the observed fluxes.

### 1.3.3.2 1st Order Fermi Acceleration

A modified version of the original theory describes a more efficient method of acceleration that occurs at strong astrophysical shock fronts. In this scenario, charged CR particles are able to scatter off the turbulent magnetic fields that exist on either side of the shock front. Each of these collisions are ‘head-on’, resulting in a rapid increase in particle energy. This is unlike 2nd order Fermi acceleration, in which both head-on and overtaking collisions lead to a slow average gain in energy. As will be explained below, the average energy gain in this process is proportional to some variable  $\beta_s$ , and is known as ‘1st order Fermi acceleration’. This process is also commonly referred to as ‘diffusive shock acceleration’, due to the charged particles being accelerated as they diffusively cross the shock multiple times.

Consider a scenario in which a shock front is formed by the pile up of ambient interstellar medium and associated magnetic fields in front of some rapidly moving ejecta from a violent astrophysical event (e.g. a supernova explosion). CR particles are scattered off the magnetic irregularities on either side of the shock front as illustrated in Figure 1.5. These collisions cause the particles to diffusively cross the shock

multiple times, moving between the regions ‘upstream’ and ‘downstream’ of the shock front, before eventually escaping the system.

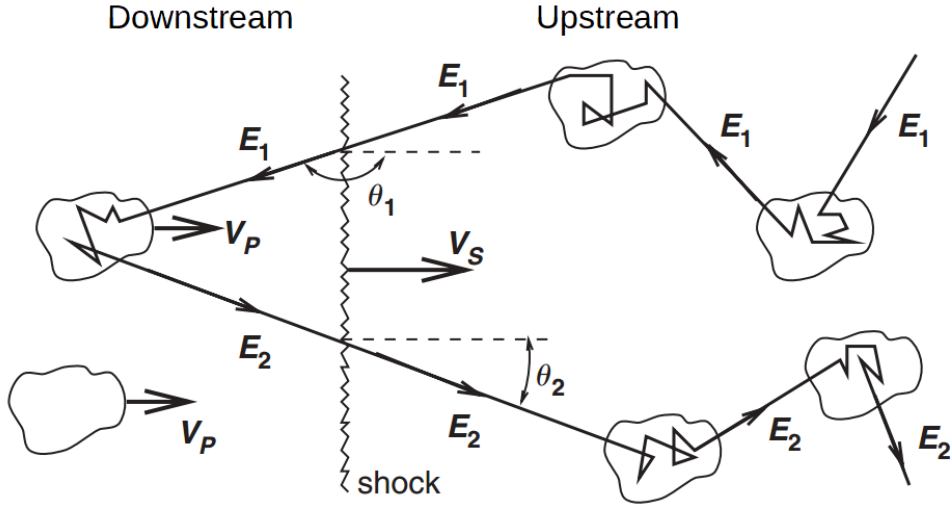


Figure 1.5: Particles being scattered off turbulent magnetic fields that exist on either side of a shock. These magnetic irregularities can be visualised as magnetised clouds as in 2nd order Fermi acceleration (§1.3.3.1).  $v_p$  and  $v_s$  are the velocities of the ejecta and shock respectively. Particles will cross the shock many times, but in this simplified diagram, the particle is only shown crossing the shock twice. Image is adapted from Protheroe & Clay (2004).

Charged particles will cross at a rate from upstream to downstream,  $R_{u \rightarrow d}$ , and at a rate from downstream to upstream,  $R_{d \rightarrow u}$ , given by:

$$\begin{aligned} R_{u \rightarrow d} &\approx -n_{\text{CR}} v \cos \theta_1 & (\text{m}^{-2} \text{s}^{-1}) \\ R_{d \rightarrow u} &\approx n_{\text{CR}} v \cos \theta_2' & (\text{m}^{-2} \text{s}^{-1}) \end{aligned} \quad (1.15)$$

where  $n_{\text{CR}}$  is the CR number density,  $v$  is the velocity of the CRs,  $\theta_1$  is the angle between the direction of the shock and CR particle as it moves downstream through the shock in the lab frame ( $90^\circ < \theta_1 < 180^\circ$ ), and  $\theta_2'$  is the angle between direction of the shock and CR particle as it moves upstream through the shock in the frame of the shock ( $0^\circ < \theta_2' < 90^\circ$ ). The probability density of  $\cos \theta_1$  on shock crossing,  $P(\cos \theta_1) \propto -\cos \theta_1$ , and the probability density of  $\cos \theta_2'$  on shock crossing,  $P(\cos \theta_2') \propto \cos \theta_2'$ .

For an isotropic distribution of CRs, the average values for  $\cos \theta_1$  and  $\cos \theta_2'$  are given by:

$$\begin{aligned}\langle \cos \theta_1 \rangle &= \frac{\int_{-1}^0 p(\cos \theta_1) \cos \theta_1 d \cos \theta_1}{\int_{-1}^0 p(\cos \theta_1) d \cos \theta_1} = \frac{\int_{-1}^0 \cos^2 \theta_1 d \cos \theta_1}{\int_{-1}^0 \cos \theta_1 d \cos \theta_1} = -\frac{2}{3} \\ \langle \cos \theta'_2 \rangle &= \frac{\int_0^1 p(\cos \theta'_2) \cos \theta'_2 d \cos \theta'_2}{\int_0^1 p(\cos \theta'_2) d \cos \theta'_2} = \frac{\int_0^1 \cos^2 \theta'_2 d \cos \theta'_2}{\int_0^1 \cos \theta'_2 d \cos \theta'_2} = \frac{2}{3}\end{aligned}\tag{1.16}$$

Let  $\beta_p = V_p/c$ . The average fractional change in energy of a charged CR crossing the shock is given by:

$$\left\langle \frac{\Delta E}{E} \right\rangle = \frac{1 - \beta_p \langle \cos \theta_1 \rangle + \beta_p \langle \cos \theta'_2 \rangle - \beta_p^2 \langle \cos \theta_1 \rangle \langle \cos \theta'_2 \rangle}{1 - \beta_p^2} - 1\tag{1.17}$$

Hence, using Equation 1.16 and Equation 1.17:

$$\left\langle \frac{\Delta E}{E} \right\rangle \simeq \frac{4}{3} \beta_p = \frac{4}{3} \frac{V_p}{c}\tag{1.18}$$

The velocity of the ejecta,  $V_p$ , and the velocity of the shock  $V_s$  are related by the compression ratio,  $R$ , which is the ratio between densities of the shocked and unshocked gas:  $R = p_{\text{shocked}}/p_{\text{unshocked}}$ . In the ideal case of a strong shock, where  $V_s$  is much greater than the local speed of sound in the medium,  $R = 4$  and  $V_p$  is related to  $V_s$  by:

$$\frac{V_s}{V_p} = \frac{R}{R-1} = \frac{4}{3}\tag{1.19}$$

Thus, the average gain in energy per crossing (Equation 1.18) is then:

$$\left\langle \frac{\Delta E}{E} \right\rangle \simeq \frac{V_s}{c} = \beta_s\tag{1.20}$$

The average energy gain in the process is 1st order in  $\beta_s = V_s/c$ , hence the name ‘1st order Fermi acceleration’. Compared to 2nd order Fermi acceleration, 1st order Fermi acceleration is a much more efficient method of accelerating charged particles, and hence a more probable mechanism to explain the observed CR flux.

It can be shown (See §A.2 of Appendix A) that the CR spectrum generated from 1st order Fermi acceleration is given by:

$$\begin{aligned}Q(> E) &\propto E^{-\frac{3}{R-1}} && \text{(integral form)} \\ Q(E) &\propto E^{-\frac{R+2}{R-1}} && \text{(differential form)}\end{aligned}\tag{1.21}$$

In the case for strong shocks, the compression ratio  $R = 4$ , and so for this ideal case the CR differential energy spectrum  $Q(E) \propto E^{-2}$ . Introduction of other factors into the dynamics of the shock will cause discrepancies in the spectral index of the CR spectrum (e.g. Marcowith et al. 2006), as will energy-dependent escape and loss effects during CR propagation. For example, heavier CR nuclei will experience spallation in collisions during propagation, leading to the production of lighter secondary CR nuclei. The result of the factors is the steepening of the CR energy spectrum, and may explain why the observed CR spectrum at Earth has a spectral index  $\alpha \sim 2.7$  (see §1.3.1). For a further discussion on production of the CR spectrum, see Protheroe & Clay (2004).

## 1.4 Production Processes of High-Energy Radiation

Thermal radiation produces much of the electromagnetic radiation that is observed throughout the universe. The radiation produced from thermal sources is well described by Planck's Law, with the peak frequency proportional to the temperature, and total intensity proportional to temperature to the 4th power (see §2.1). However, thermal sources do not account for all radiation, especially that at higher energies. Non-thermal processes produce electromagnetic radiation over a vast energy range, from low energy radio synchrotron emission up to the very highest energy  $\gamma$ -rays observed. These processes are divided into two groups, leptonic processes and hadronic processes, which involve interactions with leptons and hadrons respectively. Common processes involved in the production of  $\gamma$ -rays and other high-energy radiation are outlined in the following sections.

### 1.4.1 Inverse-Compton Scattering

The inverse-Compton effect involves the up-scattering of lower energy photons to produce higher energy photons via a transfer of energy from high energy particles (Blumenthal & Gould, 1970). In an astrophysical setting, the high energy particles involved are relativistic electrons. Low energy photons are found in various photon fields, including the cosmic microwave background (CMB) which permeates the universe. The average energy loss rate of energetic electrons interacting with an isotropic radiation field via the inverse Compton effect is given by:

$$\frac{dE}{dt} \Big|_{IC} = -\frac{4}{3} U_{\text{rad}} \sigma c \gamma^2 \quad (1.22)$$

where  $U_{\text{rad}}$  is the radiation energy density,  $\sigma$  is the interaction cross-section, and  $\gamma$  is the electron Lorentz factor. When the electron energy is much less than the rest mass energy,  $\sigma$  is equal to the Thompson cross-section,  $\sigma_T$ :

$$\sigma_T = \frac{8\pi}{3} \left( \frac{q^2}{4\pi\epsilon_0 mc^2} \right) \quad (1.23)$$

where  $q$  is the charge,  $m$  is the mass, and  $\epsilon_0$  is the permittivity of free space. In the case of electrons,  $\sigma_T = 6.65 \times 10^{-29} \text{ m}^{-2}$ . For higher energies, in the Klein-Nishina regime, high-energy suppression occurs (Moderski et al., 2005). This causes a cut-off in the photon spectrum at energies of  $\sim 50$  TeV. In the Klein-Nishina regime, the total interaction cross-section  $\sigma_{KN}$  is given by:

$$\sigma_{KN} = \pi r_e^2 \frac{1}{x} \left( \left[ 1 - \frac{2(x+1)}{x^2} \right] \ln(2x+1) + \frac{1}{2} + \frac{4}{x} - \frac{1}{2(2x+1)^2} \right) \quad (1.24)$$

where  $x = \hbar\omega/m_ec^2$  and the electron radius  $r_e = e^2/(4\pi\epsilon_0 m_e c^2)$ . In the ultra-relativistic limit ( $\gamma \gg 1$ ), this cross section is approximately:

$$\sigma_{KN} = \pi r_e^2 \frac{1}{x} \left( \ln(2x) + \frac{1}{2} \right) \quad (1.25)$$

The approximate energy of the photon,  $E_\gamma$ , after undergoing inverse-Compton scattering with an electron of energy  $E_e$  is given by:

$$E_\gamma \simeq \left( \frac{E_e}{mc^2} \right)^2 \epsilon_i = \gamma_e^2 \epsilon_i \quad (1.26)$$

where  $\epsilon_i$  is the initial photon energy.

The energy spectrum of inverse-Compton scattering emission in our galaxy has a power-law form, as the energy spectrum of CR electrons also follows a power-law distribution. Inverse-Compton processes compete with other leptonic energy loss processes, such as synchrotron losses, and the ratio of energy loss is dependent on the local magnetic field strength.

### 1.4.2 Synchrotron Emission

Charged particles are accelerated by magnetic fields and tend to spiral around magnetic field lines, causing the continuous emission of polarised light known as synchrotron radiation. This process is most significant for leptons, and the intensity of

## 1.4. PRODUCTION PROCESSES OF HIGH-ENERGY RADIATION

---

the synchrotron radiation depends on the magnetic field strength and the energy of the charged particles. The average energy loss rate for a charged particle via synchrotron emission is given by:

$$\frac{dE}{dt} \Big|_{sync} = -\frac{4}{3}\sigma_T c U_B \gamma^2 \quad (1.27)$$

where  $\sigma_T$  is the Thompson cross section (Equation 1.23),  $U_B = B^2/2\mu_0$  is the energy density in the magnetic field and  $\gamma = (E/mc^2)$  is the Lorentz factor of the charged particle. The characteristic frequency of the produced synchrotron radiation,  $\nu_c$ , is:

$$\nu_c = \frac{3}{2}\gamma^2 \nu_{cycl} \sin \alpha \quad (1.28)$$

where  $\nu_{cycl} = eB/2\pi m_e$  is the cyclotron frequency of the electron and  $\alpha$  is the ‘pitch angle’ between the electron’s direction and the magnetic field.

Synchrotron emission can produce photons over a large energy range. Synchrotron photons produced from highly accelerated TeV electrons are typically in the X-ray band, while lower energy electrons can produce photons anywhere between the radio and UV bands, depending on the local magnetic field strength, and is the main source of non-thermal emission observed. Like inverse-Compton scattering emission, the astrophysical energy spectrum of synchrotron emission is described by a power law, which reflects the power law form of the CR electron source population.

Synchrotron and inverse-Compton processes will compete with each other for the energy in a population of leptons. The ratio of energy loss to synchrotron and inverse-Compton processes depends on the local magnetic field strength. For a given magnetic field, the relative photon fluxes due to synchrotron radiation,  $F_{sync}$ , and inverse-Compton scattering of CMB photons in the Thompson regime,  $F_{IC}$ , can be approximated by (Aharonian et al., 1997):

$$F_{IC} \simeq \frac{F_{sync}}{10(B/10\mu G)^2} \quad (1.29)$$

It is clear that synchrotron emission will tend to dominate in regions of strong magnetic fields. This can also be seen by comparing the respective energy-loss timescales (see §1.4.5) for synchrotron and inverse-Compton processes.

### 1.4.3 Bremsstrahlung

Bremsstrahlung ('braking radiation') is the radiation that is produced by the deflection and deceleration of charged particles when interacting with electric fields of other particles. This process is most significant for electrons. The average electron energy loss rate due to Bremsstrahlung, propagating through material with atomic number  $Z$ , is given by:

$$\frac{dE}{dt} \Big|_{Br} = -E_e \frac{n_Z Z(Z+1.3)e^6}{16\pi^3 \hbar \epsilon_0^3 c^5 m_e^2} \left[ \ln \left( \frac{183}{Z^{1/3}} \right) + \frac{1}{8} \right] = -\frac{E_{epc}}{X_0} \quad (1.30)$$

where the  $n_Z$  is the number density of the target material,  $E_e$  is the electron energy,  $p$  is the density and  $X_0$  is the Bremsstrahlung radiation length. For hydrogen gas,  $H_2$ ,  $Z = 1$  and  $X_0 = 61.28 \text{ g cm}^{-2}$ . In the interstellar environment, the density of target material can be very low ( $\sim 1 \text{ cm}^{-3}$ ) and as such the effect of Bremsstrahlung on high energy electrons is often not significant compared to that of synchrotron and inverse Compton processes.

### 1.4.4 Cosmic-ray and Interstellar Medium Collisions

Collisions between relativistic protons (such as CRs) and other protons or nuclei produce a shower of secondary particles. These processes are known as 'proton-proton interactions' (p-p interactions). Many of the secondary particles are pions, which are hadronic particles consisting of two quarks. There are 3 types of pions; positively charged, negatively charged and neutral, all of which are produced in roughly equal quantities via these collisions (Allan, 1971). Charged pions have a mean life of  $\sim 10^{-8} \text{ s}$  and quickly decay into a muon and muon neutrino. The neutral pions,  $\pi_0$ , have a mean life of  $\sim 10^{-16} \text{ s}$  and decay even more rapidly into a pair of gamma-ray photons. In p-p interactions, roughly half the energy of the primary proton is carried away by the leading proton or nuclei, while the rest goes into the generation of pions and a small number of heavier hadrons. As a consequence, approximately 1/6 of the energy of the primary CR proton is carried away by the gamma-rays generated through neutral pion decay. The average energy loss-rate for CRs via p-p interactions is given by:

$$\frac{dE}{dt} \Big|_{pp} = n_p \sigma_{pp} f c E_p \quad (1.31)$$

where  $n_p$  is the proton density of the target,  $\sigma_{pp}$  is the total p-p interaction cross-section,  $f$  is the inelasticity of interactions and  $E_p$  is the energy of the original proton.

A more detailed review of this process can be found in Aharonian (2004). Throughout this thesis, the ‘hadronic’ production of gamma-rays refers to this process of neutral pion production and decay. However, it is worth noting that additional channels such as the production of other neutral mesons also contribute sub-dominantly to the hadronic gamma-ray population.

Taking a power law injection spectrum of CRs, the spectrum of gamma-rays produced by p-p interactions and neutral-pion decay will also be a power law distribution. Above a few GeV, the gamma-ray spectrum will closely follow that of the parent population of protons (Aharonian, 2004).

#### 1.4.5 Energy-Loss Timescales

In order to compare the energy loss rates of the above described processes, one can consider the approximate time for a particle to give up all its energy through a single process, assuming a constant energy loss rate. This parameter,  $\tau \sim E/(dE/dt)$ , is known as the cooling time of the process.

For inverse Compton emission (leptons), the cooling time  $\tau_{IC}$  is:

$$\tau_{IC} \sim 3 \times 10^8 \left( \frac{U_{\text{rad}}}{\text{eV cm}^{-3}} \right)^{-1} \left( \frac{E}{\text{GeV}} \right)^{-1} \quad [\text{yr}] \quad (1.32)$$

For synchrotron emission (leptons), the cooling time  $\tau_{sync}$  is:

$$\tau_{sync} \sim 1.3 \times 10^5 \left( \frac{E}{\text{TeV}} \right)^{-1} \left( \frac{B}{10 \mu\text{G}} \right)^{-2} \quad [\text{yr}] \quad (1.33)$$

For Bremsstrahlung (leptons), the cooling time  $\tau_{Br}$  is:

$$\tau_{Br} \sim 4 \times 10^7 \left( \frac{n}{\text{cm}^{-3}} \right)^{-1} \quad [\text{yr}] \quad (1.34)$$

For pion decay from proton-proton scattering (hadrons), the cooling time  $\tau_{pp}$  is:

$$\tau_{pp} \sim 5.3 \times 10^7 \left( \frac{n}{\text{cm}^{-3}} \right)^{-1} \quad [\text{yr}] \quad (1.35)$$

For highly energetic TeV leptons in the interstellar medium, synchrotron and inverse-Compton will be the main energy-loss processes competing, as the effect of Bremsstrahlung is often not significant given the relatively low gas densities. As described in the above sections, the local magnetic field strength and the relative interstellar radiation field will determine the relative dominance between synchrotron and inverse-Compton. In

---

## CHAPTER 1. COSMIC-RAYS, GAMMA-RAYS AND HIGH ENERGY ASTROPHYSICS

---

regions of strong magnetic fields, high energy leptons may emit non-thermal X-rays via synchrotron, while an absence of such magnetic fields in a region may result in the up-scattering of ambient photons to gamma-ray energies via inverse-Compton.

It is often difficult to discern which processes produce the gamma-rays that are observed from a given region. In many cases, both hadronic and leptonic emission mechanisms can be invoked to explain the gamma-ray flux. However, hadronic production via p-p interactions requires target material for energetic hadrons (CRs) to interact with. Thus, observations of the interstellar gas, which may act as the required target material, is a useful tool to aid in distinguishing between hadronic and leptonic production of gamma-rays. Gamma-rays produced hadronically are expected to have overlap with gas, and will be less likely to occur towards regions where there is little or no gas present.

## 1.5 Ground Based Gamma-ray Astronomy

Very high energy (VHE,  $E > 100$  GeV) gamma-rays cannot be observed directly on the surface of the Earth, due to attenuation caused by the atmosphere. In addition, the low flux of these gamma-rays limit the use of space-based detectors, as the required collection area would be both physically and economically impractical. The relatively recent advent of ground based detection techniques, however, has allowed for the rapid progression in the exploration of VHE gamma-ray sky.

Ground based gamma-ray astronomy takes advantage of the cascade of secondary particles that are produced when an incident gamma-ray interacts with the Earth's atmosphere. These energetic secondary particles, collectively known as an extended air-shower, produce Cherenkov light as they travel at speeds greater than the local speed of light. Ground-based Imaging Atmospheric Cherenkov Telescopes (IACTs) collect this Cherenkov light, and analysis techniques are applied to the image to reconstruct the parameters of the original gamma-ray. Current generation instruments, such as the High Energy Stereoscopic System (HESS) utilise multiple IACTs in an array which allows for the observation of air showers from several different angles to uniquely determine the shower direction, improving angular and energy resolution.

### 1.5.1 Extensive Air-Showers

When highly energetic CRs and gamma-rays enter the Earth's atmosphere, they will eventually interact with atmospheric nuclei, producing secondary particles. The nature of the interaction differs depending on whether the ‘primary particle’ is a hadron (a CR) or a gamma-ray. These secondary particles will go on to interact with other atmospheric nuclei, producing additional particles. This process repeats

again and again, forming a cascade of secondary particles called an extended air-shower. Extended air-showers initiated by CRs are known as hadronic extended air-showers, while those initiated by gamma-rays are known as electromagnetic extended air showers. Figure 1.6 shows simulated examples of the extended air-showers. The properties of these two types of extended air-showers differ, and are briefly described in the following section.

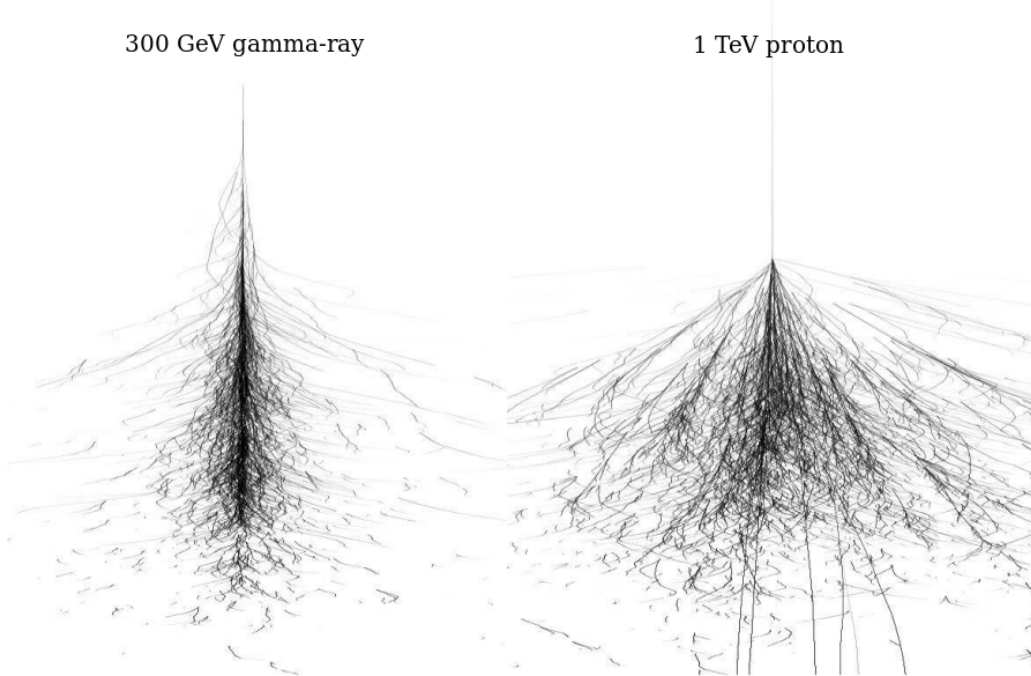


Figure 1.6: Simulated tracks of secondary particles and photons in extended air-showers. *Left:* An electromagnetic extended air-shower initiated by a 300 GeV gamma-ray. *Right:* A hadronic extended air-shower initiated by a 1 TeV proton. Image is adapted from Völk & Bernlöhr (2009).

### 1.5.2 Electromagnetic Extensive Air-Showers

Gamma-rays incident on the Earth's atmosphere will initiate an electromagnetic extended air-shower. In the presence of atmospheric nuclei, a gamma-ray will undergo the process of pair production to create an electron-positron pair. This electron-positron pair will interact with atmospheric nuclei via Bremsstrahlung to create new photons. These new photons, which are of high energy, can further go on to produce more electron-positron pairs through pair production. The cycle continues, resulting in a cascade of particles and photons. The process will continue to exponentially grow until the energy of the particles fall below some critical energy,  $E_c$ , where the energy loss rate from ionisation processes dominate over the energy loss from Bremsstrahlung.

## CHAPTER 1. COSMIC-RAYS, GAMMA-RAYS AND HIGH ENERGY ASTROPHYSICS

---

At this point, the number of particles and photons no longer increase and the shower terminates.

One idealised model that is used to understand this secondary particle shower is the Heitler model, formulated by Heitler (1954). For simplicity, this model only considers pair production and Bremsstrahlung processes, and assumes that the interaction length and radiation length,  $\lambda$  [ $\text{g cm}^{-2}$ ], is equal (true to within  $\sim 25\%$ ). For every individual interaction, it is assumed that the energy is split evenly between the photons and particles. Thus, a Bremsstrahlung photon will carry half the energy of the lepton, and pair production will result in two photons of the same energy. Figure 1.7 is a schematic diagram of the Heitler model for an electromagnetic extended air-shower.

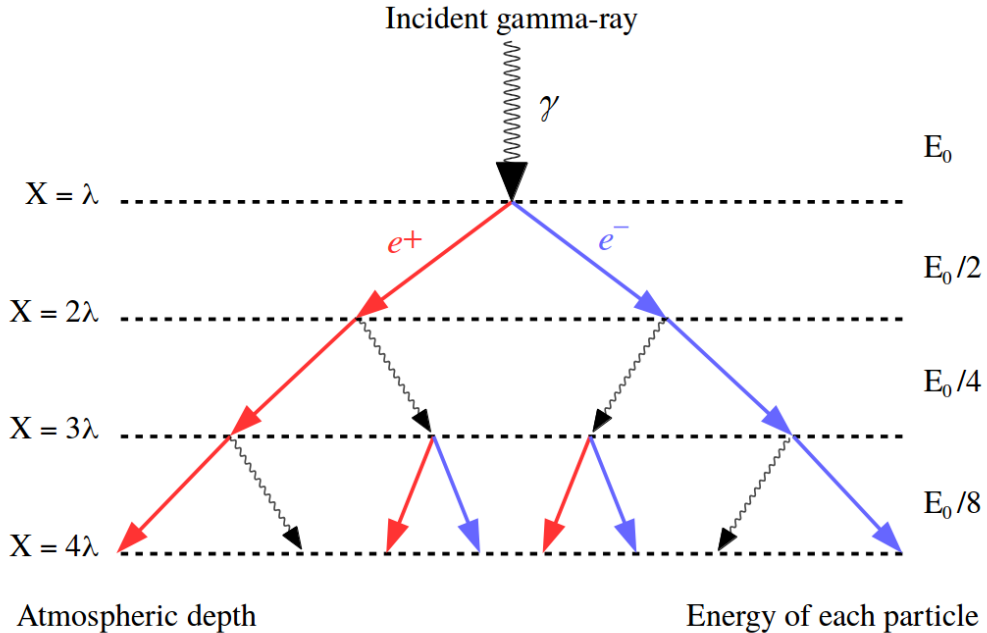


Figure 1.7: A schematic diagram of the Heitler model for an electromagnetic extended air-shower. Four interaction lengths,  $\lambda$ , are shown in this diagram, indicated by the left-hand scale. The primary gamma-ray has an initial energy of  $E_0$ , and the energy of each particle is shown on the right-hand scale.

In the Heitler model, the number of secondary particles double after each interaction length. After  $n$  number of interaction lengths, the number of secondary particles is then  $2^n$ , each with some energy given by:

$$E(n) = \frac{E_0}{2^n} \quad (1.36)$$

There exists some critical energy,  $E_c$ , at which energy losses are dominated by ionisation processes and the number of particles in the shower begin to decline. Thus, the maximum number of particles that can occur in the shower is:

$$N_{\max} = \frac{E_0}{E_c} \quad (1.37)$$

Since the maximum depth of the shower is given by  $X_{\max} = n\lambda$ , the maximum number of particles can also be expressed as:

$$N_{\max} = 2^{X_{\max}/\lambda} \quad (1.38)$$

By combining Equations 1.37 and 1.38, an expression for the maximum shower depth can be derived:

$$X_{\max} = \lambda \frac{\ln\left(\frac{E_0}{E_c}\right)}{\ln(2)} \quad (1.39)$$

The above equations show that the number of particles at the shower maximum is directly proportional to the initial energy of the gamma-ray  $E_0$ , and that the atmospheric depth at the shower maximum is logarithmically proportional to  $E_0$ . Both of these are results that are important for energy reconstruction.

### 1.5.3 Hadronic Extensive Air-Showers

CRs incident on the Earth's atmosphere will initiate a hadronic extended air-shower. Compared to electromagnetic extended air-showers, additional hadronic interactions occur, leading to creation of larger variety of secondary particles. These particles include muons, pions and nucleons, which are produced from nuclear fragmentation, along with pair produced electron-positrons and Bremsstrahlung photons. The hadronic components of the air-shower often have larger interaction lengths than those present in electromagnetic air-showers, and hence the shower maximum is generally reached at a lower point in the atmosphere.

In a hadronic extended air-shower, the initial primary hadron interacts with the atmosphere via a p-p interaction producing charged and neutral pions,  $\pi^{\pm,0}$ , along

## CHAPTER 1. COSMIC-RAYS, GAMMA-RAYS AND HIGH ENERGY ASTROPHYSICS

---

with other mesons and baryons. The nucleons can then go on to interact via further p-p interactions. Neutral pions will rapidly decay into a pair of gamma-rays. These gamma-rays can undergo pair production, spawning an electron-positron pair, initiating an sub-electromagnetic shower component (§1.5.2). The charged pions can decay into a charged muon-neutrino pair, and the charged muons will further decay into electron/positrons and more neutrinos. The decay chain of pions are summarised below:

$$\begin{aligned}\pi^+ &\rightarrow \mu^+ + \nu_\mu & \mu^+ &\rightarrow e^+ + \nu_e + \bar{\nu}_\mu \\ \pi^- &\rightarrow \mu^- + \bar{\nu}_\mu & \mu^- &\rightarrow e^- + \bar{\nu}_e + \nu_\mu \\ \pi^0 &\rightarrow 2\gamma\end{aligned}\tag{1.40}$$

Figure 1.8 is a schematic diagram of a hadronic extended air-shower, illustrating the various decay paths and sub-components within.

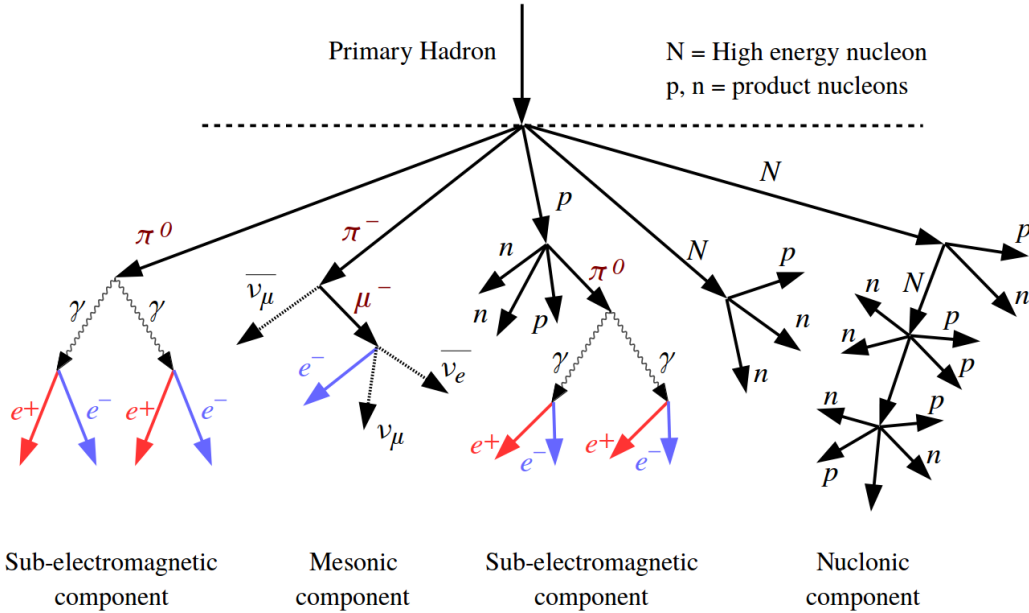


Figure 1.8: A schematic diagram of a hadronic extended air-shower. These extended air-showers contain sub-electromagnetic components, mesonic components and nuclonic components.

Compared with electromagnetic extended air-showers, inelastic scattering in a hadronic extended air-showers cause a greater lateral spread in the particles and shower structure. Thus CR initiated air-showers can often be distinguished from gamma-ray initiated showers based on their lateral extents. This difference is clearly seen when comparing the simulated air-showers displayed in Figure 1.6.

### 1.5.4 Cherenkov Light and its Imaging

Cherenkov light is radiation that is emitted when a charged particle moves through a dielectric medium at a velocity greater than that of the local phase velocity of light. As the high velocity charged particles propagate through the medium, the surrounding molecules are temporarily polarised due to the electromagnetic disruption. These polarised molecules oscillate back to restore equilibrium and in the process emit electromagnetic radiation. Typically, for charged particles moving at velocities less than the local speed of light, destructive interference occurs between the photons and the radiation is not detected. In the case where the velocity of the charged particle is greater than the speed of light in the medium, constructive interference occurs in an electromagnetic scenario analogous to a sonic boom (see Figure 1.9). This light is known as Cherenkov light and is produced by the relativistic secondary particles that form in an extended air-shower.

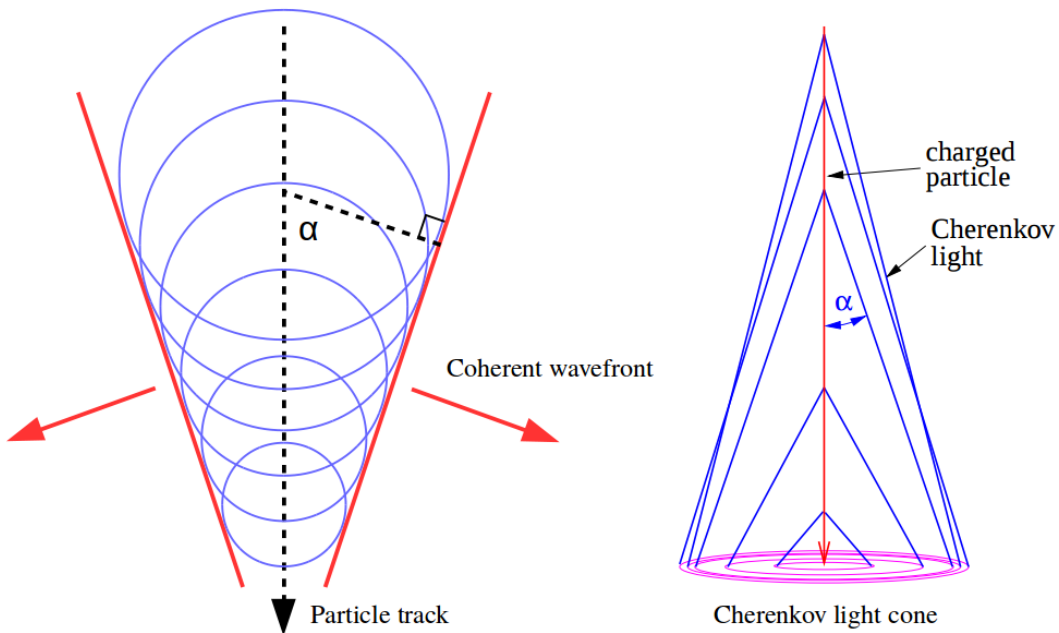


Figure 1.9: Schematic diagram illustrating the geometry of Cherenkov light produced by a charged particle moving faster than the local speed of light. **Left:** Huygens construction of wavelets (blue) show how a coherent wave-front of Cherenkov light (red) is formed due to constructive interference. **Right:** Adapted from Völk & Bernlöhr (2009), this shows the atmospheric Cherenkov emission from a downward-moving single particle.

The Cherenkov light for a single particle can be shown to be emitted in a forward cone as illustrated in Figure 1.9. The angle of the cone,  $\alpha$ , is given by:

$$\cos \alpha = \frac{1}{v} \frac{c}{n} \quad \text{for } v > \frac{c}{n} \quad (1.41)$$

where  $v > c/n$  is the velocity of the particle, and  $n$  is the refractive index of the medium. In the case of the atmosphere, the refractive index increases with lower altitude and consequently the value of  $\alpha$  is greater at lower altitudes.  $\alpha$  reaches a value of  $\sim 1.3^\circ$  at sea-level. The sum of the Cherenkov light generated by the secondary particles in an electromagnetic extended air-shower due to a high energy gamma-ray will create an approximately uniformly distributed ‘light pool’ at ground level. The light pool will have a radius of about  $\sim 150$  m for initial gamma-ray energies of  $\sim 100$  GeV, but can extend up to  $\sim 1$  km for gamma-rays of energies  $\geq 100$  TeV.

IACTs used in ground based gamma-ray observatories image the Cherenkov light generated by the particles of an extended air-shower. When projected onto the 2D focal plane, the Cherenkov light cone appears as an illuminated ellipse. Hence, the combined Cherenkov light from the many secondary particles in the shower will be seen as an elliptical burst of light by IACTs. These ellipses are described geometrically by the semi-major (‘length’,  $l$ ) and semi-minor (‘width’,  $w$ ) axes, and are calculated from the IACT images (see e.g. Aharonian et al. 2006b for the analysis carried out by HESS).

The parameters of the ellipse are useful in distinguishing between gamma-ray and CR initiated extended air-showers. Since hadronic extended air-showers have a larger lateral extent than electromagnetic extended air-showers (see §1.5.3), Cherenkov light images of hadronic air-showers are generally less ‘tight’ than electromagnetic air-shower. This can be seen in Figure 1.10, which shows an example of the Cherenkov images seen from electromagnetic and hadronic extended air-showers. This allows of the rejection of the CR background, which comprises of  $\sim 99.9\%$  of observed events.

### 1.5.5 High Energy Stereoscopic System

The High Energy Stereoscopic System (HESS), is an array of IACTs used to detect gamma-rays in the GeV to TeV energy range (see HESS website 2017). It is located on the Khomas Highlands of Namibia. HESS, as part of ‘Phase I’, consisted of four, 12 m diameter IACTs arranged in a square formation with sides of length 120 m. These telescopes came to full operation at the end of 2003. As part of Phase II, a much larger 28 m IACT was built at the centre of the array, and has been operating since 2012. A photograph of the HESS site with the 5 IACTs can be seen in Figure 1.11.

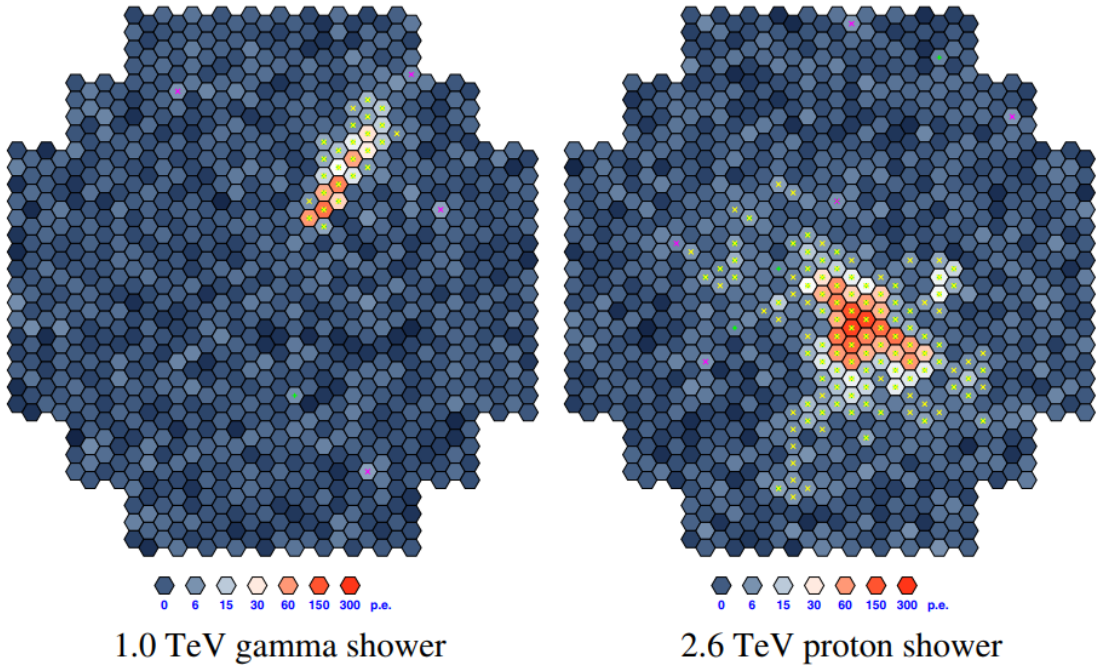


Figure 1.10: Examples of Cherenkov light images that are seen from gamma-ray induced (electromagnetic) extended air-showers and from CR induced (hadronic) extended air-showers. Image is from Völk & Bernlöhr (2009).

HESS has an energy threshold of  $\sim 100$  GeV before selection cuts and an angular resolution of  $\sim 0.1^\circ$  for individual gamma-rays. The sensitivity of HESS between several hundred GeV and few tens of TeV is  $\sim 1\%$  of the flux of the Crab Nebula, given an observation time of  $\sim 25$  hours. Details on the analyses conducted on the images taken by HESS can be found in Aharonian et al. (2006b).

Throughout its operation, HESS has discovered and observed the majority of VHE gamma-ray sources along the Galactic plane (Aharonian et al., 2005a, 2006c; Deil et al., 2015). Many of these extended, Galactic sources have been associated with high-energy phenomena, such as pulsar wind nebulae (PWN), supernova remnants (SNRs) and binaries (Renaud et al. (2008); Aharonian et al. (2005b, 2008) etc.). In addition, a large population of VHE sources appear to have no clear counterparts seen in other wavelengths, and are considered dark or unidentified sources (Aharonian et al., 2005a; Deil et al., 2015). A discussion of these sources can be found in an earlier section of this chapter (§1.2).

To investigate the nature of dark TeV gamma-ray sources, we can study the interstellar medium towards where these sources are located. These studies may provide contextual clues about the sources, and morphological similarities between gamma-ray emission and interstellar gas may suggest sites of CR interactions. In order

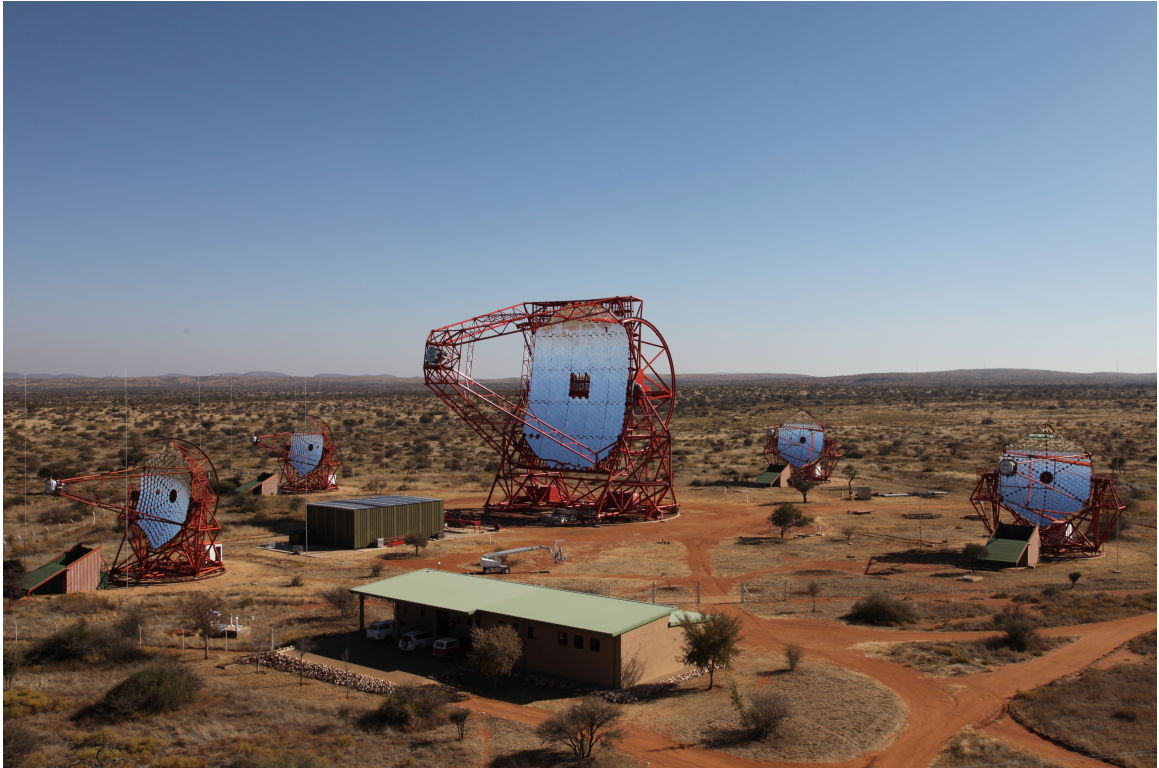


Figure 1.11: The High Energy Stereoscopic System (HESS) in the Khomas Highlands of Namibia. The four smaller IACTs are located at the corners of a square with side lengths of 120 m. The larger IACT, HESS II, is located at the center of the arrangement. Image credit: HESS Collaboration, Clementina Medina.

to study the interstellar medium towards VHE gamma-ray sources, radio astronomy techniques can be applied to study spectral lines emitted by the gas. This is discussed in more detail in the following chapter.

## 1.6 TeV gamma-ray sources studied

The interstellar medium towards five TeV gamma-ray sources, each unique in their own way, were studied as part of this thesis.

**HESS J1640–465 and HESS J1641–463** are a pair of gamma-ray sources each coincident with a SNR, and bridged by a complex structure of bright HII regions. HESS J1641–463 is peculiar in that it is one of the strongest PeVatron candidates known, with a very hard gamma-ray spectrum which extends into several tens of TeV with no sign of a cutoff. The study of the interstellar medium towards this pair of sources is presented in Chapter 3.

**HESS J1614–518** has no immediately obvious counterparts seen in any other wavelengths, and is one of the best examples of a dark TeV gamma-ray source. The nearby TeV source **HESS J1616–508** has several potential counterparts, including two SNRs and three pulsars, though none have been firmly associated with the TeV emission. The interstellar medium study conducted towards these sources as part of this thesis is presented in Chapter 4.

Finally, **HESS J1702–420** is another dark TeV gamma-ray source. While a SNR and pulsar are seen near the outskirts of this source, neither have been considered strong contenders for association. This source is also considered a potential PeVatron candidate, with a hard gamma-ray spectrum extending to at least several tens of TeV. The study of the interstellar medium towards HESS J1702–420 is presented in Chapter 5.

CHAPTER 1. COSMIC-RAYS, GAMMA-RAYS AND HIGH ENERGY  
ASTROPHYSICS

---

# Chapter 2

## Spectral Lines and Radio Astronomy

As briefly touched upon in the previous chapter, a detailed understand of the interstellar medium (ISM) is required in order to help identify the production mechanisms responsible for TeV gamma-ray sources. In particular, to distinguish between the hadronic and leptonic nature of the TeV emission. An accurate understanding of the ISM may also yield contextual clues, such as the conditions of the local environment and the distance to the emission, all of which are useful in unravelling the nature of the TeV source.

One method to study the ISM is to observe the spectral line radiation emitted by excited molecules. Radio observations targeting the various molecular spectral lines can provide information on the physical parameters of the ISM. Understanding the distribution of the local ISM is useful in the modelling of TeV gamma-rays produced by energetic CRs or electrons from nearby high energy sources.

This chapter begins with a review of basic radiation theory (§2.1) and the underlying physics behind molecular line emission (§2.2). Following this, an explanation of the techniques used in single-dish radio astronomy is given (§2.3), as well as an overview of the physical parameters that can be calculated from spectral line observations (§2.4, §2.5). Finally, the atomic and molecular lines tracers utilised in this thesis are discussed (§2.6). Much of the following is based on Townes & Schawlow (1955), Rybicki & Lightman (1979), Goldsmith & Langer (1999) and Wilson et al. (2009).

## 2.1 Basic Radiation Theory

### 2.1.1 Intensity, Flux and Luminosity

The specific intensity,  $I_\nu$ , of radiation in the frequency range  $\nu$  to  $\nu + d\nu$  is given by:

$$I_\nu = \frac{dE}{dA dt d\nu d\Omega} \quad [\text{W m}^{-2} \text{Hz}^{-1} \text{sr}^{-1}] \quad (2.1)$$

where  $dE$  is the energy of the radiation received over area  $dA$  in the time interval  $dt$  from some solid angle  $d\Omega$ .

Consider some astrophysical source of radiation with angular diameter  $d\Omega_s$ . The specific flux,  $F_\nu$ , of the source can be derived by integrating  $I_\nu$  over  $d\Omega_s$ :

$$F_\nu = \int_{d\Omega_s} I_\nu(\Omega) d\Omega \quad [\text{W m}^{-2} \text{Hz}^{-1}] \quad (2.2)$$

which is also commonly expressed in units of Jansky ( $1 \text{ Jy} = 10^{23} \text{ erg cm}^{-2} \text{s}^{-1} \text{Hz}^{-1}$ ). In the case where the source has a uniform intensity, the expression for  $F_\nu$  can be simplified as:

$$F_\nu = I_\nu \Delta\Omega_s \quad [\text{W m}^{-2} \text{Hz}^{-1}] \quad (2.3)$$

For an isotropically radiating source, the flux is dependent on the distance. In this case, the radiative energy is distributed evenly on a sphere of surface area  $4\pi d^2$ , where  $d$  is the distance from the source. The specific luminosity of a source,  $L_\nu$ , is the total radiative energy emitted between the frequency range  $\nu$  to  $\nu + d\nu$ . For an isotropically emitting source,  $L_\nu$  can be given in terms of  $F_\nu$  by:

$$L_\nu = 4\pi d^2 F_\nu \quad [\text{W Hz}^{-1}] \quad (2.4)$$

The bolometric intensity, bolometric flux and bolometric luminosity can be obtained by integrating  $I_\nu$ ,  $F_\nu$  and  $L_\nu$  respectively over the entire frequency range.

### 2.1.2 Thermal Radiation and Brightness Temperature

Thermal radiation is the radiation that is produced by the thermal motion of particles. A black body is an idealised object which absorbs all incident radiation. In thermal equilibrium, where there is no heat flow to or from the object, the intensity of the thermal radiation of frequency  $\nu$  produced by a black body is described by Planck's Law:

$$I_\nu = B_\nu(T) = \frac{2h\nu^3}{c^2} \frac{1}{\exp(h\nu/kT) - 1} \quad (2.5)$$

where  $h$  is Planck's constant ( $6.626 \times 10^{-34}$  J s),  $c$  is the speed of light ( $3 \times 10^8$  m s $^{-1}$ ) and  $k$  is Boltzmann's constant ( $1.380 \times 10^{-23}$  J K $^{-1}$ ). For a given temperature, this distribution has a maximum intensity at some frequency  $\nu_{\text{peak}}$  and corresponding wavelength  $\lambda_{\text{peak}}$  which can be calculated using Wien's displacement law:

$$\lambda_{\text{peak}} = \frac{b}{T} \quad (2.6)$$

where  $b$  is the constant of proportionality ( $2.898 \times 10^{-3}$  m K)

The total radiative energy flux from a black body can be obtained by integrating Planck's Law (Equation 2.5) over the entire frequency range, and is described by the Stefan-Boltzmann law:

$$F = \sigma T^4 \quad (2.7)$$

where  $\sigma$  is the Stefan-Boltzmann constant ( $5.670 \times 10^{-8}$  W m $^{-2}$  T $^4$ ).

In the radio band, where  $h\nu \ll kT$ , a Taylor series expansion can be used to simplify Planck's Law (Equation 2.5) to the Rayleigh-Jeans Law:

$$I_\nu = B_\nu(T) = \frac{2\nu^2 kT}{c^2} \quad (2.8)$$

In radio astronomy, it is common practice to express the observed intensity of an object in terms of a 'brightness temperature'  $T_b$ , which is the equivalent temperature required to thermally produce the same observed radiation at frequency  $\nu$ . Rearranging Equation 2.8 gives the expression for  $T_b$  as:

$$T_b = \frac{c^2}{2\nu^2 k} I_\nu = \frac{h\nu}{k} J_\nu(T) \quad (2.9)$$

where  $J_\nu(T) = [\exp(h\nu/kT) - 1]^{-1}$ .

### 2.1.3 Radiative Transfer

Radiation from astrophysical sources will propagate some distance through the ISM before it is able to be detected here on Earth, and it is important to consider any changes that may occur during this process.

Photons have a finite probability of being absorbed as they propagate through a medium. Conversely, particles in the medium may also emit photons, increasing the overall intensity. Figure 2.1 illustrates the effect that particles in a medium have on the intensity of incident radiation.

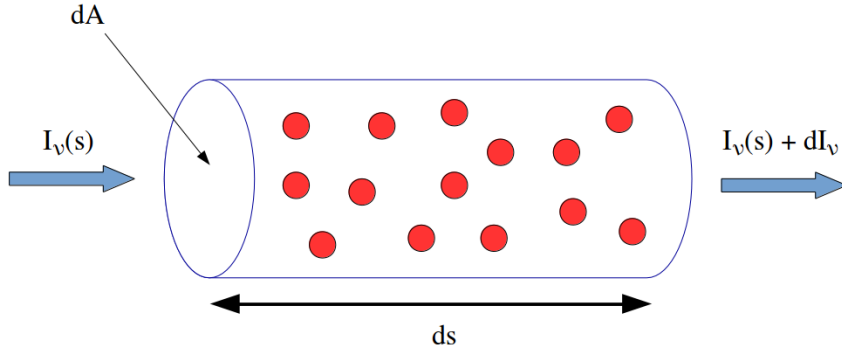


Figure 2.1: Radiation with frequency  $\nu$  and intensity  $I_\nu$  enters a column of particles with length  $ds$  and cross-sectional area  $dA$ . The particles in this column absorb and emit radiation, changing the intensity by  $dI_\nu$  as described by the equation of radiative transfer (Equation 2.10).

Considering these two factors, the propagation of radiation of some frequency  $\nu$  through the ISM can be described by the equation of radiative transfer:

$$\frac{dI_\nu}{ds} = -\alpha_\nu(s)I_\nu(s) + j_\nu(s) \quad (2.10)$$

This equation gives the net intensity change,  $dI_\nu$ , over a given infinitesimal distance,  $ds$ .

The emission coefficient,  $j_\nu(s)$  [ $\text{W m}^{-3} \text{Hz}^{-1} \text{sr}^{-1}$ ], describes the power emitted at frequency  $\nu$  per unit volume of the medium. The absorption coefficient,  $\alpha_\nu(s)$  [ $\text{m}^{-1}$ ], describes the number of absorption interactions per unit distance. For a medium with density  $n$  and a constant absorption cross-section  $\sigma_\nu$ , the absorption coefficient is given by  $\alpha_\nu = n\sigma_\nu$ . The mean free path length,  $l_\nu$ , is the inverse of the absorption coefficient ( $l_\nu = \alpha_\nu^{-1}$ ) and is the distance that photons will travel through the medium before  $1/e$  are absorbed.

The absorption coefficient is not a directly measurable quantity, and so the absorption of radiation is better characterised by the optical depth,  $\tau_\nu$ , which is defined by:

$$d\tau_\nu = \alpha_\nu ds \quad (2.11)$$

Dividing Equation 2.10 by the absorption coefficient, one can express the equation of radiative transfer in terms of optical depth as:

$$\frac{dI_\nu}{d\tau_\nu} = -I_\nu(\tau_\nu) + S_\nu(\tau_\nu) \quad (2.12)$$

where  $S_\nu(\tau_\nu) = j_\nu(\tau_\nu)/\alpha_\nu(\tau_\nu)$  is the source function, which describes the ratio of photons emitted and absorbed by the particles in the medium.

The solution to Equation 2.12, a 1st Order Linear Differential Equation, is:

$$I_\nu(\tau_\nu) = I_\nu(0)e^{-\tau_\nu} + \int_0^{\tau_\nu} e^{-(\tau_\nu - \tau'_\nu)} S_\nu(\tau'_\nu) d\tau'_\nu \quad (2.13)$$

The first term in Equation 2.13,  $I_\nu(0)e^{-\tau_\nu}$ , is the radiation from a background source which is attenuated as it passes through the medium. The second term is the radiation contribution from the medium itself. In the case where the source function  $S_\nu$  remains constant in the medium, Equation 2.13 becomes:

$$I_\nu(\tau_\nu) = S_\nu + e^{-\tau_\nu}[I_\nu(0) - S_\nu] \quad (2.14)$$

There are two limiting cases in terms of optical depth. In the case where the medium is ‘optically thin’ ( $\tau_\nu \ll 1$ ), Equation 2.14 becomes:

$$I_\nu(\tau_\nu) = (1 - \tau_\nu)I_\nu(0) + S_\nu\tau_\nu \quad (2.15)$$

In this case, a small fraction of the intensity will be absorbed by the particles in the medium, and an observer will be able to see radiation from background sources together with a contribution from the medium via the source function. In the case where the medium is ‘optically thick’ ( $\tau_\nu \gg 1$ ), Equation 2.14 becomes:

$$I_\nu(\tau_\nu) = S_\nu(\tau_\nu) \quad (2.16)$$

In this case, the medium is opaque, and an observer will only see photons emitted from the outside envelope of the medium.

Equation 2.14 can be expressed in terms of brightness temperature,  $T_b$  (see Equation 2.9):

$$T_b = \frac{h\nu}{k} J_\nu(T_{bg}) e^{-\tau_\nu} + \frac{h\nu}{k} J_\nu(T_s)(1 - e^{-\tau_\nu}) \quad (2.17)$$

where  $T_s$  is the source temperature, and  $T_{bg}$  is the background temperature.

Many astronomical telescopes employ a source and background subtraction method in observations in order to remove contributions to the measured signal that arise from the atmosphere, telescope electronics, and background noise. This can be achieved by subtracting the brightness temperature of a background position from the brightness temperature of the ‘on-source’ position, and is characterised by the detection equation:

$$T_b = \frac{h\nu}{k} [J_\nu(T_s) - J_\nu(T_{bg})](1 - e^{-\tau_\nu}) \quad (2.18)$$

## 2.2 Molecular Line Emission

Molecules are able to store their internal energy in several different ways, such as in rotational and vibrational modes. These internal energy levels are discrete, and the transitions between molecular energy levels are accompanied by the emission or absorption of photons with specific frequencies. The frequency of the photon emitted/absorbed when transitioning from some energy state  $j$  to another energy state  $k$  is given by:

$$\nu_{jk} = \frac{|E_j - E_k|}{h} \quad (2.19)$$

where  $h$  is Planck's constant. This type of radiation is known as line emission. Different species of molecules have unique characteristic spectral lines, and the detection of such emission allows us to gain information on the distribution and population of molecules.

### 2.2.1 Rotational Molecular Energy Levels

Within much of the cold and quiescent ISM, the temperature does not typically reach temperatures required to activate vibrational energy modes (above  $\sim 100$  K). However, the excitation of rotational energy states only require several tens of Kelvin to occur, and consequently most molecular spectral lines seen in the ISM are from the transitions between these energy levels. These rotational molecular line emissions are generally within the radio to microwave frequency bands.

For a single molecule, the rotational energy is described by its angular momentum, which is quantised in multiples of  $\hbar = h/2\pi$ . Consider 3 perpendicular axes  $x$ ,  $y$  and  $z$  through the centre-of-mass of a molecule, with the corresponding angular momentum components  $J_x$ ,  $J_y$ , and  $J_z$ . The total rotational energy of the molecule is given by:

$$E_{\text{rot}} = \frac{J_x^2}{2I_x} + \frac{J_y^2}{2I_y} + \frac{J_z^2}{2I_z} \quad (2.20)$$

where  $I_x$ ,  $I_y$ , and  $I_z$  are the moments of inertia about the  $x$ ,  $y$  and  $z$  axes. The rotational energy can also be written as:

$$E_{\text{rot}} = \frac{1}{2}(I_x\omega_x^2 + I_y\omega_y^2 + I_z\omega_z^2) \quad (2.21)$$

where  $\omega_i$  is the angular velocity of component  $i$ . Molecules can be divided up into four different rotor groups, which depend on the relative values of the three moments of inertia. These classifications are summarised in Table 2.1.

Table 2.1: Classifications and examples of molecular rotors.  $I_x$ ,  $I_y$  and  $I_z$  are the moments of inertia about the  $x$ ,  $y$  and  $z$  axes respectively.

Rotor Type	Moment of inertia	Example molecules
Spherical Rotors	$I_x = I_y = I_z$	$\text{CH}_4$ , $\text{SiH}_4$
Linear Rotors	$I_x = 0, I_y = I_z$	$\text{CO}$ , $\text{CS}$ , $\text{OH}$ , $\text{SiO}$
Symmetric Rotors	$I_x = I_y \neq I_z$	$\text{NH}_3$ , $\text{CH}_3\text{CN}$
Asymmetric Rotors	$I_x \neq I_y \neq I_z$	$\text{CH}_3\text{OH}$ , $\text{H}_2\text{O}$

Of the different rotor types, linear rotor molecules are some of the most common in the ISM (see §2.6). Linear rotors have one principal axis ( $I_x = 0$ ) and two identical perpendicular axes ( $I_y = I_z \equiv I_{\perp}$ ). The rotational energy of a linear rotor is then:

$$E_{\text{rot}} = \frac{J_{\perp}^2}{2I_{\perp}} \quad (2.22)$$

where  $J_{\perp}$  is the angular momentum component perpendicular to the principal axis. By using the correspondence principle in the quantum regime, the angular momentum term can be replaced with  $J^2 \rightarrow J(J+1)\hbar^2$ , where  $J$  now represents the angular momentum quantum number. Equation 2.22 then becomes:

$$E_{\text{rot}} = \frac{\hbar^2}{2I} J(J+1) \quad (2.23)$$

Each linear rotor molecule species has a unique moment of inertia  $I$ , and Equation 2.23 allows the calculation of the rotational energy levels for any linear rotor molecule. In the case of a change in the rotational energy of a linear rotor molecule, the frequency of the emitted or absorbed photon is given by  $\nu = \Delta E_{\text{rot}}/2\pi\hbar$  (see Equation 2.19), where  $\Delta E_{\text{rot}}$  is the difference in the energy of the rotational levels. Photons have a spin of 1, due to conservation of angular momentum will only be able to change  $J$  by  $\Delta J = \pm 1$  via emission/absorption processes. Thus, the frequency of the photon is given by:

$$\nu = \frac{\hbar}{2\pi I} (J_{\text{L}} + 1) \quad (2.24)$$

where  $J_{\text{L}}$  is the lower rotational quantum number.

### 2.2.2 Einstein Coefficients

There are several radiative mechanisms involved with the emission and absorption of photons due to a change in a molecule energy state, as illustrated in Figure 2.2. The rate at which each process occurs is characterised by their corresponding Einstein coefficient.

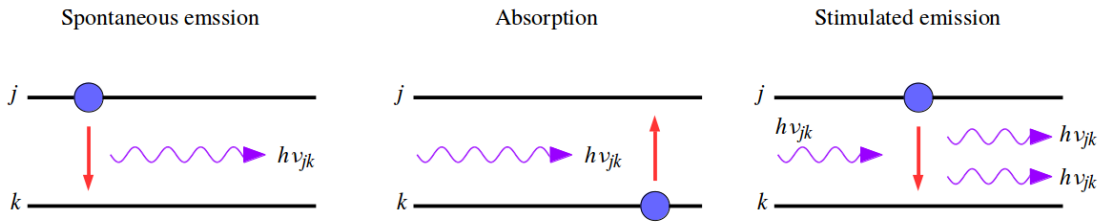


Figure 2.2: The mechanisms associated with line emission, which results in a change in the energy state of the molecule.  $\nu_{jk}$  is the frequency of the photon with energy equivalent to the difference in energy states  $j$  and  $k$  (see Equation 2.19).

**Spontaneous emission** (Figure 2.2, left panel) occurs when a single photon is radiated spontaneously from a molecule. This takes place together with a transition from a higher energy state  $j$  to a lower energy state  $k$  within the molecule. The rate at which this occurs is given by the Einstein coefficient  $A_{jk}$ :

$$A_{jk} = \frac{16\pi^3\nu_{jk}^3}{3\epsilon_0hc^3} |\mu_{jk}^2| \quad [\text{s}^{-1}] \quad (2.25)$$

where  $\nu_{jk}$  is the frequency of light corresponding to this transition and  $\mu_{jk}$  is the electric dipole moment of the molecular transition.

**Absorption** (Figure 2.2, centre panel) occurs when a molecule transitions to a higher energy level by absorbing a photon of the specific frequency corresponding to the energy gap. This process depends on the specific intensity of the photons,  $I_\nu$ , and the Einstein coefficient  $B_{kj}$  [ $\text{W}^{-1}\text{cm}^2 \text{ sr Hz s}^{-1}$ ].

**Stimulated emission** (Figure 2.2, right panel) is also known as negative absorption. A molecule in an energy state  $j$  can interact with a photon of frequency  $\nu_{jk}$  which stimulates a transition into the lower energy state  $k$ . This results in the emission of another photon with the same frequency  $\nu_{jk}$ . Stimulated emission is dependent on the specific intensity of the radiation,  $I_\nu$ , and the Einstein coefficient  $B_{jk}$  [ $\text{W}^{-1}\text{cm}^2 \text{ sr Hz s}^{-1}$ ].

The Einstein A and B coefficients are related by the following:

$$B_{jk} = \frac{c^2}{2h\nu^3} A_{jk} \quad B_{kj}g_k = B_{jk}g_u \quad (2.26)$$

where  $g_j$  and  $g_k$  are the degeneracies of the states  $j$  and  $k$  respectively.

In addition to radiative processes, atoms and molecules can be excited and de-excited between energy states via collisions. These process are described by the Einstein coefficients  $C_{jk}$  and  $C_{kj}$ , where  $C_{jk}$  is the collisional de-excitation rate and  $C_{kj}$  is the collisional excitation rate. These Einstein coefficients are proportional to the number density of the molecules,  $n$ . In the astrophysical case, the most abundant molecular species is  $\text{H}_2$ , and it is assumed that  $\text{H}_2$  molecules are the dominant collisional partner. Thus,  $C_{jk}$  and  $C_{kj}$  are defined as:

$$C_{jk} = n_{\text{H}_2} \gamma_{jk} \quad \text{and} \quad C_{kj} = n_{\text{H}_2} \gamma_{kj} \quad (2.27)$$

where  $n_{\text{H}_2}$  is the number density of  $\text{H}_2$  and  $\gamma_{jk}$  and  $\gamma_{kj}$  are the coefficients for downward and upward collision processes respectively (with units of molecules per second per  $\text{H}_2$  molecule).

In a steady state, where the number of molecules in the upper and lower energy states remain constant, the Einstein  $A$ ,  $B$ , and  $C$  coefficients are related by:

$$n_j(A_{jk} + B_{jk}I_\nu + C_{jk}) = n_k(B_{kj}I_\nu + C_{kj}) \quad (2.28)$$

where  $n_j$  and  $n_k$  are the number density of molecules in the  $j$  and  $k$  energy states respectively.

Consider now the system under the conditions of local thermal equilibrium (LTE), an idealised scenario in which the population density of molecules in some state  $i$  with energy  $E_i$  follows the Boltzmann distribution:

$$n_i \propto g_i \exp\left(-\frac{E_i}{kT}\right) \quad (2.29)$$

where  $g_i$  is the degeneracy of the state  $i$ . For a population of molecules in LTE, the ratio of the number density of molecules in energy states  $j$  and  $k$  is given by:

$$\frac{n_j}{n_k} = \frac{g_j}{g_k} \exp\left(-\frac{E_j - E_k}{kT_x}\right) \quad (2.30)$$

where  $T_x$  is called the excitation temperature of the transition. Combining Equations 2.28 and 2.30 relates  $T_x$  with the Einstein coefficients:

$$\frac{g_j}{g_k} \exp\left(-\frac{E_j - E_k}{kT_x}\right) = \frac{B_{kj}I_\nu + C_{kj}}{A_{jk} + B_{jk}I_\nu + C_{jk}} \quad (2.31)$$

If we consider the case of only collisions (i.e. Equation 2.28  $\Rightarrow n_jC_{jk} = n_kC_{kj}$ ), then by using Equation 2.30 we obtain:

$$\frac{C_{kj}}{C_{jk}} = \frac{g_j}{g_k} \exp\left(-\frac{E_j - E_k}{kT_k}\right) \quad (2.32)$$

where  $T_k$  is the kinetic temperature of the molecules. This relationship is known as the ‘detailed balance’ condition, and always holds true regardless of the radiation field as it only depends on the parameters of the molecule. If we assume that the radiation field the population of molecules are subject to is from a blackbody with temperature  $T_{bk}$ , then the intensity  $I_\nu$  will be given by Plank’s Law (Equation 2.5). Substituting this into Equation 2.31 together with Equation 2.32 returns a expression that relates  $T_x$  to  $T_k$  for a population of molecules exposed to some blackbody radiation field:

$$\exp\left(\frac{E_j - E_k}{kT_x}\right) = \frac{A_{jk}[1 + J_\nu(T_{bk})] + C_{jk}}{A_{jk}J_\nu(T_{bk}) + C_{jk} \exp(-E_j/kT_k)} \quad (2.33)$$

where  $J_\nu = [\exp((E_j - E_k)/kT_b) - 1]^{-1}$ .

### 2.2.3 Critical Density

To determine whether a particular spectral line is observable from population of molecules, a useful parameter to consider is the critical density. The critical density is the density at which the rate of downward radiative processes is equal to the rate of collisional de-excitation. In a steady state situation, the downward process terms are given by:

$$A_{jk} + A_{jk}J_\nu(T_b) = n_{H_2}\gamma_{jk} \quad (2.34)$$

The critical density,  $n_c$ , is then defined as:

$$n_c = \frac{A_{jk}(1 + J(T_{bk}))}{\gamma_{jk}} \approx \frac{A_{jk}}{\gamma_{jk}} \quad (2.35)$$

The critical density is the density at which collision excitation (with  $H_2$  molecules) is

effective. Below  $n_c$ , the rate of collisions is too low to excite the gas, and a spectral line will not be visible against the background radiation. Different species of molecules have different critical densities, and these properties are used for the detection of molecular gas in a range of densities within the ISM. Table 2.2 lists the critical densities of some useful molecular transitions. More in-depth discussion of these molecules can be found in §2.6.

Table 2.2: Critical densities of several useful molecular transitions

Molecule	Transition	Critical density [cm <sup>-3</sup> ]
CO	(1–0)	~ $5.0 \times 10^2$
CS	(1–0)	~ $1.8 \times 10^4$
$\text{C}^{34}\text{S}$	(1–0)	~ $1.7 \times 10^4$
SiO	(1–0, v=0)	~ $6.0 \times 10^4$

## 2.3 Millimetre Radio Astronomy

Much of the spectral line emission from molecules within the ISM are found in the radio band of the electromagnetic spectrum. As such, radio telescopes are employed to target these specific frequencies in regions of interest. In this thesis, most of the observations of the ISM come from the Mopra radio telescope.

### 2.3.1 Mopra

Mopra is a 22 metre, single dish radio telescope located near Coonabarabran in New South Wales, Australia, at an elevation of ~ 850 m above sea level. It was part of the Australia Telescope National Facility (ATNF) operated by the Commonwealth Scientific and Industrial Research Organisation (CSIRO). Since 2013, operations have been funded (first in part, now in whole) by external groups. From 2013 to 2015, funding came from the National Astronomical Observatory of Japan (NAOJ), the University of New South Wales (UNSW) and the University of Adelaide (UoA). Since 2016, funding has come from UNSW, UoA, Western Sydney University (WSU), Nagoya University and a Linkage Infrastructure, Equipment and Facilities (LIEF) grant from the Australian Research Council (ARC).

Mopra has a suite of three receivers that can be used for single-dish observations in the 3 mm band (76-117 GHz), 7 mm band (30-50 GHz), and 12 mm band (12-28 GHz). The Mopra spectrometer (MOPS) can operate in two modes: ‘wideband’ and

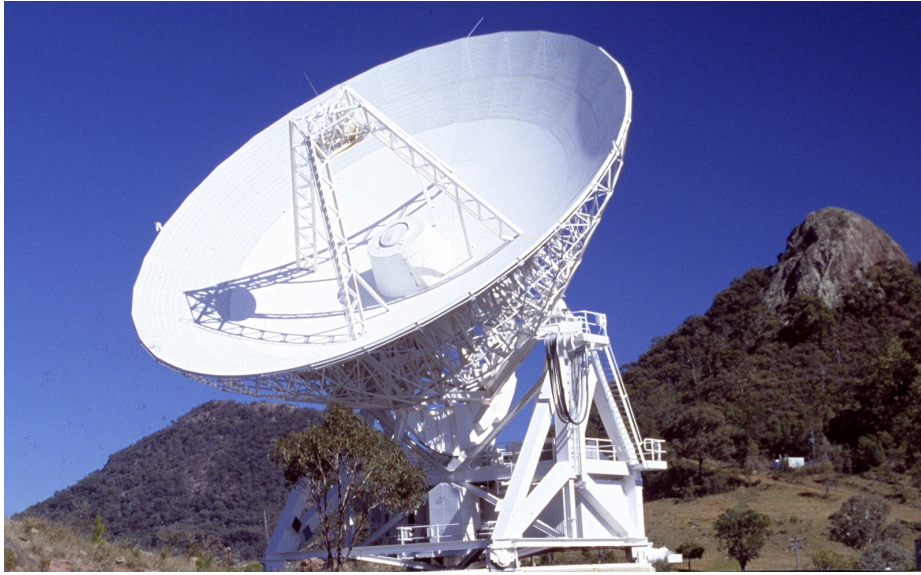


Figure 2.3: The Mopra radio telescope (Image credit: Mopra CSIRO website 2017).

‘zoom’. In wideband mode, MOPS provides four overlapping 2.2 GHz sub-bands over a 8.3 GHz range with 8096 channels. In zoom mode, each of the four sub-bands are further divided into four zoom bands, or windows, each of 137.5 MHz in width with 4096 channels. This allows for the observation of 16 frequency bands simultaneously, each tuned to a specific spectral line. Table 2.3 displays the characteristics of Mopra operating in these modes in the 3 mm, 7 mm and 12 mm bands. A wide range of molecular transitions are observable utilising Mopra, and a non-exhaustive list is displayed in Table 2.4.

Table 2.3: Characteristics of the Mopra radio telescope in wideband and zoom modes using the 3 mm, 7 mm and 12 mm receivers. (Ladd et al., 2005; Urquhart et al., 2010)

Band	Centre Frequency (GHz)	FWHM ( $\text{''}$ )	Bandwidth ( $\text{km s}^{-1}$ )		Spectral Resolution ( $\text{km s}^{-1}$ )	
			Wide	Zoom	Wide	Zoom
3 mm	90	35	30378	505	0.915	0.11
7 mm	42	70	56025	932	1.69	0.21
12 mm	24	120	112050	1863	3.38	0.41

### 2.3.2 Source Temperature and Antenna Temperature

When performing observations with single dish radio telescopes, the antenna temperature  $T_A^*$  from given regions in the sky are recorded. Typically, any observations

Table 2.4: List of sample atomic and molecular tracers observable with Mopra.

3 mm		7 mm		12 mm	
Transition	Freq. (GHz)	Transition	Freq. (GHz)	Transition	Freq. (GHz)
HCO <sup>+</sup> (1–0)	89.188526	SiO(1–0, v=3)	42.519373	H69 $\alpha$	19.591110
<sup>13</sup> CS(2–1)	92.494720	SiO(1–0, v=2)	42.820582	CH <sub>3</sub> OH(II)	19.967396
C <sup>34</sup> S(2–1)	96.412950	SiO(1–0, v=1)	43.122079	H <sub>2</sub> O	22.235253
CS(2–1)	97.980953	SiO(1–0, v=0)	43.423824	H65 $\alpha$	23.404280
C <sup>18</sup> O(1–0)	109.781176	CH <sub>3</sub> OH(I)	44.069476	NH <sub>3</sub> (1,1)	23.694471
<sup>13</sup> CO(1–0)	110.201354	HC <sub>3</sub> N(5–4, F=4–3)	45.090264	NH <sub>3</sub> (2,2)	23.722634
CO(1–0)	115.271202	H51 $\alpha$	45.453720	NH <sub>3</sub> (3,3)	23.870127
		<sup>13</sup> CS(1–0)	46.247580	NH <sub>3</sub> (6,6)	25.056025
		C <sup>34</sup> S(1–0)	48.206946	H62 $\alpha$	26.959170
		CS(1–0)	48.990957	NH <sub>3</sub> (9,9)	27.477943

of a source will use the position switching method which involves comparing observations towards the source (ON) against observations of a background reference position (OFF). During ON observations, the telescope will detect  $T_A^*$  together with the background radiation temperature  $T_{bk}$ , which is usually due to the cosmic microwave background (CMB). In addition, particles in the atmosphere and instrument electronics with brightness temperatures  $T_{atm}$  and  $T_{rx}$  respectively will further contribute to the total recorded signal. In the case of OFF observations, no source signal is expected to be recorded and  $T_A^* = 0$ . Figure 2.4 is a schematic diagram illustrating ON and OFF positions and the sources of radiation which contribute to the total detected signal.

The power received by the telescope during ON and OFF positions,  $P_{ON}$  and  $P_{OFF}$  respectively, is given by:

$$\begin{aligned} P_{ON} &= C[T_A^*e^{-\tau_\nu} + T_{bk}e^{-\tau_\nu} + T_{atm}(1 - e^{-\tau_\nu}) + T_{rx}] \\ P_{OFF} &= C[T_{bk}e^{-\tau_\nu} + T_{atm}(1 - e^{-\tau_\nu}) + T_{rx}] \end{aligned} \quad (2.36)$$

where  $C$  is a constant used to convert between brightness temperature and power, and  $\tau_\nu$  is the optical depth of the atmosphere. From Equation 2.36,  $T_A^*$  can be written as:

$$T_A^* = \frac{(P_{ON} - P_{OFF})}{C}e^{\tau_\nu} \quad (2.37)$$

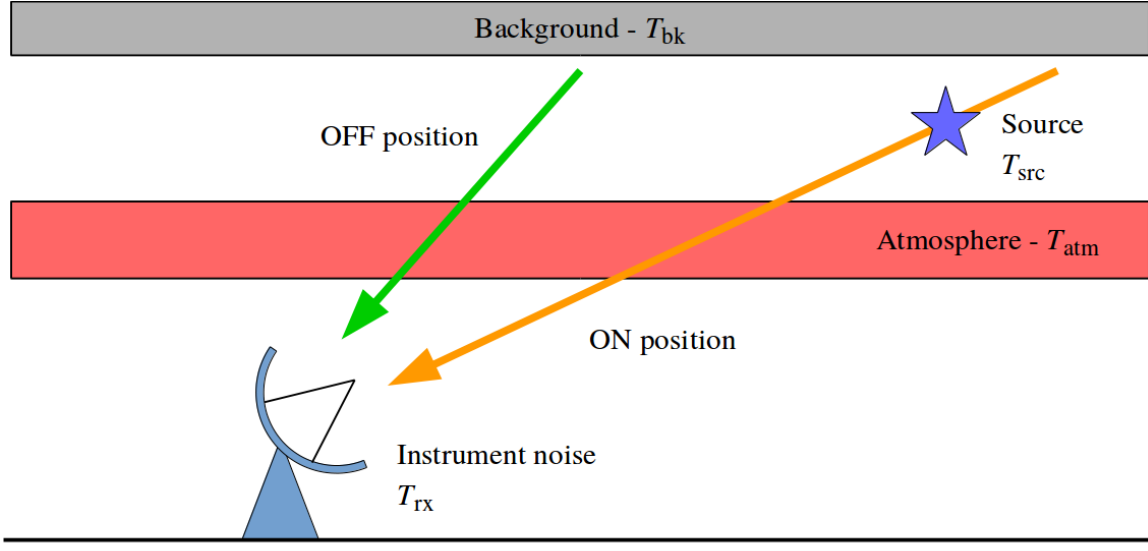


Figure 2.4: An illustration of the sources of radiation involved in ON and OFF position observations. The total signal measured during ON observations of an extraterrestrial source will be a combination of the source ( $T_{\text{src}}$ ), the background ( $T_{\text{bk}}$ ), the atmosphere ( $T_{\text{atm}}$ ) and the electronics of the telescope ( $T_{\text{rx}}$ ).

For convenience, the system temperature,  $T_{\text{sys}}$ , is defined to account for the noise in the system from background radiation, atmospheric effects and telescope electronics:

$$T_{\text{sys}} = \frac{P_{\text{OFF}}}{C} e^{\tau_\nu} = T_{\text{atm}}(e^{\tau_\nu} - 1) + T_{\text{bk}} + T_{\text{rx}} e^{\tau_\nu} \quad (2.38)$$

Equation 2.37 can then be written as:

$$T_A^* = \frac{(P_{\text{ON}} - P_{\text{OFF}})}{P_{\text{OFF}}} T_{\text{sys}} \quad [\text{K}] \quad (2.39)$$

The main beam of a radio telescope is often accompanied by several side lobes, and as such only a fraction of the total power collected by the telescope is contained within the main beam. This fraction  $\eta_{\text{mb}}$  needs to be accounted for to recover the main beam temperature  $T_A^{*\prime}$ :

$$T_A^{*\prime} = \frac{T_A^*}{\eta_{\text{mb}}} \quad (2.40)$$

This holds for the case where the angular size of the source  $\theta_S$  is comparable or smaller than that of the main beam  $\theta_{\text{FWHM}}$ . In the case where  $\theta_S$  is larger than  $\theta_{\text{FWHM}}$ , the

side lobes will receive some fraction of the incident power, and the extended beam coefficient  $\eta_{\text{xb}}$  (which is specific for Mopra, see Ladd et al. 2005) is used to obtain the main beam temperature:

$$T_A^{*'} = \frac{T_A^*}{\eta_{\text{xb}}} \quad (2.41)$$

With knowledge of the main beam temperature, it is possible to recover the brightness temperature of the source  $T_{\text{scr}}$ . For a source with uniform intensity with an angular area  $\Delta\Omega_s$  that is small when compared to the angular area of the beam  $\Delta\Omega_a$ , the relationship between  $T_{\text{scr}}$  and  $T_A^{*'}$  is given by:

$$T_{\text{scr}} = T_A^{*'} \left( \frac{\Delta\Omega_a}{\Delta\Omega_s} \right) \quad (2.42)$$

The main beam pattern can be approximated as a Gaussian function, and so the main beam area is described by:

$$\begin{aligned} \Delta\Omega_a &= \int_{\phi=0}^{\phi=2\pi} \int_{\theta=0}^{\infty} \exp \left( -\frac{4\theta^2}{\theta_{\text{FWHM}}^2} \ln 2 \right) \theta d\theta d\phi \\ &= \frac{\pi\theta_{\text{FWHM}}^2}{4 \ln 2} \end{aligned} \quad (2.43)$$

For a source that is small compared to the beam size, we assume that the angular area can be described as a disk such that  $\Delta\Omega_s = \pi\theta_s^2/4$ . The beam dilution factor  $f$  is defined to be the ratio between  $\Delta\Omega_a$  and  $\Delta\Omega_s$ :

$$f = \frac{\Delta\Omega_a}{\Delta\Omega_s} = \frac{\theta_{\text{FWHM}}^2}{\theta_s^2 \ln 2} \quad (2.44)$$

which can be used to convert the main beam temperature to the brightness temperature of a source when the source angular size is small compared to the beam size. However, in the case where this is not true and  $\Delta\Omega_s$  is not negligible compared to  $\Delta\Omega_a$ , the gain pattern across the beam of the telescope needs to be accounted for we can rewrite Equation 2.42 as:

$$T_A^{*'} = T_{\text{scr}} \frac{1}{\Delta\Omega_a} \int_{\phi=0}^{\phi=2\pi} \int_{\theta=0}^{\theta_s} \exp \left( -\frac{4\theta^2}{\theta_{\text{FWHM}}^2} \ln 2 \right) \theta d\theta d\phi \quad (2.45)$$

Combining Equation 2.45 with Equation 2.43 gives:

$$T_A^{*'} = T_{\text{scr}} \left[ 1 - \exp \left( -\frac{\theta_s^2}{\theta_{\text{FWHM}}^2} \ln 2 \right) \right] \quad (2.46)$$

which is a more general expression which relates  $T_A^{*'} \text{ and } T_{\text{scr}}$ . An extra correction factor  $K$  is now introduced:

$$K = \frac{f^{-1}}{1 - \exp(-f^{-1})} \quad (2.47)$$

Thus, in the general case, the source temperature  $T_{\text{scr}}$  is recovered from the antenna temperature  $T_A^{*'} \text{ by applying the beam dilution factor } f \text{ and the correction factor } K$ :

$$T_{\text{scr}} = T_A^{*'} f K \quad (2.48)$$

For the case of the Mopra radio telescope, the values of  $f$  and  $K$  have been studied and published by Ladd et al. (2005) (3 mm receiver) and Urquhart et al. (2010) (7 mm and 12 mm receivers).

## 2.4 Physical parameters from observations

Using radio telescopes, it is possible to observe many different spectral line transitions from atoms and molecules within the ISM. From these observations, the physical parameters of the ISM gas are able to be derived, including the column density and the optical depth. The following discusses the concepts and general methods used in obtaining physical properties from observational data.

### 2.4.1 Column Density

The column density is an important parameter that is used to estimate the amount of material present in the ISM. To determine the column density of a molecular transition, first consider the definition of the absorption coefficient  $\alpha_\nu$  in terms of the Einstein coefficients:

$$\alpha_\nu = \frac{h\nu_{jk}}{4\pi} (n_j B_{jk} - n_k B_{kj}) \phi(\nu) \quad (2.49)$$

Here, the normalised shape function  $\phi(\nu)$  is introduced, which characterises the spectral line emission as a function of frequency. This function takes into account the line profile (see §2.4.4) of the emission caused by the Doppler effects (§2.4.3) from the thermal motions of the emitting particles. Assuming LTE and using the relationships between the Einstein coefficients described in Equation 2.26 (with a Boltzmann distribution relation between the populations  $n_j$  and  $n_k$ ),  $\alpha_\nu$  can be written as:

$$\alpha_\nu = \frac{c^2}{8\pi\nu_{jk}^2} A_{jk} n_j \left( \exp\left(\frac{h\nu_{jk}}{kT}\right) - 1 \right) \phi(\nu) \quad (2.50)$$

---

## 2.4. PHYSICAL PARAMETERS FROM OBSERVATIONS

---

The column density of the upper state  $j$  is defined by  $N_j = \int n_j ds$ , where  $ds$  is an infinitesimal distance along a line of sight. By integrating the expression for  $\alpha_\nu$  in Equation 2.50 along the line of sight, the optical depth can be expressed in terms of column density:

$$\tau_\nu = \int \alpha_\nu ds = \frac{c^2}{8\pi\nu_{jk}^2} A_{jk} N_j \left( \exp\left(\frac{h\nu_{jk}}{kT}\right) - 1 \right) \phi(\nu) \quad (2.51)$$

For the case where there is no background radiation, multiplying the detection equation (Equation 2.18) by  $\tau_\nu/\tau_\nu$  gives:

$$\begin{aligned} T_A^* \equiv T_b &= \frac{h\nu}{k} J_\nu(T) \left( \frac{1 - e^{-\tau_\nu}}{\tau_\nu} \right) \tau_\nu \\ &= \frac{h\nu}{k} \left[ \exp\left(\frac{h\nu_{jk}}{kT} - 1\right) \right]^{-1} \left( \frac{1 - e^{-\tau_\nu}}{\tau_\nu} \right) \tau_\nu \end{aligned} \quad (2.52)$$

By combining Equations 2.51 and 2.52, a relationship between the antenna temperature  $T_A^*$  and the column density of the upper state  $N_j$  is obtained:

$$T_A^* = \frac{hc^2}{8k\pi\nu_{jk}} A_{jk} N_j \left( \frac{1 - e^{-\tau_\nu}}{\tau_\nu} \right) \phi(\nu) \quad (2.53)$$

Integrating over the width of the line yields:

$$\int_{-\infty}^{\infty} T_A^* d\nu = \frac{hc^2}{8k\pi\nu_{jk}} A_{jk} N_j \left( \frac{1 - e^{-\tau_\nu}}{\tau_\nu} \right) \int_{-\infty}^{\infty} \phi(\nu) d\nu \quad (2.54)$$

where the integral of the normalised shape function  $\int_{-\infty}^{\infty} \phi(\nu) d\nu = 1$ . Because the antenna temperature is often expressed in term of Doppler-shifted velocity along the line of sight (see §2.4.3), a substitution  $\int T_A^* d\nu = \frac{v}{c} \int T_A^* dv$  can be made, and hence the column density of the upper state,  $N_j$ , is given by:

$$N_j = \frac{8k\pi\nu_{jk}^2}{hc^3 A_{jk}} \left( \frac{\tau_\nu}{1 - e^{-\tau_\nu}} \right) \int_{-\infty}^{\infty} T_A^* dv \quad (2.55)$$

In the optically thin case, the optical depth term in Equation 2.55 ( $\frac{\tau_\nu}{1 - e^{-\tau_\nu}}$ )  $\sim 1$ .

In LTE, the total column density of the molecule,  $N_{\text{mol}}$ , can be found from Equation 2.55 by considering that the energy levels of molecules are populated following the Boltzmann distribution:

$$N_{\text{mol}} = \frac{N_j}{g_j} \exp\left(\frac{E_j}{kT}\right) Z(T_x) \quad \text{where} \quad Z(T_x) = \sum_{i=0}^{i=\infty} g_i \exp\left(-\frac{E_i}{kT_x}\right) \quad (2.56)$$

## 2.4.2 Optical Depth

Consider, from some source, a pair of spectral line emissions. It is possible to derive the column density, assuming knowledge of the expected flux ratios. The ratio of the column densities between the upper-state responsible for two spectral lines (denoted ‘1’ and ‘2’) can be found using Equation 2.55:

$$\frac{N_{j|1}}{N_{j|2}} = \left( \frac{\nu_1}{\nu_2} \right)^2 \left( \frac{A_{jk|2}}{A_{jk|1}} \right) \left( \frac{\int T_{b|1} d\nu}{\int T_{b|2} d\nu} \right) \left( \frac{\tau_1}{\tau_2} \right) \left( \frac{1 - e^{-\tau_2}}{1 - e^{-\tau_1}} \right) \quad (2.57)$$

In the case where  $\tau \rightarrow 0$ , it is sometimes possible to define a factor  $R$  that fulfils the following conditions:

$$R = \frac{\tau_1}{\tau_2} \quad \text{and} \quad R = \frac{N_{j|1}}{N_{j|2}} \quad (2.58)$$

Equation 2.57 can then be rearranged as:

$$\frac{\int T_{b|2} d\nu}{\int T_{b|1} d\nu} = \left( \frac{\nu_1}{\nu_2} \right)^2 \left( \frac{A_{jk|2}}{A_{jk|1}} \right) \left( \frac{1 - e^{-\tau_2}}{1 - e^{-R\tau_2}} \right) \quad (2.59)$$

allowing the optical depth to be numerically derived. Pairs of emission lines are typically found between molecular isotopologues (e.g. CS and C<sup>34</sup>S, see §2.6.3), or within molecules with hyperfine structure (e.g. OH, NH<sub>3</sub>). For isotopologue pairs,  $R$  can be estimated by the isotopic abundance ratio, while for molecules with hyperfine structure,  $R$  can be estimated by the relative degeneracies of the involved energy levels.

## 2.4.3 The Doppler Effect

The Doppler effect is the change in the frequency of a wave for an observer who has some velocity along the line-of-sight relative to the wave source. The effect of this phenomenon is characterised by the Doppler equation:

$$\nu_{\text{obs}} = \frac{v + v_{\text{obs}}}{v + v_{\text{source}}} \nu_0 \quad (2.60)$$

where  $\nu_{\text{obs}}$  is the observed frequency of the wave,  $\nu_0$  is the original frequency at the source,  $v$  is the velocity of the wave,  $v_{\text{obs}}$  is the velocity of the observer towards the source, and  $v_{\text{source}}$  is the velocity of the source away from the observer.

It is convenient to express the frequency of a detected line signal in terms of its Doppler shifted velocity. While the rest frequencies of spectral lines are well known,

the motion of the particles cause slight frequency deviations in their emission and absorption lines. For a specific spectral line, a signal in frequency-space is expressed in velocity-space by converting the frequency into some Doppler shifted velocity with respect to some rest frame:

$$v_{\text{LSR}} = c \frac{(\nu_0 - \nu)}{\nu_0} \quad (2.61)$$

where  $c$  is the speed of light. For observations of Galactic objects, the reference position is typically the local standard of rest (LSR); a point coincident with the position of the Sun moving at the local circular velocity about the Galactic Centre. After processing and reduction, the final data products from radio telescopes used in this thesis all have their spectral axes in terms of Doppler shifted velocities,  $v_{\text{LSR}}$ .

There are several causes of Doppler shifts in the spectral line observations of the ISM in our Galaxy:

- Random thermal motions of atoms and molecules (see §2.4.4)
- Local gas dynamics, including cloud-cloud collisions, shock interactions etc.
- Bulk motion of the ISM gas as it rotates about the Galactic center (see §2.5)

#### 2.4.4 Line Profiles

Spectral emission lines always have some natural spread in their frequencies, described by Heisenberg's Uncertainty Principle ( $\Delta E \Delta t \geq \hbar/2$ ). The uncertainties involved with the energy and lifetime of the transitions results in a Lorentzian line shape, with a shape function  $\phi(\nu)$  given by:

$$\phi(\nu) = \frac{(A_{jk} + C)/4\pi^2}{(\nu - \nu_0)^2 + (A_{jk} + C)/4\pi^2} \quad (2.62)$$

where  $A_{jk}$  is the Einstein A coefficient,  $\nu_0$  is the central frequency of the emission line and  $C$  is some constant.

The random thermal motions of molecules cause the emission to be Doppler shifted (§2.4.3), resulting in a Gaussian line shape:

$$\phi(\nu) = \sqrt{\frac{mc^2}{2\pi kT\nu_0^2}} \exp\left(-\frac{(\nu - \nu_0)^2 mc^2}{2kT\nu_0^2}\right) \quad (2.63)$$

where  $m$  is the mass of the molecule and  $T$  is the kinetic temperature. Emission lines profiles are hence a convolution of the Lorentzian and Gaussian shape functions.

However, in most cases, the thermal Gaussian component is dominant. Equation 2.63 can be expressed in terms of Doppler-shifted velocity  $v_{\text{LSR}}$  as:

$$\phi(v_{\text{LSR}}) = \sqrt{\frac{mc^2}{2\pi kT\nu_0^2}} \exp\left(-\frac{m(v_{\text{LSR}} - v_{\text{centre}})^2}{2kT}\right) \quad (2.64)$$

where  $v_{\text{centre}}$  is the Doppler-shifted velocity of  $\nu_0$ . Hence, most spectral line emission profiles are well fit by a Gaussian function of the form:

$$f(v_{\text{LSR}}) = A \exp\left(-\frac{4(v_{\text{LSR}} - v_{\text{centre}})^2}{\Delta v_{\text{FWHM}}^2} \ln 2\right) \quad (2.65)$$

where  $A$  is the amplitude of the emission line, and  $\Delta v_{\text{FWHM}}$  is the full width half maximum. Assuming the broadness of the linewidth is solely due to thermal motions of the molecule,  $v_{\text{FWHM}}$  is given by:

$$\Delta v_{\text{FWHM}} = \sqrt{\frac{8kT \ln 2}{m}} \quad (2.66)$$

For line emission produced by the ISM within the Galaxy, additional broadening effects are caused by turbulence, especially in the case of cold molecular clouds. These turbulences may be caused by external shocks produced by star formation regions, SNRs etc., as well as large scale processes such as Galactic sheer and gravitational instability.

If the spectral line is fitted with a Gaussian function, the total integrated intensity (in velocity space) will be given by the area under the Gaussian:

$$\text{Area} = \frac{A\Delta v_{\text{FWHM}}\sqrt{\pi}}{2\sqrt{\ln 2}} \quad (2.67)$$

## 2.5 Kinematic Distances and the Rotation of the Galaxy

As mentioned in §2.4.3, the relative motion of particles will cause a Doppler shift in the detected frequencies of their spectral lines. In addition to thermal motion and random turbulence, atoms and molecules that make up the Galactic ISM have bulk motion from their intrinsic orbit around the centre of the Galaxy. Using the Doppler-shifted velocity of an observed spectral line,  $v_{\text{LSR}}$ , from some Galactic object, it is possible to estimate the distance to said object if the rotation parameters of the Galaxy are known.

## 2.5. KINEMATIC DISTANCES AND THE ROTATION OF THE GALAXY

---

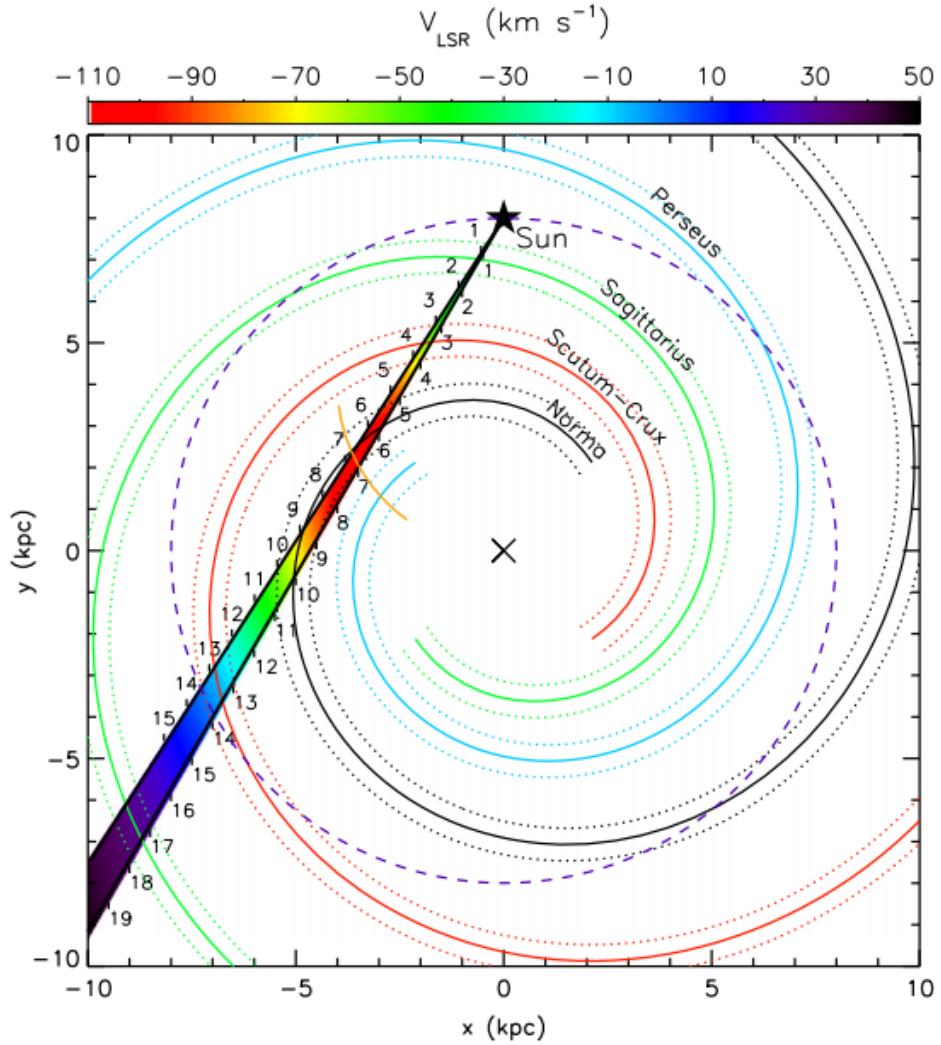


Figure 2.5: Schematic 4-arm model of our Galaxy, described in Vallée (2014), rotating clockwise as viewed from above. The colour shading within the wedge represents the expected  $v_{\text{LSR}}$  according to the rotation curve from Brand & Blitz (1993), along the  $l = 327.8^\circ$  to  $328.7^\circ$  sightline. The numbers along the wedge indicate the corresponding distance from the Sun in kpc, and the short yellow arc indicates the tangent point along this sightline. The solar circle is indicated by the dashed purple circle. Image is taken from Burton et al. (2015).

The rotation of the Galaxy is described by a Galactic rotation curve, which gives the average velocity of objects in circular orbits as a function of distance from the centre of the Galaxy. Rotation curves are observationally derived models. For example, the commonly used Galactic rotation curve presented by Brand & Blitz (1993) was derived from observations of stars and the  $v_{\text{LSR}}$  of associated HII regions. The  $v_{\text{LSR}}$  for an object located at Galactic coordinates  $l$  and  $b$  (Galactic longitude and latitude) is given by:

$$v_{\text{LSR}} = \left( \frac{\Theta R_0}{R} - \Theta_0 \right) \sin(l) \cos(b) \quad (2.68)$$

where  $R$  and  $\Theta$  are the galacto-centric distance and circular rotation velocity of the object respectively, while  $R_0$  and  $\Theta_0$  are the galacto-centric distance and circular rotation velocity at the position of the Sun. The values for  $R_0$  and  $\Theta_0$  are taken to be 8.5 kpc and  $220 \text{ km s}^{-1}$  respectively (Kerr & Lynden-Bell, 1986).  $R$  and  $\Theta$  are related to  $R_0$  and  $\Theta_0$  by:

$$\frac{\Theta}{\Theta_0} = a_1 \left( \frac{R}{R_0} \right)^{a_2} + a_3 \quad (2.69)$$

where  $a_1$ ,  $a_2$  and  $a_3$  are observationally derived Galactic curve rotation parameters. The rotation curve from Brand & Blitz (1993) give the values of  $a_1 = 1.00767$ ,  $a_2 = 0.0394$  and  $a_3 = 0.00712$ .

Using simple trigonometry,  $R$  can be expressed in terms of the heliocentric distance  $d$  as:

$$R^2 = d^2 \cos^2(b) + R_0^2 - 2R_0 d \cos(b) \cos(l) \quad (2.70)$$

Using Equations 2.68 and 2.69, the distance to some Galactic object  $d$  can be solved numerically given a measured Doppler-shifted velocity  $v_{\text{LSR}}$ . An example of how distance and  $v_{\text{LSR}}$  are related by the Galactic rotation curve is given in Figure 2.5. For the case where  $R < R_0$ , a degeneracy occurs, resulting in a pair of ‘near’ and ‘far’ distance solutions. Complimentary techniques can be used to address this ambiguity, such as using HI absorption lines (e.g. Anderson & Bania 2009; Roman-Duval et al. 2010, see §2.6.6)

## 2.6 Tracers of Interstellar Gas

A large number of atomic and molecular species exist within the ISM, many of which readily emit spectral lines in their local environment. These spectral lines allow the nature of the ISM to be probed through radio telescope observations, as was described in the previous sections. This section focuses on the properties of the individual atomic and molecular species and their line transitions that have been exploited in this thesis, and of which are important to the subsequent TeV gamma-ray studies.

## 2.6.1 Molecular Hydrogen

Hydrogen is the most abundant element in the universe, making up approximately 75% of baryonic matter. Molecular hydrogen, H<sub>2</sub>, is central to the evolution of stars and galaxies and is the largest component of molecular clouds and the ISM.

Despite being abundant, however, H<sub>2</sub> is difficult to observe directly. Due to the molecule's small mass and lack of an associated permanent dipole, the lowest energy transitions of the molecule are very weak rotational quadrupole transitions with wavelengths in the far-infrared ( $\lambda = 28.22 \mu\text{m}$ ), with decay lifetimes of over 100 years. These transitions are only achievable when the gas temperatures are in excess of 100 K, with the lowest vibrational modes of H<sub>2</sub> activating at even larger temperatures (e.g. Habart et al. 2005, and references therein). Consequently, the cold molecular H<sub>2</sub> which makes up most of the ISM is essentially invisible in emission.

For these reasons, an alternative to direct observations of H<sub>2</sub> is required. This is done via the use of 'tracer' molecules that act as a proxy for H<sub>2</sub>. The excitation of these tracer molecules occur through collisions with H<sub>2</sub>, and above some critical density,  $n_c$  (see §2.2.3), spectral line signals from the tracer molecule will be observable. Common tracer molecules include CO (§2.6.2) and CS (§2.6.3), and are used extensively in this thesis.

### 2.6.1.1 Column density and X-factors

Since the ISM mostly consists of H<sub>2</sub>, it is desirable to convert the calculated column density of some tracer molecule,  $N_{\text{mol}}$  (see §2.4.1), into the column density of H<sub>2</sub>,  $N_{\text{H}_2}$ . This can be done via the use of an abundance ratio  $\chi_{\text{mol}} = [\text{mol}]/[\text{H}_2]$ , which gives the ratio between the expected number of tracer and H<sub>2</sub> molecules.  $N_{\text{H}_2}$  is then given by:

$$N_{\text{H}_2} = \chi_{\text{mol}} N_{\text{mol}} \quad (2.71)$$

Tables of the average  $\chi_{\text{mol}}$  of the various molecular species used in the thesis can be found in Irvine et al. (1987).

An alternative way to estimate the H<sub>2</sub> column density is the use of an 'X-factor',  $X_{\text{mol}}$ . This is a conversion factor which relates the integrated intensity of some molecular line transition,  $W_{\text{mol}}$ , to  $N_{\text{H}_2}$  by:

$$N_{\text{H}_2} = X_{\text{mol}} W_{\text{mol}} \quad (2.72)$$

X-factors are experimentally derived values (e.g. Strong et al. 2004), and the use of an X-factor is common with the CO(1-0) emission line (see §2.6.2). However, uncertainties arise from the use of a X-factor, as the value may fluctuate due to deviations

in the local conditions. The uncertainty in  $X_{\text{CO}(1-0)}$ , for example, is estimated to be  $\sim 30\%$  across the disk of the Galaxy (Bolatto et al., 2013; Heyer & Dame, 2015). Nevertheless, X-factors remain a useful tool to easily convert measured molecular line intensities to  $\text{H}_2$  column densities, especially in the case of large scale survey datasets.

### 2.6.1.2 Mass and Density

From the  $\text{H}_2$  column density,  $N_{\text{H}_2}$ , the mass,  $M$ , of the gas contained within a region of interest can be calculated by:

$$M = \mu m_{\text{H}} N_{\text{H}_2} A \quad (2.73)$$

where  $m_{\text{H}}$  is the mass of a hydrogen atom, and  $A$  is the cross-sectional area of the region.  $\mu$  is the weight factor, and is often taken that  $\mu = 2.8$  to account for the assumed 20% helium number content of molecular gas.

The  $\text{H}_2$  number density,  $n_{\text{H}_2}$ , can then be calculated from the mass estimated via:

$$n_{\text{H}_2} = \frac{M}{V \mu m_{\text{H}}} \quad (2.74)$$

where  $V$  is the volume that is assumed to be occupied by the gas. For the case of the work in this thesis, it is useful to consider the proton number density,  $n = \mu n_{\text{H}}$ , in a region, as hadronic proton-proton interactions between CRs and target material may produce TeV gamma-rays (see §1.4.4).

## 2.6.2 Carbon Monoxide

Carbon monoxide, ( $^{12}\text{C}^{16}\text{O} \equiv \text{CO}$ ), is one of the most abundant molecules in the ISM, second only to  $\text{H}_2$ . Favourable physical characteristics make CO a commonly used tracer in studies of the ISM. CO is a linear rotor molecule (see §2.2.1) with a weak electric dipole moment of 0.122 D (1 D =  $3.335 \times 10^{-30}$  C·m). The molecule is easily excited from its ground rotational state to the 1st rotational energy level by collisions with  $\text{H}_2$  molecules, even within cold molecular clouds. Due to its low spontaneous emission rate, the CO(1–0) transition has a low critical density (see §2.2.3) of  $n_c \sim 5 \times 10^2 \text{ cm}^{-3}$  making CO(1–0) an ideal tracer of gas in the ISM. A recent review of CO and its use in tracing molecular clouds in our Galaxy can be found in Heyer & Dame (2015).

### CO-to- $\text{H}_2$ X-factor

As mentioned in §2.6.1.1, a CO-to- $\text{H}_2$  X-factor,  $X_{\text{CO}}$ , is often employed to convert the integrated intensity of the CO(1–0) line,  $W_{\text{CO}}$ , into the column density of  $\text{H}_2$  via

Equation 2.72. As an experimentally derived value, many methods have been used to find the value of  $X_{\text{CO}}$ , including comparisons between CO emission with the dust emission (e.g. Planck Collaboration et al. 2011) and the diffuse gamma-ray emission (e.g. Strong & Mattox 1996) within the Galaxy. A recent review of the various experiments and values derived for  $X_{\text{CO}}$  can be found in Bolatto et al. (2013). For the work in this thesis, the value of  $X_{\text{CO}} = 1.5 \times 10^{20} \text{ cm}^{-2} (\text{K km s}^{-1})^{-1}$  from Strong et al. (2004) was adopted. As mentioned previously, the uncertainties involved in using the  $X_{\text{CO}}$  factor is  $\sim 30\%$  across the Galactic disk (Bolatto et al., 2013).

### CO Isotopologues

CO has a high abundance in the ISM, and the low critical density of the 1–0 rotational transition makes observations of CO(1–0) relatively simple to achieve. However, this causes radiative trapping processes to be non-negligible and regions can often become optically thick to this emission. The isotopologues  $^{13}\text{CO}$  and  $\text{C}^{18}\text{O}$  are often used to help combat this issue, as they have significantly lower abundance levels ( $\chi_{\text{CO}}/\chi_{^{13}\text{CO}} \sim 20 - 90$  and  $\chi_{\text{CO}}/\chi_{\text{C}^{18}\text{O}} \sim 490$ , Garden et al. 1991). The lower abundance levels imply that the transitions are less likely to be optically thick. In the limit where  $^{12}\text{CO}$  and  $^{13}\text{CO}$  are optically thick and thin respectively, the optical depth of the  $^{12}\text{CO}(1-0)$  transition can be estimated by:

$$\tau = \frac{X_{12/13}}{R_{12/13}} \quad (2.75)$$

where  $X_{12/13}$  is the isotope abundance ratio and  $R_{12/13}$  is the ratio of the measured brightness temperatures between the  $^{12}\text{CO}$  and  $^{13}\text{CO}$  emission (Burton et al., 2013).

It should be noted that the abundance ratio of isotopologues will vary across the galaxy due to differences in the local environment. In this thesis, for the case of  $^{13}\text{CO}$ , the abundance ratio was determined via the relation  $\chi_{\text{CO}}/\chi_{^{13}\text{CO}} = 5.5r + 24.2$ , where  $r$  is the galactocentric radius in kpc (Henkel et al., 1982).

### CO freeze out

An issue that arises with CO, however is that, at low temperatures ( $\sim 10$  K) or in particularly dense regions ( $n_{\text{H}} \sim 10^5 - 10^6 \text{ cm}^{-3}$ ), CO molecules may ‘freeze-out’ onto dust grains. This lowers the abundance of CO, which may lead to an underestimation of the mass if not accounted for. This issue is not unique to CO though, and is common to all molecules in varying degrees. An example of CO freeze-out was observed by Tafalla et al. (2004), where a decrease in CO abundance by a factor of  $\sim 3 - 10$  was found towards the dense, starless cores L1498 and L1517B.

### 2.6.3 Carbon Monosulfide

Carbon monosulfide, ( $^{12}\text{C}^{32}\text{S} \equiv \text{CS}$ ), is another commonly used tracer molecule in studies of the ISM. Like CO, CS is a linear rotor molecule, though its electric dipole moment is much larger ( $\mu = 1.9$  D). As a result, the critical density for the 1st excited rotational state is  $n_c \sim 5 \times 10^4 \text{ cm}^{-3}$ . Compared with CO(1–0), CS(1–0) is used to provide a complementary tracer of the dense molecular cores and clumps that can exist towards the centre of molecular clouds.

While CS is not as abundant as CO (Irvine et al., 1987), the CS(1–0) line is still sometimes found to be optically thick. If observations of the isotopologue lines  $\text{C}^{34}\text{S}(1–0)$  and  $^{13}\text{CS}(1–0)$  are available, then Equation 2.59 can be used to constrain the optical depth, where the  $R$  term is the relative abundance ratio between CS and the isotopologue. Equation 2.59 will simplify to the following:

$$\frac{T_{b|\text{cs}}}{T_{b|\text{cs}^*}} \approx \frac{1 - e^{-\tau_{\text{cs}}}}{1 - e^{-R\tau_{\text{cs}}}} \quad (2.76)$$

where  $\text{CS}^*$  denotes an isotopologue of CS.

The abundance ratio of CS to  $\text{H}_2$ ,  $\chi_{\text{CS}}$ , is used to convert the CS column density in  $\text{H}_2$  column density. However, the value of  $\chi_{\text{CS}}$  can vary by an order of magnitude between  $10^{-9}$  and  $10^{-8}$  (Irvine et al., 1987). Additionally, CS freeze out onto dust grains in cold and dense cores may also occur (e.g. Tafalla et al. 2004), similar to that of CO. For the work in this thesis, the value of  $\chi_{\text{CS}} \sim 10^{-9}$  was adopted, typical of dense and quiescent gas and, as such, calculated gas parameter values are considered to be upper limits.

### 2.6.4 Silicon Monoxide

Silicon monoxide ( $\text{SiO}$ ) is often used as a tracer in regions that have been shocked and disrupted, or in energetic environments.  $\text{SiO}$  itself is a linear rotor molecule with a large electric dipole moment of  $\mu = 3.087$  D, resulting in a high  $\text{SiO}(1–0)$  critical density of  $n_c \sim 6 \times 10^4 \text{ cm}^{-3}$ .

Unlike the easily detectable CO transitions, emission from  $\text{SiO}$  is more rarely seen, as large fractions of Si deplete onto dust grains. However, the bombardment of dust particles by molecules (such as CO) in shocks are thought to release silicates, which are then eroded by oxygen atoms and eventually form  $\text{SiO}$  (Gusdorf et al., 2008). The emission of the  $\text{SiO}(1–0)$  line has been observed behind the passage of shocks with velocities  $v_s \sim 25 \text{ km s}^{-1}$  in regions with ambient densities of  $n_{\text{H}_2} \sim 10^4$  to  $10^5 \text{ cm}^{-3}$ . These types of shocks are typical of star forming regions, as well as SNRs as they cross regions of dense ISM. As such, detections of  $\text{SiO}$  line emission are considered

strong signposts indicating the presence of interstellar shocks (e.g. Nicholas et al. 2012).

### 2.6.5 Methanol and masers

Methanol ( $\text{CH}_3\text{OH}$ ) is an important tracer of star formation regions, and the emission from this molecule appears in the form of masers.

Astrophysical masers (Microwave Amplification by Stimulated Emission of Radiation) are strong sources of stimulated spectral line emission, and are closely related to the more familiar lasers. The emission from an astrophysical maser is monochromatic, and has a frequency corresponding to the gap between two energy levels of a particular species in the gain medium. The species in the gain medium are pumped via collisions or radiation mechanisms into a population inversion. Like a laser, emission is generated by the stimulated emission of light (see §2.2.2). However, astrophysical masers lack the resonance cavity found in lasers, and the emission is generated by a single pass through the gain medium.

Methanol masers come in two classes. Class I masers,  $\text{CH}_3\text{OH(I)}$ , are formed where the population inversion is due to collisional excitation, while Class II masers,  $\text{CH}_3\text{OH(II)}$ , are radiatively pumped.  $\text{CH}_3\text{OH(I)}$  masers typically occur at the outskirts of star formation regions, although Nicholas et al. (2012) saw  $\text{CH}_3\text{OH(I)}$  masers towards the SNR W28.  $\text{CH}_3\text{OH(II)}$  masers typically occur more towards the central regions of star formation regions (see e.g. Voronkov et al. 2014).

### 2.6.6 Atomic Hydrogen

In addition to molecular hydrogen gas, much of the Galactic ISM consists of atomic gas. The most common tool used to probe atomic gas is the 21 cm  $\text{H}\text{I}$  emission line. Neutral atomic hydrogen consists solely of an electron in orbit about a proton. The electron and proton each have an associated spin which may be aligned parallel or anti-parallel. The resulting magnetic interactions cause the parallel spin state to have a higher energy compared with the anti-parallel spin state, and the 21 cm  $\text{H}\text{I}$  line is caused by the transition between these two states.

This transition has very low spontaneous emission rate,  $A = 2.85 \times 10^{-15} \text{ s}^{-1}$ , and a low critical density  $n_c \sim 10^{-3} \text{ cm}^{-3}$ . In addition, atomic hydrogen has a very large column density in the ISM ( $N_{\text{HI}} \sim 10^{21} \text{ cm}^{-2}$ ), and hence  $\text{H}\text{I}$  emission is easily observable from the interstellar diffuse atomic gas.

Assuming an optical thin case, the integrated intensity of  $\text{H}\text{I}$  emission,  $W_{\text{HI}}$ , can be converted to atomic hydrogen column density,  $N_{\text{HI}}$ , via the relation:

$$N_{\text{HI}} = W_{\text{HI}} X_{\text{HI}} \quad (2.77)$$

where the conversion X-factor  $X_{\text{HI}} = 1.823 \times 10^{18} \text{ cm}^{-2} (\text{K kms}^{-1})^{-1}$ . Note that, unlike the CO X-factor, this conversion factor is not an empirically derived value, but rather an exact relation that comes from the expressions for radiative transfer and column density in an optically thin scenario (see Dickey & Lockman 1990). Combining  $N_{\text{HI}}$  with the molecular hydrogen column density,  $N_{\text{H}_2}$ , obtained from observations in molecular tracers, the total hydrogen column density in a region can be estimated:

$$N_{\text{H}} = N_{\text{HI}} + 2N_{\text{H}_2} \quad (2.78)$$

Absorption features can often appear in the HI spectra. This can occur when radiation from background continuum sources is absorbed by foreground gas clouds. This can be exploited to discriminate between the near and far kinematic distances (see §2.5) obtained from using Galactic rotation curves, provided the location of the continuum source is known. A more detailed overview of this method is outlined in Roman-Duval et al. (2010). Absorption features can also be caused by HI self-absorption, which may occur in optically thick and cold sources. This may lead to an underestimation of the atomic column density if not taken into consideration. Additional analysis techniques, such as those employed in Fukui et al. (2012), can be used to account for these effects. These techniques involve estimating the expected HI profiles without the self-absorption in order to correct for the missing ‘dark’ HI.

### 2.6.7 Atomic Carbon

Carbon is one of the most abundant element in the universe (after hydrogen, helium and oxygen). In the ISM, carbon can be found in molecular forms, such as in CO and CS (see §2.6.2 and §2.6.3 respectively), as well as in ionised ( $\text{C}^+$ ) and atomic (C) forms. Emission lines for  $\text{C}^+$  and C are produced in the terahertz portion of the spectrum, compared with the millimetre portion for CO and CS.

While the standard tracer for molecular hydrogen is CO, the abundance of CO molecules can be greatly diminished from photo-dissociation by UV radiation and interactions with CRs (Bolatto et al., 2013), particularly in the outer envelopes of ISM molecular clouds. Within these regions, carbon will be found as C or  $\text{C}^+$ . Emission from neutral atomic carbon, [CI], typically arises from gas where molecular hydrogen exists without significant amounts of CO (van Dishoeck & Black, 1988). Thus, [CI] can be used to survey molecular hydrogen that is ‘dark’ to the standard CO tracer (e.g. Burton et al. 2015).

Extremely dry skies are required to detect C and  $\text{C}^+$  lines, and observation by ground based observatories are difficult. For example, the High Elevation Antarctic Terahertz (HEAT) telescope (see HEAT website 2017) is located at Ridge A on the

Antarctic plateau, as this location is one of the few places on Earth where the skies are dry and stable enough to perform observations in these carbon lines. Data from this telescope were used in the ISM study of one particular TeV  $\gamma$ -ray source in this thesis (HESS J1616–508, see Chapter 4).

The following three chapters consist of the studies of the ISM towards the TeV gamma-ray sources HESS J1640–465, HESS J1641–463, HESS J1614–518, HESS J1616–508 and HESS J1702–420, that were conducted as part of this thesis.



## Chapter 3

# The ISM towards HESS J1640–465 and HESS J1641–463

The following is a paper published in the peer-reviewed journal, Monthly Notices of the Royal Astronomical Society (MNRAS). The paper consists of a detailed analysis of the interstellar medium towards HESS J1640–465 and HESS J1641–463, and the implications the findings have on the origins of these TeV gamma-ray sources.



# Statement of Authorship

Title of Paper	Interstellar gas towards the TeV $\gamma$ -ray sources HESS J1640-465 and HESS J1641-463		
Publication Status	<input checked="" type="checkbox"/> Published <input type="checkbox"/> Accepted for Publication <input type="checkbox"/> Submitted for Publication <input type="checkbox"/> Unpublished and Unsubmitted work written in manuscript style		
Publication Details	Lau J. C. et al., 2017, MNRAS, 464, 3757 Author list: J. C. Lau, G. Rowell, M. G. Burton, Y. Fukui, F. A. Aharonian, I. Oya, J. Vink, S. Ohm and S. Casanova		

## Principal Author

Name of Principal Author (Candidate)	James Cheuk-Heng Lau		
Contribution to the Paper	Mopra data observations, data reduction, spectral line analysis, interstellar medium and high energy interpretations, and writing of the paper.		
Overall percentage (%)	70%		
Certification:	This paper reports on original research I conducted during the period of my Higher Degree by Research candidature and is not subject to any obligations or contractual agreements with a third party that would constrain its inclusion in this thesis. I am the primary author of this paper.		
Signature		Date	24/10/17

## Co-Author Contributions

By signing the Statement of Authorship, each author certifies that:

- i. the candidate's stated contribution to the publication is accurate (as detailed above);
- ii. permission is granted for the candidate to include the publication in the thesis; and
- iii. the sum of all co-author contributions is equal to 100% less the candidate's stated contribution.

Name of Co-Author	Gavin Rowell		
Contribution to the Paper	ISM analysis, ISM and high energy interpretations and general reviewing of paper (12%)		
Signature		Date	15/9/17

Name of Co-Author	Michael Burton		
Contribution to the Paper	Mopra observations, ISM interpretations and general reviewing (6%)		
Signature		Date	23/10/17

Name of Co-Author	Yasuo Fukui	
Contribution to the Paper	ISM interpretation (2%)	
Signature	Date	19th September. 2017

Name of Co-Author	Felix Aharonian	
Contribution to the Paper	High energy interpretation (2%)	
Signature	Date	18 Sep 2017

Name of Co-Author	Igor Oya	
Contribution to the Paper	High energy interpretation (2%)	
Signature	Date	18.09.2017

Name of Co-Author	Jacco Vink	
Contribution to the Paper	High energy interpretation (2%)	
Signature	Date	October 3, 2017

Name of Co-Author	Stefan Ohm	
Contribution to the Paper	High energy interpretation (2%)	
Signature	Date	18.09.2017

Name of Co-Author	Sabrina Casanova	
Contribution to the Paper	High energy interpretation (2%)	
Signature	Date	20.09.2017



# Interstellar gas towards the TeV $\gamma$ -ray sources HESS J1640–465 and HESS J1641–463

J. C. Lau,<sup>1</sup>★ G. Rowell,<sup>1</sup> M. G. Burton,<sup>2,3</sup> Y. Fukui,<sup>4</sup> F. A. Aharonian,<sup>5,6,7</sup> I. Oya,<sup>8</sup> J. Vink,<sup>9</sup> S. Ohm<sup>8</sup> and S. Casanova<sup>5,10</sup>

<sup>1</sup>School of Physical Sciences, University of Adelaide, Adelaide, SA 5005, Australia

<sup>2</sup>School of Physics, University of New South Wales, Sydney, NSW 2052, Australia

<sup>3</sup>Armagh Observatory and Planetarium, College Hill, Armagh, BT61 9DG, Northern Ireland, UK

<sup>4</sup>Department of Physics, University of Nagoya, Furo-cho, Chikusa-ku, Nagoya, 464-8601, Japan

<sup>5</sup>Max-Planck-Institut für Kernphysik, PO Box 103980, D-69029 Heidelberg, Germany

<sup>6</sup>Dublin Institute for Advanced Studies, 31 Fitzwilliam Place, Dublin 2, Ireland

<sup>7</sup>National Research Nuclear University (MEPHI), 115409, Moscow, Russia

<sup>8</sup>DESY, D-15738 Zeuthen, Germany

<sup>9</sup>GRAPPA, Anton Pannekoek Institute for Astronomy, University of Amsterdam, Science Park 904, NL-1098 XH Amsterdam, the Netherlands

<sup>10</sup>Instytut Fizyki Jądrowej PAN, ul. Radzikowskiego 152, PL-31-342 Krakow, Poland

Accepted 2016 October 18. Received 2016 October 16; in original form 2016 July 13; Editorial Decision 2016 October 17

## ABSTRACT

We present a detailed analysis of the interstellar medium towards the tera electron volt (TeV)  $\gamma$ -ray sources HESS J1640–465 and HESS J1641–463 using results from the Mopra Southern Galactic Plane CO Survey and from a Mopra 7 mm-wavelength study. The  $\gamma$ -ray sources are positionally coincident with two supernova remnants (SNRs) G338.3–0.0 and G338.5+0.1, respectively. A bright complex of H II regions connect the two SNRs and TeV objects. Observations in the CO(1–0) transition lines reveal substantial amounts of diffuse gas positionally coincident with the  $\gamma$ -ray sources at multiple velocities along the line of sight, while 7 mm observations in CS, SiO, HC<sub>3</sub>N and CH<sub>3</sub>OH transition lines reveal regions of dense, shocked gas. Archival H I data from the Southern Galactic Plane Survey was used to account for the diffuse atomic gas. Physical parameters of the gas towards the TeV sources were calculated from the data. We find that for a hadronic origin for the  $\gamma$ -ray emission, the cosmic ray enhancement rates are  $\sim 10^3$  and  $10^2$  times the local solar value for HESS J1640–465 and HESS J1641–463, respectively.

**Key words:** molecular data – supernovae: individual: SNR G338.3–0.0 – supernovae: individual: SNR G338.5+0.1 – ISM: clouds – cosmic rays – gamma-rays: ISM.

## 1 INTRODUCTION

HESS J1640–465 and HESS J1641–463 are two adjacent and intriguing very high energy (VHE,  $E > 100$  GeV)  $\gamma$ -ray sources whose origins are uncertain. Knowledge of the distribution of interstellar gas towards these sources is vital in order to differentiate between possible models of tera electron volt (TeV)  $\gamma$ -ray production. In particular, understanding the hadronic production model of TeV  $\gamma$ -rays in which highly accelerated cosmic rays (CRs) interact with target atomic and molecular gas.

HESS J1640–465 is a VHE  $\gamma$ -ray source first discovered by the High Energy Stereoscopic System (HESS) during a survey of the Galactic plane (Aharonian et al. 2006). It is positionally coincident with the supernova remnant G338.3–0.0 (Whiteoak & Green 1996).

Observations with *XMM-Newton* detected a slightly extended and asymmetric X-ray source towards the geometric centre of the supernova remnant (SNR) G338.3–0.0 (Funk et al. 2007). Follow-up observations with *Chandra* in X-rays revealed an extended nebula with a point-like source, a possible associated pulsar (Lemiere et al. 2009). It was suggested that the X-rays and VHE  $\gamma$ -rays were then due to synchrotron and inverse-Compton emission from a pulsar wind nebula (PWN). Multifrequency radio analysis by Castelletti et al. (2011) placed upper limits on the radio flux from the region of the supposed PWN. Observations with the *Fermi* Large Area Telescope (*Fermi*-LAT) revealed a high energy (HE)  $\gamma$ -ray source (1FGL 1640.8–4634) coincident with HESS J1640–465 (Slane et al. 2010).

Further observations by HESS (Abramowski et al. 2014a) show that the VHE  $\gamma$ -rays seen from HESS J1640–465 overlap significantly with the SNR shell of G338.3–0.0. The VHE  $\gamma$ -ray spectrum connects smoothly with the giga electron volt (GeV)  $\gamma$ -ray spectrum

\* E-mail: james.lau@adelaide.edu.au

obtained by the analysis of 5 yr worth of *Fermi*-LAT data towards HESS J1640–465 (Lemoine-Goumard et al. 2014). The smooth, flat and featureless  $\gamma$ -ray spectrum strengthened the hadronic scenario in which CRs accelerated by the SNR are interacting with nearby gas (Abramowski et al. 2014a; Lemoine-Goumard et al. 2014). However, a contribution to the detected flux by a pulsar or PWN could not be ruled out. Recent work by Supan, Supanitsky & Castelletti (2016) looked at the spectral energy distribution (SED) of HESS J1640–465 using latest data from HESS and *Fermi*-LAT observations, together with an updated hadronic  $\gamma$ -ray model (Kafexhiu et al. 2014) and archival atomic (HI) and molecular data. Their fit yielded a spectra index  $\Gamma = 2.13$  with a cut-off energy  $E_{\text{cut}} = 54$  TeV. This hadronic model was found to fully describe the  $\gamma$ -ray spectrum of HESS J1640–465.

Shortly after the HESS publication (Abramowski et al. 2014a), Gotthelf et al. (2014) discovered pulsed X-ray emission using the Nuclear Spectroscopic Telescope Array emanating from the previously discovered X-ray source seen towards the centre of HESS J1640–465. The newly discovered pulsar PSR J1640–4631 has a period of 206 ms with a spin-down luminosity of  $4.4 \times 10^{36}$  erg s $^{-1}$  and a characteristic age of 3350 yr. Modelling of leptonic  $\gamma$ -ray production suggested that a PWN could be responsible for the TeV emission from HESS J1640–465, although fine-tuning is required to explain the smooth GeV and TeV spectrum.

HESS J1641–463 was initially unnoticed by standard HESS detection techniques due to its low brightness and proximity to the bright source HESS J1640–465. Energy cuts and deeper observations led to the positive identification of the new TeV  $\gamma$ -ray source at a significance of  $8.5\sigma$  at energies above 4 TeV (Abramowski et al. 2014b). HESS J1641–463 has an unusually hard spectrum (photon index  $\Gamma \approx 2$ ) with no obvious sign of a cut-off. Analysis of *Fermi*-LAT data (Lemoine-Goumard et al. 2014) reported the detection of two distinct GeV sources positionally coincident with HESS J1641–463 and the nearby HESS J1640–465. HESS J1641–463 is positionally coincident with the radio SNR G338.5+0.1. The SNR itself is seen as a poorly defined circle of non-thermal emission (Whiteoak & Green 1996). The pair of SNRs seen towards the two HESS sources are connected by a complex of H II regions, which includes G338.4+0.0 and G338.45+0.06.

The production of TeV  $\gamma$ -ray emission from HESS J1641–463 via leptonic processes via a population of electrons with energies of several hundred TeV upscattering background photons was considered by Abramowski et al. (2014b). These electrons could be sourced from the coincident SNR G338.5+0.1 or even from a nearby PWN. This leptonic scenario, however, should be accompanied by a characteristic break in the  $\gamma$ -ray spectrum at multiTeV energies resulting from the Klein–Nishina effect on the cross-section for inverse-Compton scattering at high energies. The lack of such a characteristic break in the  $\gamma$ -ray spectrum of HESS J1641–463 led the authors to disfavour the leptonic scenario.

A more promising scenario is that the  $\gamma$ -ray emission from HESS J1641–463 is due to interstellar medium (ISM) illuminated by highly accelerated CRs. Modelling by Abramowski et al. (2014b) indicate that the TeV spectrum of HESS J1641–463 could be produced by distribution of protons (with a power-law slope of  $-2.1$ ) interacting with molecular gas seen by using CO(1–0) data taken with the Nanten radio telescope. The proton spectrum would need to have a high cut-off energy ( $>100$  TeV) and represents one of the hardest spectra associated with a TeV  $\gamma$ -ray source extending into the PeV energy range; a so-called PeVatron. The coincident SNR G338.5+0.1 could possibly be the source of these CR protons, provided it had a young age ( $\lesssim 1$  kyr), as the proton spectrum

agrees with predictions of diffusive shock acceleration in young SNRs. However, an older SNR (5–17 kyr; Abramowski et al. 2014b) would not be able to accelerate CRs up to PeV energies (Bell et al. 2013), and would require another CR source. An intriguing idea is that VHE protons accelerated by the young SNR coincident with HESS J1640–465, SNR G338.3–0.0 (with an age of 1–2 to 5–8 kyr (Slane et al. 2010; Abramowski et al. 2014a) could be diffusively reaching the gas towards HESS J1641–463. The energy-dependent process of diffusion would preferentially allow higher energy CRs to reach the target material earlier (Aharonian & Atoyan 1996), producing the hard proton spectrum that is needed to generate the TeV  $\gamma$ -ray spectrum of HESS J1641–463.

Another puzzling aspect about HESS J1641–463 is the marked difference between the GeV and TeV components of its  $\gamma$ -ray spectrum. The GeV spectrum as measured by *Fermi*-LAT is very soft, which is in stark contrast to the very hard TeV spectrum as measured by HESS. This suggests that there may be two different sources to the GeV and TeV components. A possible scenario would be GeV  $\gamma$ -rays are produced by less energetic CRs from the old SNR G338.5+0.1 illuminating ambient gas, with TeV emission produced by higher energy CRs from the younger SNR G338.3–0.0.

Any attempt to fully understand the origin scenarios of both HESS J1640–465 and HESS J1641–463 requires a detailed understanding of the distribution of the ISM in the surrounding environment. Thus, we have used high-resolution data collected by the Mopra radio telescope in this study. As part of the Mopra Southern Galactic Plane CO Survey, the distribution of diffuse ( $\bar{n} \lesssim 10^3$  cm $^{-3}$ ) ISM was traced towards HESS J1640–465 and HESS J1641–463. In addition, we have taken complimentary data in the 7 mm wavelength band, targeting the dense ( $\bar{n} \gtrsim 10^4$  cm $^{-3}$ ) gas tracer CS(1–0) as well as the tracers SiO(1–0), CH<sub>3</sub>OH and HC<sub>3</sub>N.

In Section 2, we describe the parameters of the data taken by the Mopra radio telescope and the data reduction processes. The gas parameter calculations we apply to these data are described in Section 3. In Section 4, we investigate the gas distribution towards HESS J1640–465 and HESS J1641–463 and, in Section 5, we discuss the impact our results have on the possible emission scenarios for the TeV sources.

## 1.1 Distance to SNRs and H II complex

The distance to SNR G338.3–0.0 and SNR G338.5+0.1 and the H II complex containing G338.4+0.0 and G338.45+0.06 have previously been reported in several studies utilizing observations in the 21 cm H I spectral line.

Lemiere et al. (2009) derived a distance of 8–13 kpc for SNR G338.3–0.0 and the H II surrounding region based on H I absorption features. This is in agreement with previous work presented by Kothes & Dougherty (2007), who also used H I absorption to derive a distance of  $11.7_{-0.5}^{+2.0}$  kpc for G338.4+0.0. The nearby SNR G338.5+0.1, coincident with HESS J1641–463, was found to have a very similar H I absorption profile as G338.4+0.0, which led to the assertion that it too was most likely located at  $\sim 11$  kpc.

The velocity along the line of sight ( $v_{\text{LSR}}$ ) of the H II regions in the complex have been measured to have values of  $\sim -40$  to  $-30$  km s $^{-1}$  (Caswell & Haynes 1987; Russeil 2003; Urquhart et al. 2012). The kinematic distance ambiguities towards these H II regions have been addressed and they have been constrained to the far distance (Urquhart et al. 2012).

This places the two SNRs and the H II complex in the Norma II spiral arm at the far side of the Galaxy. In our results in Section 4, we have used the Galactic rotation curve in Kothes & Dougherty

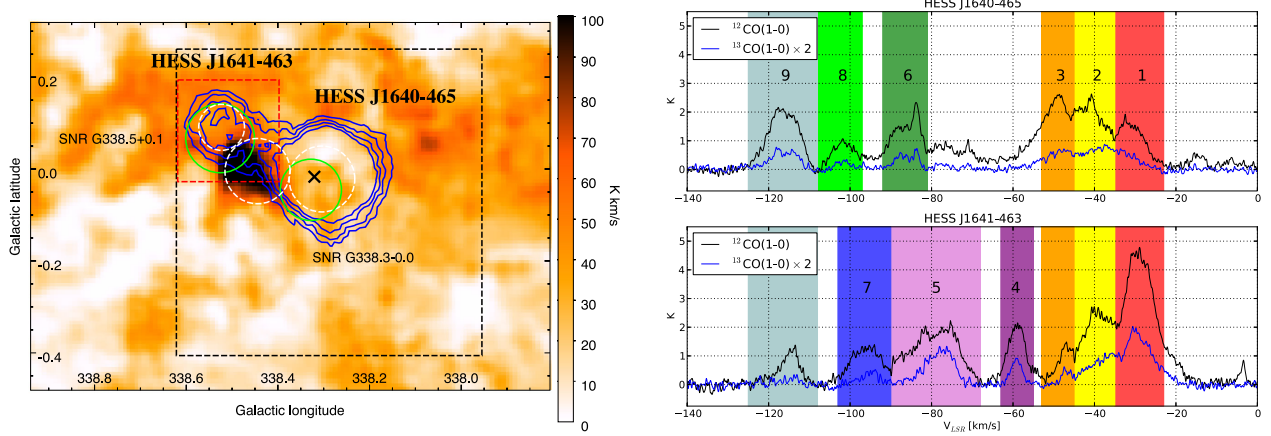


**Figure 1.** Left: Mopra  $^{12}\text{CO}(1-0)$  image [ $\text{K km s}^{-1}$ ] integrated between  $-53$  and  $-23 \text{ km s}^{-1}$  towards HESS 1641–463 and HESS 1640–465. Blue contours are HESS significance contours towards the TeV sources at the  $5\sigma$ ,  $6\sigma$ ,  $7\sigma$  and  $8\sigma$  levels at  $E > 4 \text{ TeV}$  (Abramowski et al. 2014b). Dashed black and red boxes are the extent of the 7 mm observations and region of additional observations as discussed in text. Solid green circles are the positions of the labelled SNRs. The black X is the position of PSR J1640–4631. The three dashed white circles are the regions from which CO spectra were extracted, as discussed in text. Right: solid black and blue lines are the average  $^{12}\text{CO}(1-0)$  and  $^{13}\text{CO}(1-0)$  emission spectra, respectively, within the rightmost and leftmost dashed white circles towards the TeV sources.  $^{13}\text{CO}$  scaled by factor of 2 for clarity. Velocity integration intervals used in Fig. 2 are numbered and indicated by the shaded boxes.

(2007) to calculate distances for corresponding  $v_{\text{LSR}}$ . For purposes of our discussion in Section 5, we adopt a distance of 11 kpc for the two SNRs, H II regions and both HESS J1640–465 and HESS J1641–463.

## 2 MOPRA OBSERVATIONS AND DATA REDUCTION

For the 7 mm targeted studies, initial Mopra observations towards HESS J1640–465 and HESS J1641–463 were taken in 2012 April. Four Mopra ‘On-the-fly’ (OTF)  $20 \text{ arcmin} \times 20 \text{ arcmin}$  area maps were taken resulting in a  $40 \text{ arcmin} \times 40 \text{ arcmin}$  region centred at  $[l, b] = [338:26, -0:072]$ . The scan length was 7.6 arcsec per cycle time of 2.0 s with spacings of 31.2 arcsec between each scan row. Each scan consisted of 79 cycles ( $\sim 158$  s). After every two scans, a sky reference position was observed for 18 cycles ( $\sim 36$  s) which was used for subtraction in the data reduction process. Three passes were observed towards each  $20 \text{ arcmin} \times 20 \text{ arcmin}$  region in alternating  $l$  and  $b$  scanning directions. This resulted in  $\sim 9$  h of observations per  $20 \text{ arcmin} \times 20 \text{ arcmin}$  map. The 7 mm coverage is indicated by the large dashed black box in left-hand panel of Fig. 1.

In 2013 May, additional observations were taken in a smaller,  $12 \text{ arcmin} \times 12 \text{ arcmin}$  region centred at  $[l, b] = [338:51, -0:083]$  towards HESS J1641–463. Similar scan parameters were used as in the  $20 \text{ arcmin} \times 20 \text{ arcmin}$  maps over six new passes resulting in  $\sim 3$  times the observation time in this region. The additional observations resulted in greater sensitivity and a lower  $T_{\text{RMS}}$  by a factor of  $\sim 1.7$ . This region is indicated by the dashed red box in the left-hand panel of Fig. 1.

The Mopra spectrometer, MOPS, was used to target specific molecular line tracers. MOPS is capable of recording in sixteen 4096-channel bands simultaneously whilst in its ‘zoom’ mode as employed here in our 7 mm observations. The list of the targeted molecular transitions and  $T_{\text{RMS}}$  levels are displayed in Table 1. The beam full width at half-maximum (FWHM) of Mopra across the 7 mm band varies from 1.37 arcmin (31 GHz) to 0.99 arcmin

**Table 1.** The Mopra Spectrometer (MOPS) set-up for 7 mm observations. Displayed are the targeted molecular lines, targeted frequencies, whether the line was detected in our observations and the achieved mapping  $T_{\text{RMS}}$ .

Molecular line	Frequency (GHz)	Detection	$T_{\text{RMS}}^a$ (K/channel)
$^{30}\text{SiO}(J = 1-0, v = 0)$	42.373 365	–	0.04
$\text{SiO}(J = 1-0, v = 3)$	42.519 373	–	0.04
$\text{SiO}(J = 1-0, v = 2)$	42.820 582	–	0.04
$^{29}\text{SiO}(J = 1-0, v = 0)$	42.879 922	–	0.04
$\text{SiO}(J = 1-0, v = 1)$	43.122 079	–	0.04
$\text{SiO}(J = 1-0, v = 0)$	43.423 864	Yes	0.04
$\text{CH}_3\text{OH-I}$	44.069 476	Yes	0.04
$\text{HC}_7\text{N}(J = 40-39)$	45.119 064	–	0.04
$\text{HC}_5\text{N}(J = 17-16)$	45.264 750	–	0.04
$\text{HC}_3\text{N}(J = 5-4, F = 4-3)$	45.490 264	Yes	0.05
$^{13}\text{CS}(J = 1-0)$	46.247 580	–	0.05
$\text{HC}_5\text{N}(J = 16-15)$	47.927 275	–	0.05
$\text{C}^{34}\text{S}(J = 1-0)$	48.206 946	Yes	0.06
$\text{OCS}(J = 4-3)$	48.651 604	–	0.06
$\text{CS}(J = 1-0)$	48.990 957	Yes	0.06

*Notes.* <sup>a</sup>Map  $T_{\text{RMS}}$  values are for the smaller  $12 \text{ arcmin} \times 12 \text{ arcmin}$  region described in the text. This is where detections in all of the 7 mm lines were made except for CS( $J = 1-0$ ). For the detections in CS( $J = 1-0$ ) outside the  $12 \text{ arcmin} \times 12 \text{ arcmin}$  region, the  $T_{\text{RMS}}$  value was  $\sim 0.1$ .

(49 GHz) and the velocity resolution of 7 mm zoom-mode data is  $\sim 0.2 \text{ km s}^{-1}$ .

The CO(1-0) line emission data are from the Mopra Southern Galactic Plane CO Survey (Burton et al. 2013; Braiding et al. 2015). This is a survey in the  $^{12}\text{CO}$ ,  $^{13}\text{CO}$  and  $\text{C}^{18}\text{O}$   $J = 1-0$  lines over the  $l = 305^\circ$ – $345^\circ$ ,  $b = \pm 0.5$  region of the Galaxy. The beam FWHM and spectral resolutions of the survey are  $0.6 \text{ arcmin}$  and  $0.1 \text{ km s}^{-1}$ , respectively. Full details about the observational parameters used in this survey can be found within the aforementioned papers.

OTF mapping data were reduced and analysed using ATNF analysis software, LIVEDATA, GRIDZILLA and MIRIAD, as well as custom IDL routines.

LIVEDATA was used to calibrate each scan row/column data against a sky reference position and to apply a polynomial baseline-subtraction. GRIDZILLA was used to re-grid and combine the data from multiple mapping scans into individual three-dimensional data cubes. MIRIAD and custom IDL routines were used to generate integrated velocity, peak velocity and position–velocity images from the data cubes.

### 3 GAS PARAMETER CALCULATIONS (SPECTRAL LINE ANALYSIS)

To investigate the gas distribution towards HESS J1640–465 and HESS J1641–463, we calculated mass and density parameters using CO(1–0), CS(1–0) and H I data. Using the custom IDL routine `dgomom`, we produced integrated intensity maps of the different molecular lines. The average column density of molecular hydrogen,  $\bar{N}_{\text{H}_2}$ , was calculated from these maps following the corresponding methods outlined in the subsequent sections. The mass of gas in a region,  $M$ , is then estimated via the relation:

$$M = 2m_{\text{H}}\bar{N}_{\text{H}_2}A, \quad (1)$$

where  $A$  is the cross-sectional area of the region and  $m_{\text{H}}$  is the mass of a hydrogen atom. From this, the average number density of the region  $\bar{n}$  was estimated assuming that the thickness of the region (along the line of sight) had the same value as the height and width. Note that before the intensity values from the velocity-integrated maps could be used to find the column density, they first had to be scaled by a correction factor to account for the beam efficiencies of Mopra at different frequencies. The Mopra extended beam efficiency at 115 GHz (CO(1–0) lines) is  $\eta_{\text{XB}} = 0.55$  (Ladd et al. 2005), while in the 7 mm band at 49 GHz (CS(1–0) lines),  $\eta_{\text{XB}} = 0.56$  (Urquhart et al. 2010).

#### 3.1 CO

In this work, to convert brightness temperature to column density, we have adopted the value of the CO(1–0) X-factor to be  $X_{\text{CO}(1-0)} \sim 1.5 \times 10^{20} \text{ cm}^{-2}(\text{K km s}^{-1})^{-1}$  (Strong et al. 2004). This allows us to calculate the average  $\text{H}_2$  column density in a region,  $\bar{N}_{\text{H}_2} = X_{\text{CO}(1-0)}W_{\text{CO}(1-0)}$ , where  $W_{\text{CO}(1-0)}$  is the measured  $^{12}\text{CO}$ (1–0) intensity.

The optical depth of the  $^{12}\text{CO}$  line,  $\tau_{12}$ , was calculated by comparing  $^{12}\text{CO}$  and  $^{13}\text{CO}$  line emission. Following Burton et al. (2013), in the limit where the  $^{12}\text{CO}$  line is optically thick and the  $^{13}\text{CO}$  line is optically thin,  $\tau_{12}$  is given by

$$\tau_{12} = \frac{X_{12/13}}{R_{12/13}}, \quad (2)$$

where  $R_{12/13}$  is the ratio of the brightness temperature of the  $^{12}\text{CO}$  and  $^{13}\text{CO}$  lines and  $X_{12/13} = [^{12}\text{C}/^{13}\text{C}]$  is the isotope abundance ratio. This abundance ratio was determined via  $X_{12/13} = 5.5R + 24.2$ , where  $R$  is the galactocentric radius in kiloparsec (Henkel, Wilson & Bieging 1982).

#### 3.2 CS

The CS( $J = 1$ ) column density was calculated using equation (9) from Goldsmith & Langer (1999). This equation expresses the upper level column density in terms of the observed integrated line intensity. The optical depth term required in this equation was determined from the CS(1–0)–C<sup>34</sup>S(1–0) intensity ratio in regions where C<sup>34</sup>S(1–0) was detected. We adopted the elemental abundance ratio

of 22.5 for [CS]/[C<sup>34</sup>S] and calculate the optical depth following equation (1) of Zinchenko et al. (1994).

Assuming local thermodynamic equilibrium at  $T_{\text{rot}} \sim 10$  K, the total column density of CS is a factor of  $\sim 3.5$  times than of the CS( $J = 1$ ) column density. This temperature assumption introduces a small systematic error into our CS(1–0) column density estimates. A factor of 0.7–1.2 error would be associated with a temperature variation between 5 and 15 K. We assume a molecular abundance of CS to molecular hydrogen to be  $\sim 10^{-9}$  (Frerking et al. 1980).

#### 3.3 H I

The Southern Galactic Plane Survey (SGPS; McClure-Griffiths et al. 2005) provided H I data towards HESS J1640–465 and HESS J1641–463. Strong absorption features due to continuum sources are seen in data corresponding to the H II regions G338.4+0.0, G338.45+0.06 and G338.39+0.16. Where H I emission features are present, we calculate the column density using an H I X-factor,  $X_{\text{H}_1} = 1.823 \times 10^{18} \text{ cm}^{-2}(\text{K km s}^{-1})^{-1}$  (Dickey & Lockman 1990).

## 4 RESULTS

Overall, the CO transitions reveal a distribution of gas along the line of sight towards the TeV sources. Significant detections made in CS(1–0) transitions reveal dense molecular cores within the gas distribution. We also note that detections were made in the SiO(1–0), CH<sub>3</sub>OH (I) and HC<sub>3</sub>N(5–4, F = 4–3) transitions towards the dense cores. We discuss these detections in more detail below.

#### 4.1 CO(1–0) emission

$^{12}\text{CO}$  and  $^{13}\text{CO}$  line emission data from the Mopra survey was studied towards HESS J1640–465 and HESS J1641–463.  $^{12}\text{CO}$ (1–0) is the standard tracer for diffuse molecular hydrogen gas, while the  $^{13}\text{CO}$ (1–0) line is generally optically thin with  $^{13}\text{CO}$  being approximately 50 times less abundant than  $^{12}\text{CO}$ . Detections in both isotopologues lines were made towards the TeV sources, as well as in other adjacent regions.

#### CO(1–0) emission towards HESS J1640–465 and HESS J1641–463

A substantial amount of CO(1–0) emission appears to be overlapping the line of sight towards HESS J1640–465 and HESS J1641–463. The left-hand panel in Fig. 1 is an integrated emission image of  $^{12}\text{CO}$ (1–0) data from the Mopra survey between  $-53$  and  $-23 \text{ km s}^{-1}$  towards the two TeV sources. The right-hand panel of Fig. 1 displays the average  $^{12}\text{CO}$ (1–0) and  $^{13}\text{CO}$ (1–0) emission spectra of the regions corresponding to the reported intrinsic Gaussian size of HESS J1640–465 and the maximum Gaussian extent of HESS J1641–463 indicated in the left-hand panel by rightmost and leftmost white dashed circles, respectively. The central white dashed circle in the left-hand panel of Fig. 1 indicates the location of intense CO(1–0) emission seen towards a region that bridges HESS J1640–465 and HESS J1641–463 and is discussed further in a later part of this section.

Multiple broad emission components are seen in the CO(1–0) spectra towards HESS J1640–465 and HESS J1641–463 in the right-hand panel of Fig. 1 between  $-140$  and  $0 \text{ km s}^{-1}$ . The velocity positions of these components are indicated by the shaded rectangles in the right-hand panel of Fig. 1 and are labelled as indicated.

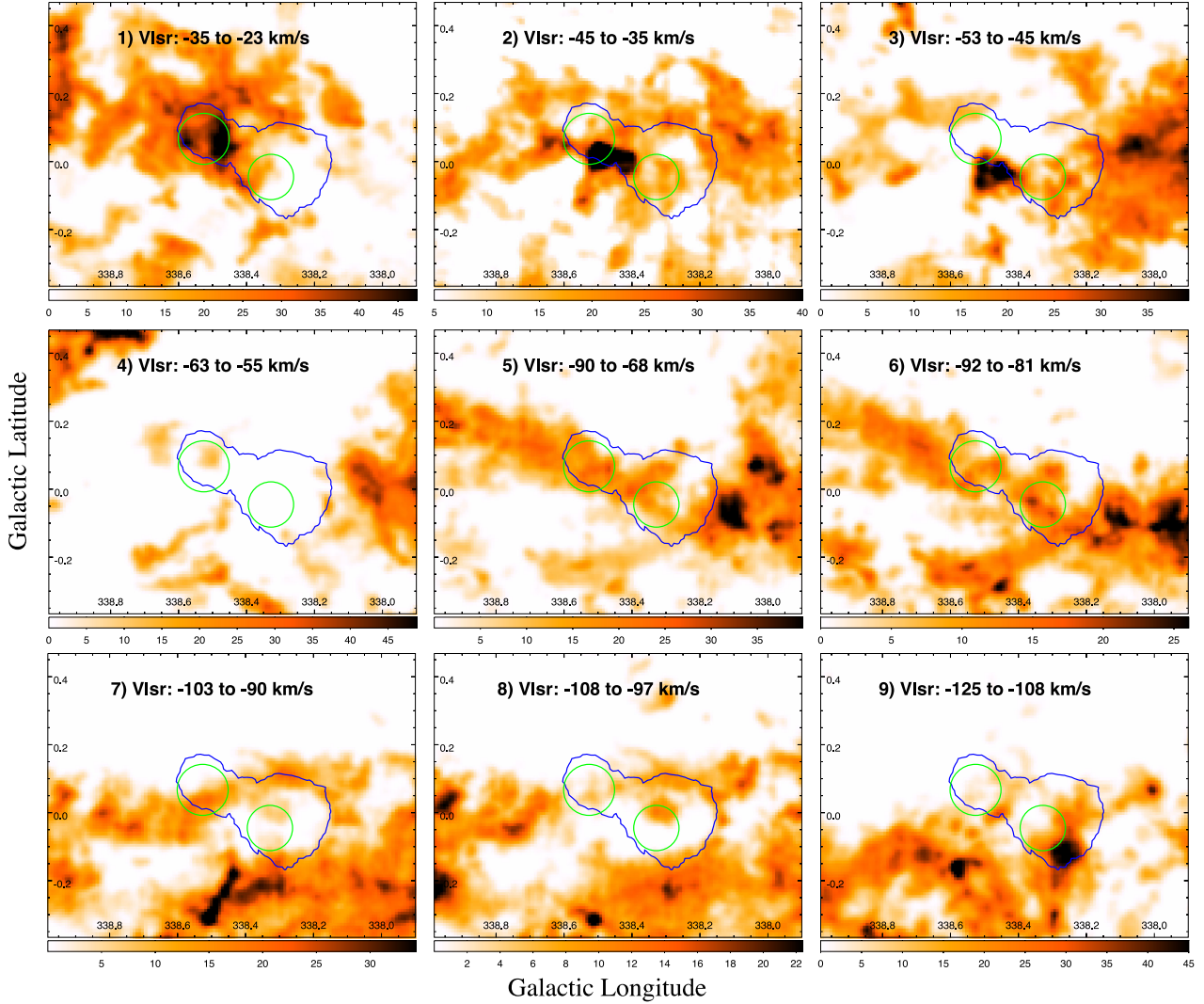


**Figure 2.** Integrated  $^{12}\text{CO}(1-0)$  emission images [ $\text{K km s}^{-1}$ ] over indicated velocity intervals. Single blue  $5\sigma$  significance HESS contour used for clarity. The position and extent of SNR G338.5+0.1 and SNR G338.3-0.0 are indicated by the left and right solid green circles, respectively, in each panel.

Fig. 2 shows panels of the integrated  $^{12}\text{CO}(1-0)$  emission over said velocity intervals.

Components 1, 2 and 3 (red, yellow and orange shaded boxes) appear both towards HESS J1640–465 and HESS J1641–463 and are centred at  $\sim -30$ ,  $-40$  and  $-50 \text{ km s}^{-1}$ , respectively. The gas traced in these components are the most likely candidates to be associated with the  $\text{H II}$  complex, which includes G338.4+0.0 and G338.45+0.06 with  $v_{\text{LSR}} \sim -30$  to  $-40 \text{ km s}^{-1}$ . This motivates the integration range used in the left-hand panel of Fig. 1 which corresponds to the velocity space spanned by these three components.

In component 1 ( $-35$  to  $-23 \text{ km s}^{-1}$ ), the  $^{12}\text{CO}(1-0)$  emission is very prominent in the spectrum towards HESS J1641–463. The corresponding integrated intensity image shows a molecular cloud positionally coincident with HESS J1641–463 that extends spatially to at least the Galactic-west and Galactic-north-western parts of SNR G338.3-0.0.

Gas is seen overlapping both TeV sources, as well as all around these sources, in the integrated image for component 2 ( $-45$  to

$-35 \text{ km s}^{-1}$ ). Additionally, intense CO emission appears in the region between the TeV sources. An approximate ring of emission can be made out towards HESS J1641–463 and is discussed in a later section.

In the integrated image for component 3 ( $-53$  to  $-45 \text{ km s}^{-1}$ ), the gas overlapping HESS J1640–465 appears to be connected to a cloud complex to the Galactic-west. Less gas appears to be directly overlapping HESS J1641–463 and the intense emission between the two TeV sources appears more towards the Galactic-south than in component 2.

The broad features in components 1, 2 and 3 in both  $^{12}\text{CO}$  and  $^{13}\text{CO}$  spectra appear to overlap each other. Thus, it is difficult to say with certainty if these are physically connected structures. As such, the mass and density parameters for these features were calculated individually. The spectrum in these components were fit with a multiGaussian function and the individual Gaussian functions were used to calculate mass and density parameters. The parameters of the fitted Gaussian functions and the calculated properties of the diffuse  $\text{H}_2$  gas are displayed in Table 2.

**Table 2.**  $^{12}\text{CO}(1-0)$  line parameters, and the corresponding calculated gas parameters, from the apertures as indicated in Fig. 1. The line-of-sight velocity,  $v_{\text{LSR}}$ , linewidth (full width at half-maximum),  $\Delta v_{\text{FWHM}}$  and peak intensity,  $T_{\text{peak}}$ , were found by fitting Gaussian functions to the  $^{12}\text{CO}(1-0)$  spectra. The optical depth was calculated by comparing the  $^{12}\text{CO}$  and  $^{13}\text{CO}$  line emission following Section 3.1. Masses and density have been scaled to account for an additional 20 per cent He component.

Component	Region	$v_{\text{LSR}}$ (km s $^{-1}$ )	Distance $^a$ (kpc)	$\Delta v_{\text{FWHM}}$ (km s $^{-1}$ )	Peak (K)	Optical depth	$\overline{N}_{\text{H}_2}^{\text{b}}$ (10 $^{21}$ cm $^{-2}$ )	Mass $^b$ (M $_{\odot}$ × 10 $^4$ )	$\bar{n}^{\text{b}}$ (10 $^2$ cm $^{-3}$ )
1	HESS J1640–465	$-31.6 \pm 1.1$	11.9	$3.9 \pm 0.1$	$1.6 \pm 0.1$	10.5	4.3	6.8	2.0
	HESS J1641–463	$-29.0 \pm 0.1$	11.9	$4.1 \pm 0.1$	$4.5 \pm 0.1$	11.7	12.8	9.7	8.4
	Bridge	$-28.1 \pm 0.1$	11.9	$5.2 \pm 0.1$	$3.5 \pm 0.1$	13.1	12.5	19.0	5.8
2	HESS J1640–465	$-40.7 \pm 0.1$	11.2	$2.6 \pm 0.1$	$1.9 \pm 0.1$	8.5	3.4	4.7	1.6
	HESS J1641–463	$-39.8 \pm 0.1$	11.2	$2.7 \pm 0.1$	$2.5 \pm 0.1$	10.3	4.6	3.1	3.2
	Bridge	$-40.5 \pm 0.1$	11.2	$2.4 \pm 0.1$	$4.4 \pm 0.1$	11.1	7.4	9.9	3.6
3	HESS J1640–465	$-49.2 \pm 0.1$	10.8	$4.2 \pm 0.1$	$2.4 \pm 0.1$	6.9	6.9	8.8	3.5
	HESS J1641–463	$-47.0 \pm 0.2$	10.8	$2.3 \pm 0.2$	$1.2 \pm 0.1$	11.1	1.8	1.1	1.3
	Bridge	$-48.3 \pm 0.1$	10.8	$4.2 \pm 0.1$	$3.9 \pm 0.1$	9.3	11.0	13.9	5.6

Notes.  $^a$ Assumed distances,  $d_0$ , used for mass and density calculations are derived from the Galactic rotation curve presented in Kothes & Dougherty (2007). However, these values are easily scaled for an arbitrary distance,  $d$ , by multiplying by  $(d/d_0)^2$  and  $(d/d_0)^{-1}$  for mass and density, respectively.

$^b$ The error in the calculated physical parameters are dominated by the statistical uncertainties associated with the CO to H<sub>2</sub> conversion factor ( $X_{\text{CO}(1-0)}$ ) and is of the order of 30 per cent (Bolatto, Wolfire & Leroy 2013).

Emission in component 4 ( $-63$  to  $-55$  km s $^{-1}$ ) is seen only in the region towards HESS J1641–463. A small molecular cloud appears overlapping the Galactic-north upper half of TeV source.

Component 5 ( $-90$  to  $-68$  km s $^{-1}$ ) and component 6 ( $-92$  to  $-81$  km s $^{-1}$ ) both include emission in a long band of gas that passes through both TeV sources. Emission in component 6 has an additional tail end that extends to the Galactic-south-east of HESS J1640–465.

Component 7 ( $-103$  to  $-90$  km s $^{-1}$ ) has an arm-like structure of emission that overlaps through HESS J1641–463, while a minor amount of wispy gas is seen in component 8 ( $-108$  to  $-97$  km s $^{-1}$ ) in the Galactic-northern region of HESS J1640–465.

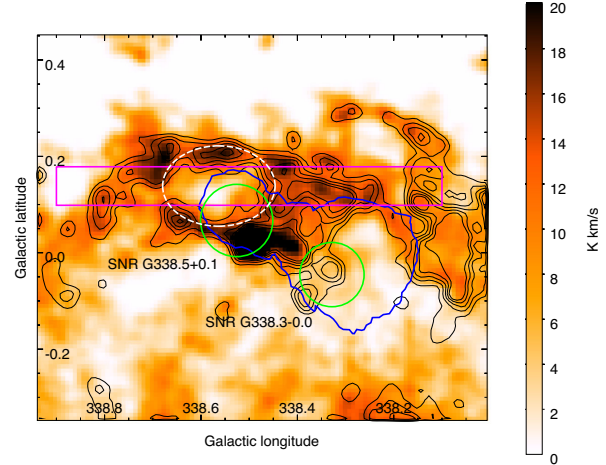
Component 9 ( $-125$  to  $-108$  km s $^{-1}$ ) includes features in the gas that overlap much of HESS J1640–465 and appears to be connected to a gas structure immediately to the Galactic-south.

As mentioned in Section 1.1, the H II complex and both SNRs have been established in literature to be at the far distance, with associated kinematic velocities of  $\sim -40$  to  $-30$  km s $^{-1}$ . This corresponds to a distance of  $\sim 11$  to 12 kpc along the line of sight (using the rotation curve from Kothes & Dougherty 2007). The gas traced in components 1, 2 and 3 are the only candidates for association with the H II complex and SNRs from kinematic distance considerations, as the  $v_{\text{LSR}}$  of other gas components along the line of sight will not yield a far distance solution of  $\sim 11$ –12 kpc.

It is possible that not all gas traced in components 1, 2 and 3 are located at the far distance, as contamination from molecular material located at the near solution may occur. However, the likely need for molecular gas to support the H II complex suggests that a significant fraction of the CO emission in components 1, 2 and 3 traces associated gas located at the far distance.

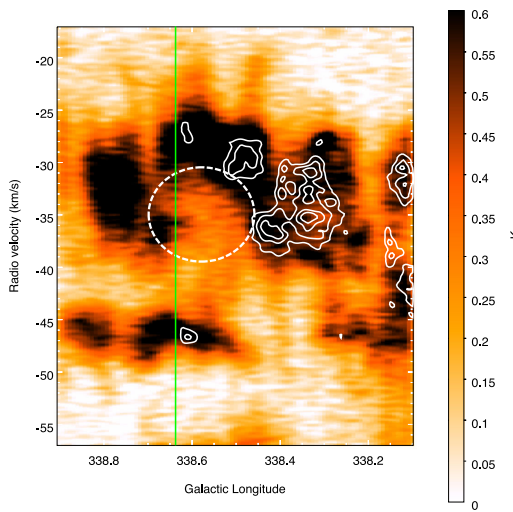
#### CO bubble feature seen at $v_{\text{LSR}} \sim -40$ to $-35$ km s $^{-1}$

Fig. 3 shows the integrated  $^{12}\text{CO}(1-0)$  emission between  $-40$  and  $-35$  km s $^{-1}$ . Overlaid are black contours indicating integrated  $^{13}\text{CO}(1-0)$  emission in the same velocity interval. Both data show an ellipse-like ring of emission seen approximately positionally coincident with HESS J1641–463. The location of this ring is indicated by the white dashed ellipse in the figure. The ellipse has semimajor and semiminor axis lengths of  $\sim 7$  and 5 arcmin, respectively.



**Figure 3.** Mopra  $^{12}\text{CO}(1-0)$  emission image [K km s $^{-1}$ ] integrated between  $-40$  and  $-35$  km s $^{-1}$ . Single solid blue contour is  $5\sigma$  significance from HESS observations towards HESS 1640–465 and HESS 1641–463. The white dashed ellipse is the approximate position of a ring feature discussed in the text and the solid magenta box is the integration region for the position–velocity plot shown in Fig. 4. Overlaid black contours are from Mopra  $^{13}\text{CO}(1-0)$  observations. SNRs are indicated by green circles.

Fig. 4 is a position–velocity plot (in longitude) of the  $^{12}\text{CO}(1-0)$  emission in the magenta rectangle region shown in Fig. 3. A cavity is seen in the gas at the  $\sim -40$  to  $-30$  km s $^{-1}$  velocity range, the approximate position of which is illustrated by the dashed white ellipse. The overlaid white contours indicate integrated emission in the dense gas tracer CS(1-0) seen in our 7 mm observations in the same velocity interval. Note that the extent of the coverage in 7 mm only partially covers the position–velocity plot. The image suggests that the bubble-like feature may have been blown out from one side of the molecular cloud seen in component 1 (velocity range  $\sim -35$  to  $-23$  km s $^{-1}$ ) in Fig. 2. It is possible that this bubble has been blown out by the SNR G338.5+0.1 or perhaps the result of the stellar wind from a progenitor star.



**Figure 4.** Position–velocity image [K] (in Galactic longitude) of  $^{12}\text{CO}(1-0)$  emission towards the bubble feature seen towards HESS J1641–463 in the region indicated in Fig. 3. The approximate position of the cavity discussed in text is indicated by the dashed white ellipse. The solid white contours indicate CS(1–0) emission detected in our 7 mm observations. Note that the extent of the coverage in 7 mm only reaches the vertical green line in longitude.

From Fig. 3, the thickness of the ring is  $\sim 3$  arcmin. The kinematic distance along the line of sight is  $\sim 11.4$  kpc at  $-40$  to  $-35$   $\text{km s}^{-1}$ . Under these assumptions, the column density of the gas enclosed by the ring is  $\bar{N}_{\text{H}_2} \sim 4 \times 10^{21} \text{ cm}^{-2}$ , with a total mass of  $\sim 8 \times 10^4 \text{ M}_\odot$ . From Fig. 4, the expansion velocity of the bubble appears to be  $\sim 5$ – $10$   $\text{km s}^{-1}$ . The expansion of the bubble would then have a kinetic energy of  $\sim 2$ – $8 \times 10^{49}$  erg.

If this were a wind-blown bubble, an O-type progenitor star with mass  $\sim 27 \text{ M}_\odot$  would be able to create it, based on the bubble size of radius  $\sim 25$  pc at a distance of  $\sim 11.4$  kpc (Chen, Zhou & Chu 2013, and references therein). The energy required to produce such a bubble can then be calculated following the model presented by Chevalier (1999) and is  $\sim 4 \times 10^{49}$  erg.

#### CO(1–0) emission towards dense ‘bridge’ between HESS J1640–465 and HESS J1641–463

In components 1, 2 and 3 of Fig. 2, we see an area of intense CO emission located towards the Galactic-south part of the region that bridges HESS J1640–465 and HESS J1641–463 which appears to span between  $\sim -35$  and  $-55$   $\text{km s}^{-1}$ . This region is indicated by the central white dashed circle in Fig. 1. Fig. 5 shows the average  $^{12}\text{CO}(1-0)$  and  $^{13}\text{CO}(1-0)$  emission spectra in this region. Three components are seen in the  $^{12}\text{CO}$  spectra that match well with components 1, 2 and 3 in Fig. 1. Calculated mass and density parameters for these components are displayed in Table 2.

#### CO(1–0) emission towards the Galactic-west of HESS J1640–465 and HESS J1641–463

CO(1–0) emission over a very broad ( $\sim 60$   $\text{km s}^{-1}$ ) velocity range can be seen in an extended molecular cloud structure to the Galactic-west of HESS J1640–465. The top panel of Fig. 6 displays an integrated image of the  $^{12}\text{CO}(1-0)$  emission between  $-80$  and  $-20$   $\text{km s}^{-1}$  over an extended region from  $l$

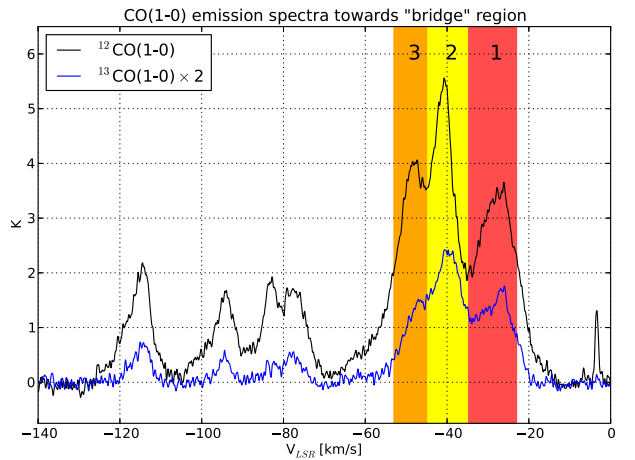


**Figure 5.**  $^{12}\text{CO}(1-0)$  (black) and  $^{13}\text{CO}(1-0)$  (blue) emission spectra towards the ‘bridge’ between HESS J1640–465 and HESS J1641–463 indicated by the central white dashed circle in Fig. 1.  $^{13}\text{CO}$  scaled by a factor of 2 for clarity. Velocity ranges for components 1, 2 and 3 are indicated by the shaded boxes.

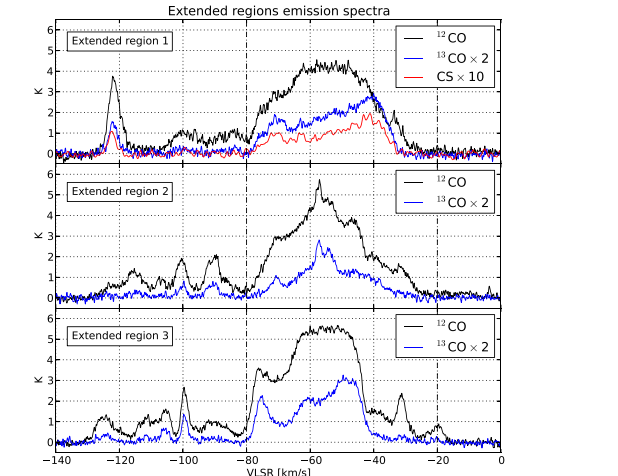
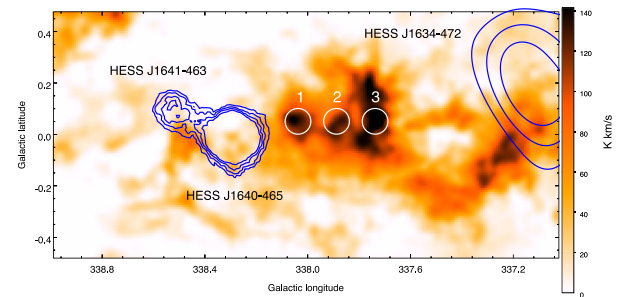


**Figure 6.** Top: integrated  $^{12}\text{CO}$  emission image [ $\text{K km s}^{-1}$ ] between  $-80$  and  $-20$   $\text{km s}^{-1}$  from  $l = 339^\circ$  to  $337^\circ$ . Blue contours indicate the positions of HESS J1640–465 and HESS J1641–463 (Abramowski et al. 2014b). Contours for the TeV source HESS J1634–472 are also shown in blue for completeness (Aharonian et al. 2006). Bottom: average  $^{12}\text{CO}(1-0)$  (black) and  $^{13}\text{CO}(1-0)$  (blue) emission spectra in three circular regions indicated above in white. CS(1–0) emission from 7 mm observations is displayed in red for extended region 1.  $^{13}\text{CO}$  and CS(1–0) emission have been scaled by a factor of 2 and 10, respectively, for clarity. Vertical dashed lines indicate the integration range used to produce the image in the top panel.

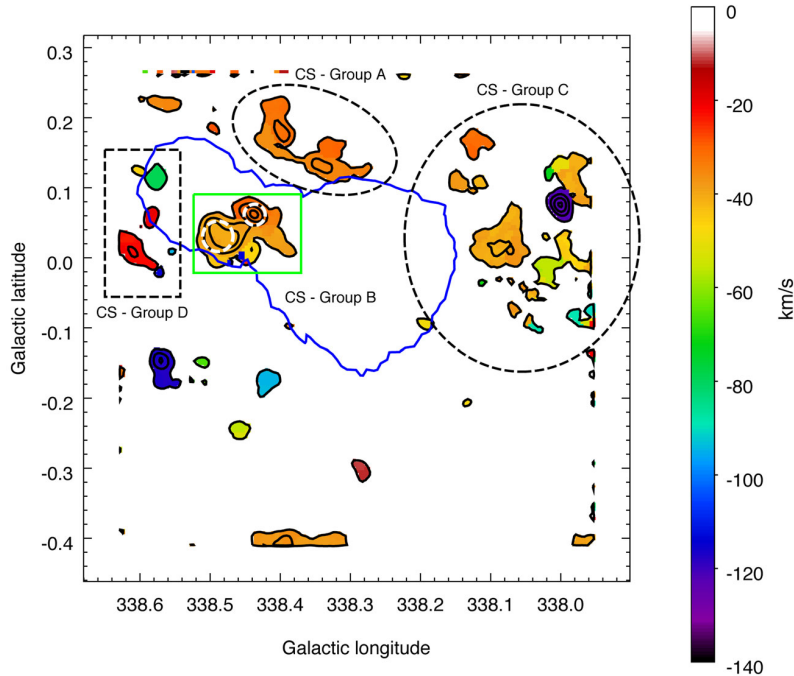


**Figure 7.** Velocity of peak pixel CS(1–0) map [ $\text{km s}^{-1}$ ] in the 7 mm observations region. Overlaid solid black contours show the intensity of the peak pixel. HESS  $5\sigma$  significance contour is in solid blue. Regions of interest discussed in the text are labelled by black dashed ellipses. The CS – Group B region, however, is outlined by a solid green box and indicates the integration region for the position–velocity plot shown in Fig. 9. Dashed white circles indicate apertures used to extract spectra for Bridge Core 1 (left circle) and Bridge Core 2 (right circle) discussed in the text.

=  $339^\circ$  to  $337^\circ$  taken from the Mopra CO survey. Contours of the TeV source HESS J1634–472 are shown in addition to those of HESS J1640–465 and HESS J1641–463 for completeness. Spectra in three representative regions in this extended structure, indicated by white circles in the top panel, are shown in the bottom panel. The average  $^{12}\text{CO}(1-0)$  and  $^{13}\text{CO}(1-0)$  spectra are shown by black and blue lines, respectively. Our 7 mm observations had coverage over the region labelled ‘1’ in the top panel of Fig. 6 and we include the spectrum for CS(1–0) emission in red in the corresponding set of axes. Note that the  $^{13}\text{CO}(1-0)$  and CS(1–0) emission have been scaled by a factor of 2 and 10, respectively, for clarity.

Broad emission from  $\sim -80$  to  $-20 \text{ km s}^{-1}$  is seen in these regions which may be due to multiple contributing components. The broadness of this emission makes it difficult to place the gas at a distance with any certainty using Galactic rotation curve calculations. The rotation curve from Kishes & Dougherty (2007) yields a distance estimate of 1.6–4.6 kpc (near solution) and 9.5–12.5 kpc (far solution). The far distance solutions overlap with the estimated distances to HESS J1640–465 and HESS J1641–463, so it is important to give consideration to the gas structure as CR-target material. This is discussed further in Section 5.1.

#### 4.2 7 mm line emission

In our 7 mm observations towards HESS J1640–465 and HESS J1641–463, detections were made in the CS(1–0),  $\text{C}^{34}\text{S}(1-0)$ ,  $\text{SiO}(J = 1-0, v = 0)$ ,  $\text{HC}_3\text{N}(5-4, F = 4-3)$  and  $\text{CH}_3\text{OH}$  (I) lines.

Dense gas in the region was traced by CS(1–0) and  $\text{C}^{34}\text{S}(1-0)$  emission. The CS(1–0) transition has a critical density for emission of  $\sim \times 10^5 \text{ cm}^{-3}$  at a temperature of  $\sim 10 \text{ K}$ , making it an ideal tracer

for probing the deeper and denser inner regions of molecular clouds. SiO emission is usually produced behind shocks moving through molecular clouds (Gusdorf et al. 2008) from which the  $\text{SiO}(J = 1-0, v = 0)$  line can be detected.  $\text{HC}_3\text{N}$  is often detected in warm molecular clouds and is associated with star forming regions, while the  $\text{CH}_3\text{OH}$  (I) maser generally traces star formation outflows.

The location of the dense gas traced by the CS(1–0) line in our study are displayed via a velocity-of-peak-pixel map in Fig. 7. From the figure, we can see that most of strongest CS(1–0) emission occurs at a velocity consistent with components 1, 2 and 3 ( $-53$  to  $-23 \text{ km s}^{-1}$ ) in the CO(1–0) data. Several regions of significant CS(1–0) emission present themselves and are roughly grouped together as illustrated in Fig. 7. These groups are discussed below together with other detections made in the 7 mm band. The detections of the 7 mm lines aside from CS are shown in Fig. 8 overlaid on a *Spitzer* 8.0  $\mu\text{m}$  image of the region.

#### 7 mm emission in Group A

Group A is located slightly to the Galactic-north of HESS J1640–465 and HESS J1641–463 and is approximately coincident with a bright H II region G338.39+0.16. CS(1–0) emission in this region appears in the  $\sim -40$  to  $-30 \text{ km s}^{-1}$  velocity range. The morphology of the emission is extended in nature, forming a slight arc with what appears to be two dense clumps.

#### 7 mm emission in Group B or ‘bridge’ region

Group B is the central bridge coincident with the H II complex between HESS J1640–465 and HESS J1641–463. A markedly strong amount of CS(1–0) emission is seen here spanning a broad

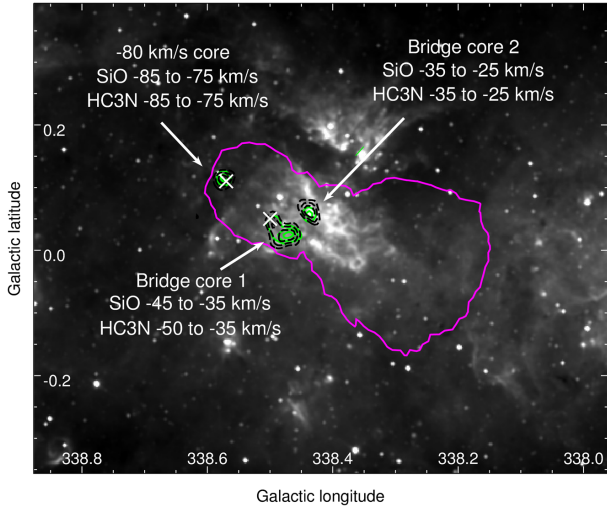


**Figure 8.** *Spitzer* 8.0  $\mu\text{m}$  image towards HESS J1640–465 and HESS J1641–463. Single magenta contour is  $5\sigma$  significance from HESS observations. Green solid contours are integrated SiO(1–0) emission. Dashed black contours are integrated HC<sub>3</sub>N(5–4,  $F = 4–3$ ) emission. The velocities over which they are integrated are as labelled. White Xs indicate positions of observed CH<sub>3</sub>OH (I) masers.

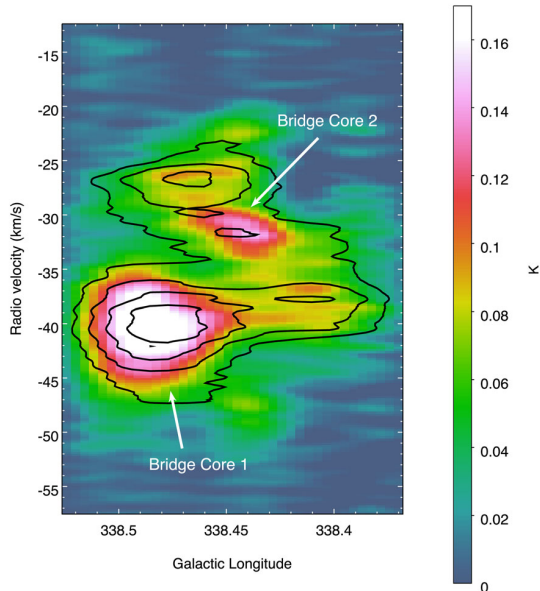


**Figure 9.** Position–velocity image [K] of CS in the region indicated by a solid green box in Fig. 7. Locations of Bridge Core 1 and Bridge Core 2 are labelled with arrows. Black contours are from Mopra 13CO(1–0) observations.

( $\sim 20 \text{ km s}^{-1}$ ) velocity space. Group B is also roughly positionally coincident with the intense emission seen in the CO ‘bridge’ discussed earlier, with emission features at similar velocities.

Fig. 9 is a longitude–velocity image of CS(1–0) data in the region indicated by a solid green box in Fig. 7. From this image, there appears to be two separate dense cores with broad CS(1–0) emission in this region separated in velocity, but somewhat overlapping spatially along the line of sight. We label these Bridge Core 1 and Bridge Core 2 as illustrated. These cores appear to be embedded

in an extended bridge of emission linking themselves as well as other smaller clumpy features. We note the good correlation between Bridge Core 1 and emission in <sup>13</sup>CO(1–0) (indicated by the solid black contours in Fig. 9). Bridge Core 2, however, appears to be offset from the local maximum traced in <sup>13</sup>CO.

Detections in the isotopologue transition C<sup>34</sup>S(1–0), as well as in SiO(1–0) and HC<sub>3</sub>N(–4,  $F = 4–3$ ) were made towards core 1 and core 2. The left and centre panels of Fig. 10 displays the emission spectra in these lines towards Bridge Core 1 and Bridge Core 2. The spatial size of the cores was determined by fitting a Gaussian function to the line profile drawn through the centre of each core and the spectra extracted from circular apertures with sizes equal to the FWHMs (1.3 and 0.9 arcmin for Bridge Core 1 and 2, respectively). We note that all the 7 mm line emission peaks at the same velocity as the intense emission in CS(1–0);  $-40$  and  $-32 \text{ km s}^{-1}$  for Bridge Core 1 and 2, respectively. Table 3 displays the 7 mm detection parameters and mass estimates calculated from the data in these cores. Mass parameters were calculated following Section 3.2 assuming the gas is at a distance of 11 kpc.

SiO(1–0) emission appears positionally coincident with Bridge Core 1 and Bridge Core 2 at the same velocity as that observed in CS(1–0). This suggests that both these cores have been disturbed by a shock passing through. A CH<sub>3</sub>OH (I) maser is seen at the Galactic-north-east edge of Bridge Core 1, suggesting the presence of an outflow. Combined with the detection of HC<sub>3</sub>N at the same position and velocity and that Bridge Core 1 and 2 appear to be embedded in the complex of H II regions, the shock is likely to be caused by recent nearby star formation.

### 7 mm emission in Group C

Group C is a region towards the Galactic-eastern side of the gas structure located to the Galactic-west of HESS J1640–465 and HESS J1641–463 as traced in CO. Note that the extension of our 7 mm observations only reaches to include the region labelled ‘1’ in the top panel of Fig. 6. We see large-scale extended and broad emission in the region in CS(1–0). This emission is in the same kinematic velocity ranges as that of the CO(1–0) emission. In Fig. 6, the average spectra shown for Extended region 1 include the CS(1–0) emission spectrum in red. Emission is seen between  $\sim -80$  and  $-30 \text{ km s}^{-1}$ , similar to the profile seen in the <sup>12</sup>CO and <sup>13</sup>CO, and is likely tracing denser regions that exist inside cloud. There is also one dense core traced in CS which appears at  $\sim -120 \text{ km s}^{-1}$  (dark blue in Fig. 7).

### 7 mm emission in Group D

Emission in CS(1–0) is seen in the Group D region slightly overlapping the Galactic-east side of the HESS J1641–463 contours in the  $\sim -25$  to  $-20 \text{ km s}^{-1}$  velocity range. It has a marginally extended morphology. The most intense emission, located towards the middle, is positionally coincident with a dense core detected in the NH<sub>3</sub>(1–1) transition line by the H<sub>2</sub>O Southern Galactic Plane Survey (HOPS; Purcell et al. 2012).

A core of gas traced by CS emission is seen at  $-80 \text{ km s}^{-1}$  (green in Fig. 7) within the Galactic-north-east bounds of HESS J1641–463. This  $-80 \text{ km s}^{-1}$  core appears marginally extended and is positionally coincident with detections made in NH<sub>3</sub>(1,1) in the HOPS survey. Detections in the isotopologue transition C<sup>34</sup>S(1–0) were also made at this position, as well as in SiO( $J = 1–0, v = 0$ ) and HC<sub>3</sub>N(5–4,  $F = 4–3$ ). The average spectra of the 7 mm lines detected in an aperture centred at this core is

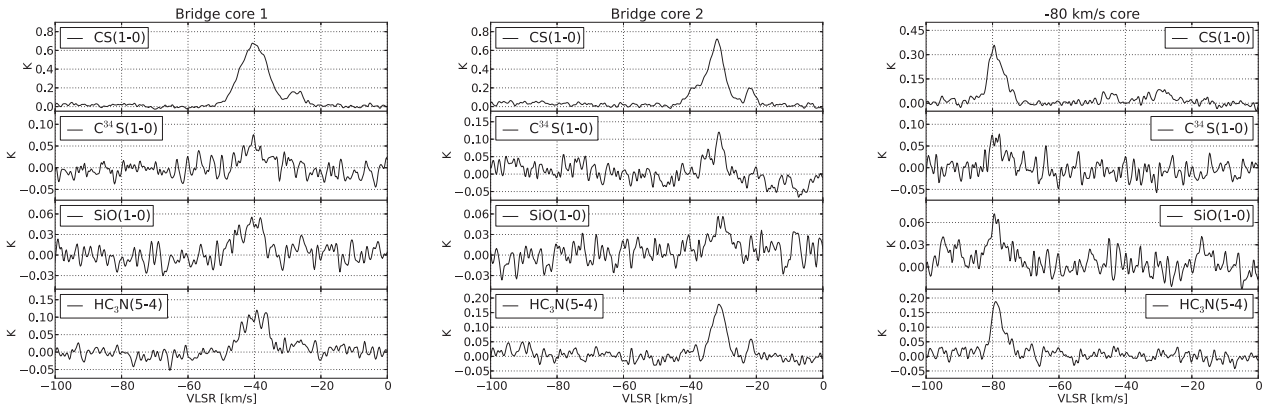


**Figure 10.** Average spectra of detected 7 mm lines within apertures centred at Bridge Core 1 (left-hand panel), Bridge Core 2 (centre panel) and the  $-80 \text{ km s}^{-1}$  core (right-hand panel).

**Table 3.** 7 mm line parameters extracted from apertures towards Bridge Core 1 and Bridge Core 2 (as shown in Fig. 7). The line-of-sight velocity,  $v_{\text{LSR}}$ , peak intensity,  $T_{\text{peak}}$ , and linewidth,  $\Delta v_{\text{FWHM}}$ , were found by fitting Gaussian functions to the spectra in Fig. 10. The optical depth, together with mass and density calculations, used the CS(1–0) and C<sup>34</sup>S(1–0) data following Section 3.2.<sup>a</sup>

Object	Detected lines	$v_{\text{LSR}}$ (km s <sup>-1</sup> )	$T_{\text{peak}}$ (K)	$\Delta v_{\text{FWHM}}$ (km s <sup>-1</sup> )	Optical depth	$\overline{N_{\text{H}_2}}$ ( $\times 10^{23} \text{ cm}^{-2}$ )	Mass (M <sub>⊙</sub> )	$\bar{n}$ ( $\times 10^4 \text{ cm}^{-3}$ )
Bridge Core 1	CS(1–0)	$-40.2 \pm 0.1$	$0.66 \pm 0.01$	$4.1 \pm 0.1$	1.3	2.0	$1.8 \times 10^5$	2.4
	C <sup>34</sup> S(1–0)	$-40.3 \pm 0.4$	$0.05 \pm 0.01$	$3.2 \pm 0.4$				
	SiO( $J = 1-0, v = 0$ )	$-41.1 \pm 0.3$	$0.05 \pm 0.01$	$3.7 \pm 0.3$				
	HC <sub>3</sub> N(5–4, F = 4–3)	$-39.6 \pm 0.2$	$0.11 \pm 0.01$	$3.8 \pm 0.2$				
Bridge Core 2	CS(1–0)	$-32.5 \pm 0.1$	$0.58 \pm 0.01$	$3.3 \pm 0.1$	3.1	2.6	$1.1 \times 10^5$	4.5
	C <sup>34</sup> S(1–0)	$-32.0 \pm 0.3$	$0.08 \pm 0.01$	$2.5 \pm 0.3$				
	SiO( $J = 1-0, v = 0$ )	$-30.7 \pm 0.4$	$0.04 \pm 0.01$	$3.2 \pm 0.5$				
	HC <sub>3</sub> N(5–4, F = 4–3)	$-31.3 \pm 0.1$	$0.18 \pm 0.01$	$2.0 \pm 0.1$				

*Notes.* <sup>a</sup>An assumed distance,  $d_0 = 11 \text{ kpc}$ , was used for mass and density calculations. However, these values are easily scaled for an arbitrary distance,  $d$ , by multiplying by  $(d/d_0)^2$  and  $(d/d_0)^{-1}$  for mass and density, respectively.

<sup>b</sup>The error in the calculated physical parameters are dominated by the statistical uncertainties associated with the abundance ratio of CS to molecular hydrogen. This uncertainty can be of the factor of 2 (e.g. Irvine, Goldsmith & Hjalmarson 1987).

displayed in the right-hand panel of Fig. 10 and we note that the emission in each line peaks at  $-80 \text{ km s}^{-1}$ . A CH<sub>3</sub>OH (I) maser is also seen positionally coincident with this core at  $-79 \text{ km s}^{-1}$ . The velocity at which this core is detected suggests that it is not associated with the H II complex (which has  $v_{\text{LSR}} \sim -30$  to  $-40 \text{ km s}^{-1}$ ).

### 4.3 H i emission

The atomic gas towards HESS J1640–465 and HESS J1641–463 was studied using H i data from the SGPS (McClure-Griffiths et al. 2005). Integrated velocity maps were generated from the H i emission cubes over the same velocity intervals as the components traced in CO. Images of the H i-integrated velocity maps can be found in the appendix Fig. A2. We note that a study of atomic gas using SGPS data towards HESS J1640–465 was carried out by Supan et al. (2016), which focused on the velocity ranges from  $-121$  to  $-111 \text{ km s}^{-1}$  and from  $-40$  to  $-25 \text{ km s}^{-1}$ . We find that our results are similar to those presented towards HESS J1640–465.

There are prominent dips in the H i spectra towards the TeV sources which occur at velocities where emission features are seen in the CO spectra. These dips may be the result of H i self-absorption, caused by residual H i embedded in the CO. Fig. A3 in the appendix is an example of such a dip in the spectrum towards HESS J1641–463 in component 1 and the corresponding

intense emission that is seen in CO. To reduce the effect that these self-absorption dips may have on the calculation of the atomic gas parameters and following the analysis technique in Fukui et al. (2012), we estimate the actual H i emission level by a linear interpolation connecting the adjacent shoulders of a dip. The dotted line in Fig. A3 demonstrates this interpolation. This is a conservative estimate as the true spectrum is likely peaked, rather than just a straight line.

From the corrected spectra and, following Section 3, mass and density estimates of the atomic gas contained in each component were calculated. Similar to the work by Supan et al. (2016), we find that when comparing the molecular gas traced by CO and the atomic gas traced by H i, the physical parameters of the atomic gas are a small fraction of molecular gas. The calculated masses of atomic gas in each component can be found in Table 4 in Section 5 and in Table A2 in the appendix.

## 5 DISCUSSION

As mentioned previously in Section 1, the production of  $\gamma$ -rays from the TeV sources HESS J1640–465 and HESS J1641–463 may be the result of hadronic scenarios, in which the accelerated CRs are interacting with ambient gas, or leptonic scenarios, in which energetic electrons upscatter background photons. We now consider

**Table 4.** Calculated cosmic ray enhancement values,  $k_{\text{CR}}$ , for the intrinsic Gaussian size of HESS J1640–465 and the maximum Gaussian extent of HESS J1641–463 for the gas related to components 1, 2 and 3 as defined in Fig. 1. Molecular mass comes from CO analysis and atomic mass from H I analysis.

Region	Velocity range (km s <sup>-1</sup> )	Assumed distance (kpc)	Molecular mass (M <sub>⊕</sub> )	Atomic mass (M <sub>⊕</sub> )	Total mass (M <sub>⊕</sub> )	$k_{\text{CR}}^a$
HESS J1640–465	–35 to –23 (Component 1)	11.9	68 000	12 000	80 000	1000
	–45 to –35 (Component 2)	11.2	47 000	9300	56 000	1400
	–53 to –45 (Component 3)	10.8	88 000	7100	95 000	850
	–53 to –23 (Components 1, 2 and 3)	11.0	203 000	28 000	230 000	350
HESS J1641–463	–35 to –23 (Component 1)	11.9	97 000	5000	102 000	150
	–45 to –35 (Component 2)	11.2	31 000	3200	34 000	450
	–53 to –45 (Component 3)	10.8	11 000	2100	13 000	1200
	–53 to –23 (Components 1, 2 and 3)	11.0	139 000	10 000	149 000	100

Notes. <sup>a</sup>Note that the CR enhancement factor,  $k_{\text{CR}}$ , is effectively independent of assumed distance as the distance terms in equation (3) cancel with the distance assumptions for the mass calculations.

the implications that our study of the interstellar gas towards these TeV sources have on the aforementioned origin scenarios.

### 5.1 Hadronic scenarios

The segment of emission that includes components 1, 2 and 3 in the CO spectra traces gas which is at a velocity within  $\sim 10$ –20 km s<sup>-1</sup> of the reported systematic velocity of the H II regions in the H II complex (see Section 1.1). Assuming SNRs G338.3–0.0 and G338.5+0.1 and the TeV sources are all linked with this H II complex, the gas traced here is a potential target for accelerated CRs. The dense gas traced by CS at these velocities is found in a bridging region between the two TeV sources and may also be acting as CR-target material.

A relationship to calculate the flux of  $\gamma$ -rays above a given energy level produced by hadronic interactions between CRs and CR-target material from the mass of the target material was derived by Aharonian (1991). The expected  $\gamma$ -ray flux above some energy  $E_\gamma$ , assuming an  $E^{-1.6}$  integral power law spectrum, is given by

$$F(\geq E_\gamma) = 2.85 \times 10^{-13} E_\gamma^{-1.6} \left( \frac{M_5}{d_{\text{kpc}}^2} \right) k_{\text{CR}} \text{ cm}^{-2}\text{s}^{-1}, \quad (3)$$

where  $M_5$  is the mass of the CR-target material in units of  $10^5$  M<sub>⊕</sub>,  $d_{\text{kpc}}$  is the distance in kiloparsec,  $k_{\text{CR}}$  is the CR enhancement factor above that observed at Earth and  $E_\gamma$  is the minimum energy of  $\gamma$ -rays in TeV.

From the results in Abramowski et al. (2014a), the  $\gamma$ -ray flux photon above 1 TeV towards HESS J1640–465 is determined to be  $F(>1 \text{ TeV}) \sim 1.9 \times 10^{-12} \text{ cm}^{-2}\text{s}^{-1}$ . From Abramowski et al. (2014b), the flux above 1 TeV towards HESS J1641–463 is  $\sim 3.6 \times 10^{-13} \text{ cm}^{-2}\text{s}^{-1}$ .

The total amount of CR-target material towards HESS J1640–465 and HESS J1641–463 is taken to be the sum of the molecular and atomic mass traced by emission in CO(1–0) and H I, respectively. These masses, together with the calculated CR enhancement factors  $k_{\text{CR}}$  for the total mass in components 1, 2 and 3, are displayed in Table 4. A complete list of  $k_{\text{CR}}$  values for every gas component along the line of sight can be found in Table A2 in the appendix. It should be noted that the  $k_{\text{CR}}$  values here refer to  $E > 1$  TeV  $\gamma$ -rays and pertain only to higher energy CRs ( $\gtrsim 10$  TeV). Thus, any CR energetics should be considered lower limits on the total CR energy. In addition, equation (3) assumes an  $E^{-1.6}$  integral power-law CR spectrum. This is different from the  $\sim E^{-1.1}$  CR integral spectra needed to fit the  $\gamma$ -ray spectra

of HESS J1640–465 and HESS J1641–463 (Abramowski et al. 2014b; Supan et al. 2016). By scaling equation (3) appropriately, the calculated CR enhancement factors would reduce by  $\sim 40$  per cent for HESS J1640–465 and HESS J1641–463.

A similar study was conducted by Supan et al. (2016) on the physical properties of the ISM towards HESS J1640–465 using the same SGPS H I data, but with archival CO data from Dame, Hartmann & Thaddeus (2001). The authors used different sized regions of integration and velocity ranges compared to those used here. Analyses utilizing the same region size and velocity ranges on Mopra CO survey data return mass and densities parameters consistent with those presented in Supan et al. (2016).

The CR enhancement factor  $k_{\text{CR}}$  above 1 TeV towards HESS J1640–465 for the gas traced in components 1, 2 and 3 are of the order of  $\sim 10^3$ . This value is consistent with a nearby (within a few parsec) and young SNR ( $\lesssim 5$  kyr), such as G338.3–0.0 accelerating and injecting CRs into the ambient gas (Aharonian & Atoyan 1996). Thus, assuming the gas at either components 1, 2 or 3 are associated with the location of HESS J1640–465, a hadronic scenario is plausible. In a case where all of the gas traced in these components are summed and considered as CR-target material associated with HESS J1640–465, the required  $k_{\text{CR}}$  value becomes 350.

In the case of HESS J1641–463, the required  $k_{\text{CR}}$  value for the molecular cloud positionally coincident (component 1) is 150. Component 1 is dominant whereby summing the gas traced in components 2 and 3 marginally decreases the required  $k_{\text{CR}}$  value. If the molecular cloud in component 1 is indeed associated with HESS J1641–463, the hadronic scenario would be possible given its proximity with potential CR accelerators.

If the hadronic scenario holds true in both HESS J1640–465 and HESS J1641–463, then the total CR energy budget,  $W_p$ , can be given as  $W_p = L_\gamma \tau_{\text{pp}}$ , where  $L_\gamma$  is the luminosity in  $\gamma$ -rays.  $\tau_{\text{pp}}$  is the cooling time of protons through proton–proton collisions and is given by (Aharonian & Atoyan 1996):  $\tau_{\text{pp}} \approx 6 \times 10^7 (n/1 \text{ cm}^{-3})^{-1}$  yr, where  $n$  is the number density of the ambient gas.

HESS J1640–465 has a  $\gamma$ -ray luminosity of  $L_\gamma = 9 \times 10^{34} \text{ erg s}^{-1}$  above 1 TeV at 11 kpc (Abramowski et al. 2014a), while HESS J1641–463 has a luminosity of  $4 \times 10^{34} \text{ erg s}^{-1}$  above 0.64 TeV at 11 kpc (Abramowski et al. 2014b). Thus,  $W_p \sim 10^{50} (n/1 \text{ cm}^{-3})^{-1}$  erg for HESS J1640–465, and  $W_p \sim 10^{49} (n/1 \text{ cm}^{-3})^{-1}$  erg for HESS J1641–463. The number densities for both TeV sources presented in Table 2 in components

1, 2 and 3 are of the order of  $\sim 10^2 \text{ cm}^{-3}$ .  $W_p$  is then  $\sim 10^{48}$  and  $\sim 10^{47}$  for HESS J1640–465 and HESS J1641–463, respectively, which is a fraction of the canonical amount of energy channelled into accelerated CRs by a SNR ( $\sim 10^{50}$  erg).

We note here that the hadronic modelling of HESS J1640–465 done in Supan et al. (2016) used the parametrization of the  $\gamma$ -ray differential cross-section in the proton–proton interactions from Kafexhiu et al. (2014). Using ambient proton densities of  $\sim 10^2 \text{ cm}^{-3}$ , they found the total energy in accelerated protons to be  $\sim 10^{49}$ – $10^{50}$  erg, consistent to first order with an SNR scenario.

In one of the scenarios discussed in Abramowski et al. (2014b) and Tang et al. (2015), CRs accelerated by the SNR G338.3–0.0, coincident with HESS J1640–465, have diffusively reached a molecular cloud coincident with HESS J1641–463. The centre of G338.3–0.0 lies  $\sim 0.3$  from the far side of the maximum extent of HESS J1641–463, equivalent to  $\sim 60$  pc at the assumed distance of 11 kpc. The maximum Gaussian extent of HESS J1641–463 is  $0.05$  or  $\sim 10$  pc at this distance. Thus, the filling factor of HESS J1641–463, assuming a spherical geometry with radius 10 pc, compared to the 60 pc radius sphere centred at SNR G338.3–0.0 is  $\sim 0.005$ . Assuming that  $10^{50}$  erg was injected into accelerating CRs by G338.3–0.0 and assuming that the CRs are uniformly distributed within the sphere, the total amount of energy in CRs at HESS J1641–463 is  $\sim 5 \times 10^{47}$  erg. This value is consistent with the value of  $W_p$  calculated above for HESS J1641–463 and thus the presented origin scenario is energetically plausible for the observed ISM.

The separation from the Galactic-eastern edge of the SNR G338.3–0.0 to the position of HESS J1641–463 is  $\sim 0.15$  or 30 pc (at a distance of 11 kpc). The required CR enhancement factor of  $k_{\text{CR}} \sim 100$  resulting from the diffusion of CRs from the SNR towards HESS J1641–463 is achievable according to Aharonian & Atoyan (1996). Fig. 1(b) of their paper shows the  $k_{\text{CR}}$  values at several time epochs at a distance of 30 pc from an SNR. A  $k_{\text{CR}}$  of  $\sim 100$  is acquired at a source age between  $10^3$  and  $10^4$  yr, similar to the estimated age of SNR G338.3–0.0. Their calculations assumed a source spectral index of 2.2 and that  $D_{10} = 10^{26} \text{ cm}^2 \text{s}^{-1}$ , where  $D_{10}$  is the diffusion coefficient when energy = 10 GeV. This value corresponds to slow diffusion and is not unexpected given the substantial amount of gas traced in the region between HESS J1640–465 and HESS J1641–463 in both CO and CS observations. This is because gas with larger values of  $\bar{n}$  will have greater magnetic fields. The corresponding increase in the interaction between CR particles and magnetic fields would increase the rate of scattering, thereby decreasing the diffusion coefficient.

We can estimate the diffusion coefficient through the gas in this bridge region using equation (2) from Gabici, Aharonian & Blasi (2007). The required value of the magnetic field inside the ISM is a function of  $\bar{n}$  and is calculated following Crutcher et al. (2010). In Section 4, we have calculated the values of  $\bar{n}$  for the diffuse and dense gas in the bridge region from CO and CS data respectively. These values have been presented in Tables 2 and 3. For the diffuse CO-traced gas,  $B \sim 15 \mu\text{G}$  and  $D_{10} \sim \chi(4 \times 10^{27}) \text{ cm}^2 \text{s}^{-1}$ . For the dense CS-traced cores,  $B \sim 500 \mu\text{G}$  and  $D_{10} \sim \chi(7 \times 10^{26}) \text{ cm}^2 \text{s}^{-1}$ . The parameter  $\chi < 1$  is a suppression factor that accounts for the suppression of the diffusion coefficient inside a turbulent cloud. For a moderate value of  $\chi \sim 0.1$ , the diffusion coefficient in this region would agree with a slow diffusion scenario. This diffusion scenario is a theoretically plausible explanation for the  $\gamma$ -ray emission from HESS J1641–463. The hardness of the TeV emission would be explained by higher energy protons preferentially reaching CR target

material earlier and the effective exclusion of low-energy CR due to the dense gas bridge.

As mentioned in Section 4.1, emission in CO(1–0) traces an extended molecular cloud structure to the Galactic-west of HESS J1640–465. The angular separation of this cloud is comparable to the separation between SNR G338.3–0.0 and HESS J1641–463 ( $\sim 0.3$ ). If the scenario in which CRs escaping from SNR G338.3–0.0 are generating the TeV emission of HESS J1641–463 is true, then one might have expected this other giant molecular cloud to glow in  $\gamma$ -rays. However, while at similar angular separations from the SNR, this molecular cloud may be at different distance along the line of sight. The CO(1–0) and CS(1–0) emission (see Fig. 6) is very broad and is seen between  $\sim -80$  and  $-20 \text{ km s}^{-1}$  in velocity. This is in contrast with the emission from molecular cloud seen towards HESS J1641–463 which is seen at  $\sim -30 \text{ km s}^{-1}$ . Differences between the Galactic-rotation curve solution at these velocities range up to several kiloparsecs. Since an increase in distance of even  $\sim 100$  pc from the source SNR would drastically diminish the available CRs (Aharonian & Atoyan 1996), it is possible that CRs may not have yet reached this molecular cloud. In addition, CRs escaping from an accelerator can diffuse anisotropically, tending to propagate along magnetic field lines (e.g. Nava & Gabici 2013). It is possible that the orientation of the magnetic fields in this region are directing CRs away from this molecular cloud.

An alternate scenario is that SNR G338.5+0.1, coincident with HESS J1641–463, is accelerating CRs that are interacting with the ISM. Modelling by Abramowski et al. (2014b) indicate that the hard proton spectrum required to generate the  $\gamma$ -ray emission agrees well with CRs accelerated by a young SNR. The critical factor is then the age of SNR G338.5+0.1. A 5–17 kyr middle-aged SNR (Abramowski et al. 2014b) would disfavour this scenario and lend support to the diffusion scenario discussed above. In either case, the molecular cloud found in component 1 of our study towards HESS J1641–463 provides ample target material for accelerated CRs to interact with, producing  $\gamma$ -rays through the hadronic channel.

## 5.2 Leptonic scenarios

We now consider the leptonic scenarios, in which TeV emission is primarily due to accelerated electrons interacting with ambient photons via the inverse-Compton effect, for HESS J1640–465 and HESS J1641–463 in light of our ISM study.

The leptonic scenario for HESS J1640–465 has been developed and explored by several previous works (Funk et al. 2007; Lemoine-Goumard et al. 2009; Slane et al. 2010; Abramowski et al. 2014a; Gotthelf et al. 2014). In particular, the scenario involves the electrons being accelerated at the termination shock of a PWN near the centroid of the TeVs source which is powered by PSR J1640–4631 (Gotthelf et al. 2014). In our ISM study and considerations in the previous section, we have shown that there is sufficient target material towards HESS J1640–465 for a purely hadronic origin, given a local CR accelerator such as SNR G338.3–0.0. As such, our study does not rule out either model and it possible that the TeV emission from HESS J1640–465 has contributions from both leptonic and hadronic processes, although some fine-tuning is required to explain the smooth power-law spectrum seen by *Fermi*-LAT (Lemoine-Goumard et al. 2014).

A leptonic origin has been previously considered for HESS J1641–463 (Abramowski et al. 2014b) but was strongly disfavoured, stemming from the lack of a characteristic break in the  $\gamma$ -ray spectrum and the extreme difficulty in accelerating a population of electrons to the required energies. For completeness, however, we now consider a leptonic diffusion scenario in which CR electrons, perhaps from the PSR J1640–4631, are diffusing through the gas bridge between HESS J1640–465 and HESS J1641–463.

The cooling time of CR electrons due to synchrotron radiation can be given by  $\tau_{\text{sync}} \approx (b_s \gamma)^{-1}$  s, where  $b_s = 1.292 \times 10^{-15} (B/\text{mG})^2 \text{ s}^{-1}$ , and the diffusion time of CRs over a distance  $d$  is given by  $\tau_{\text{diff}} = d^2/(6D(E))$ , where  $D(E)$  is the diffusion coefficient at energy  $E$  (Ginzburg & Syrovatskii 1964). We consider the case where  $E_e = 5 \text{ TeV}$ . At this energy,  $\gamma$ -rays produced via inverse-Compton scattering would have energies  $\sim 200 \text{ GeV}$  (in the Thompson regime) which is near the lower limit of detectability by HESS.

Dense cores of gas within the bridge region are traced in CS observations with  $\bar{n} \sim 10^5 \text{ cm}^{-3}$ . These cores have a diameter of  $\sim 2 \text{ arcmin}$ , which corresponds to  $\sim 6 \text{ pc}$  at a line-of-sight distance of  $11 \text{ kpc}$ . The magnetic field in these cores are calculated following Crutcher et al. (2010), using the values of  $\bar{n}$  presented in Section 4. Using this,  $\tau_{\text{sync}}$  and  $\tau_{\text{diff}}$  were found to be  $\sim 10 \text{ yr}$  and  $\sim 1 \text{ kyr}$ , respectively. This implies that CR electrons would rapidly lose their energy via synchrotron losses and would be unable to pass through the dense cores. For completeness, we note that calculations using emission from the diffuse gas tracers  $^{12}\text{CO}$  and  $^{13}\text{CO}$  in these core regions give  $\bar{n} \sim 4 \times 10^3 \text{ cm}^{-3}$ .

In an optimistic scenario, CR electrons could have paths that avoid the dense cores while diffusing through the gas bridge region. From Section 4, the diffuse gas traced by CO observations across the whole bridge region have  $\bar{n} \sim 5 \times 10^2 \text{ cm}^{-3}$ . Assuming that the distance across the gas bridge is  $\sim 30 \text{ pc}$ ,  $\tau_{\text{sync}}$  and  $\tau_{\text{diff}}$  are calculated to be  $\sim 11$  and  $\sim 4 \text{ kyr}$ , respectively. Hence, in an optimistic scenario, some electrons would be able to diffuse through the gas bridge. However, realistically, this is somewhat unlikely given the prevalence of dense gas in the region, as traced by CS emission. CR electrons would be effectively blocked by the dense regions of the gas bridge and be unable to generate  $\gamma$ -rays which may be contributing to HESS J1641–463.

## 6 CONCLUSIONS

In this paper, we have used data collected by the Mopra Radio Telescope in the 3 and 7 mm wavelengths as well as archival H I data to investigate the molecular and atomic gas towards the VHE  $\gamma$ -ray sources HESS J1640–465 and HESS J1641–463. The gas investigated here may be target material for accelerated CRs, producing TeV  $\gamma$ -rays via hadronic interactions.

CO(1–0) observations from the Mopra Galactic Plane Survey revealed multiple diffuse molecular gas components at numerous velocities along the line-of-sight positionally coincident with both TeV sources. In particular, substantial detections were made at velocities within  $\sim 10$ – $20 \text{ km s}^{-1}$  of the reported systematic velocity of the H II region ( $-32 \text{ km s}^{-1}$ ). The gas traced in Components 1, 2 and 3 as described in Section 4 ( $-53$  to  $-23 \text{ km s}^{-1}$ ) may be then associated with the SNRs, H II region and the VHE  $\gamma$ -ray sources. Of particular note is the molecular cloud traced in Component 1 positionally coincident with HESS J1641–463.

7 mm observations in the CS(1–0) lines revealed a region of dense gas cores coincident with intense emission in the CO(1–0)

lines. This gas formed a ‘bridge’ of material located between the two TeV  $\gamma$ -ray sources.

Mass and density estimates derived from CO, CS and H I for gas components towards HESS J1640–465 and HESS J1641–463 allowed for an investigation of the available CR target mass. Assuming that the total gas mass in Components 1, 2 or 3 towards HESS J1640–465 is CR-target material in a hadronic scenario for TeV  $\gamma$ -ray production, the required  $W_p$  is  $\sim 10^{48} \text{ erg}$  and the required CR density would be of the order of  $\sim 10^3$  times that seen at Earth. For HESS J1641–463, if the molecular cloud positionally coincident traced in Component 1 is CR-target material, then the required  $W_p$  is  $\sim 10^{47} \text{ erg}$  and the required CR density would be of the order of  $\sim 10^2$  times than seen at Earth.

We also investigated the scenario in which TeV emission from HESS J1641–463 is due to HE CRs from SNR G338.0–0.0, coincident with HESS J1640–465, diffusively reaching CR target material seen in our data. We find that the scenario is a plausible explanation which readily explains the hardness of the TeV emission from HESS J1641–463. We do not, however, discount the scenario in which SNR G338.5+0.1 coincident with HESS J1641–463 is providing the required CRs.

A scenario in which CR electrons from PSR J1640–4631 were diffusing towards HESS J1641–463 was considered. However, it is somewhat unlikely due to dense cores of gas present in the bridge between HESS J1640–465 and HESS J1641–463 which would effectively block the path of the electrons. This is in addition to arguments presented by Abramowski et al. (2014b) that disfavour a leptonic origin.

Future  $\gamma$ -ray measurements taken by next-generation ground-based  $\gamma$ -ray telescope systems (e.g. Cherenkov Telescope Array) will have greatly increased sensitivity above 10 TeV and have angular resolutions similar to that in this study of the interstellar gas. This will allow more detailed morphological comparison between the TeV  $\gamma$ -ray emission and gas and allow a deeper investigation of the nature of HESS J1640–465 and HESS J1641–463.

## ACKNOWLEDGEMENTS

The Mopra radio telescope is part of the Australia Telescope National Facility. Operations support was provided by the University of New South Wales (UNSW) and the University of Adelaide. The UNSW Digital Filter Bank used for the observations with Mopra was provided with financial support from the Australian Research Council (ARC), UNSW, Sydney and Monash universities. We also acknowledge ARC support through Discovery Project DP120101585. Sabrina Casanova acknowledges the support of the Polish Science Centre through the Opus grant UMO-2014/13/B/ST9/00945.

## REFERENCES

- Abramowski A. et al., 2014a, MNRAS, 439, 2828
- Abramowski A. et al., 2014b, ApJ, 794, L1
- Aharonian F. A., 1991, Ap&SS, 180, 305
- Aharonian F. A., Atoyan A. M., 1996, A&A, 309, 917
- Aharonian F., Akhperjanian A. G., Bazer-Bachi A. R., Beilicke M., Benbow W., Berge D., 2006, ApJ, 636, 777
- Bell A. R., Schure K. M., Reville B., Giacinti G., 2013, MNRAS, 431, 415
- Bolatto A. D., Wolfire M., Leroy A. K., 2013, ARA&A, 51, 207
- Braiding C. et al., 2015, Publ. Astron. Soc. Aust., 32
- Burton M. G. et al., 2013, Publ. Astron. Soc. Aust., 30, 44
- Castelletti G., Giacani E., Dubner G., Joshi B. C., Rao A. P., Terrier R., 2011, A&A, 536, A98

- Caswell J. L., Haynes R. F., 1987, A&A, 171, 261
- Chen Y., Zhou P., Chu Y.-H., 2013, ApJ, 769, L16
- Chevalier R. A., 1999, ApJ, 511, 798
- Crutcher R. M., Wandelt B., Heiles C., Falgarone E., Troland T. H., 2010, ApJ, 725, 466
- Dame T. M., Hartmann D., Thaddeus P., 2001, ApJ, 547, 792
- Dickey J. M., Lockman F. J., 1990, ARA&A, 28, 215
- Frerking M. A., Wilson R. W., Linke R. A., Wannier P. G., 1980, ApJ, 240, 65
- Fukui Y. et al., 2012, ApJ, 746, 82
- Funk S., Hinton J. A., Pühlhofer G., Aharonian F. A., Hofmann W., Reimer O., Wagner S., 2007, Astrophys. J., 662, 517
- Gabici S., Aharonian F. A., Blasi P., 2007, Ap&SS, 309, 365
- Ginzburg V. L., Syrovatskii S. I., 1964, *The Origin of Cosmic Rays*. Macmillan, New York
- Goldsmith P. F., Langer W. D., 1999, ApJ, 517, 209
- Gotthelf E. V. et al., 2014, ApJ, 788, 155
- Gusdorf A., Cabrit S., Flower D. R., Pineau Des Forets G., 2008, A&A, 482, 809
- Henkel C., Wilson T. L., Bieging J., 1982, A&A, 109, 344
- Irvine W. M., Goldsmith P. F., Hjalmarson A., 1987 Vol. 134 of *Astrophysics and Space Science Library*, Chemical abundances in molecular clouds. p. 561
- Kafexhiu E., Aharonian F., Taylor A. M., Vila G. S., 2014, Phys. Rev. D, 90, 123014
- Kothes R., Dougherty S. M., 2007, A&A, 468, 993
- Ladd N., Purcell C., Wong T., Robertson S., 2005, Publ. Astron. Soc. Aust., 22, 62
- Lemiere A., Slane P., Gaensler B. M., Murray S., 2009, ApJ, 706, 1269
- Lemoine-Goumard M., Grondin M.-H., Acero F., Ballet J., Laffon H., Reposeur T., 2014, ApJ, 794, L16
- McClure-Griffiths N. M., Dickey J. M., Gaensler B. M., Green A. J., Havercorn M., Strasser S., 2005, ApJS, 158, 178
- Nava L., Gabici S., 2013, MNRAS, 429, 1643
- Purcell C. R., Longmore S. N., Walsh A. J., Whiting M. T., Breen S. L., 2012, MNRAS, 426, 1972
- Russeil D., 2003, A&A, 397, 133
- Simon R., Jackson J. M., Clemens D. P., Bania T. M., Heyer M. H., 2001, ApJ, 551, 747
- Slane P., Castro D., Funk S., Uchiyama Y., Lemiere A., Gelfand J. D., Lemoine-Goumard M., 2010, ApJ, 720, 266
- Strong A. W., Moskalenko I. V., Reimer O., Digel S., Diehl R., 2004, A&A, 422, L47
- Supan L., Supanitsky A. D., Castelletti G., 2016, A&A, 589, A51
- Tang Y., Yang C., Zhang L., Wang J., 2015, ApJ, 812, 32
- Urquhart J. S. et al., 2010, Publ. Astron. Soc. Aust., 27, 321
- Urquhart J. S. et al., 2012, MNRAS, 420, 1656
- Whiteoak J. B. Z., Green A. J., 1996, A&AS, 118, 329
- Zinchenko I., Forsstroem V., Lapinov A., Mattila K., 1994, A&A, 288, 601

## APPENDIX A

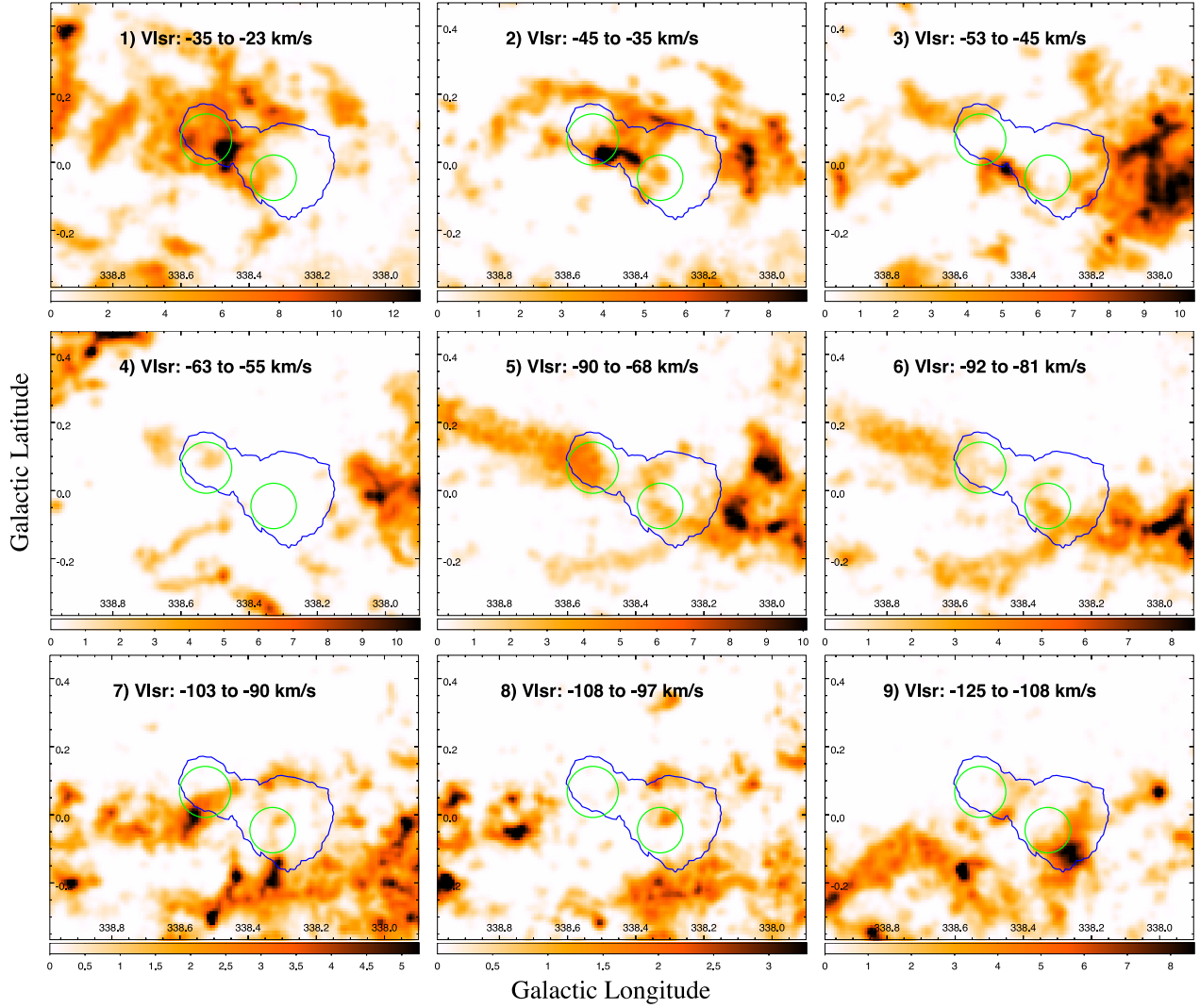


**Figure A1.** Integrated  $^{13}\text{CO}$ (1–0) emission images ( $\text{K km s}^{-1}$ ) over indicated velocity intervals. Single blue  $5\sigma$  significance HESS contour used for clarity and illustration purposes. The position and extent of SNR G338.5+0.1 and SNR G338.3-0.0 are indicated by the left and right solid green circles, respectively, in each panel.

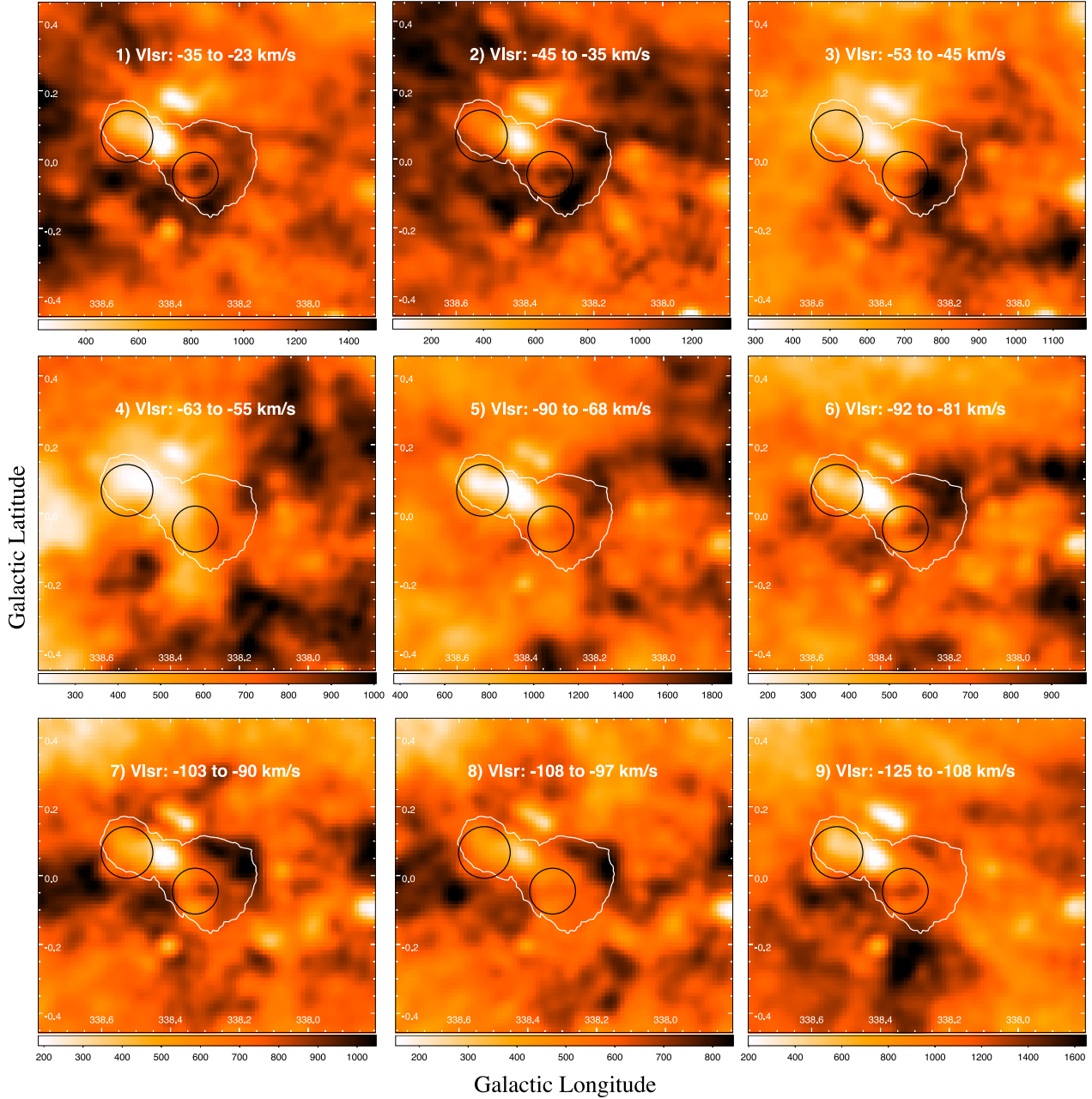


**Figure A2.** Integrated  $\text{H I}$  emission images [ $\text{K km s}^{-1}$ ] from SGPS data over indicated velocity intervals. Single white  $5\sigma$  significance HESS contour used for clarity and illustration purposes. The position and extent of SNR G338.5+0.1 and SNR G338.3-0.0 are indicated by the left and right solid black circles, respectively, in each panel.

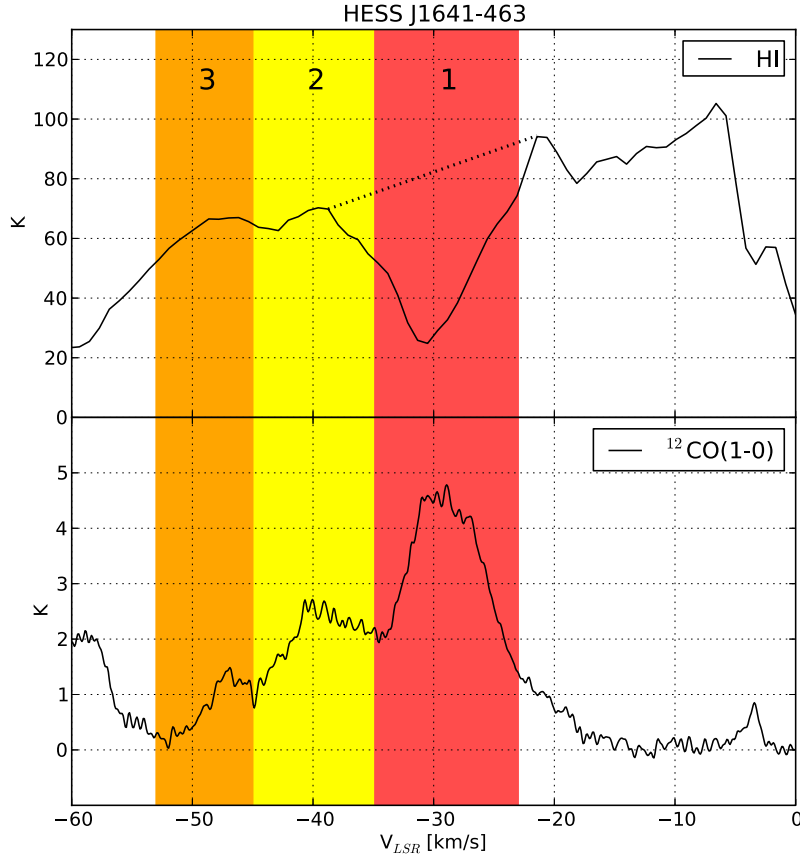


**Figure A3.** Average H I and  $^{12}\text{CO}(1-0)$  emission spectrum towards HESS J1641–463 from the SGPS and Mopra CO survey, respectively. A possible example of a self-absorption dip in the H I is seen at  $\sim -30 \text{ km s}^{-1}$  in component 1, where a corresponding peak exists in the CO. The dashed line is the linear interpolation used to estimate the true H I emission.

**Table A1.**  $^{13}\text{CO}(1-0)$  line parameters, and the corresponding calculated gas parameters, from the apertures as indicated in Fig. 1. Calculations were made following Section 3.1, but using the  $^{13}\text{CO}(1-0)$  X-factor,  $X_{^{13}\text{CO}(1-0)} = 4.92 \times 10^{20} (\text{K km s}^{-1})^{-1}$  (Simon et al. 2001). Masses and density have been scaled to account for an additional 20 per cent He component.

Velocity range ( $\text{km s}^{-1}$ )	Region	Distance <sup>a</sup> (kpc)	$\overline{N_{\text{H}_2}}^b$ ( $10^{21} \text{ cm}^{-2}$ )	Mass <sup>b</sup> ( $M_{\odot} \times 10^4$ )	$\bar{n}^b$ ( $10^2 \text{ cm}^{-3}$ )
−35 to −23 (Component 1)	HESS J1640–465	11.9	1.7	2.7	0.8
	HESS J1641–463	11.9	6.7	5.1	4.4
	Bridge	11.9	7.1	10.1	3.3
−45 to −35 (Component 2)	HESS J1640–465	11.2	2.9	4.3	1.4
	HESS J1641–463	11.2	3.0	2.0	2.1
	Bridge	11.2	8.7	11.7	4.3
−53 to −45 (Component 3)	HESS J1640–465	10.8	1.9	2.5	0.9
	HESS J1641–463	10.8	0.6	0.4	0.4
	Bridge	10.8	3.9	4.9	2.0

*Notes.* <sup>a</sup>Assumed distances,  $d_0$ , used for mass and density calculations are derived from the Galactic rotation curve presented in Kothes & Dougherty (2007). However, these values are easily scaled for an arbitrary distance,  $d$ , by multiplying by  $(d/d_0)^2$  and  $(d/d_0)^{-1}$  for mass and density, respectively.

<sup>b</sup>The error in the calculated physical parameters are dominated by the statistical uncertainties associated with the  $^{13}\text{CO}$  to H<sub>2</sub> conversion factor ( $X_{^{13}\text{CO}(1-0)}$ ) and is of the order of 30 per cent.

**Table A2.** Calculated CR enhancement values,  $k_{\text{CR}}$ , for the intrinsic Gaussian size of HESS J1640–465 and the maximum Gaussian extent of HESS J1641–463 for the gas related to all individual components as defined in Fig. 1. Molecular mass comes from CO analysis and atomic mass from H I analysis.

Region	$v_{\text{LSR}}$ range (km s $^{-1}$ )	Assumed distance $^a$ (kpc)	Molecular mass (M $_{\odot}$ )	Atomic mass (M $_{\odot}$ )	Total mass (M $_{\odot}$ )	$k_{\text{CR}}^b$
HESS J1640-465	–35 to –23 (Component 1)	11.9	68 000	12 000	80 000	1000
	–45 to –35 (Component 2)	11.2	47 000	9300	56 000	1400
	–53 to –45 (Component 3)	10.8	88 000	7100	95 000	850
	–63 to –55 (Component 4)	10.4	15 000	4400	19 000	3800
	–90 to –68 (Component 5)	9.6	58 000	8000	64 000	950
	–92 to –81 (Component 6)	9.3	39 000	4200	43 000	1300
	–103 to –90 (Component 7)	8.9	20 000	4300	24 000	2210
	–108 to –97 (Component 8)	8.7	15 000	3000	18 000	2800
	–125 to –108 (Component 9)	8.15	40 000	4700	45 000	990
HESS J1641-463	–35 to –23 (Component 1)	11.9	97 000	5000	102 000	150
	–45 to –35 (Component 2)	11.2	31 000	3200	34 000	450
	–53 to –45 (Component 3)	10.8	11 000	2100	13 000	1200
	–63 to –55 (Component 4)	10.4	17 000	1000	18 000	750
	–90 to –68 (Component 5)	9.6	37 000	1700	39 000	300
	–92 to –81 (Component 6)	9.3	15 000	1100	16 000	680
	–103 to –90 (Component 7)	8.9	13 000	1400	14 000	720
	–108 to –97 (Component 8)	8.7	5500	1200	7000	1400
	–125 to –108 (Component 9)	8.15	7100	1300	8000	1000

*Notes.*  $^a$ The assumed distance was calculated using the average  $v_{\text{LSR}}$  in the interval with the Galactic rotation curve presented by Kothes & Dougherty (2007). For consistency, we have used the far distance solutions for every component. Masses can be scaled for an arbitrary distance,  $d$ , by multiplying by  $(d/d_0)^2$  where  $d_0$  is the assumed distance.

$^b$ The CR enhancement factor,  $k_{\text{CR}}$ , was calculated following equation (10) from Aharonian (1991) considering the total masses presented in this table as CR-target material. Note also that  $k_{\text{CR}}$  is independent of assumed distance as the distance terms in the equation cancel with the distance assumptions for the mass calculations.

This paper has been typeset from a TeX/LaTeX file prepared by the author.

## Chapter 4

# The ISM towards HESS J1614–518 and HESS J1616–508

The following is a paper that was submitted to the peer-reviewed journal, Publications of the Astronomical Society of Australia (PASA), and resubmitted after comments from an anonymous referee. HESS J1614–518 and HESS J1616–508 are dark TeV gamma-ray sources which have not been firmly associated with any counterpart at other wavelengths. This paper presents an analysis of the distribution of the interstellar medium towards the TeV sources, as well as an investigation into potential origin scenarios in light of this new understanding.

During the thesis examination period, the paper was accepted by PASA and has since been published (Lau et al., 2017).

# Statement of Authorship

Title of Paper	A study of the interstellar medium towards the unidentified dark TeV $\gamma$ -ray sources HESS J1614-518 and HESS J1616-508		
Publication Status	<input type="checkbox"/> Published	<input type="checkbox"/> Accepted for Publication	<input checked="" type="checkbox"/> Submitted for Publication
Publication Details	Submitted to the peer reviewed journal, Publications of the Astronomical Society of Australia (PASA), and resubmitted after consideration of comments from an anonymous reviewer		

## Principal Author

Name of Principal Author (Candidate)	James Cheuk-Heng Lau		
Contribution to the Paper	Mopra data observations, data reduction, spectral line analysis, interstellar medium and high energy interpretations, and writing of the paper.		
Overall percentage (%)	70%		
Certification:	This paper reports on original research I conducted during the period of my Higher Degree by Research candidature and is not subject to any obligations or contractual agreements with a third party that would constrain its inclusion in this thesis. I am the primary author of this paper.		
Signature		Date	24/10/17

## Co-Author Contributions

By signing the Statement of Authorship, each author certifies that:

- i. the candidate's stated contribution to the publication is accurate (as detailed above);
- ii. permission is granted for the candidate to include the publication in the thesis; and
- iii. the sum of all co-author contributions is equal to 100% less the candidate's stated contribution.

Name of Co-Author	Gavin Rowell		
Contribution to the Paper	ISM analysis, ISM and high energy interpretations and general reviewing of paper (11%)		
Signature		Date	15/09/17

Name of Co-Author	Fabien Voisin		
Contribution to the Paper	ISM and high energy interpretations (5%)		
Signature		Date	15/09/2017

Name of Co-Author	Catherine Braiding	
Contribution to the Paper	Mopra observations and data (2%)	
Signature	Date	14/10/17

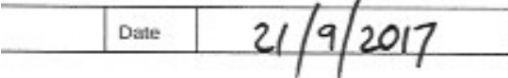
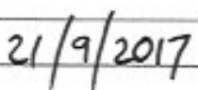
Name of Co-Author	Michael Burton	
Contribution to the Paper	Mopra observations, ISM interpretations and general reviewing (2%)	
Signature	Date	23/10/17

Name of Co-Author	Yasuo Fukui	
Contribution to the Paper	ISM interpretation (2%)	
Signature	Date	October 5th, 2017

Name of Co-Author	Stephanie Pointon	
Contribution to the Paper	ISM interpretation (2%)	
Signature	Date	29/09/2017

Name of Co-Author	Michael Ashley	
Contribution to the Paper	HEAT data and ISM interpretation (2%)	
Signature	Date	10 October 2017

Name of Co-Author	Christopher Jordan	
Contribution to the Paper	MALT-45 data and ISM interpretation (2%)	
Signature	Date	10/10/17

Name of Co-Author	Andrew Walsh
Contribution to the Paper	MALT-45 data (2%)
Signature	 Date 

# A study of the interstellar medium towards the unidentified dark TeV $\gamma$ -ray sources HESS J1614–518 and HESS J1616–508

J. C. Lau<sup>1\*</sup>, G. Rowell<sup>1</sup>, F. Voisin<sup>1</sup>, C. Braiding<sup>2</sup>, M. Burton<sup>2,3</sup>, Y. Fukui<sup>4</sup>, S. Pointon<sup>5</sup>, M. Ashley<sup>6</sup>, C. Jordan<sup>7</sup> and A. Walsh<sup>7</sup>

<sup>1</sup>School of Physical Sciences, University of Adelaide, Adelaide, SA 5005, Australia

<sup>2</sup>School of Physics, University of New South Wales, Sydney, NSW 2052, Australia

<sup>3</sup>Armagh Observatory and Planetarium, College Hill, Armagh, BT61 9DG, Northern Ireland, UK

<sup>4</sup>Department of Physics, University of Nagoya, Furo-cho, Chikusa-ku, Nagoya, 464-8601, Japan

<sup>5</sup>Centre for Astrophysics and Supercomputing, Swinburne University of Technology, Hawthorn, Victoria 3122, Australia

<sup>6</sup>School of Physics, University of New South Wales, Sydney NSW 2052, Australia

<sup>7</sup>International Centre for Radio Astronomy Research, Curtin University, Bentley, WA 6845, Australia

## Abstract

HESS J1614–518 and HESS J1616–508 are two tera-electron volt (TeV)  $\gamma$ -ray sources that are not firmly associated with any known counterparts at other wavelengths. We investigate the distribution of interstellar medium towards the TeV  $\gamma$ -ray sources using results from a 7 mm-wavelength Mopra study, the Mopra Southern Galactic Plane CO Survey, the Millimetre Astronomer’s Legacy Team - 45 GHz survey and [CI] data from the HEAT telescope. Data in the CO(1–0) transition lines reveal diffuse gas overlapping the two TeV sources at several velocities along the line of sight, while observations in the CS(1–0) transition line reveal several interesting dense gas features. To account for the diffuse atomic gas, archival HI data was taken from the Southern Galactic Plane Survey. The observations reveal gas components with masses  $\sim 10^3$  to  $10^5 M_{\odot}$  and with densities  $\sim 10^2$  to  $10^3 \text{ cm}^{-3}$  overlapping the two TeV sources. Several origin scenarios potentially associated with the TeV  $\gamma$ -ray sources are discussed in light of the distribution of the local interstellar medium. We find no strong convincing evidence linking any counterpart with HESS J1614–518 or HESS J1616–508.

**Keywords:** ISM:clouds – ISM: cosmic rays – gamma-rays: ISM – molecular data

## 1 Introduction

Exploration into the nature of the very high energy (VHE,  $E > 100$  GeV)  $\gamma$ -ray sky has rapidly progressed with the use of Imaging Air Cherenkov Telescopes (IACTs). Telescopes such as the High Energy Stereoscopic System (HESS), an array of IACTs, have found many VHE  $\gamma$ -ray sources along the Galactic plane (Aharonian et al. 2005a, 2006; Deil et al. 2015). Many of the extended, Galactic sources have been associated with high-energy phenomena, such as pulsar wind nebulae (PWN), supernova remnants (SNRs) and binaries (Renaud et al. 2008; Aharonian et al. 2005b, 2008b etc.). However, a large population of VHE sources remain unassociated, and appear to have no clear counterparts seen in other wavelengths (Deil et al. 2015; Donath et al. 2017).

Astrophysical TeV  $\gamma$ -rays have two main mechanisms of production: the decay of neutral pions produced by the hadronic interactions between highly accelerated cosmic-ray particles and ambient interstellar medium (ISM); and the leptonic interaction of upscattering background photons via the inverse-Compton effect by high energy electrons. Understanding the distribution of the ISM towards unidentified TeV sources is thus critical in order to constrain the possible TeV  $\gamma$ -ray production scenarios. Here, we focus on HESS J1614–518 and HESS J1616–508, two of the most prominent unidentified TeV sources detected in the first HESS Galactic Plane Survey (Aharonian et al. 2005a, 2006).

HESS J1614–518 is a TeV  $\gamma$ -ray source that was first discovered by HESS as part of a survey of the Galactic plane (Aharonian et al. 2005a). It was the brightest of

\*E-mail: james.lau@adelaide.edu.au

the new sources discovered in the survey, with a flux 25% that of the Crab Nebula above 200 GeV. It has a TeV  $\gamma$ -ray spectrum that is well fit by a power-law,  $dN/dE = N_0 E^{-\Gamma}$ , with a photon index  $\Gamma = 2.46 \pm 0.21$ . The TeV emission has an elliptical morphology, with semi-major and semi-minor axes of  $14 \pm 1$  and  $9 \pm 1$  arcmin respectively. It is also characterised by two peaks of emission in the Galactic North-East and Galactic South-West of the source. No immediately obvious counterpart to this source appeared in other wavelengths, and HESS J1614–518 was considered a “dark-accelerator”.

Recent preliminary results from HESS, following a systematic search for new TeV-emitting SNRs, suggest that HESS J1614–518 may have a shell-like TeV  $\gamma$ -ray morphology (Gottschall et al. 2017). As no evidence of an associated SNR has been seen so far in other wavelengths, HESS J1614–518 is currently considered a SNR candidate.

Observations towards HESS J1614–518 in X-rays made by *Suzaku* revealed three X-ray sources within the TeV  $\gamma$ -ray source (Matsumoto et al. 2008). The first source, Suzaku Src A, is extended and is located close (within  $\sim 8$  arcmin) to the brightest TeV peak of HESS J1614–518. The 2nd X-ray source, Suzaku Src B, is located towards the centre of HESS J1614–518. Additional *Suzaku* observations and analysis of *XMM-Newton* archival data revealed that Suzaku Src B was comprised of several point sources (Sakai et al. 2011). The brightest of these, XMM-Newton source B1, had the largest count rate by a factor  $\sim 5$ , and indicated that it was the main object of Suzaku Src B. Sakai et al. (2011) postulated that HESS J1614–518 could be an SNR associated with an Anomalous X-ray Pulsar (AXP). This scenario has XMM-Newton source B1 as the AXP produced by a supernova explosion, and Suzaku source A as the shocked region of the SNR. The other X-ray source found by *Suzaku*, Suzaku source C, was found to be a late-type B star (Matsumoto et al. 2008).

The X-ray telescope (XRT) aboard *Swift* observed the region towards HESS J1614–518 and found six point-like X-ray sources (Landi et al. 2007b). Four of these (Swift sources 1, 2, 3 and 5 in Landi et al. 2007b) were identified as stars, while the others (Swift sources 4 and 6) remain unidentified. The Swift source 1 and 4 are coincident with Suzaku source B and C respectively. Suzaku source A was not seen by the *Swift* XRT in these observations.

A GeV source is seen towards HESS J1614–518 by the *Fermi* Large Area Telescope (*Fermi*-LAT). Designated 3FGL J1615.3–5146e in the 3rd *Fermi* point source catalogue (Acero et al. 2015), the extended source was classified as being ‘disk-like’, and has a relative large diameter of  $\sim 0.8^\circ$  which covers a major fraction of HESS J1614–518.

Several HII regions and molecular cloud complexes appear to the Galactic-North of HESS J1614–518. Figure 1 is a *Spitzer* GLIMPSE 8.0  $\mu$ m image (Churchwell et al. 2009) of the region towards HESS J1614–518 and the neighbouring TeV source HESS J1616–508, with nearby HII regions labelled in yellow. While there are several HII regions in the vicinity of HESS J1614–518, none appear to overlap the TeV source.

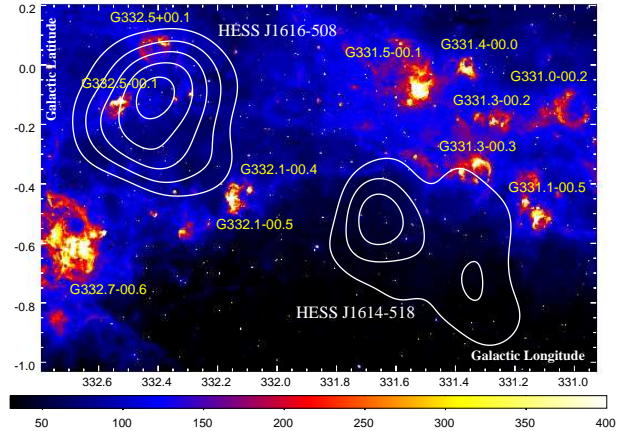


**Figure 1.** *Spitzer* GLIMPSE 8.0  $\mu$ m image [MJy sr $^{-1}$ ] towards HESS J1614–518 and HESS J1616–508 (Churchwell et al. 2009). White contours are HESS excess counts contours at the 30, 45, 60, 75 and 90 levels (Aharonian et al. 2006). Nearby HII regions are labelled in yellow (Paladini et al. 2003).

A multi-wavelength counterpart study of HESS J1614–518 was conducted by Rowell et al. (2008). The known pulsars towards HESS J1614–518 were thought likely not responsible for the TeV  $\gamma$ -ray emission due to their insufficient spin-down powers, though a small fractional contribution could not be ruled out. A possible association between HESS J1614–518 and the young open stellar cluster Pismis 22 (Piatti et al. 2000) was suggested in scenarios where stellar winds from several B-type stars or undetected SNRs from deceased members of the cluster would accelerate cosmic-rays that would interact with ambient gas to produce  $\gamma$ -rays hadronically.

Mizukami et al. (2011) used the CANGAROO-III telescopes to study the TeV  $\gamma$ -ray emission towards HESS J1614–518, and also investigated the plausibility of several radiation mechanisms. A leptonic scenario based on an undetected SNR was rejected as it was not able to reproduce the observed spectral energy distribution (SED) in  $\gamma$ -rays. On the other hand, hadronic models that involved either a SNR or stellar winds from Pismis 22 were found to produce a good reproduction of the SED. Certain requirements, however, on the number density of the ISM were needed, and the initial investigation of the Nanten  $^{12}\text{CO}(1-0)$

survey data by [Rowell et al. \(2008\)](#) in this region had revealed no obvious overlapping molecular clouds along the line of sight up to a kinematic distance of  $\sim 6$  kpc. More detailed and higher resolution ISM data were needed in order to test the validity of these models.

HESS J1616–508 is located less than a degree away from HESS J1614–518. It too was discovered as part of the HESS Galactic plane survey ([Aharonian et al. 2005a](#)), with a  $\gamma$ -ray flux 19% that of the Crab Nebula above 200 GeV. The TeV spectrum is fit by a power-law model with a photon index  $\Gamma = 2.35 \pm 0.06$ . It has a roughly circular extended morphology, with an angular diameter of  $\sim 16$  arcmin. There are two SNRs near HESS J1616–508, Kes 32 (G332.4+0.1) and RCW 103 (G332.4–0.4), located 17 and 13 arcmin away respectively. Due to the distance from the centre of HESS J1616–508, an association between the TeV source and either SNR has been disfavoured ([Landi et al. 2007a; Kargaltsev et al. 2009](#)).

Three pulsars are seen towards the vicinity of HESS J1616–508. Two of them, PSR J1616–5109 and PSR J1614–5048 are unlikely to be associated with the TeV emission due to their large separation from HESS J1616–508. On the other hand, the young ( $\sim 8$  kyr) pulsar PSR J1617–5055 ([Kaspi et al. 1998](#)) and associated pulsar wind nebula (PWN) have been suggested as candidate objects responsible for the TeV emission ([Landi et al. 2007a; Aharonian et al. 2008a; Tibolla 2011; Acero et al. 2013](#)). PSR J1617–5055 has a spin-down power sufficient to supply the appropriate energetics, but is offset from the centre of the TeV source by  $\sim 9$  arcmin. Observations in X-rays by *Chandra* revealed a faint PWN extending from PSR J1617–5055 ([Kargaltsev et al. 2009](#)). However, PWNs associated with offset TeV  $\gamma$ -ray emission typically have an extension of the X-ray emission towards said  $\gamma$ -rays, and the *Chandra* observations found no evidence of any X-ray asymmetry in the PWN towards HESS J1616–508. Recent analysis of three *Chandra* observations covering most of HESS J1616–508 was performed by [Hare et al. \(2017\)](#), finding 56 X-rays sources within the fields. Many of the sources were identified as active galactic nuclei (AGN) and non-degenerate stars, but none were found to be promising counterparts to the TeV source.

Observations by *Fermi*-LAT reveal a GeV  $\gamma$ -ray source, 3FGL J1616.2–5054e towards HESS J1616–508 ([Acero et al. 2015](#)). It has a diameter of  $\sim 0.6^\circ$  and is positionally coincident with the TeV source.

A number of HII regions are seen towards HESS J1616–508, with several overlapping the TeV source as shown in Figure 1.

To better understand the origins of HESS J1614–518 and HESS J1616–508, a detailed understanding of the

distribution and characteristics of the ISM towards these two sources is required. In order to achieve this, we have used molecular line data taken by the Mopra radio telescope and the Australia Telescope Compact Array (ATCA). The diffuse ( $\overline{n} \gtrsim 10^3 \text{ cm}^{-3}$ ) gas towards the two TeV sources were traced as part of the Mopra Southern Galactic Plane CO Survey ([Burton et al. 2013](#)). Data were taken from the Millimetre Astronomer's Legacy Team - 45 GHz (MALT-45) survey ([Jordan et al. 2015](#)) which targeted the dense ( $\overline{n} \gtrsim 10^4 \text{ cm}^{-3}$ ) gas tracers in the 7 mm wavelength band including CS(1–0) and SiO(1–0, v=0). As the MALT-45 survey did not extend to encompass HESS J1614–518 entirely, we took further observations in the 7 mm wavelength band with Mopra to complete the coverage in the dense gas tracers.

Section 2 describes the parameters and reduction process involved with the data taken with the Mopra radio telescope, as well as the parameters of the data taken from the MALT-45 survey. Section 3 describes the gas parameter calculations that we apply to the data. In Section 4, we present our findings of the the distribution of the ISM towards the TeV sources. Finally, in Section 5, we discuss our results and the implications they have on the possible production scenarios for HESS J1614–518 and HESS J1616–508.

## 2 Datasets, observations and data reduction

High resolution data in the 7 mm wavelength band was taken from the MALT-45 survey ([Jordan et al. 2015](#)). This survey made use of ATCA to survey an area of 5 square-degrees along the Galactic plane ( $l = 330^\circ - 335^\circ, b = \pm 0.5$ ). Across the 7 mm band, the survey FWHM ranged from  $57''$  (49 GHz) to  $66''$  (43 GHz) with a velocity resolution of  $\sim 0.2 \text{ km s}^{-1}$ . Complete details of the survey are presented in the aforementioned paper. The survey area of MALT-45 completely covered HESS J1616–508, but only covered the northern-half of HESS J1614–518.

A 7 mm targeted study was carried out with the Mopra radio telescope to complement the MALT-45 survey, completing the coverage of HESS J1614–518. The Mopra observations were taken between September and November 2013. Two Mopra ‘On-the-fly’ (OTF) maps were taken, each with a size of  $20' \times 20'$ . Together, this formed a  $40' \times 20'$  map which was centred on  $[l, b] = [331^\circ.50, -0^\circ.67]$ . For these observations, we used the same scan settings as per [Lau et al. \(2017\)](#).

These observations utilised the Mopra spectrometer, MOPS, in its ‘zoom’ mode, allowing for recording of sixteen sub-bands simultaneous, each with 4096-channels and a 137.5 MHz bandwidth. The beam FWHM of Mopra in the 7 mm band is  $\sim 1'$  at 49 GHz, with a velocity resolution of  $\sim 0.2 \text{ km s}^{-1}$ . The specific molecular line transitions that were targeted by MOPS are

**Table 1** The set-up for the Mopra Spectrometer (MOPS) for the 7 mm observations. The targeted molecular lines, targeted frequencies and achieved mapping  $T_{\text{RMS}}$  are displayed.

Molecular line	Frequency (GHz)	$T_{\text{RMS}}$ (K/channel)
$^{30}\text{SiO}(J=1-0, v=0)$	42.373365	0.07
$\text{SiO}(J=1-0, v=3)$	42.519373	0.07
$\text{SiO}(J=1-0, v=2)$	42.820582	0.07
$^{29}\text{SiO}(J=1-0, v=0)$	42.879922	0.07
$\text{SiO}(J=1-0, v=1)$	43.122079	0.07
$\text{SiO}(J=1-0, v=0)$	43.423864	0.07
$\text{CH}_3\text{OH-I}$	44.069476	0.07
$\text{HC}_7\text{N}(J=40-39)$	45.119064	0.07
$\text{HC}_5\text{N}(J=17-16)$	45.264750	0.07
$\text{HC}_3\text{N}(J=5-4, F=4-3)$	45.490264	0.08
$^{13}\text{CS}(J=1-0)$	46.247580	0.08
$\text{HC}_5\text{N}(J=16-15)$	47.927275	0.08
$\text{C}^{34}\text{S}(J=1-0)$	48.206946	0.09
$\text{OCS}(J=4-3)$	48.651604	0.09
$\text{CS}(J=1-0)$	48.990957	0.09

listed along with the achieved  $T_{\text{RMS}}$  levels in Table 1. We note that MALT-45 had increased sensitivities compared with that of our Mopra observations. In particular, the MALT-45  $T_{\text{RMS}}$  for the CS(1–0) line was  $\sim 0.034$  K compared with the  $\sim 0.09$  K we achieved with Mopra.

Data in the CO(1–0) lines was provided by the Mopra Southern Galactic Plane CO Survey (Burton et al. 2013; Braiding et al. 2015). The survey targets the  $^{12}\text{CO}$ ,  $^{13}\text{CO}$  and  $\text{C}^{18}\text{O}$   $J = 1-0$  molecular lines within the fourth quadrant of the Galaxy ( $l = 305^\circ$  to  $345^\circ$ , and  $b = \pm 0^\circ.5$ ). The beamsize of this survey is  $0'.6$ , with a velocity resolution of  $0.1 \text{ km s}^{-1}$ . The  $T_{\text{RMS}}$  for the  $^{12}\text{CO}$  and  $^{13}\text{CO}$  lines is  $\sim 1.5$  K  $\sim 0.7$  K respectively. We refer to the aforementioned papers for further details about the survey.

We used ATNF analysis software, Livedata<sup>1</sup>, Gridzilla<sup>1</sup>, and Miriad<sup>2</sup>, together with custom IDL routines, in order to reduce and perform analysis on the OTF mapping data. Using Livedata, we calibrated the spectra with the reference OFF position, and then subtracted the baseline using a polynomial fit. Combining the data from separate scans using Gridzilla, we created three-dimensional cubes for each sub-band. Finally, the integrated emission maps were generated from the cubes via the use of Miriad and custom IDL routines.

### 3 Spectral line analysis

The spectral line analyses performed on the CO(1–0), CS(1–0) and HI data to calculate gas mass and density parameters are outlined in Lau et al. (2017), and are summarised here for completeness.

Spectral components and features were fit with Gaussian functions, and the integrated intensity of the line emission was then used to calculate the average column density of molecular hydrogen,  $\overline{N_{\text{H}_2}}$ . From here, the mass of the gas in the region of interest is estimated by  $M = \mu m_{\text{H}} \overline{N_{\text{H}_2}} A$ , where  $m_{\text{H}}$  is the mass of a single hydrogen atom and  $A$  is the cross-sectional area of the region in which the spectra was extracted from. The average molecular weight  $\mu$  is taken to be 2.8 to account for the assumed  $\sim 20\%$  helium content. Within the region of interest, the average number density,  $\overline{n}$ , is estimated by assuming a geometry with depth equal to the average height and width.

#### 3.1 CO

We convert the  $^{12}\text{CO}(1-0)$  integrated brightness temperature to an average  $\text{H}_2$  column density in a region via the relation  $\overline{N_{\text{H}_2}} = X_{^{12}\text{CO}(1-0)} W_{^{12}\text{CO}(1-0)}$ , where  $W_{^{12}\text{CO}(1-0)}$  is the integrated  $^{12}\text{CO}(1-0)$  intensity and  $X_{^{12}\text{CO}(1-0)}$  is the  $^{12}\text{CO}(1-0)$  X-factor. In this work, we adopt the  $^{12}\text{CO}(1-0)$  X-factor  $X_{^{12}\text{CO}(1-0)} \sim 1.5 \times 10^{20} \text{ cm}^{-2}(\text{K km/s})^{-1}$  (Strong et al. 2004). For simplicity, we apply the same method to convert  $^{13}\text{CO}(1-0)$  integrated brightness temperatures to average  $\text{H}_2$  column densities, using the  $^{13}\text{CO}(1-0)$  X-factor  $X_{^{13}\text{CO}(1-0)} \sim 4.9 \times 10^{20} \text{ cm}^{-2}(\text{K km/s})^{-1}$  (Simon et al. 2001). Following Burton et al. (2013), we calculate the optical thickness of the  $^{12}\text{CO}$  line,  $\tau_{12}$ , by comparing the  $^{12}\text{CO}$  and  $^{13}\text{CO}$  lines. In the limit where the  $^{12}\text{CO}$  and  $^{13}\text{CO}$  lines are optically thick and optically thin respectively,  $\tau_{12}$  can be given by:

$$\tau_{12} = \frac{X_{12/13}}{R_{12/13}} \quad (1)$$

where  $R_{12/13}$  is the ratio between the brightness temperatures of the  $^{12}\text{CO}$  and  $^{13}\text{CO}$  emission, with  $X_{12/13} = [^{12}\text{C}/^{13}\text{C}]$  being the isotope abundance ratio. Using results presented in Henkel et al. (1982), the abundance ratio was taken to be  $X_{12/13} = 5.5R + 24.2$ , where  $R$  is the galactocentric radius given in kpc. In the case where no  $^{13}\text{CO}$  was detected, we take an upper limit on the  $^{13}\text{CO}$  peak intensity to be the RMS sensitivity of the data ( $\sim 0.7$  K, Burton et al. 2013).

#### 3.2 CS

Transitions in the 7 mm CS(1–0) line gave a complementary probe of the denser gas ( $\overline{n} \gtrsim 10^4 \text{ cm}^{-3}$ , Evans 1999) in regions of interest. The CS(1–0) optical depth

<sup>1</sup><http://www.atnf.csiro.au/computing/software/livedata/>

<sup>2</sup><http://www.atnf.csiro.au/computing/software/miriad/>

was found using the ratio between the CS(1–0) and C<sup>34</sup>S(1–0) lines in regions where detections were made in C<sup>34</sup>S(1–0). We adopted the [CS]/[C<sup>34</sup>S] ratio of 22.5, and calculated the optical depth via Equation 1 of Zinchenko et al. (1994). Where no C<sup>34</sup>S(1–0) was detected, the CS(1–0) was assumed to be optically thin.

Using Equation 9 from Goldsmith & Langer (1999), together with the optical depth and the integrated line intensity, we calculate the column density of CS(J=1). We assume Local Thermodynamic Equilibrium (LTE) at a rotational temperature of  $T_{\text{rot}} = 10$  K, typical of cold and dense molecular clouds, to convert the column density of CS(J=1) to total CS column density,  $N_{\text{CS}}$ . Here,  $N_{\text{CS}}$  is  $\sim 3.5$  times the CS(J=1) column density. A small systematic error in  $N_{\text{CS}}$  is produced by this temperature assumption ( $\sim 20\%$  for a 50% change in  $T_{\text{rot}}$ ).

We note that the abundance ratio between molecular hydrogen and CS molecules in dense molecular clumps can vary by an order of magnitude between  $10^{-9}$  and  $10^{-8}$  (Irvine et al. 1987). In this work, we adopt the CS to H<sub>2</sub> abundance ratio  $X_{\text{CS}} \sim 1 \times 10^{-9}$  (Frerking et al. 1980) which is typical of dense quiescent gas. As such the calculated gas parameters presented here should be considered as upper limits.

### 3.3 HI

HI data towards HESS J1614–518 and HESS J1616–508 was obtained from the Southern Galactic Plane Survey (SGPS) (McClure-Griffiths et al. 2005). The column density of atomic HI,  $N_{\text{HI}}$ , was calculated via the relation  $\overline{N}_{\text{HI}} = X_{\text{HI}} W_{\text{HI}}$ , where  $W_{\text{HI}}$  is the integrated HI intensity and the conversion factor  $X_{\text{HI}} = 1.823 \times 10^{18} \text{ cm}^{-2} (\text{K kms}^{-1})^{-1}$  (Dickey & Lockman 1990). Combining this with the molecular hydrogen column density,  $N_{\text{H}_2}$ , we are able to estimate the total hydrogen column density as  $N_{\text{H}} = N_{\text{HI}} + 2N_{\text{H}_2}$ .

## 4 Results

The distribution of the ISM towards HESS J1614–518 and HESS J1616–508 is presented in this section. We consider the morphology of the gas towards each TeV source separately. <sup>12</sup>CO(1–0) and <sup>13</sup>CO(1–0) line emission data was taken from the Mopra Galactic Plane Survey and was used to study the diffuse molecular hydrogen gas distribution. 7 mm wavelength data from MALT-45 and our targeted 7 mm Mopra observations were used to reveal the denser gas as traced by detections in the CS(1–0) and C<sup>34</sup>S(1–0) lines. Detections in the thermal SiO(J=1–0, v=0) line, which is often excited behind shocks that move through molecular clouds (e.g. Martin-Pintado et al. 1992; Flower et al. 1996), were also found in the dataset.

To estimate the distance to the ISM traced by the line emission, we use the Galactic rotation model from Brand & Blitz (1993) to obtain the kinematic distance, based on the detection velocity along the line-of-sight ( $v_{\text{LSR}}$ ). In the absence of firm evidence to resolve the near/far distance ambiguities, we have assumed the near solution in our calculations as an approximation, as gas closer to us is more likely to be seen.

### 4.1 ISM towards HESS J1614–518

CO(1–0) line emission is seen overlapping HESS J1614–518 in several kinematic velocity intervals along the line-of-sight. Figure 2 displays the average spectra of the <sup>12</sup>CO(1–0) and <sup>13</sup>CO(1–0) emission within the reported root-mean-squared (RMS) extent of HESS J1614–518 as described in Aharonian et al. (2006), which is indicated by the dashed ellipses in Figure 3. Overall, the spectra indicates that there are three main velocity ranges in which emission is prominent;  $v_{\text{LSR}} \sim -50$  to  $-40 \text{ km s}^{-1}$ ,  $v_{\text{LSR}} \sim -75$  to  $-60 \text{ km s}^{-1}$  and  $v_{\text{LSR}} \sim -115$  to  $-90 \text{ km s}^{-1}$ , which we have denoted as components 1, 2, and 3 respectively. Additionally, one minor component of emission is seen in the  $v_{\text{LSR}} \sim -15$  to  $0 \text{ km s}^{-1}$  range, which we denote as component 4. For component 1, there appears to be several blended features in the spectra, and we have chosen the velocity range that encompasses the dominant feature of interest. For the other components, we have chosen velocity ranges that cover all the emission, as the nature and degree of blending is more difficult to discern.

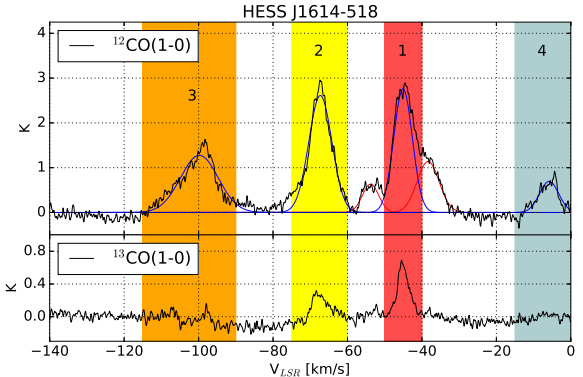


**Figure 2.** The average spectra of <sup>12</sup>CO(1–0) (top) and <sup>13</sup>CO(1–0) (bottom) emission within the RMS extent of HESS J1614–518 as described in Aharonian et al. (2006). The velocity intervals of the components used in the integrated images shown in Figure 3 are indicated by the shaded rectangles. Overlaid blue and red lines are the Gaussian fits to the emission, as described in text.

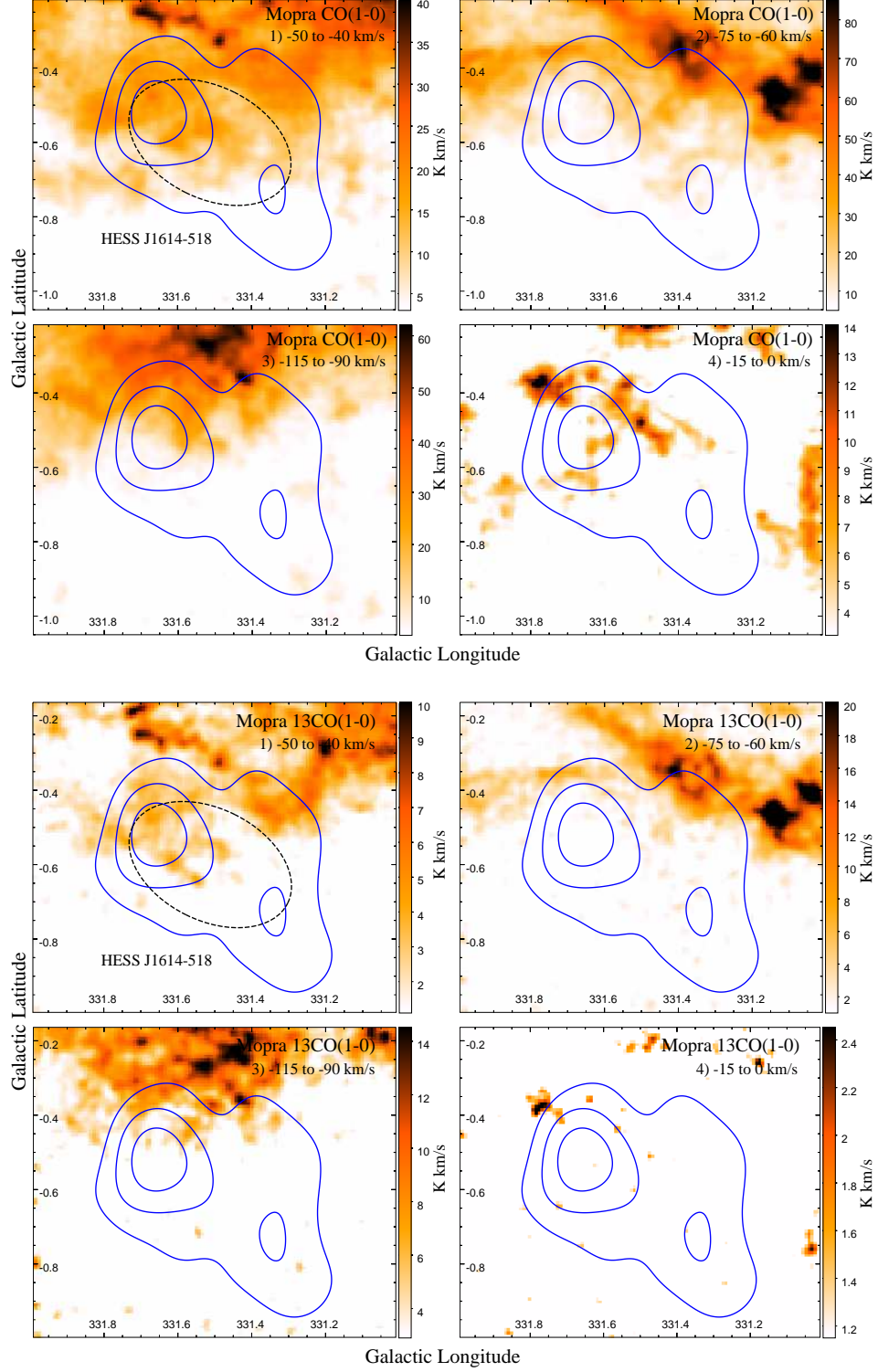


**Figure 3.** Mosaic of  $^{12}\text{CO}(1-0)$  and  $^{13}\text{CO}(1-0)$  integrated intensity images [ $\text{K km s}^{-1}$ ] within the labelled velocity intervals. Overlaid are HESS excess counts contours (blue) towards HESS J1614-518 at the 30, 45 and 60 levels. The dashed black ellipse in the top left panel of both mosaics is the elliptical extent of HESS J1614-518 as described in [Aharanion et al. \(2006\)](#). The average CO(1-0) spectra within this region is displayed in Figure 2.

The  $^{12}\text{CO}(1-0)$  spectrum was fit by a series of Gaussian functions to calculate the mass and density parameters of the molecular gas following §3. Component 1 was fit with three Gaussian functions, as while the dominant feature was blended with features on both the positive and negative velocity sides, each feature is clearly resolvable. We use the Gaussian corresponding to the dominant feature in our calculations to minimise the contamination from the other blended features. For the other components, we cannot resolve the individual features that may be present, and it is unclear to the degree at which blending is occurring. For this reason, we approximate each spectrum using a single Gaussian function. The derived masses and densities from these fits and those obtained by simply integrating the raw spectrum over the velocity ranges differ by less than 10% in all cases. The Gaussian functions used have been overlaid on the  $^{12}\text{CO}(1-0)$  spectrum in Figure 2. Blue functions indicate those that were used in the mass and density calculations for the corresponding labelled components, while red functions are those that were fit to the extra blended features. The parameters of the blue functions as well as the calculated gas parameters are displayed in Table 2.

Figure 3 shows a mosaic of integrated  $^{12}\text{CO}(1-0)$  and  $^{12}\text{CO}(1-0)$  emission images towards HESS J1614–518 in the velocity ranges of each component.

In component 1 ( $v_{\text{LSR}} = -50$  to  $-40 \text{ km s}^{-1}$ ), emission in  $^{12}\text{CO}(1-0)$  is seen overlapping most of HESS J1614–518. This emission appears not to be a localized molecular cloud as it extends North beyond the TeV source as part of widespread  $^{12}\text{CO}(1-0)$  emission. The  $^{13}\text{CO}(1-0)$  emission in this component is seen mainly towards the TeV  $\gamma$ -ray peak, and also extends North beyond the TeV source.

There is some overlap between  $^{12}\text{CO}(1-0)$  emission and HESS J1614–518 in component 2 ( $v_{\text{LSR}} = -75$  to  $-60 \text{ km s}^{-1}$ ), mainly in the Galactic North and Northwest of the TeV source. However, there appears to be very little overlap in the  $^{13}\text{CO}(1-0)$  emission. Two regions of more intense emission are seen clearly in the  $^{12}\text{CO}(1-0)$  and  $^{13}\text{CO}(1-0)$ , appearing at the Galactic North-West edges of HESS J1614–518. That being said, neither of the two features are likely to be associated with the HESS source, as they have no morphological correspondence with  $\gamma$ -ray emission. These features are coincident, and morphologically similar, to the HII regions G331.3-00.3 and G331.1-00.5 which are labelled in Figure 1. It is likely that the CO(1-0) emission here traces gas associated with those HII regions.

The emission in  $^{12}\text{CO}(1-0)$  and  $^{13}\text{CO}(1-0)$  appearing in component 3 ( $v_{\text{LSR}} = -115$  to  $-90 \text{ km s}^{-1}$ ) only overlap a small portion of the TeV source in the Galactic North and North-East regions.

Component 4 ( $v_{\text{LSR}} = -15$  to  $0 \text{ km s}^{-1}$ ) has the weakest CO(1-0) emission feature detected towards HESS J1614–518. Some scattered gas is seen in  $^{12}\text{CO}(1-0)$  which overlaps the Galactic North-East region of the TeV source, while almost no emission is seen in the  $^{13}\text{CO}(1-0)$ .

CS(1-0) line emission traced the dense gas towards HESS J1614–518. Coverage of the TeV source in the northern and southern halves was provided by MALT-45 and Mopra observations respectively. No significant detection in CS(1-0) overlapping the TeV source was found in the MALT-45 dataset. However, inspection of the data obtained from Mopra 7 mm observations revealed a peculiar feature in the narrow velocity range  $v_{\text{LSR}} = -47$  to  $-44 \text{ km s}^{-1}$ . No detections in other 7 mm lines that overlapped HESS J1614–518 were found in the MALT-45 or Mopra datasets.

Figure 4 is an integrated image of CS(1-0) emission in this velocity interval, clearly revealing an open ring of dense gas near the centre of HESS J1614–518, as well as several dense clumps towards the Galactic-east side of the source. Also displayed in Figure 4 are the locations of various objects of interest in the region. Several pulsars, Wolf-Rayet stars and X-ray sources are seen towards HESS J1614–518, with PSR J1614-5144 and the X-ray source Suzaku Src C located on the rim of the dense gas ring. The gas ring is seen within the extent of the stellar cluster Pismis 22.

The panels on the left side of Figure 5 are integrated images of  $^{12}\text{CO}(1-0)$  and  $^{13}\text{CO}(1-0)$  emission in the  $v_{\text{LSR}} = -47$  to  $-44 \text{ km s}^{-1}$  range. The solid green broken annulus encompasses the approximate region in which the open ring in CS appears. The ring feature, while not as pronounced as that seen in CS(1-0), can also be seen in this narrow velocity range in the  $^{12}\text{CO}(1-0)$  and  $^{13}\text{CO}(1-0)$  images.

The panels on the right side of Figure 5 show the average spectra of the CS(1-0),  $^{12}\text{CO}(1-0)$  and  $^{13}\text{CO}(1-0)$  within the green broken annulus and the dashed white ellipses. For the broken annulus spectra, an obvious component is seen in all three tracers centred at  $v_{\text{LSR}} \sim -45 \text{ km s}^{-1}$  (with corresponding kinematic distance  $\sim 3.1 \text{ kpc}$  following Brand & Blitz 1993). The average gas mass and density parameters within the broken annulus were estimated following §3. These values, and the fitted Gaussian parameters to the spectra, are displayed in Table 3. For the broken annulus region, the volume chosen for mass and density calculations was a prism formed by the projection of the broken annulus with depth equal to the average annular radius. We note that the calculated CS parameters should be treated as upper limits, due to the choice of the CS/H<sub>2</sub> abundance ratio (see §3.2).

The properties of diffuse gas appear to be non-uniform about the open ring. Regions 1 and 2, indicated

**Table 2** The parameters of the  $^{12}\text{CO}(1-0)$  line emission and the calculated physical parameters for the gas within the indicated aperture in Figure 3 towards HESS J1614–518. Gaussian fits to the spectra were used to determine the line-of-sight velocity,  $v_{\text{LSR}}$ , line-width (full-width-half-maximum),  $\Delta v_{\text{FWHM}}$ , and peak intensity,  $T_{\text{peak}}$ . The  $^{12}\text{CO}/^{13}\text{CO}$  abundance ratio,  $X_{12/13}$ , and optical depth were found following §3.1. The assumed distances,  $d_0$ , used in mass and density calculations are the near solutions derived from the Galactic rotation curve presented in Brand & Blitz (1993). Calculated mass and density values can be scaled for an arbitrary distance,  $d$ , using a factor of  $(d/d_0)^2$  and  $(d/d_0)^{-1}$  respectively.

Component	Distance (kpc)	$v_{\text{LSR}}$ (km/s)	$\Delta v_{\text{FWHM}}$ (km/s)	$T_{\text{peak}}$ (K)	$X_{12/13}$	Optical depth	$N_{H_2}$ ( $10^{21} \text{ cm}^{-2}$ )	Mass ( $10^4 M_\odot$ )	$\bar{n}$ ( $10^2 \text{ cm}^{-3}$ )
1	3.1	−45.1	5.9	2.8	57.0	12.6	2.6	1.9	1.8
2	4.3	−67.3	7.3	2.7	52.5	5.6	3.1	4.3	1.5
3	5.9	−99.8	12.0	1.3	48.1	0.1	2.5	6.5	0.9
4	0.4	−5.8	6.1	0.7	69.0	0.1	0.7	0.01	3.6

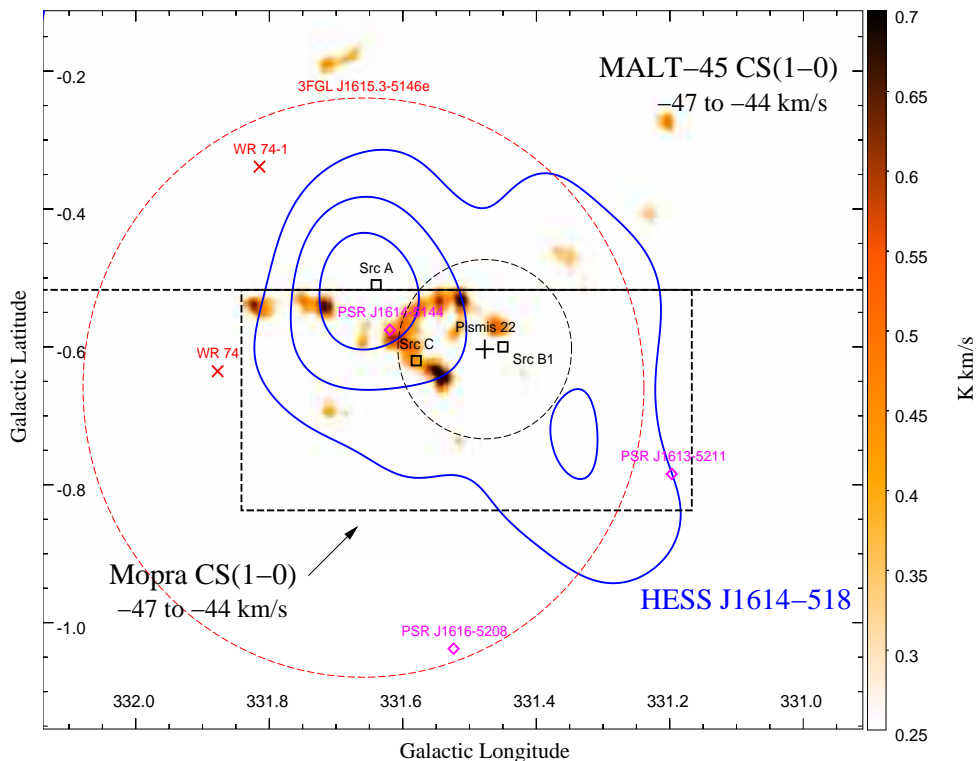


**Figure 4.** CS(1–0) integrated intensity image [ $\text{K km s}^{-1}$ ] between  $-47$  and  $-44 \text{ km s}^{-1}$ . Overlaid blue contours are HESS excess counts contours towards HESS J1614–518 at the 30, 45 and 60 levels (Aharonian et al. 2006). Purple diamonds indicate positions of known pulsars (Manchester et al. 2005). Wolf-Rayet stars WR 74 (van der Hucht 2001) and WR 74-1 (Mauerhan et al. 2011) are shown as red X’s. The 95% confidence region of the Fermi source 3FGL J1615.3–5146e is marked as a dashed red circle (Acero et al. 2015). The centre and extent of the open stellar cluster Pismis 22 is shown as a black plus and dashed circle respectively (Kharchenko et al. 2013). The positions of the X-ray sources Suzaku Src A, XMM-Newton Src B1 and Suzaku Src C are indicated as black squares (Matsumoto et al. 2008; Sakai et al. 2011). The large dashed black rectangle is the extent of the 7mm observations carried out by Mopra. The regions above this rectangle in this image was covered by MALT-45 (Jordan et al. 2015).

in Figure 5, are apertures containing two of the brightest regions of the ring. Their spectra show very similar features in CS(1–0) and  $^{13}\text{CO}(1-0)$  emission. However, the  $^{12}\text{CO}(1-0)$  emission is significantly reduced in region 1 compared with region 2. The gas parameters for these regions are displayed in Table 3. The contrast between the  $^{12}\text{CO}$  and  $^{13}\text{CO}$  line ratios between regions 1

and 2 are reflected in the  $\sim 5\times$  difference in calculated  $^{12}\text{CO}$  optical depth. The difference in optical thickness about the ring may be caused by variations in the physical properties, such as temperature and density, of the local gas.

Region 3 encloses dense gas clumps seen in CS(1–0) in the Galactic-east of HESS J1614–518. The emission

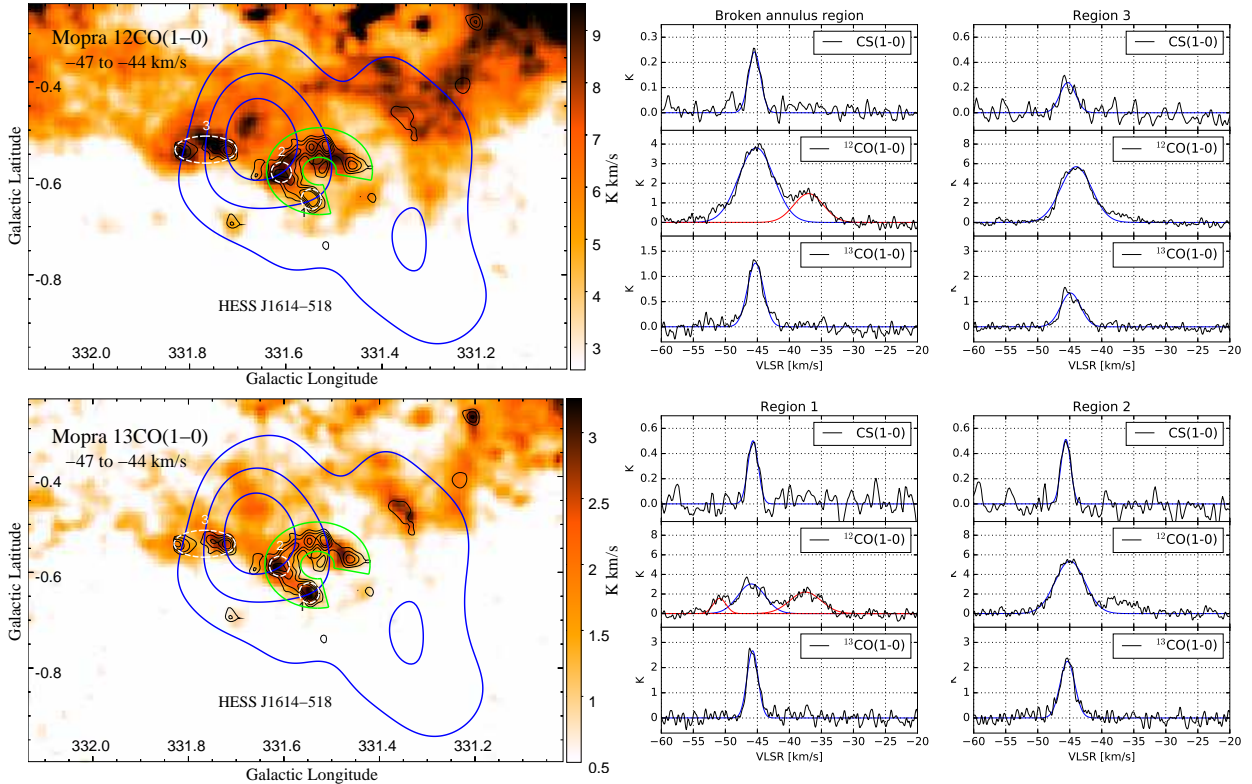


**Figure 5.** Left:  $^{12}\text{CO}(1-0)$  and  $^{13}\text{CO}(1-0)$  integrated intensity images [ $\text{K km s}^{-1}$ ] between  $-47$  and  $-44 \text{ km s}^{-1}$ . Overlaid are the CS(1-0) emission contours (black) in the same velocity interval and the HESS excess counts contours (blue) (Aharonian et al. 2006). The solid green broken annulus indicates the region in which an open ring feature is seen clearly in the CS emission. White dashed ellipses indicate additional regions in which spectra were extracted from. Right: Solid black lines are the average emission spectra for CS(1-0),  $^{12}\text{CO}(1-0)$  and  $^{13}\text{CO}(1-0)$  within the broken annulus and 3 additional regions indicated in the left panels. The blue lines indicate the Gaussian functions that were used to parametrise the emission. The fit parameters are displayed in Table 3. The red lines are additional Gaussian fits to unrelated gas components seen at different  $v_{\text{LSR}}$ .

seen in the spectra for this region is similar to that in the open ring regions in that it is centred at the same kinematic velocity of  $\sim -45 \text{ km s}^{-1}$ . The average gas mass and density parameters for this region is also displayed in Table 3.

#### Column density towards X-ray sources

X-ray observations towards HESS J1614–518 with *Suzaku* and *XMM-Newton* have revealed the presence of several X-ray sources as mentioned in §1. The positions of the *Suzaku* sources Src A, Src B and Src C are shown in Figure 4. The X-ray spectrum of *Suzaku* Src A is well fit by an absorbed power-law model with a hydrogen column density of  $N_{\text{H}} = 1.21^{+0.50}_{-0.41} \times 10^{22} \text{ cm}^{-2}$  (Matsumoto et al. 2008). The spectrum of *XMM-Newton* Src B1, thought to be the main component of *Suzaku* Src B, is described by either an absorbed power-law or an absorbed blackbody model with  $N_{\text{H}} = 2.4^{+0.4}_{-0.4} \times 10^{22} \text{ cm}^{-2}$  and  $N_{\text{H}} = 1.1^{+0.3}_{-0.2} \times 10^{22} \text{ cm}^{-2}$  respectively (Sakai et al. 2011). *Suzaku* Src

C is a late type B star and would not be a counterpart to HESS J1614–518.

In order to constrain the distance to *Suzaku* Src A and *XMM-Newton* Src B1, we extracted the average spectra from the  $^{12}\text{CO}(1-0)$  and HI line data within the X-ray source extents as given in Matsumoto et al. (2008) and Sakai et al. (2011). Integrating the emission spectra allows us to calculate  $N_{\text{H}}$  by following §3, and we are then able to find the total cumulative  $N_{\text{H}}$  as a function of  $v_{\text{lsr}}$ . Here, we assume that the gas traced by  $^{12}\text{CO}(1-0)$  and HI emission is located at the near distance.

In Figure 6, we plot the total cumulative  $N_{\text{H}}$  towards *Suzaku* Src A and *XMM-Newton* Src B1 against  $v_{\text{lsr}}$  as a solid black line. We also plot the cumulative  $N_{\text{H}_2}$  and  $N_{\text{H}}$  that was found using  $^{12}\text{CO}(1-0)$  and HI line emission. The shaded regions indicate the values of  $N_{\text{H}}$  that was required to fit the X-ray spectra with an absorbed power-law model (cyan) and an absorbed blackbody model (pink; Src B1 only).

**Table 3** Line parameters for the CS(1–0),  $^{12}\text{CO}(1–0)$  and  $^{13}\text{CO}(1–0)$  emission component at  $v_{\text{LSR}} \sim -45 \text{ km s}^{-1}$  in the broken annulus and additional region apertures indicated in the left panels of Figure 5 towards HESS J1614–518. Gaussian fits to the component seen in the spectra (blue functions in the right panels of Figure 5) were used to find  $v_{\text{LSR}}$ ,  $\Delta v_{\text{FWHM}}$  and  $T_{\text{peak}}$ . Corresponding calculated gas parameters for the regions are also displayed, which were calculated following §3. The CS parameters should be treated as upper limits (see §3.2). Distance for all calculations has been assumed to be 3.1 kpc. The  $^{12}\text{CO}/^{13}\text{CO}$  abundance ratio,  $X_{12/13}$ , at this distance was taken to be 57.0 (see §3.1).

Region	Tracer	$v_{\text{LSR}}$ (km/s)	$\Delta v_{\text{FWHM}}$ (km/s)	$T_{\text{peak}}$ (K)	Optical depth	$N_{H_2}$ ( $10^{21} \text{ cm}^{-2}$ )	Mass ( $M_{\odot} \times 10^3$ )	$\bar{n}$ ( $10^2 \text{ cm}^{-3}$ )
Broken annulus	CS(1–0)	-45.5	2.4	0.2		9.5	8.4	11.0
	$^{12}\text{CO}(1–0)$	-45.1	6.4	3.6	18.1	3.9	4.9	6.4
	$^{13}\text{CO}(1–0)$	-45.3	2.8	1.1		2.0	2.4	3.2
1	CS(1–0)	-45.7	1.9	0.5		9.3	0.6	40.1
	$^{12}\text{CO}(1–0)$	-46.0	4.9	3.0	50.3	2.4	0.2	14.8
	$^{13}\text{CO}(1–0)$	-45.8	2.1	2.7		2.9	0.3	18.6
2	CS(1–0)	-45.6	1.6	0.5		8.8	0.6	38.0
	$^{12}\text{CO}(1–0)$	-45.0	5.4	5.4	11.7	4.8	0.4	29.0
	$^{13}\text{CO}(1–0)$	-45.4	2.6	2.3		3.2	0.3	19.5
3	CS(1–0)	-45.3	2.8	0.2		6.8	1.7	14.5
	$^{12}\text{CO}(1–0)$	-44.0	5.7	5.7	8.5	5.3	1.9	16.1
	$^{13}\text{CO}(1–0)$	-44.9	3.8	1.3		2.7	1.0	8.3

For Src A, the required  $N_{\text{H}}$  for the absorbed power-law model occurs in the  $v_{\text{lsr}}$  range of  $\sim -37$  to  $-47 \text{ km s}^{-1}$ , corresponding to a distance of  $\sim 2.6$  to  $3.2 \text{ kpc}$  (Brand & Blitz 1993). The  $N_{\text{H}}$  needed for the Src B1 absorbed power-law model falls in the  $v_{\text{lsr}} \sim -50$  to  $-67 \text{ km s}^{-1}$  range, with associated kinematic distance of  $\sim 3.4$  to  $4.3 \text{ kpc}$ . The  $N_{\text{H}}$  requirement for the absorbed blackbody model for Src B1 occurs in the  $v_{\text{lsr}} \sim -36$  to  $-43 \text{ km s}^{-1}$  range, which corresponds to a distance of  $\sim 2.6$  to  $3.0 \text{ kpc}$ .

A distance of 10 kpc was assigned to Suzaku Src A and XMM-Newton Src B1 (Matsumoto et al. 2008; Sakai et al. 2011) based on the comparisons between the best-fit hydrogen column density and the total Galactic HI column density ( $\sim 2.2 \times 10^{22} \text{ cm}^{-2}$ , Dickey & Lockman 1990). The blackbody model was assumed for Src B1 in this case, as it returned similar  $N_{\text{H}}$  values as that in the Src A model. In this section, we have considered the contributions to the total column density from both atomic and molecular hydrogen gas (traced by HI and CO(1–0) respectively). This allowed for a more accurate estimation of the column density along the line-of-sight, and hence a better estimate of the distance towards these X-ray sources. If it is the case that Src A is physically related to Src B1, as alluded to in Sakai et al. (2011), then by assuming the blackbody model for Src B1 we estimate a distance of  $\sim 3 \text{ kpc}$  to both sources, based on the hydrogen column density requirements.

## 4.2 ISM towards HESS J1616–508

Figure 7 displays the average  $^{12}\text{CO}(1–0)$  and  $^{13}\text{CO}(1–0)$  spectra within the reported RMS extent of HESS J1616–508 (Aharonian et al. 2006), which is indicated by the black dashed circles in Figure 8. Various features along the line of sight in the diffuse gas traced by CO(1–0) emission is seen overlapping HESS J1616–508, with multiple broad components between  $-120$  and  $0 \text{ km s}^{-1}$  appearing in the spectra. We have divided the spectra into five velocity components in which emission is prominent. These components are indicated by the shaded rectangles and labelled numerically in Figure 8.

The features in components 1 through 4 appear to be somewhat blended together, and so we have chosen velocity ranges in which the dominant feature of interest is seen. The spectra for component 5 appears to be composed of several features that overlap and blend together, likely as a result of the line-of-sight being down the tangent of the Norma spiral arm. As we cannot discern an obvious dominant feature, we have chosen a velocity range over all the emission for this component as a first-look approximation.

A series of Gaussian functions were fit to the  $^{12}\text{CO}(1–0)$  spectrum in order to calculate the mass and density parameters of the molecular gas following §3. The dominant features in components 1 to 4 appeared have some overlap, yet they are very obviously resolvable. Hence we fit Gaussian functions in order to minimise the effects of cross-contamination. We note

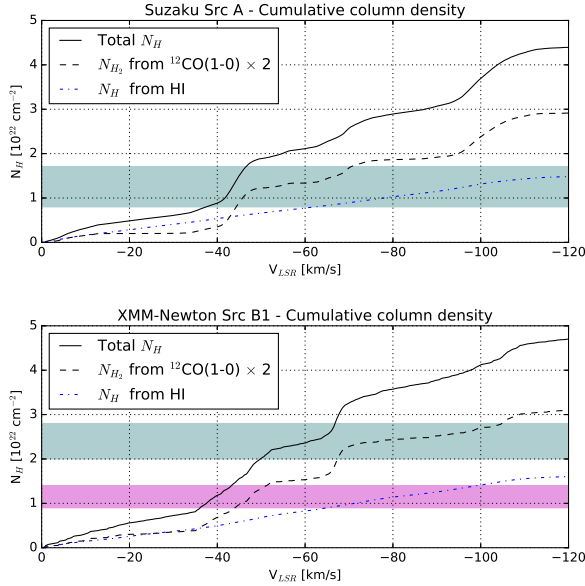


**Figure 6.** Total cumulative hydrogen column density  $N_H$  as a function of  $v_{LSR}$  (solid lines) towards the X-rays sources Suzaku Src A (top) and XMM-Newton Src B1 (bottom) which overlap HESS J1614–518. The cumulative molecular and atomic hydrogen column densities, calculated from CO(1–0) and HI data, are shown as dashed and dot-dashed lines respectively. The cyan shaded regions indicate the  $N_H$  that were used to fit the spectra of the X-rays sources with absorbed power-law models (Matsumoto et al. 2008; Sakai et al. 2011). The pink shaded region indicates the  $N_H$  used in the absorbed blackbody model to fit XMM-Newton Src B1 (Sakai et al. 2011).

that to remove contamination from the extra tail of emission seen towards more positive velocities in component 1, one extra Gaussian function was used in the fitting process. Component 5 appears to consist of at least three or more blended emission features which we cannot resolve. In this case, we roughly approximate the entire emission of component 5 as a single Gaussian function. The fitted Gaussian functions are overlaid on the  $^{12}\text{CO}(1-0)$  spectrum in Figure 7. Blue functions indicate those that were used in the mass and density calculations for the corresponding labelled components. The red function was the Gaussian used to fit the extra tail of emission near component 1. The parameters of the blue Gaussian functions as well as the calculated gas parameters for each component are displayed in Table 4.

Figure 8 shows a mosaic of the integrated  $^{12}\text{CO}(1-0)$  and  $^{13}\text{CO}(1-0)$  emission images towards HESS J1616–508 over the velocity ranges of each component.

In the integrated emission image corresponding to component 1 ( $-47$  to  $-39 \text{ km s}^{-1}$ ), the molecular gas appears to overlap HESS J1616–508. The gas extends

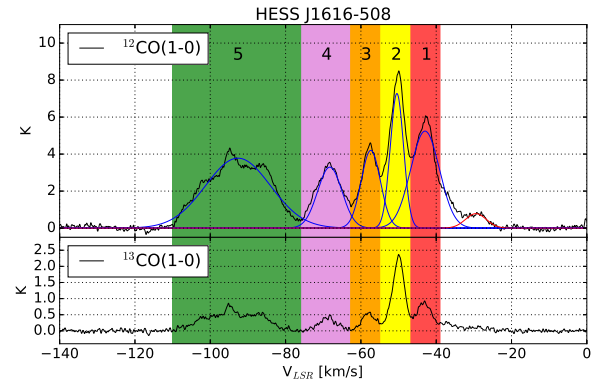


**Figure 7.** The average spectra of  $^{12}\text{CO}(1-0)$  and  $^{13}\text{CO}(1-0)$  emission within the RMS extent of HESS J1616–508 as described in Aharonian et al. (2006). The velocity intervals of the components used in the integrated images shown in Figure 8 are indicated by the shaded rectangles. Overlaid blue and red lines are the Gaussian fits to the emission, as described in text.

past the TeV source somewhat in all directions. Interestingly, there appears to be a dip in the  $^{12}\text{CO}(1-0)$  emission towards the peak of the TeV emission. The void/dip is much more clearly pronounced in the corresponding integrated  $^{13}\text{CO}(1-0)$  emission image. Additionally, there seems to be a thin line of emission extending to the Galactic-east from the peak of the TeV emission which appears more prominently in  $^{13}\text{CO}(1-0)$  emission. The intensity of the  $^{13}\text{CO}(1-0)$  emission along the thin line appears fairly consistent. However, the intensity of the  $^{12}\text{CO}(1-0)$  emission varies, with weaker emission towards the Galactic-east portion of the line, and more intense emission seen in a clump towards the Galactic-west portion. This contrast between the  $^{12}\text{CO}$  and  $^{13}\text{CO}$  line ratios suggests that the  $^{12}\text{CO}$  is more optically thick in the Galactic-east portion of the line feature compared to the clump towards the Galactic-west.

The clump at the Galactic-east end of the line feature is spatially coincident with the HII region G332.5-00.1 (see Figure 1). The systematic velocity of the HII region is  $\sim -46 \text{ km s}^{-1}$  (Bronfman et al. 1996), consistent with the velocity of the gas. This suggests that the gas clump in component 1 may be associated with this HII region.

Component 2 ( $-55$  to  $-47 \text{ km s}^{-1}$ ) has the strongest feature in the CO spectra. A loop of gas overlaps the TeV source which cuts through the centre of HESS J1616–508 before looping up and back on itself through the Galactic-north segment.

The morphology of the gas seen in component 3 ( $-62$  to  $-55 \text{ km s}^{-1}$ ) is patchwork-like, with several regions of gas dispersed mainly in the Galactic-southern parts of HESS J1616–508.

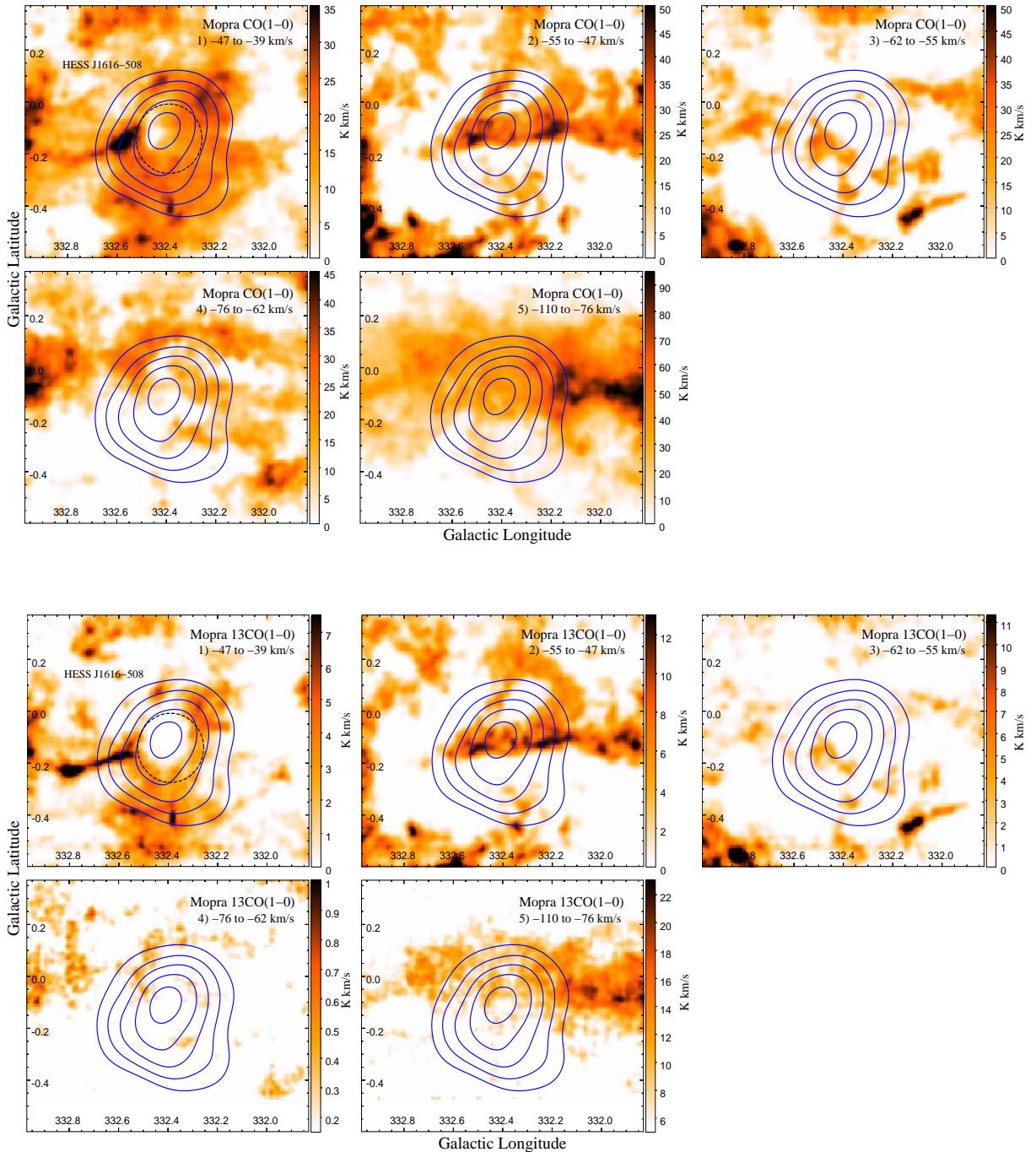


**Figure 8.** Mosaic of  $^{12}\text{CO}(1-0)$  (Top) and  $^{13}\text{CO}(1-0)$  (Bottom) integrated intensity images [ $\text{K km s}^{-1}$ ] within the labelled velocity intervals towards HESS J1616–508. Overlaid are HESS excess counts contours (blue) at the 30, 45, 60, 75 and 90 levels, and the dashed black circle in the top left panel of both mosaics is the RMS extent of HESS J1616–508 (Aharonian et al. 2006). The average CO(1–0) spectra within this region is displayed in Figure 7.

There is less defined structure in the integrated images of components 4 and 5 ( $-76$  to  $-62 \text{ km s}^{-1}$  and  $-110$  to  $-76 \text{ km s}^{-1}$  respectively). Gas is seen overlapping HESS J1616–508 in both component 4 and 5, and appear to extend further towards the Galactic-east and Galactic-west. As mentioned before, the spectra for component 5 is very broad ( $\sim 34 \text{ km s}^{-1}$ ) and appears to be composed of several features that overlap and blend together. It is likely that the broad emission here is the result of the sight-line being down the tangent of the Norma spiral arm, and as such there is difficulty in discerning whether these features are physically connected or not.

Dense gas was traced towards HESS J1616–508 using CS(1–0) emission from the MALT-45 7 mm survey. CS(1–0) emission is seen overlapping the TeV source in the velocity range  $\sim -55$  to  $-45 \text{ km s}^{-1}$ , which corresponds to component 2 in the CO(1–0) emission. The left panel of Figure 9 is a integrated image of CS(1–0) emission over said velocity ranges. The morphology of the emission matches very well with the CO(1–0) emission in component 2. This suggests that the CS is tracing the dense molecular gas embedded in the inner region of the loop structure traced in CO.

A large fraction of the loop feature cuts across HESS J1616–508. The solid green rectangle in the left panel of Figure 9 (labelled ‘A’) is the approximate region of where CS(1–0) emission in this loop overlaps the TeV source. Detection in the isotopologue transition C<sup>34</sup>S(1–0) was also made within this region. The top right panel of Figure 9 shows the average spectra of the CS(1–0), C<sup>34</sup>S(1–0), <sup>12</sup>CO(1–0) and <sup>13</sup>CO(1–0) emission extracted from the green rectangular aperture. A significant feature is seen in all three tracers centred at  $v_{\text{LSR}} \sim -49 \text{ km s}^{-1}$ , which corresponds to a kinematic distance of  $\sim 3.4 \text{ kpc}$  (following Brand & Blitz 1993). Using these spectra, the average gas mass and density parameters for this region were calculated following §3. The Gaussian function parameters used to fit the spectra and the calculated gas parameters are displayed in Table 5. For these mass and density calculations, the geometry of the assumed volume was a prism with depth equal to the smaller side of the rectangle. The calculated CS parameters should be treated as upper limits, due to the choice of the CS/H<sub>2</sub> abundance ratio (see §3.2).

Emission in the SiO(1–0,  $v=0$ ) line was found in a small region labelled ‘B’ in the left panel of Figure 9 at the same velocity as the loop feature ( $\sim -49 \text{ km s}^{-1}$ ). The average SiO spectrum within this region is shown in the bottom-right panel of Figure 9.

An IR dark cloud is seen in the *Spitzer* GLIMPSE data with similar morphology to the ‘hook’ region of the gas loop feature towards the Galactic North-West of HESS J1616–508. IR emission in the ‘bar’ region of the gas loop that cuts through the TeV source suggest

regions of star formation activity. The SiO emission in region B indicates a shocked region, likely due to recent star formation. A more detailed analysis and discussion of this gas loop feature focusing particularly on the star formation activity will be presented in an upcoming paper (Romano et al. 2017 *in prep*).

## HI data

HI data was available towards HESS J1614–518 and HESS J1616–508 from the SGPS (McClure-Griffiths et al. 2005) which was used to study the distribution of atomic gas towards the TeV sources. Using the same velocity intervals where components of emission were seen in the CO data (see Figures 3 and 8), integrated HI maps were generated. These integrated maps can be seen in the appendix Figures A2 and A3. Also displayed in these figures are the average HI emission spectra within the extents of HESS J1614–518 and HESS J1616–508.

The integrated HI images towards HESS J1614–518 show no obvious morphological features overlapping or anti-correlating the TeV source. In the integrated HI image towards HESS J1616–508 for component 1 ( $-47$  to  $-39 \text{ km s}^{-1}$ ), a relative increase in the amount of emission is seen towards the central peak of the TeV source. This is anti-correlated with the void observed in CO(1–0) emission in the same velocity interval. There also appears to be a localised region of diminished emission to the Galactic-east of the TeV peak, which is coincident with the clump at the end of the line feature seen in CO (Figure 8, see §4.2). In component 5 ( $-110$  to  $-76 \text{ km s}^{-1}$ ), a region of more intense HI emission is seen in the Galactic-southeast portion of HESS J1614–518. This feature does not appear in the molecular gas data.

A broken ring-like feature of diminished HI brightness temperature is seen towards the northern part of HESS J1616–508 in all of integrated images except in component 4 ( $-76$  to  $-62 \text{ km s}^{-1}$ ). This feature is likely associated with SNR Kes 32 as it is both positionally coincident and morphologically similar. Inspection of the HI data shows that this feature appears in several negative velocities up to  $\sim -90 \text{ km s}^{-1}$ . If this HI feature is associated with Kes 32, it would imply a distance of at least  $\sim 5.3 \text{ kpc}$  to the SNR (using the rotation curve in Brand & Blitz 1993).

## HEAT [CI] data

Data in the atomic carbon [CI] ( $J=2-1$ ) line towards HESS J1616–508 was available in the second data release (DR2) from the High Elevation Antarctic Terahertz (HEAT) telescope<sup>3</sup>.

<sup>3</sup><http://soral.as.arizona.edu/heat/>

**Table 4** The parameters of the  $^{12}\text{CO}(1-0)$  line emission and the calculated physical parameters for the gas within the indicated RMS extent of HESS J1616–508 in Figure 8. Gaussian fits to the spectra were used to determine the line-of-sight velocity,  $v_{\text{LSR}}$ , line-width (full-width-half-maximum),  $\Delta v_{\text{FWHM}}$ , and peak intensity,  $T_{\text{peak}}$ . The  $^{12}\text{CO}/^{13}\text{CO}$  abundance ratio,  $X_{12/13}$ , and optical depth were found following §3.1. The assumed distances,  $d_0$ , used in mass and density calculations are the near solutions derived from the Galactic rotation curve presented in Brand & Blitz (1993). Calculated mass and density values can be scaled for an arbitrary distance,  $d$ , using a factor of  $(d/d_0)^2$  and  $(d/d_0)^{-1}$  respectively.

Component	Distance (kpc)	$v_{\text{LSR}}$ (km/s)	$\Delta v_{\text{FWHM}}$ (km/s)	$T_{\text{peak}}$ (K)	$X_{12/13}$	Optical depth	$N_{\text{H}_2}$ ( $10^{21} \text{ cm}^{-2}$ )	Mass ( $M_{\odot} \times 10^4$ )	$\bar{n}$ ( $10^2 \text{ cm}^{-3}$ )
1	3.0	-43.0	8.9	5.3	57.1	8.7	7.7	2.7	7.4
2	3.5	-50.4	4.2	7.4	55.3	17.0	4.9	2.3	4.2
3	3.8	-57.4	6.1	4.3	53.0	6.6	4.1	2.3	3.1
4	4.4	-68.3	7.5	3.4	51.9	6.4	4.1	3.0	2.7
5	5.6	-92.6	20.3	3.8	48.4	7.8	12.4	14.8	6.5

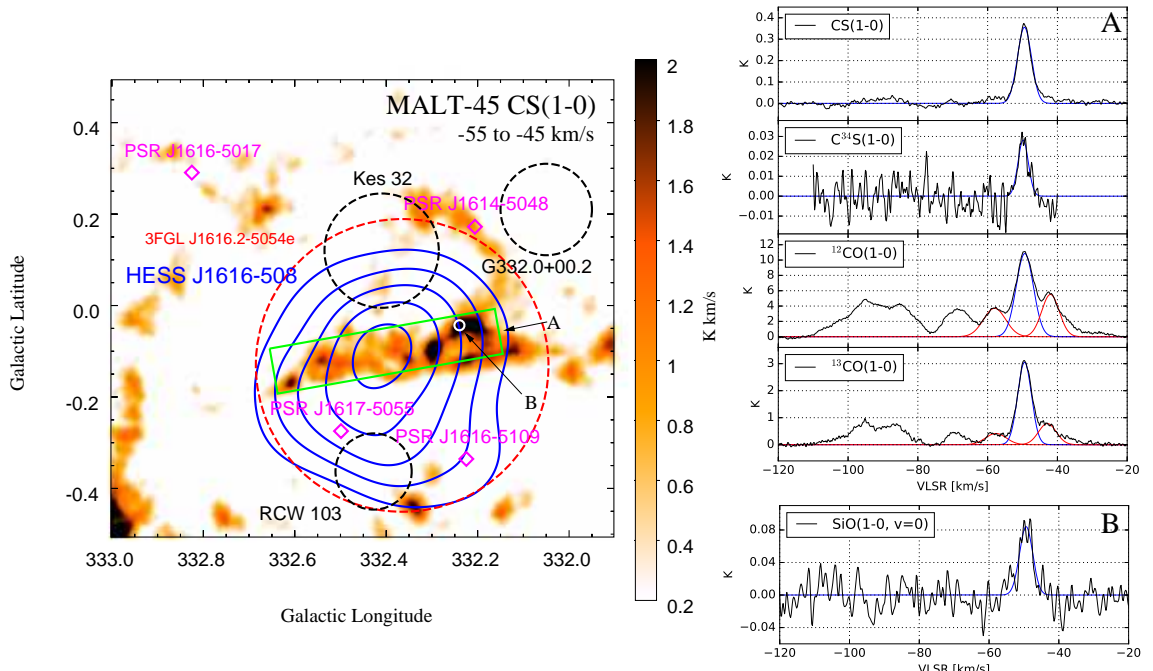


**Figure 9.** Left: CS(1–0) integrated intensity image [ $\text{K km s}^{-1}$ ] between  $-55$  and  $-45 \text{ km s}^{-1}$  towards HESS J1616–508. Overlaid blue contours are HESS excess counts contours at the 30, 45, 60, 75 and 90 levels (Aharonian et al. 2006). The 95% confidence region of the Fermi source 3FGL J1616.2–5054e is marked as a dashed red circle (Acero et al. 2015). Purple diamonds indicate positions of known pulsars (Manchester et al. 2005), and black dashed circles indicate extent of known SNRs in the region (Green 2014). The solid green rectangle indicates the region of the loop feature seen in CS(1–0) emission that cuts horizontally through the TeV source. Top right: Average emission spectra (black) for CS(1–0),  $\text{C}^{34}\text{S}(1-0)$ ,  $^{12}\text{CO}(1-0)$  and  $^{13}\text{CO}(1-0)$  within the green rectangular region (region ‘A’) indicated in the left panel. Blue lines indicate Gaussian functions used to parametrise the emission seen in the  $\sim -55$  to  $-45 \text{ km s}^{-1}$  velocity range. Fit parameters are displayed in Table 5. Red lines indicate Gaussian fits to other gas components seen in nearby velocities. Bottom-right: Average  $\text{SiO}(1-0, v=0)$  spectrum in the small circular aperture labelled ‘B’ in the left panel.

While the standard tracer of molecular hydrogen gas is CO, the abundance of the CO can be greatly reduced due to photo-dissociation by far-UV radiation and interactions with CRs (e.g. Bolatto et al. 2013) in the outer envelopes of molecular cloud structures. The carbon in these outer envelopes will then exist as C or  $\text{C}^+$ . Emission from neutral atomic carbon, [CI], generally occurs in gas where molecular hydrogen exists without signif-

icant CO, and thus [CI] is a good tracer for molecular gas that is “dark” to standard survey techniques (e.g. Burton et al. 2015 and references within).

Figure A1 in the appendix displays a series of integrated [CI] emission images in the same velocity intervals as that in Figure 8. The bottom-right panel of Figure A1 shows the [CI] spectra (in blue) within the reported RMS extend of HESS J1616–508.

**Table 5** CS(1–0), C<sup>34</sup>S(1–0), <sup>12</sup>CO(1–0) and <sup>13</sup>CO(1–0) line parameters for the emission feature at  $v_{\text{LSR}} \sim -49 \text{ km s}^{-1}$  within the green rectangular aperture indicated in the left panel of Figure 9. Gaussian fits to the component seen in the spectra (blue functions in the right panels of Figure 9) were used to find  $v_{\text{LSR}}$ ,  $\Delta v_{\text{FWHM}}$  and  $T_{\text{peak}}$ . Corresponding calculated gas parameters for the region are also displayed, calculated following §3. The CS parameters should be treated as upper limits (see §3.2). Distance for the calculations has been assumed to be 3.4 kpc. Following §3.1, the <sup>12</sup>CO/<sup>13</sup>CO abundance ratio,  $X_{12/13}$ , at this distance was taken to be 55.5.

Tracer	$v_{\text{LSR}}$ (km/s)	$\Delta v_{\text{FWHM}}$ (km/s)	$T_{\text{peak}}$ (K)	Optical depth	$N_{H_2}$ ( $10^{21} \text{ cm}^{-2}$ )	Mass ( $M_{\odot} \times 10^4$ )	$\bar{n}$ ( $10^2 \text{ cm}^{-3}$ )
CS(1–0)	-49.5	4.7	0.36	1.3	29.4	8.4	18.9
C <sup>34</sup> S(1–0)	-49.8	3.5	0.028				
<sup>12</sup> CO(1–0)	-49.3	5.9	10.9	12.5	10.1	4.0	9.1
<sup>13</sup> CO(1–0)	-49.4	4.7	3.0		7.4	3.0	6.7

The beamsize of HEAT [CI] (2'.5) is relatively larger compared with that of Mopra CO (0'.6). However, while intricate comparisons between the [CI] and CO are unavailable, the same general distribution and morphology is seen in both HEAT [CI] and Mopra CO data. In particular, the void feature towards the peak of the TeV source and the region of more intense emission extending to the Galactic-east, seen in component 1 of the CO emission can also be identified in the [CI]. Similarly, the extended loop feature in component 2 of the CO emission is also clearly visible in the [CI]. There are no obvious discrepancies between the [CI] and CO emission.

Future investigation using the data may be able to reveal the fraction of “dark” gas traced by [CI] that is not seen by the conventional CO tracers.

## 5 Discussion

The mechanisms behind the production of TeV  $\gamma$ -rays seen from HESS J1614–518 and HESS J1616–508 are unclear, as alluded to in §1, and are a key question in unravelling the nature of these sources. In the following section, we discuss the implications of our interstellar gas study on the different origin scenarios of HESS J1614–518 and HESS J1616–508. The same general methods employed here were applied to another pair of TeV  $\gamma$ -ray sources, HESS J1640–465 and HESS J1641–463, in [Lau et al. \(2017\)](#).

### 5.1 Hadronic production of TeV $\gamma$ -rays

Gas that was traced in this study along the line of sight towards HESS J1614–518 and HESS J1616–508 may be acting as potential targets for accelerated CRs, producing TeV  $\gamma$ -rays in hadronic p-p interactions. In [Aharonian \(1991\)](#), a relationship between the flux of  $\gamma$ -rays and the mass and distance of the target material was derived. Above some energy  $E_{\gamma}$ , the expected  $\gamma$ -ray flux is given by:

$$F(\geq E_{\gamma}) = 2.85 \times 10^{-13} E_{\gamma}^{-1.6} \left( \frac{M_5}{d_{kpc}^2} \right) k_{CR} \text{ cm}^{-2} \text{s}^{-1} \quad (2)$$

where the CR-target material mass,  $M_5$ , is given in units of  $10^5 M_{\odot}$ , the distance to the material,  $d_{kpc}$ , is given in kpc, the minimum energy of  $\gamma$ -rays,  $E_{\gamma}$ , is given in TeV, and where the parameter  $k_{CR}$  is the CR enhancement factor above that observed at Earth. The above equation assumes that the target ISM is located some distance from the CR source. The spectrum of CRs, an  $E^{-1}$  integral power law at the accelerator, would have steepened to an  $E^{-1.6}$  spectrum due to diffusion in transport.

From [Aharonian et al. \(2006\)](#), the  $\gamma$ -ray flux is  $F(\geq 200 \text{ GeV}) = 57.8 \times 10^{-12} \text{ cm}^{-2} \text{s}^{-1}$  for HESS J1614–518, and  $F(\geq 200 \text{ GeV}) = 43.3 \times 10^{-12} \text{ cm}^{-2} \text{s}^{-1}$  for HESS J1616–508.

The sum of the molecular and atomic gas, as traced by CO(1–0) and HI respectively, was taken to be the total amount of CR-ray target material. We use this total mass of atomic and molecular gas seen in each ‘component’, as described in §4, to calculate the required CR enhancement factors  $k_{CR}$ . We note that  $k_{CR}$  is effectively independent of any distance assumptions as the distance term of Equation 2 is cancelled out by the distance terms used in the mass calculations. The calculated  $k_{CR}$  values are displayed in Table 6, and are discussed in more detail in §5.3 and §5.4. We find that the dominant contribution ( $\sim 70 - 90\%$ ) to the total gas mass in each component is from the molecular gas portion. We note that the  $k_{CR}$  values presented are applicable to  $\gamma$ -rays with energy  $E_{\gamma} > 200 \text{ GeV}$ , corresponding to CRs with energies  $E_p \gtrsim 1 \text{ TeV}$ . As such, any CR energetics are to be treated as lower limits on the total CR energy.

If we consider a hadronic scenario for HESS J1614–518 and HESS J1616–508, the total CR energy budget,  $W_p$ , can be expressed by the relation  $W_p = L_{\gamma} \tau_{pp}$ , where  $L_{\gamma}$  is the  $\gamma$ -ray luminosity. The cooling time of CR protons,  $\tau_{pp}$ , via proton-

**Table 6** Cosmic-ray enhancement values,  $k_{\text{CR}}$ , within the extents of HESS J16414–518 and HESS J1616–508, for the gas components discussed in §4 (see Figures 3 and 8). The molecular gas masses come from CO analysis, while the atomic gas masses are from HI analysis. The total number density  $\bar{n}$  includes both molecular and atomic gas. Note that  $k_{\text{CR}}$  is independent of the assumed distance, as described in text.

Region	$v_{\text{LSR}}$ (km/s)	Distance (kpc)	Molecular mass ( $M_{\odot}$ )	Atomic mass ( $M_{\odot}$ )	Total mass ( $M_{\odot}$ )	$\bar{n}$ ( $10^2 \text{ cm}^{-3}$ )	$k_{\text{CR}}$
HESS J1614–518	−50 to −40	3.1	19,000	4,100	23,000	2.2	650
	−75 to −60	4.3	43,000	11,000	54,000	1.9	530
	−115 to −90	5.9	65,000	21,000	86,000	1.2	630
	−15 to 0	0.4	100	100	200	7.8	1240
HESS J1616–508	−47 to −39	3.0	27,000	2,000	29,000	7.9	360
	−55 to −47	3.5	23,000	2,500	26,000	4.7	550
	−62 to −55	3.8	23,000	2,400	25,000	3.4	670
	−76 to −62	4.4	30,000	6,300	36,000	3.2	620
	−110 to −76	5.6	150,000	23,000	170,000	7.4	210

proton collisions, can be given by the expression  $\tau_{pp} \approx 6 \times 10^7 (n/1 \text{ cm}^{-3})^{-1} \text{ yr}$  (Aharonian & Atoyan 1996), where  $n$  is the number density of the target gas.

We use the number densities of the gas  $\bar{n}$  in the gas components seen towards HESS J1614–518 and HESS J1616–508 (see Tables 2, 4 and 6). The value of  $\bar{n}$  is of order  $\sim 10^2 \text{ cm}^{-3}$  for HESS J1614–518 and of order  $\sim 10^2$  to  $10^3 \text{ cm}^{-3}$  for HESS J1616–508. We calculate the  $\gamma$ -ray luminosity above 200 GeV of HESS J1614–518 and HESS J1616–508 at each of the assumed distances to the gas components.  $W_p$  is then  $\sim 10^{48} \text{ erg}$  for HESS J1614–518 and  $\sim 10^{47}$  to  $10^{48} \text{ erg}$  for HESS J1616–508, which are reasonable fractions of the canonical amount of energy which is injected by a SNR into CRs ( $\sim 10^{50} \text{ erg}$ ).

## 5.2 Leptonic production of TeV $\gamma$ -rays

The leptonic production of TeV  $\gamma$ -rays involves multi-TeV electrons and their interactions via the inverse-Compton effect with ambient background photons. In the case where a potential accelerator is spatially offset from the TeV emission, CR electrons may be travelling across the intervening ISM diffusively. Within the molecular clouds, the magnetic field strength is typically enhanced (Crutcher et al. 2010) and as a result CR electrons suffer heavy synchrotron radiation losses.

The synchrotron cooling time of CR electrons can be given by  $\tau_{\text{sync}} \approx (b_s \gamma_e)^{-1} \text{ s}$ , where  $b_s = 1.292 \times 10^{-15} (B/\text{mG})^2 \text{ s}^{-1}$  is dependent on the local magnetic field strength  $B$ , and  $\gamma_e$  is the Lorentz factor of the electron. We calculate the magnetic field strength of the ISM using the values of  $\bar{n}$  from our gas analyses and following Crutcher et al. (2010). Over a distance  $d$  from the injector, the diffusion time of CR electrons is given by  $\tau_{\text{diff}} = d^2/(6D(E))$ , where  $D(E)$  is the dif-

fusion coefficient for charged particles with energy  $E$  (Ginzburg & Syrovatskii 1964).  $D(E)$  for CR protons and electrons can be found by using equation (2) from Gabici et al. (2007):

$$D(E) = \chi D_0 \left( \frac{E/\text{GeV}}{B/3 \mu\text{G}} \right)^{\delta} \quad (3)$$

where  $D_0 = 3 \times 10^{27} \text{ cm}^2 \text{ s}^{-1}$  and  $\delta = 0.5$ . We assumed a suppression factor  $\chi = 0.1$ , consistent with values adopted in previous studies of the ISM towards the TeV  $\gamma$ -ray source W28 (Giuliani et al. 2010; Gabici et al. 2010; Li & Chen 2012).

Where appropriate in the discussion below of possible source associations with HESS J1614–518 and HESS J1616–508, we consider the synchrotron cooling and diffusion time-scales to assess the plausibility of potential leptonic scenarios. The HESS analyses for HESS J1614–518 and HESS J1616–508 were performed for all observed events. Due to the power-law nature of the  $\gamma$ -ray spectrum from these sources, most of the detected photons have energies around the HESS detection threshold of  $\sim 200 \text{ GeV}$ . As such, when discussing leptonic scenarios, we consider electron energies of  $E_e = 5 \text{ TeV}$ , as inverse-Compton scattering would produce  $\gamma$ -rays with energies near the lower limit of detectability by HESS.

In the following sections, we will discuss the hadronic and leptonic scenarios for both HESS J1614–518 and HESS J1616–508.

## 5.3 HESS J1614–518

We discuss now the implications that the gas data considered in this study have on possible TeV  $\gamma$ -ray production scenarios for HESS J1614–518 that have been previously suggested in the literature.

Recent preliminary results from HESS suggest that HESS J1614–518 has a shell-like TeV  $\gamma$ -ray morphology and may be a SNR candidate (Gottschall et al. 2017). While there are currently no known SNRs towards HESS J1614–518, it may be possible that an undetected SNR is present, responsible for the TeV  $\gamma$ -rays by accelerating CRs that interact with the ISM. It has previously been postulated that the X-ray source XMM-Newton Src B1 is an Anomalous X-ray Pulsar (APX), with Suzaku Src A being a shocked region of the related SNR (Sakai et al. 2011).

This SNR scenario was further investigated by Mizukami et al. (2011). By assuming a power-law distribution of a population of accelerated protons and a source distance of 10 kpc, an ambient matter density of  $100 \text{ cm}^{-3}$  was required to reproduce the  $\gamma$ -ray spectrum of HESS J1614–518 via a hadronic interaction model. The distance assumption was taken from those assigned to Suzaku Src A and XMM-Newton Src B1 (Matsumoto et al. 2008; Sakai et al. 2011), based on the best-fit hydrogen column density. However, this estimate was made only by comparison with the total Galactic HI column density. By considering the contribution to the column density from both atomic and molecular gas in §4.1, we estimate a distance of  $\sim 3$  kpc to both X-ray sources. If we apply this distance to the SNR scenario, scaling the results of Mizukami et al. (2011) would imply an ambient matter density of  $\sim 10 \text{ cm}^{-3}$  would be required.

In §4.1, CO(1–0) observations revealed four components where the diffuse gas is seen towards HESS J1614–518. According to Table 6, the total number density of the gas in each of these components is of the order  $10^2 \text{ cm}^{-3}$ , which would satisfy the requirements from Mizukami et al. (2011). In terms of morphology, there is no strong correspondence that is immediately obvious in any of the components. However, Component 1 would be the most likely candidate for association as the diffuse gas traced by  $^{12}\text{CO}(1–0)$  overlaps most of HESS J1614–518, with gas traced by  $^{13}\text{CO}(1–0)$  appearing towards the TeV peak. This component is also located at a distance of  $\sim 3$  kpc, which is consistent with our estimated distance to Suzaku Src A, XMM-Newton Src B1, and consequently the SNR in this scenario.

The required  $k_{\text{CR}}$  value for the total gas mass in component 1 is  $\sim 650$  (see Table 6) and is consistent with a young SNR ( $\lesssim 5$  kyr) injecting accelerated CRs into the local ISM (Aharonian & Atoyan 1996). At a distance of 3 kpc, the distance between Suzaku Src A and XMM-Newton Src B1 is calculated to be  $\sim 11$  pc. If the radius of the SNR is the same, the age of the SNR can be roughly estimated to be  $\sim 3000$  yr using typical values for SN explosions (injection energy  $E \sim 10^{51} \text{ erg}$ , density  $n_{\text{H}} \sim 1 \text{ cm}^{-3}$ ) and the Sedov-Taylor solution (Sedov 1959; Taylor 1950). Thus it is possible that the

gas in component 1 is the target material for the accelerated particles from this SNR.

In order to have such an SNR, a high mass progenitor star is required. These stars typically have large stellar winds which can blow out cavities within the ISM. The presence of the dense broken-ring of gas discussed in §4.1, located at the same distance of  $\sim 3$  kpc, may be indicative of this scenario, where dense compressed gas has been swept up by the stellar winds of the progenitor star. To create this wind blown ring of gas, an O or B type progenitor star with mass  $\sim 20 M_{\odot}$  would be required, based on an estimated radius of  $\sim 11$  pc (Chen et al. 2013). Following the model presented in Chevalier (1999), and using the parameters of the progenitor stars from Chen et al. (2013), the total energy input by the stellar winds would be  $\sim 5 \times 10^{48} \text{ erg}$  in order to produce the  $\sim 11$  pc radius ring.

A SNR may be a somewhat plausible scenario in this sense, supported by recent preliminary results suggesting a shell-like TeV  $\gamma$ -ray morphology of HESS J1614–518 (Gottschall et al. 2017). However, no evidence of an SNR has yet been detected at this position towards HESS J1614–518, and it may be that this is a SNR only seen in TeV  $\gamma$ -rays.

The stellar winds from stars in the open stellar cluster Pismis 22 have also been considered as a possible association with HESS J1614–518 (Rowell et al. 2008). Mizukami et al. (2011) calculated that, based on energetics requirements and an estimated cluster age of 40 Myr (Piatti et al. 2000), the stellar winds from two O-type stars were required to produce the TeV  $\gamma$ -rays in this scenario. However, this scenario assumed a molecular cloud of ambient density  $100 \text{ cm}^{-3}$  which, the authors noted, had not been found in previous investigations of the ISM using Nanten data (Rowell et al. 2008).

The estimated distance to the cluster is  $\sim 1$  to 2 kpc (Piatti et al. 2000; Kharchenko et al. 2013), with corresponding  $v_{\text{LSR}} \sim -13$  to  $-27 \text{ km s}^{-1}$  using the rotation curve from Brand & Blitz (1993). We find no evidence of a molecular cloud at the current estimated distances to Pismis 22, as there were no components of gas detected at the associated velocities in our ISM study. However, the stellar wind scenario may still be possible if the distance to Pismis 22 is underestimated, and if the responsible stars are instead located within the components of gas observed overlapping HESS J1614–518.

Piatti et al. (2000) estimated the distance to Pismis 22 using the E(B–V) colour excess and an interstellar absorption value of  $A_v \sim 6.0$ . Relationships between the hydrogen column density,  $N_{\text{H}}$ , and  $A_v$  have been previously established. Using the relationship  $N_{\text{H}} = (2.21 \pm 0.09) \times 10^{21} A_v$  from Güver & Özel (2009), a column density of  $N_{\text{H}} = 1.3 \pm 0.2 \times 10^{22} \text{ cm}^{-2}$  is required to obtain the value of  $A_v$  used by Piatti et al. (2000). Extracting the average  $^{12}\text{CO}(1–0)$  and HI spectra from the extent of Pismis 22 (Kharchenko et al.

2013, see Figure 4), we calculate  $N_{\text{H}}$  following §3. Assuming all the traced gas is at the near distance, we find the total cumulative  $N_{\text{H}}$  as a function of  $v_{\text{LSR}}$ , which we plot in Figure 10.

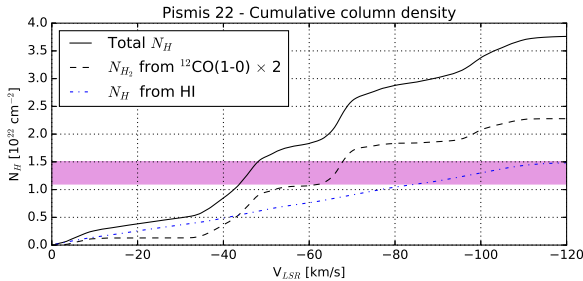


**Figure 10.** Total cumulative hydrogen column density  $N_{\text{H}}$  as a function of  $v_{\text{LSR}}$  (solid lines) towards the stellar cluster Pismis 22. The cumulative molecular and atomic hydrogen column densities, calculated from  $^{12}\text{CO}(1-0)$  and HI data, are shown as dashed and dot-dashed lines respectively. The shaded region indicates the  $N_{\text{H}}$  required to obtain the value of  $A_v$  used in Piatti et al. (2000), which was calculated using the relationship presented in Güver & Özel (2009).

From Figure 10, we see that the required value of  $N_{\text{H}}$  is achieved at  $v_{\text{LSR}} \sim -45 \text{ km s}^{-1}$ , which is similar to the velocity at which the dense open-ring of gas is seen ( $\sim -47$  to  $-44 \text{ km s}^{-1}$ ). We note that gas traced by CS only appears in a very narrow velocity range, and does not significantly alter the cumulative column density in this region. In addition, we note the conspicuous spatial coincidence between Pismis 22 and the gas ring. Hence, it is possible that the distance to Pismis 22 is currently underestimated, and the stellar cluster is at the distance of this ring seen in component 1 ( $\sim 3 \text{ kpc}$ ). In this scenario, the dense gas ring may have been the result of the stellar winds from O or B type stars in the cluster, as mentioned previously. A fraction of the energy in these stellar winds could then be accelerating CRs which interact with the nearby ISM to produce the TeV  $\gamma$ -rays (Voelk & Forman 1982).

Both the scenarios presented above, namely an undetected SNR and stellar winds from Pismis 22, are consistent with the dense ring traced in CS. The CS ring is likely evidence for stellar winds, which by itself may be behind the TeV emission from HESS J1614–518 (Rowell et al. 2008). Such stellar winds can be indicative of eventual supernova events, which lends support to a possible undetected SNR acting as a CR accelerator. In these cases, the production of the TeV  $\gamma$ -ray emission from HESS J1614–518 is via hadronic interactions of accelerated CRs and the ISM.

## 5.4 HESS J1616–508

Several potential CR accelerators lie near HESS J1616–508, including SNR Kes 32, SNR RCW 103, and PSR J1617–5055. In the following, we discuss the possible relation these candidates have with the observed  $\gamma$ -ray flux in the context of our analysis of the nearby interstellar medium.

### 5.4.1 Kes 32

Kes 32 (SNR G332.4+00.1), located  $\sim 17$  arcmin from the centre of HESS J1616–508, has somewhat uncertain distance and age associations. Vink (2004) used *Chandra* data to study the SNR in X-rays, and a single-temperature nonequilibrium ionisation model was used to fit the weak X-ray source spectrum. This was done separately with two background subtractions methods (denoted method 1 and method 2). The results of both methods required a large interstellar absorption column. Method 1 required a hydrogen column density  $N_{\text{H}} = 5.6 \pm 0.8 \times 10^{22} \text{ cm}^{-2}$ , while method 2 required column density  $N_{\text{H}} = 3.1 \pm 0.4 \times 10^{22} \text{ cm}^{-2}$ . These large column densities suggested that it would be reasonable to associate Kes 32 with the Norma spiral arm. Additionally, OH absorption at  $-88 \text{ km s}^{-1}$  towards the SNR indicate a distance of at least  $6.6 \text{ kpc}$  (Caswell & Haynes 1975). However, this distance estimate is reliant on the Galactic rotation model applied, and using the model presented by Brand & Blitz (1993) consistent in this study gives a distance of  $5.3 \text{ kpc}$ .

We extract the average  $^{12}\text{CO}(1-0)$  and HI spectra from within the extent of Kes 32 (as given in Green 2014), and use it to calculate  $N_{\text{H}}$  following §3. Assuming that the gas traced is all at the near distance, we find the total cumulative  $N_{\text{H}}$  as a function of  $v_{\text{LSR}}$ . This is displayed in Figure 11 as a solid black line. The  $N_{\text{H}}$  required in methods 1 and 2 presented in Vink (2004) are indicated by the cyan and pink shaded regions respectively. The vertical red line marks  $v_{\text{LSR}} = -88 \text{ km s}^{-1}$ , at which OH absorption is seen (Caswell & Haynes 1975).

From Figure 11, we can see that at  $v_{\text{LSR}} = -88 \text{ km s}^{-1}$  the total  $N_{\text{H}}$  is at the upper limit of the required value in method 1. Thus we suggest that Kes 32 is located at this kinematic velocity  $\sim -88 \text{ km s}^{-1}$ , which would satisfy both the  $N_{\text{H}}$  requirement and the OH absorption feature. This velocity would then imply a distance to the SNR of  $\sim 5.3 \text{ kpc}$  following Brand & Blitz (1993). This is also consistent with the HI absorption feature coincident with Kes 32 found in the SGPS data as mentioned in §4.2.

If we assume that Kes 32 is located at this distance, CRs accelerated by the SNR may be interacting with the gas traced in component 5 ( $-110$  to  $-76 \text{ km s}^{-1}$ ). In a naive scenario in which all the gas traced in component 5 is considered as target material for CRs, the

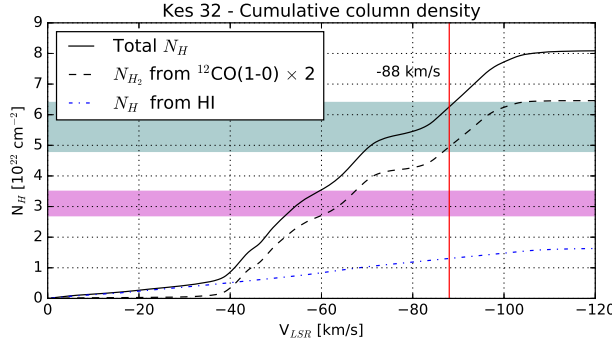


**Figure 11.** Total cumulative hydrogen column density  $N_H$  as a function of  $v_{\text{LSR}}$  (solid lines) towards the SNR Kes 32 (G332.4+00.1). The cumulative molecular and atomic hydrogen column densities, calculated from  $^{12}\text{CO}(1-0)$  and  $\text{HI}$  data, are shown as dashed and dot-dashed lines respectively. The shaded regions indicate the  $N_H$  used to model X-ray spectrum in Vink (2004) (cyan and pink for methods 1 and 2 respectively). Vertical red line marks  $v_{\text{LSR}} = -88 \text{ km s}^{-1}$ .

required CR enhancement value  $k_{\text{CR}}$  is  $\sim 200$  for the observed  $\gamma$ -ray flux (see Table 6).

CRs accelerated by Kes 32 may be diffusively reaching the gas overlapping HESS J1616–508. The centre of Kes 32 is located  $\sim 17$  arcmin from the centre of HESS J1616–508, equivalent to  $\sim 25$  pc at the assumed distance of 5.3 kpc. Figure 1a of Aharonian & Atoyan (1996) displays the modelled values of  $k_{\text{CR}}$  at a distance of 30 pc from an impulsive accelerator at a series of time epochs. A  $k_{\text{CR}}$  value of  $\sim 200$  is possible given a source age of  $\sim 10^3$  yr, similar to the estimated age of Kes 32 of  $\sim 3000$  years (Vink 2004). This assumes the diffusion coefficient at an energy of 10 GeV is  $D_{10} = 10^{28} \text{ cm}^2 \text{ s}^{-1}$ , which corresponds to relatively fast diffusion. Thus the required  $k_{\text{CR}}$  resulting from the diffusion of CRs from Kes 32 is possible, given favourable conditions. However, this scenario assumes that all the gas traced in component 5 is physically connected and is acting as target material. As mentioned in §4.2, the emission in component 5 is very broad ( $\sim 35 \text{ km s}^{-1}$ ) and possibly arises from unresolved overlapping gas features associated with the tangent of the Norma spiral arm. It is then unlikely that all the gas in this component would be acting as CR target material. Additionally there is no striking morphological correspondence between the potential target material and the TeV emission, making it difficult to explain the geometry of the  $\gamma$ -ray emission based on a hadronic scenario powered by Kes 32.

In a leptonic scenario, CR electrons diffusing from Kes 32 towards HESS J1616–508 may produce the observed TeV  $\gamma$ -rays. Assuming a separation of 25 pc at the assumed distance of 5.3 kpc, and using the value of  $\bar{n}$  from Table 6,  $\tau_{\text{diff}}$  is calculated to be  $\sim 22$  kyr, while  $\tau_{\text{sync}} \sim 8$  kyr. As mentioned previously, however,

since the gas in component 5 is likely to be distributed along the Norma arm tangent, the value of  $\bar{n}$ , and consequently the estimated magnetic field strength should be taken as upper limits. If we consider the lower limit of the magnetic field strength within interstellar clouds from Crutcher et al. (2010) ( $10 \mu\text{G}$  for  $\bar{n} \leq 300 \text{ cm}^{-3}$ ), then  $\tau_{\text{diff}}$  and  $\tau_{\text{sync}}$  are calculated to be  $\sim 16$  kyr and  $\sim 25$  kyr respectively. In both cases,  $\tau_{\text{diff}}$  is much greater than the estimated age of Kes 32 ( $\sim 3$  kyr) and thus it is unlikely that accelerated electrons would have diffused far enough from the SNR to contribute to the TeV flux of HESS J1616–508.

#### 5.4.2 RCW 103

RCW 103 (SNR G332.4-00.4), located  $\sim 13$  arcmin from the centre of HESS J1616–508, has been well studied in literature. The young SNR is bright in non-thermal X-rays (Frank et al. 2015) with an estimated age of  $\sim 2000$  years (Nugent et al. 1984; Carter et al. 1997). RCW 103 is located at a distance of  $\sim 3.3$  kpc (Caswell et al. 1975; Paron et al. 2006), with systematic velocity  $\sim -48 \text{ km s}^{-1}$  (Paron et al. 2006), which places it within the velocity interval of component 2 ( $-55$  to  $-47 \text{ km s}^{-1}$ ).

CRs accelerated by this young SNR may be interacting with the gas traced in component 2 to produce TeV  $\gamma$ -rays. If this is responsible for the  $\gamma$ -ray flux of HESS J1616–508, the required  $k_{\text{CR}}$  value is  $\sim 550$  (Table 6). However, we note that a significant amount of gas, as traced by CO(1–0) and CS(1–0) emission, cuts across the TeV source as shown in Figures 8 and 9. The estimated mass of the gas as traced in CO(1–0) within the ‘bar’ is about twice that of the gas within the adopted extent of HESS J1616–508 (see Tables 4 and 5). As  $k_{\text{CR}}$  is inversely proportional to the mass of CR-target material, if the gas within this bar was acting as target material for CR interaction, the required  $k_{\text{CR}}$  value may be as low as  $\sim 250$ .

If the distance to RCW 103 is 3.3 kpc, the separation between the SNR and the centre of HESS J1616–508 is  $\sim 12$  pc. The top panels of Figure 1 in Aharonian & Atoyan (1996) show the  $k_{\text{CR}}$  at a distance of 10 pc from an impulsive accelerator, assuming diffusion coefficients of  $D_{10} = 10^{26}$  and  $10^{28} \text{ cm}^2 \text{ s}^{-1}$ . According to the figures, at a source age of  $\sim 10^3$  years, similar to the age of RCW 103 ( $\sim 2000$  years), a  $k_{\text{CR}}$  of  $\sim 300$  is achievable for both  $D_{10}$  values. This implies that the required  $k_{\text{CR}}$  may be attained from the diffusion of CRs accelerated by RCW 103, assuming the gas bar towards HESS J1616–508 in component 2 is acting as target material.

On the other hand, it is difficult to reconcile the differences in morphology between the target material gas traced in component 2 and the TeV  $\gamma$ -ray emission of HESS J1616–508. The bar of gas that cuts across HESS J1616–508 bears little resemblance

to the roughly circular morphology of the TeV  $\gamma$ -rays. One possible explanation is that accelerated CRs from RCW 103 are interacting with the central region of the dense gas bar towards the middle of the TeV emission. This could be caused by the anisotropic diffusion of CRs preferentially propagating along magnetic field lines (Nava & Gabici 2013; Malkov et al. 2013). Even so, the differences in gas and  $\gamma$ -ray morphology make an association between HESS J1616–508 and RCW 103 somewhat contrived.

For a leptonic scenario, the diffusion time-scale for CR electrons,  $\tau_{\text{diff}}$ , is  $\sim 4.5$  kyr, based on a separation of  $\sim 12$  pc between RCW 103 and the centre of HESS J1616–508, and using the value of  $\bar{n}$  from Table 6. The synchrotron cooling time  $\tau_{\text{sync}}$  is  $\sim 14$  kyr. While the SNR is estimated to have a young age of  $\sim 2000$  yr, this is not significantly different from the value of  $\tau_{\text{diff}}$  given the considerable uncertainties on the value, and it may be possible for CR electrons to have diffusively reached HESS J1616–508.

#### 5.4.3 PSR J1617–5055

An association between with HESS J1616–508, PSR J1617–5055 and its corresponding PWN has previously been suggested (Landi et al. 2007a; Aharonian et al. 2008a; Tibolla 2011; Acero et al. 2013). Radio dispersion measurements suggest the pulsar is located at a distance between  $\sim 6.1$ – $6.9$  kpc (Kaspi et al. 1998), which would correspond to a kinematic velocity of  $\sim -102$  to  $-112$  km s $^{-1}$  following Brand & Blitz (1993). The assumed distance to the pulsar places it in the velocity range of component 5 ( $-110$  to  $-76$  km s $^{-1}$ ). PSR J1617–5055 is offset from the centre of HESS J1616–508 TeV emission by  $\sim 9$  arcmin, corresponding to  $\sim 17$  pc at its assumed distance.

We find no obvious structures in the gas morphology in component 5 that would aid in a pulsar/PWN driven scenario. In the case of a PWN driven TeV source, the ISM is typically seen adjacent to the source, with gas being anti-correlated with the TeV emission (see e.g. Blondin et al. 2001, Voisin et al. 2016). In our case however, this sort of distribution is not seen in our gas analysis.

Additionally, the lack of a bow-shock or any asymmetry in X-ray observations of the PWN (Kargaltsev et al. 2009) disfavour other scenarios such as a rapidly moving pulsar with high kick velocity (Roberts et al. 2005). Consequently, there is no convincing evidence to suggest a link between the TeV source with PSR J1617–5055.

We note that two other pulsars are seen towards HESS J1616–508; PSR J1616–5109 and PSR J1614–5048. However, neither of these pulsars have been considered likely counterparts in previous studies, stemming from their modest spin down power and relatively large offsets from the

TeV source (Landi et al. 2007a; Lande et al. 2012; Hare et al. 2017).

#### 5.4.4 An accelerator at the centre of HESS J1616–508?

Based on our ISM studies, the known accelerators in the nearby regions towards HESS J1616–508 have some issues in explaining the observed TeV emission. As mentioned in §4, the gas in component 1 ( $-47$  to  $-39$  km s $^{-1}$ ) towards HESS J1616–508 traced in  $^{12}\text{CO}(1-0)$  emission forms a molecular cloud structure that appears to overlap the TeV source (Figure 8). Additionally, there appears to be a circular void-like feature towards the centre of HESS J1616–508. This void is also present in HEAT [CI] data (Figure A1), as well as being very pronounced in the  $^{13}\text{CO}(1-0)$  emission.

We now postulate on a previously undetected accelerator at the centre of HESS J1616–508, interacting with this conspicuous gas traced in component 1. The void may be associated with some as-of-yet undetected accelerator which has blown out a cavity in the gas. This accelerator may then be the source of high energy CRs responsible for  $\gamma$ -ray emission from HESS J1616–508. Looking at the integrated  $^{12}\text{CO}(1-0)$  and  $^{13}\text{CO}(1-0)$  images (Figure 8), the diameter of the void is  $\sim 0.1$  to  $0.2$  degrees. At a kinematic distance of  $\sim 3$  kpc, would correspond to  $\sim 5$  to  $10$  pc. According to Table 6, the required CR enhancement factor for the gas in component 1 is of the order  $\sim 300$ . A young impulsive accelerator, such as a SNR, located coincident with the gas void would be readily able to supply the required  $k_{\text{CR}}$  value (Aharonian & Atoyan 1996). In this scenario, the void in the ISM may have been blown out by a progenitor star.

We also note the peculiar line of gas in component 1 which points towards the peak of the TeV emission. This line can be seen in  $^{12}\text{CO}(1-0)$  (Figure 8) and [CI] (Figure A1), but appears most prominently in  $^{13}\text{CO}(1-0)$ .

A similar thin line of molecular gas has been observed pointing towards another Galactic TeV source, HESS J1023–575 (Fukui et al. 2009). The formation of this molecular feature has been speculated to be caused by an energetic event such as an anisotropic supernova explosion. It may be the case for HESS J1616–508 that the thin line of gas in component 1 has been formed under similar circumstances. Molecular jets have been seen towards binary systems, such as the microquasar SS 433 (Yamamoto et al. 2008), which are thought to be accretion powered. However, in our case of HESS J1616–508, no suitable counterpart has been detected for such a scenario.

## 6 Conclusions

Using 3 mm data from the Mopra Radio telescope, 7 mm data from Mopra and the ATCA, archival HI data, as

well as [CI] data from HEAT, we have studied the interstellar medium towards two unidentified TeV sources, HESS J1614–518 and HESS J1616–508.

Towards HESS J1614–518, CO(1–0) observations from Mopra reveal diffuse molecular gas at several velocities along the line-of-sight that appear to overlap the TeV source. While the morphological correspondence with the TeV emission is not particularly strong,  $^{12}\text{CO}$ (1–0) in component 1 ( $-50$  to  $-40 \text{ km s}^{-1}$ ) is seen to overlap most of the TeV emission. 7 mm observations from Mopra in the CS(1–0) tracer revealed a peculiar open ring-like structure of dense gas towards the centre of HESS J1614–518, located at a velocity consistent with the  $^{12}\text{CO}$ (1–0) emission seen in component 1, and was the only dense gas feature seen overlapping the TeV source.

CO(1–0) observations towards HESS J1616–508 revealed multiple components of diffuse molecular gas overlapping the TeV source. Particularly interesting features included a loop of gas cutting through the TeV source in component 2 ( $-55$  to  $-47 \text{ km s}^{-1}$ ), and positionally coincident molecular gas overlapping the entire TeV source in component 1 ( $-47$  to  $-39 \text{ km s}^{-1}$ ). Additionally, in component 1, there appeared to be a void in the diffuse gas towards the central TeV peak. Dense gas was traced in CS(1–0) with a similar morphology and velocity as the loop feature seen in the diffuse gas in component 2.

We estimated the physical parameters of the gas using the CO, CS and HI data for the gas components and interesting features seen towards HESS J1614–518 and HESS J1616–508. For hadronic scenarios, assuming the gas in the diffuse components were acting as target material, it was found that the required values for the total CR energy budget  $W_p$  were  $\sim 10^{48}$  erg and  $\sim 10^{47}$  to  $10^{48}$  erg for HESS J1614–518 and HESS J1616–508 respectively. The required CR enhancement factors were calculated based on total gas masses for each of the gas components, and are displayed in Table 6.

For HESS J1614–518, we find that the scenario involving an as-of-yet undetected SNR, potentially associated with the X-ray sources Suzaku Src A and XMM-Newton Src B1, could generate the observed TeV  $\gamma$ -rays in a hadronic interaction scenario.

The stellar wind scenario involving the stellar cluster Pismis 22 at the estimated distance of  $\sim 1$  to  $2$  kpc was more difficult to reconcile, given the lack of gas seen at the corresponding  $v_{\text{LSR}}$ . However, the total column density towards the cluster and the spatial coincidence with the dense gas ring seen in CS(1–0) at  $\sim 3$  kpc suggests that the distance to Pismis may be underestimated. A stellar wind scenario driven by O and B type stars in the cluster and interacting with the gas traced in component 1 may then be contributing to the observed TeV  $\gamma$ -ray flux.

Several accelerator candidates towards HESS J1616–508 were investigated in light of our ISM study. Neither of the two young SNRs that flank the TeV source, Kes 32 and RCW 103, were found to be strong candidates for association. We also found no convincing evidence to link PSR J1617–5055 and its associated PWN to TeV  $\gamma$ -rays from HESS J1616–508. Due to the somewhat conspicuous nature of the diffuse gas seen in component 1 ( $-47$  to  $-39 \text{ km s}^{-1}$ ), we speculate on an undetected accelerator at the centre of the TeV source interacting with said gas. We find that a CR accelerator such as a young SNR would readily be able explain the TeV  $\gamma$ -ray flux from HESS J1616–508.

Based on our study of the ISM, we find no conclusive evidence to link either HESS J1614–518 or HESS J1616–508 to any known counterparts. However, the angular resolutions of next-generation  $\gamma$ -ray telescopes, such as the Cherenkov Telescope Array, will approach that of this ISM study. This would enable more detailed morphological comparisons in the future between the TeV  $\gamma$ -ray emission and the interstellar gas, allowing for a better understanding of these two mysterious sources.

## 7 ACKNOWLEDGEMENTS

The Mopra radio telescope is part of the Australia Telescope National Facility. Operations support was provided by the University of New South Wales and the University of Adelaide. The UNSW Digital Filter Bank used for the observations with Mopra was provided with financial support from the Australian Research Council (ARC), UNSW, Sydney and Monash universities. We also acknowledge ARC support through grants DP120101585 and LE160100094. J.C.L. and S.P. acknowledge support through the provision of Australian Government Research Training Program Scholarships. The HEAT telescope is financially supported by the National Science Foundation under award numbers ANT-0944335 and AST-1410896, with additional funding from the Australian Governments Australian Antarctic Science Grant Program and NCRIS, and with logistics through the United States Antarctic Program.

## REFERENCES

- Acero F., et al., 2013, *ApJ*, **773**, 77
- Acero F., et al., 2015, *ApJS*, 218, 23
- Aharonian F. A., 1991, *Ap&SS*, 180, 305
- Aharonian F. A., Atoyan A. M., 1996, *A&A*, **309**, 917
- Aharonian F., et al., 2005a, *Science*, **307**, 1938
- Aharonian F., et al., 2005b, *A&A*, **442**, 1
- Aharonian F., et al., 2006, *ApJ*, **636**, 777
- Aharonian F., Buckley J., Kifune T., Sinnis G., 2008a, *Reports on Progress in Physics*, **71**, 096901
- Aharonian F., et al., 2008b, *A&A*, **490**, 685
- Blondin J. M., Chevalier R. A., Frierson D. M., 2001,

- ApJ, 563, 806
- Bolatto A. D., Wolfire M., Leroy A. K., 2013, ARA&A, 51, 207
- Braiding C., et al., 2015, PASA, 32, e020
- Brand J., Blitz L., 1993, A&A, 275, 67
- Bronfman L., Nyman L.-A., May J., 1996, A&AS, 115, 81
- Burton M. G., et al., 2013, PASA, 30, e044
- Burton M. G., et al., 2015, ApJ, 811, 13
- Carter L. M., Dickel J. R., Bomans D. J., 1997, PASP, 109, 990
- Caswell J. L., Haynes R. F., 1975, MNRAS, 173, 649
- Caswell J. L., Murray J. D., Roger R. S., Cole D. J., Cooke D. J., 1975, A&A, 45, 239
- Chen Y., Zhou P., Chu Y.-H., 2013, ApJ, 769, L16
- Chevalier R. A., 1999, ApJ, 511, 798
- Churchwell E., et al., 2009, PASP, 121, 213
- Crutcher R. M., Wandelt B., Heiles C., Falgarone E., Troland T. H., 2010, ApJ, 725, 466
- Deil C., Brun F., Carrigan S., Chaves R., Donath A., Gast H., Marandon V., Terrier R., 2015, in Borisov A. S., et al., eds, International Cosmic Ray Conference Vol. 34, 34th International Cosmic Ray Conference (ICRC2015). p. 773
- Dickey J. M., Lockman F. J., 1990, ARA&A, 28, 215
- Donath A., Brun F., Chaves R. C. G., Deil C., Marandon V., Terrier R., 2017, AIP Conference Proceedings, 1792, 040001
- Evans II N. J., 1999, ARA&A, 37, 311
- Flower D. R., Pineau des Forets G., Field D., May P. W., 1996, MNRAS, 280, 447
- Frank K. A., Burrows D. N., Park S., 2015, ApJ, 810, 113
- Frerking M. A., Wilson R. W., Linke R. A., Wannier P. G., 1980, ApJ, 240, 65
- Fukui Y., et al., 2009, PASJ, 61, L23
- Gabici S., Aharonian F. A., Blasi P., 2007, Ap&SS, 309, 365
- Gabici S., Casanova S., Aharonian F. A., Rowell G., 2010, in Boissier S., Heydari-Malayeri M., Samadi R., Valls-Gabaud D., eds, SF2A-2010: Proceedings of the Annual meeting of the French Society of Astronomy and Astrophysics. p. 313
- Ginzburg V. L., Syrovatskii S. I., 1964, The Origin of Cosmic Rays
- Giuliani A., et al., 2010, A&A, 516, L11
- Goldsmith P. F., Langer W. D., 1999, ApJ, 517, 209
- Gottschall D., et al., 2017, AIP Conference Proceedings, 1792, 040030
- Green D. A., 2014, Bulletin of the Astronomical Society of India, 42, 47
- Güver T., Özel F., 2009, MNRAS, 400, 2050
- Hare J., Kargaltsev O., Pavlov G. G., Rangelov B., Volkov I., 2017, ApJ, 841, 81
- Henkel C., Wilson T. L., Bieging J., 1982, A&A, 109, 344
- Irvine W. M., Goldsmith P. F., Hjalmarson A., 1987, in Hollenbach D. J., Thronson Jr. H. A., eds, Astrophysics and Space Science Library Vol. 134, Interstellar Processes. pp 561–609
- Jordan C. H., et al., 2015, Monthly Notices of the Royal Astronomical Society, 448, 2344
- Kargaltsev O., Pavlov G. G., Wong J. A., 2009, ApJ, 690, 891
- Kaspi V. M., Crawford F., Manchester R. N., Lyne A. G., Camilo F., D'Amico N., Gaensler B. M., 1998, The Astrophysical Journal, 503, L161
- Kharchenko N. V., Piskunov A. E., Schilbach E., Röser S., Scholz R.-D., 2013, A&A, 558, A53
- Lande J., et al., 2012, ApJ, 756, 5
- Landi R., de Rosa A., Dean A. J., Bassani L., Ubertini P., Bird A. J., 2007a, MNRAS, 380, 926
- Landi R., Masetti N., Bassani L., Cellone S. A., Romero G. E., Ubertini P., Dean A. J., 2007b, The Astronomer's Telegram, 1047
- Lau J. C., et al., 2017, MNRAS, 464, 3757
- Li H., Chen Y., 2012, MNRAS, 421, 935
- Malkov M. A., Diamond P. H., Sagdeev R. Z., Aharonian F. A., Moskalenko I. V., 2013, ApJ, 768, 73
- Manchester R. N., Hobbs G. B., Teoh A., Hobbs M., 2005, The Astrophysical Journal, 129, 1993
- Martin-Pintado J., Bachiller R., Fuente A., 1992, A&A, 254, 315
- Matsumoto H., et al., 2008, PASJ, 60, S163
- Mauerhan J. C., Van Dyk S. D., Morris P. W., 2011, AJ, 142, 40
- McClure-Griffiths N. M., Dickey J. M., Gaensler B. M., Green A. J., Havercorn M., Strasser S., 2005, ApJS, 158, 178
- Mizukami T., et al., 2011, The Astrophysical Journal, 740, 78
- Nava L., Gabici S., 2013, MNRAS, 429, 1643
- Nugent J. J., Pravdo S. H., Garmire G. P., Becker R. H., Tuohy I. R., Winkler P. F., 1984, ApJ, 284, 612
- Paladini R., Burigana C., Davies R. D., Maino D., Bersanelli M., Cappellini B., Platania P., Smoot G., 2003, A&A, 397, 213
- Paron S. A., Reynolds E. M., Purcell C., Dubner G. M., Green A., 2006, PASA, 23, 69
- Piatti A. E., Clariá J. J., Bica E., 2000, A&A, 360, 529
- Renaud M., Hoppe S., Komin N., Moulin E., Marandon V., Clapson A.-C., 2008, in Aharonian F. A., Hofmann W., Rieger F., eds, American Institute of Physics Conference Series Vol. 1085, American Institute of Physics Conference Series. pp 285–288

- Roberts M. S. E., Brogan C. L., Gaensler B. M., Hessels J. W. T., Ng C.-Y., Romani R. W., 2005, *Ap&SS*, 297, 93
- Rowell G., Horns D., Fukui Y., Moriguchi Y., 2008, in Aharonian F. A., Hofmann W., Rieger F., eds, American Institute of Physics Conference Series Vol. 1085, American Institute of Physics Conference Series. pp 241–244
- Sakai M., Yajima Y., Matsumoto H., 2011, Publications of the Astronomical Society of Japan, 63, S879
- Sedov L. I., 1959, Similarity and Dimensional Methods in Mechanics
- Simon R., Jackson J. M., Clemens D. P., Bania T. M., Heyer M. H., 2001, *ApJ*, 551, 747
- Strong A. W., Moskalenko I. V., Reimer O., Digel S., Diehl R., 2004, *A&A*, 422, L47
- Taylor G., 1950, *Proceedings of the Royal Society of London Series A*, 201, 159
- Tibolla O., 2011, International Cosmic Ray Conference, 6, 202
- Vink J., 2004, *ApJ*, 604, 693
- Voelk H. J., Forman M., 1982, *ApJ*, 253, 188
- Voisin F., Rowell G., Burton M. G., Walsh A., Fukui Y., Aharonian F., 2016, *MNRAS*, 458, 2813
- Yamamoto H., et al., 2008, *PASJ*, 60, 715
- Zinchenko I., Forsstroem V., Lapinov A., Mattila K., 1994, *A&A*, 288, 601
- van der Hucht K. A., 2001, *New Astronomy Reviews*, 45, 135

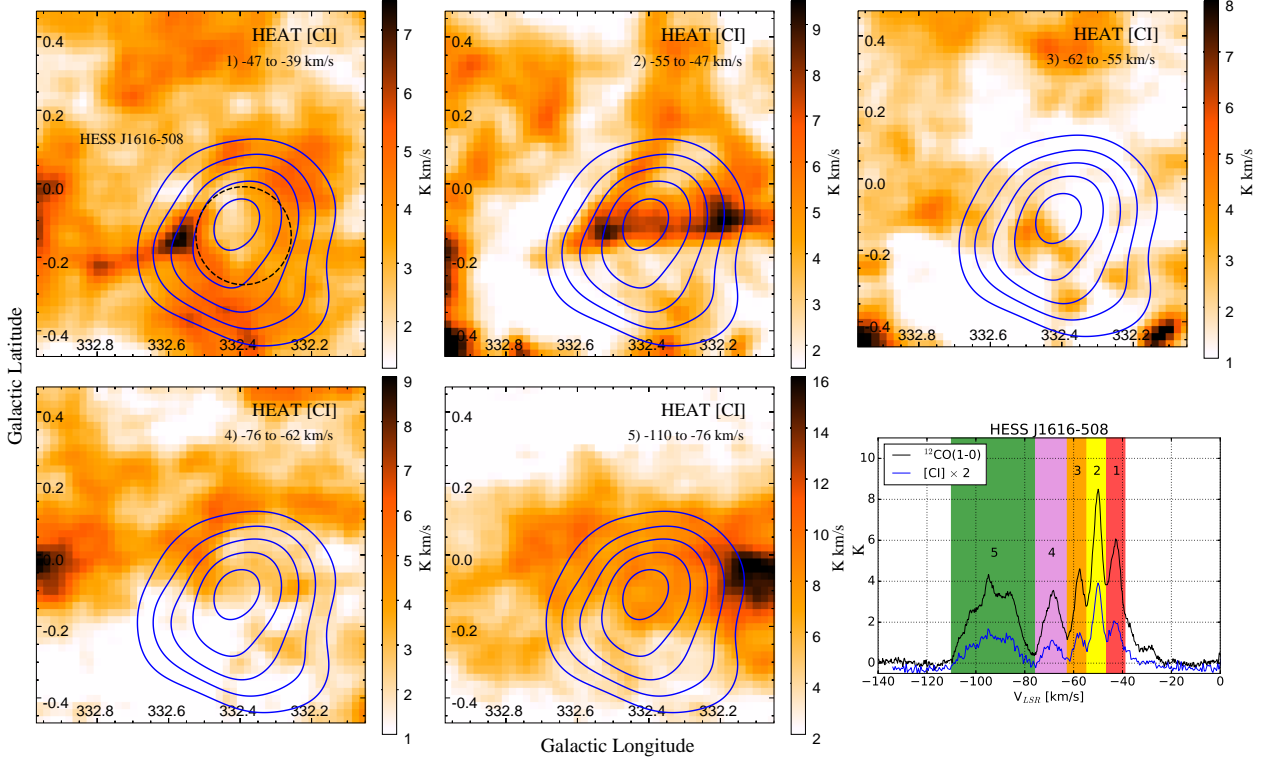


**Figure A1.** HEAT CI ( $J=2-1$ ) integrated intensity images [ $\text{K km s}^{-1}$ ] within the labelled velocity intervals towards HESS J1616–508. Overlaid are HESS excess counts contours (blue) at the 30, 45, 60, 75 and 90 levels. The dashed black circle in the top left panel is the RMS extent of HESS J1616–508 (Aharonian et al. 2006). The bottom-right panel shows average spectra of  $^{12}\text{CO}(1-0)$  (black) and [CI] (blue) emission within the circular region. For clarity, the [CI] spectrum is scaled by a factor of 2. The velocity intervals used in the integrated image panels are indicated by the shaded rectangles.

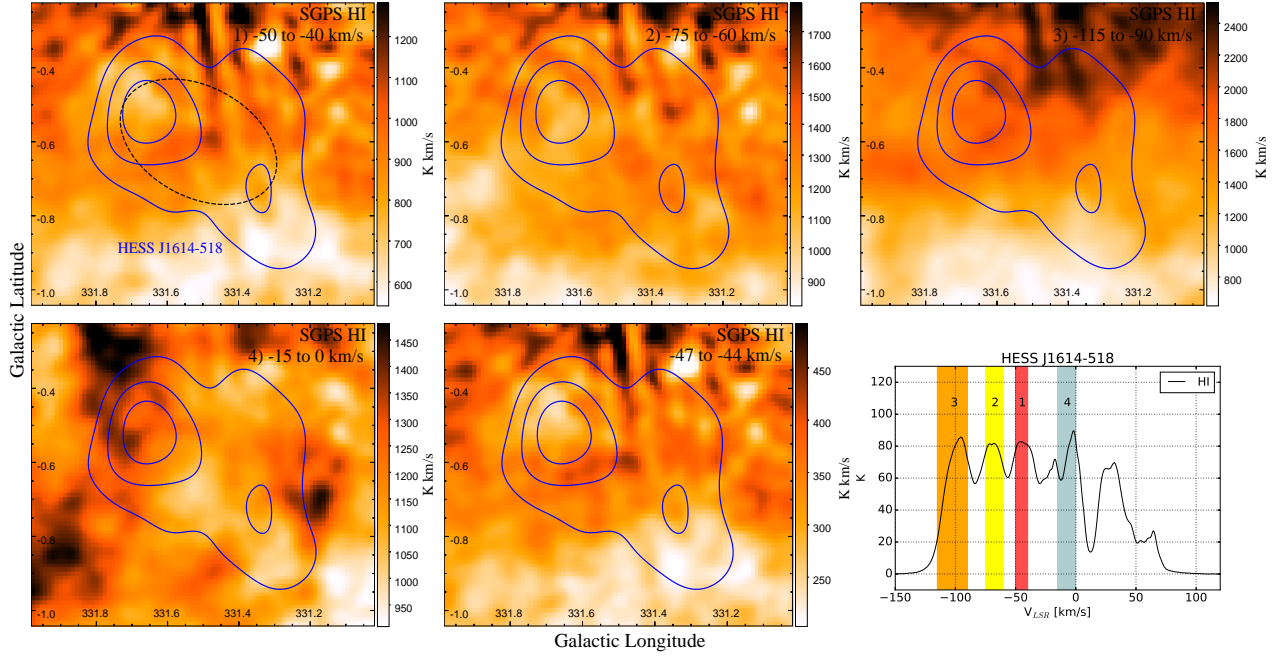


**Figure A2.** HI integrated intensity images [ $\text{K km s}^{-1}$ ] from SGPS data within the labelled velocity intervals towards HESS J1614–518. Overlaid are HESS excess counts contours (blue) at the 30, 45 and 60 levels. The dashed black ellipse is the RMS extent of HESS J1614–518 (Aharonian et al. 2006). The bottom-right panel which shows the average HI emission spectrum within the extent of the TeV source. The velocity integration intervals for each component as described in text (§4.1) is indicated by the shaded rectangles.

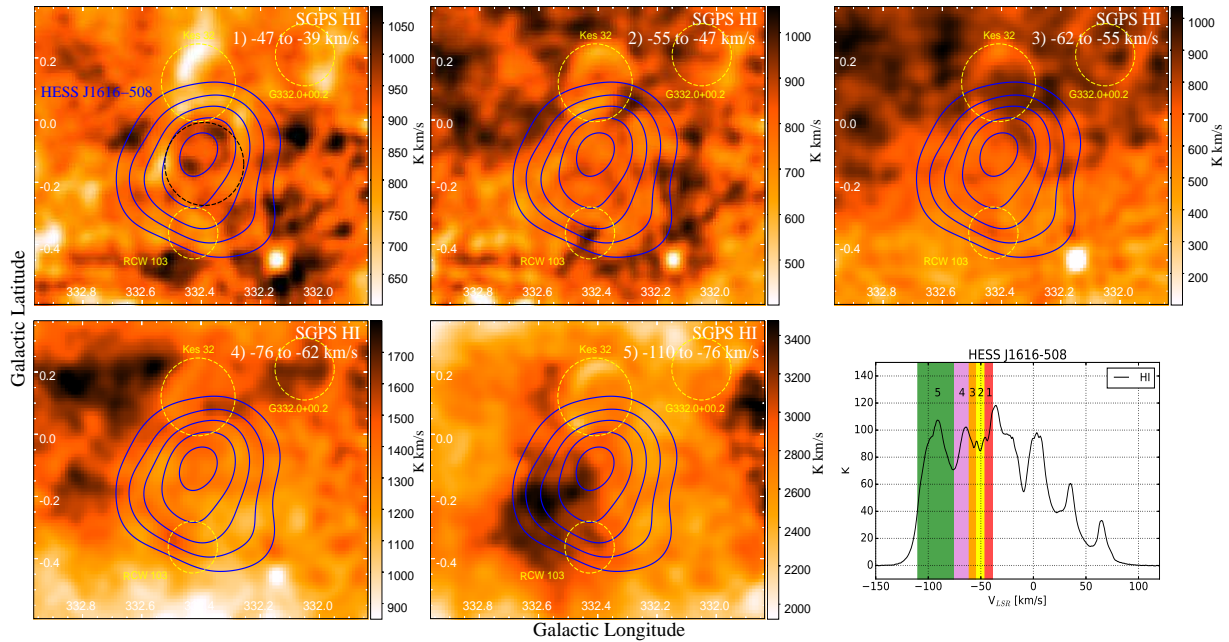


**Figure A3.** HI integrated intensity images [ $\text{K km s}^{-1}$ ] from SGPS data within the labelled velocity intervals towards HESS J1616–508. Overlaid are HESS excess counts contours (blue) at the 30, 45, 60, 75 and 90 levels. The dashed black circle is the RMS extent of HESS J1616–508 (Aharonian et al. 2006). The yellow dashed circles indicates the positions of known SNRs in the region (Green 2014). The bottom-right panel shows the average HI emission spectrum within the extent of the TeV source. The velocity integration intervals for each component as described in text (§4.2) is indicated by the shaded rectangles.



# Chapter 5

## The ISM towards HESS J1702–420

The following is a manuscript that will be submitted to the peer-reviewed journal, Publications of the Astronomical Society of Australia (PASA). This is the latest version of the manuscript at the time of thesis submission.

HESS J1702–420 is a mysterious TeV gamma-ray source which has no firmly associated counterparts in other wavelengths. The manuscript consists of a study of the interstellar medium using CO(1–0) data from the Mopra Southern Galactic Plane Survey and HI data the Southern Galactic Plane Survey towards the TeV source, as well as an investigation into the possible origin scenarios based on this knowledge of the ISM.



# Statement of Authorship

Title of Paper	The unidentified TeV γ-ray source HESS J1702-420 and the surrounding interstellar medium		
Publication Status	<input type="checkbox"/> Published	<input type="checkbox"/> Accepted for Publication	<input checked="" type="checkbox"/> Unpublished and Unsubmitted work written in manuscript style
Publication Details	To be submitted to the peer reviewed journal, Publications of the Astronomical Society of Australia (PASA).		

## Principal Author

Name of Principal Author (Candidate)	James Cheuk-Heng Lau		
Contribution to the Paper	Mopra data observations, data reduction, spectral line analysis, interstellar medium and high energy interpretations, and writing of the paper.		
Overall percentage (%)	70%		
Certification:	This paper reports on original research I conducted during the period of my Higher Degree by Research candidature and is not subject to any obligations or contractual agreements with a third party that would constrain its inclusion in this thesis. I am the primary author of this paper.		
Signature		Date	24/10/17

## Co-Author Contributions

By signing the Statement of Authorship, each author certifies that:

- i. the candidate's stated contribution to the publication is accurate (as detailed above);
- ii. permission is granted for the candidate to include the publication in the thesis; and
- iii. the sum of all co-author contributions is equal to 100% less the candidate's stated contribution.

Name of Co-Author	Gavin Rowell		
Contribution to the Paper	ISM analysis, ISM and high energy interpretations and general reviewing of paper (15%)		
Signature		Date	15/9/17

Name of Co-Author	Fabien Voisin		
Contribution to the Paper	ISM and high energy interpretations (5%)		
Signature		Date	15/09/2017

Name of Co-Author	Rebecca Blackwell	
Contribution to the Paper	ISM interpretation and data reduction (2%)	
Signature		Date <b>25/09/2017</b>

Name of Co-Author	Michael Burton	
Contribution to the Paper	Mopra observations, ISM interpretations (2%)	
Signature		Date <b>23/10/17</b>

Name of Co-Author	Catherine Braiding	
Contribution to the Paper	Mopra observations and data (2%)	
Signature		Date <b>14/10/17</b>

Name of Co-Author	Graeme Wong	
Contribution to the Paper	Mopra observations and data (2%)	
Signature		Date <b>9/10/17</b>

Name of Co-Author	Yasuo Fukui	
Contribution to the Paper	ISM interpretation (2%)	
Signature		Date <b>October 5th, 2017</b>

# The unidentified TeV $\gamma$ -ray source HESS J1702–420 and the surrounding interstellar medium

J. C. Lau<sup>1\*</sup>, G. Rowell<sup>1</sup>, F. Voisin<sup>1</sup>, R. Blackwell<sup>1</sup>, M. G. Burton<sup>2,3</sup>, C. Braiding<sup>2</sup>, G. F. Wong<sup>2,4</sup> and Y. Fukui<sup>5</sup>

<sup>1</sup>School of Physical Sciences, University of Adelaide, Adelaide, SA 5005, Australia

<sup>2</sup>School of Physics, University of New South Wales, Sydney, NSW 2052, Australia

<sup>3</sup>Armagh Observatory and Planetarium, College Hill, Armagh, BT61 9DG, Northern Ireland, UK

<sup>4</sup>Western Sydney University, Locked Bag 1797, Penrith, NSW 2751, Australia

<sup>5</sup>Department of Physics, University of Nagoya, Furo-cho, Chikusa-ku, Nagoya, 464-8601, Japan

## Abstract

The unidentified TeV  $\gamma$ -ray source HESS J1702–420 has no firm associations with any counterparts at other wavelengths. We present an analysis of the interstellar medium using results from the Mopra Southern Galactic Plane CO survey and archival HI data from the Southern Galactic Plane Survey. We find significant components of molecular and atomic gas overlapping the TeV  $\gamma$ -ray source at several velocities along the line-of-sight, with masses  $\sim 10^2$  to  $10^4 M_\odot$  and densities up to  $\sim 10^3 \text{ cm}^{-3}$ . Potentially interesting and favourable morphological correspondences between the ISM and the TeV  $\gamma$ -ray emission were found, and in a hadronic scenario, we find that cosmic-ray (CR) enhancement values of  $\sim 100$  times the local solar values are required to produce the TeV  $\gamma$ -rays. We investigate the separate scenarios in which HESS J1702–420 is powered by the nearby SNR G344.7–0.1, PSR J1702–4128, and an unknown accelerator. No evidence in the ISM was found to link the SNR with the TeV source. While the morphology of the gas located at the dispersion distance of PSR J1702–4128 (5.2 kpc,  $v_{\text{LRS}} \sim -70 \text{ km s}^{-1}$ ) did not discount the possibility of a leptonic origin, the required energetics and the broad and hard TeV spectrum disfavour such a scenario. Given the presence of potentially favourable ISM overlapping HESS J1702–420, we additionally speculate on the plausibility of scenarios involving undetected CR accelerators.

**Keywords:** ISM:clouds – ISM: cosmic rays – gamma-rays: ISM – molecular data

## 1 Introduction

With the continued advances of ground based  $\gamma$ -ray observations, a growing number of Galactic  $\gamma$ -ray sources have been discovered by instruments such as HESS (Aharonian et al. 2006b; Donath et al. 2017). A sizeable fraction of these sources, however, remain unidentified, having no clear counterparts observed in other wavelengths. In order to investigate the true nature of these TeV sources, an understanding of the local interstellar medium (ISM) is paramount, as it can aid in constraining the possible production mechanisms involved in generating the observed  $\gamma$ -rays. In particular, the distribution of the ISM is intimately linked with the hadronic interactions that produce TeV  $\gamma$ -rays between highly accelerated cosmic-rays (CRs) and ambient gas, and a spatial correspondence between the TeV  $\gamma$ -rays and ISM may support such scenario. On the other hand, a leptonic production scenario is typically

accompanied by a general anticorrelation between the TeV  $\gamma$ -rays and ISM. In this study, we explore the ISM towards HESS J1702–420, an unidentified and poorly understood TeV  $\gamma$ -ray source.

HESS J1702–420 was first discovered as part of the HESS survey of the Galactic plane (Aharonian et al. 2005, 2006b). The TeV source is reasonably bright, with a flux 7% that of the Crab nebula above 200 GeV. Further observation time with the HESS telescopes confirmed a statistically significant ‘tail’ of  $\gamma$ -ray emission extending to positive Galactic longitude and latitude from the TeV peak (Aharonian et al. 2008). The TeV  $\gamma$ -ray spectrum of HESS J1702–420 is characterised by a power law,  $dN/dE = N_0 E^{-\Gamma}$ , with a relatively hard photon index of  $\Gamma = 2.1 \pm 0.1_{\text{stat}} \pm 0.2_{\text{sys}}$ . With a hard spectrum that extends into energies of several tens of TeV that has no sign of a cut-off, HESS J1702–420 is currently considered a PeVatron candidate; a type of TeV source powered by an extreme accelerator injecting particles with energies up to the PeV range.

\*E-mail: james.lau@adelaide.edu.au

Deep X-ray observations towards the TeV  $\gamma$ -ray peak of HESS J1702–420 were carried out by *Suzaku* (Fujinaga et al. 2011). Two faint and point-like sources were detected within the field of view, though neither were considered as X-ray counterparts to the TeV source. No significant diffuse emission on the scale of the TeV source was detected in the 2–10 keV band, and the upper limit of the X-ray flux resulted in a large flux ratio of  $F_{\text{TeV}}/F_X > 12$ , similar to that of other dark TeV sources. A leptonic model in which the TeV  $\gamma$ -rays were produced via inverse-Compton scattering and X-rays via synchrotron was deemed to be unlikely, as the upper limit of the magnetic field ( $1.7 \mu\text{G}$ ) was found to be lower than that of the typical Galactic plane value ( $\sim 3 - 10 \mu\text{G}$ ). Fujinaga et al. (2011) therefore concluded that the TeV  $\gamma$ -rays from HESS J1702–420 may be produced by the hadronic interactions of CR protons.

Near the outer regions of HESS J1702–420 lie the supernova remnant (SNR) G344.7–0.1 and the pulsar PSR J1702–4128. Figure 1 shows a *Spitzer* GLIMPSE 8  $\mu\text{m}$  image (Churchwell et al. 2009) towards HESS J1702–420 with the positions of the nearby SNR and pulsar indicated. A small HII region, G344.366–0.262 with radius of  $\sim 4'$  (Anderson et al. 2014) is seen near the TeV peak.

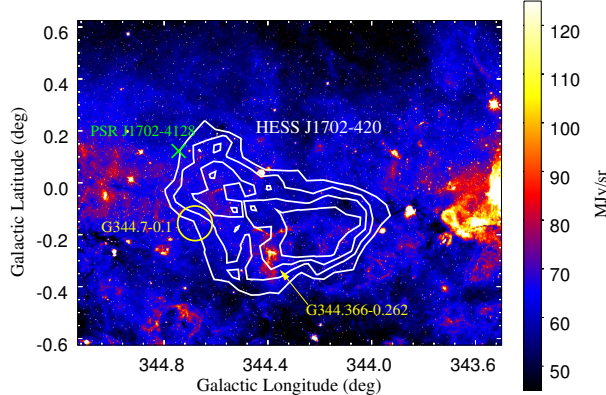


**Figure 1.** 8  $\mu\text{m}$  image [ $\text{MJy sr}^{-1}$ ] using *Spitzer* GLIMPSE data (Churchwell et al. 2009) towards HESS J1702–420. The white contours show the HESS significance at  $4\sigma$ ,  $5\sigma$ ,  $6\sigma$ , and  $7\sigma$  (Aharonian et al. 2008). The position and extent of SNR G344.7–0.1 is indicated by a yellow circle (Green 2014). The green X shows the position of PSR J1702–4128 (Manchester et al. 2005). The HII region G344.366–0.262 is labelled (Anderson et al. 2014).

SNR G344.7–0.1 has a circular, asymmetric radio shell with a small angular diameter of  $\sim 8'$  (Whiteoak & Green 1996). Observations of the SNR with *Chandra* and *XMM-Newton* confirm extended thermal X-ray emission that fill the radio structure (Yamauchi et al. 2005; Combi et al. 2010). The X-ray peak appears to be located at a position more interior to the shell when

compared to the brightest radio features (Giacani et al. 2011).

The distance to the SNR G344.7–0.1 is not well determined. Dubner et al. (1993) estimated a distance of  $\sim 14$  kpc based on the  $\Sigma$ –D relation, though this method of estimation is often unreliable due to large intrinsic dispersion. Giacani et al. (2011) estimated a distance of  $6.3 \pm 0.1$  kpc, based on HI absorption features which may be associated with SNR G344.7–0.1. However, this distance may be too small, as the large required absorption column density from X-ray observations,  $\sim 5 \times 10^{22} \text{ cm}^{-2}$  (Combi et al. 2010; Giacani et al. 2011; Yamaguchi et al. 2012), suggests a distance much further, perhaps on the opposite side of the Galaxy ( $\gtrsim 8$  kpc, Yamaguchi et al. 2012).

Due to its small angular size of SNR G344.7–0.1 compared with the TeV emission, and the very large probable distance estimate, the SNR is considered to be unassociated with HESS J1702–420 (Aharonian et al. 2008).

PSR J1702–4128, located on the outskirts of the TeV source near the tip of the extend  $\gamma$ -ray tail, has been considered as a possible counterpart to HESS J1702–420 (Gallant 2007; Aharonian et al. 2008). The spin-down power of the pulsar,  $\dot{E} = 3.4 \times 10^{35} \text{ erg s}^{-1}$  (Kramer et al. 2003), would be enough to power the observed TeV emission. However, this would require a noticeably high conversion efficiency of  $\sim 70\%$ , assuming the dispersion measure distance estimate of 5.2 kpc. The large angular separation between PSR J1702–4128 and the peak of the TeV  $\gamma$ -rays ( $\sim 50$  pc at the assumed distance) implies that an extremely asymmetric pulsar wind nebula (PWN) would be required to reconcile the TeV morphology. *Chandra* observations of the pulsar indicated a faint hint of extended X-ray emission associated with the PWN (Chang et al. 2008), though the statistics were too low to meaningfully quantify any extension. As such, no firm evidence has been found that would link the PWN with HESS J1702–420, and any association between PSR J1702–4128 and its PWN with HESS J1702–420 is considered fairly weak (Fujinaga et al. 2011). No GeV source from the *Fermi*-LAT 4-year Point Source Catalogue (3FGL) is seen towards HESS J1702–420 (Acero et al. 2015).

The mechanisms behind the production of TeV  $\gamma$ -rays observed from HESS J1702–420 are thus poorly understood. Hence, we present in this paper a study of the ISM towards HESS J1702–420 with an aim to discern and constrain the possible origin scenarios. In order to achieve this, we have used high resolution spectral line data from the Mopra Southern Galactic Plane CO Survey, which traces molecular gas, and archival HI data from the Southern Galactic Plane Survey towards the TeV source.

In Section 2, we describe our dataset and the spectral line analysis techniques that we have used in this work. In Section 3, we describe our results concerning the distribution of ISM towards HESS J1702–420. In Section 4, we discuss HESS J1702–420 and the possible origin scenarios in light of our ISM results.

## 2 Datasets and spectral line analysis

### 2.1 Survey Datasets

The CO(1–0) spectral line emission data towards HESS J1702–420 used in this study was taken from the Mopra Southern Galactic Plane CO Survey (Burton et al. 2013; Braiding et al. 2015). This survey has coverage of the Galactic plane within the  $l = 267^\circ$  to  $11^\circ$ ,  $b = \pm 0^\circ.5$  regions in the  $^{12}\text{CO}$ ,  $^{13}\text{CO}$  and  $\text{C}^{18}\text{O}$   $J = 1–0$  molecular lines. The survey was conducted using the Mopra Radio Telescope, with a beamsize and velocity resolution of  $0'.6$  and  $0.1 \text{ km s}^{-1}$  respectively after processing. The RMS sensitivity for  $^{12}\text{CO}$  was  $\sim 1.5 \text{ K}$  and  $\sim 0.7 \text{ K}$  for the other lines. Additional details about the survey can be found in the papers mentioned above.

Data in the 21 cm atomic hydrogen line towards HESS J1702–420 was taken from the Southern Galactic Plane Survey (SGPS) (McClure-Griffiths et al. 2005). The survey, providing HI data in the Southern regions of the Galaxy, was taken by the Parkes Radio Telescope and the Australian Telescope Compact Array (ATCA). The survey has an angular resolution of  $2'$ , a spectral resolution of  $0.82 \text{ km s}^{-1}$  and a RMS sensitivity of  $1 \text{ K}$ .

### 2.2 Spectral line analysis

We use the same spectral line analysis on the CO(1–0) and HI in this study as in our previous work (Lau et al. 2017). For completeness, we briefly summarise the methods below.

#### 2.2.1 CO

The  $^{12}\text{CO}(1–0)$  molecular line is the standard tracer of moderate density ( $\bar{n} \sim 10^2 – 10^3 \text{ cm}^{-3}$ ) gas in the ISM. Within a region of interest, the spectral line features found in the dataset were fit with Gaussian functions. The average column density of molecular hydrogen,  $\overline{N_{\text{H}_2}}$ , within the region was calculated using the integrated intensity of the line feature. The mass of the gas contained was then calculated via the relation  $M = \mu m_{\text{H}} \overline{N_{\text{H}_2}} A$ , where  $m_{\text{H}}$  is the mass of one hydrogen atom,  $A$  is the physical cross-sectional area of the region of interest, and  $\mu$  is the average molecular weight term which was taken to be 2.8 to account for the approximate 20% helium content present in the ISM.

We converted the integrated brightness temperature of CO(1–0) emission,  $W_{\text{CO}}$ , to an average molecular

hydrogen column density,  $\overline{N_{\text{H}_2}}$ , using the relationship  $\overline{N_{\text{H}_2}} = X_{\text{CO}(1–0)} W_{\text{CO}(1–0)}$ , where  $X_{\text{CO}(1–0)}$  is the CO to H<sub>2</sub> conversion X-factor. For the purposes of this work, we adopted the  $^{12}\text{CO}(1–0)$  X-factor as  $X_{^{12}\text{CO}(1–0)} \sim 1.5 \times 10^{20} \text{ cm}^{-2} (\text{K km s}^{-1})^{-1}$  (Strong et al. 2004).

In order to calculate the optical thickness of the  $^{12}\text{CO}(1–0)$  line,  $\tau_{12}$ , we used the method outlined in Burton et al. (2013). This involved comparing the brightness temperatures of the  $^{12}\text{CO}(1–0)$  and  $^{13}\text{CO}(1–0)$  emission under the limit in which  $^{12}\text{CO}(1–0)$  was optically thick and  $^{13}\text{CO}(1–0)$  was optically thin. With this assumption, an expression for  $\tau_{12}$  can be given as:

$$\tau_{12} = \frac{X_{12/13}}{R_{12/13}} \quad (1)$$

where  $X_{12/13}$  is the isotope abundance ratio [ $^{12}\text{C}/^{13}\text{C}$ ], and  $R_{12/13}$  is the ratio between the brightness temperatures of the  $^{12}\text{CO}$  and  $^{13}\text{CO}$  emission. To calculate  $X_{12/13}$ , we used the results from Henkel et al. (1982), which derived an expression for  $X_{12/13}$  as a function of galactocentric radius ( $R$ , in kpc) as  $X_{12/13} = 5.5R + 24.2$ .

#### 2.2.2 HI

To obtain the column density of neutral atomic hydrogen,  $\overline{N_{\text{HI}}}$ , we use the integrated brightness temperature of HI,  $W_{\text{HI}}$ , and the relationship  $\overline{N_{\text{HI}}} = X_{\text{HI}} W_{\text{HI}}$ . Here, we take the value of the conversion factor to be  $X_{\text{HI}} = 1.823 \times 10^{18} \text{ cm}^{-2} (\text{K km s}^{-1})^{-1}$  from Dickey & Lockman (1990). The average total hydrogen column density,  $\overline{N_{\text{H}}}$ , in a region of interest can then be calculated by combining the values of  $\overline{N_{\text{H}_2}}$  and  $\overline{N_{\text{HI}}}$ , obtained from  $^{12}\text{CO}(1–0)$  and HI observations respectively, using  $N_{\text{H}} = N_{\text{HI}} + 2N_{\text{H}_2}$ . Note that this assumes the case of optically thin HI, and the presence of optically thick HI may result in an underestimation of the column density by up to a factor of 2 (e.g. see Fukui et al. 2012).

## 3 Results

We present in this section our findings of the ISM distribution towards the TeV  $\gamma$ -ray source HESS J1702–420, using CO(1–0) data from the Mopra Southern Galactic Plane CO Survey and HI data from the Southern Galactic Plane Survey.

The distances to the features in the ISM were estimated by applying the Galactic rotation curve model presented in Brand & Blitz (1993) to the kinematic velocity of the detected line emission. In presenting the results of this study, the near-distance solution has been assumed for mass and density calculations with the exception of cases where there was a single distance solution. This is done as nearby gas is more likely to be seen, in the absence of other supporting evidence to resolve

the near/far distance ambiguity. For completeness, mass and density calculations using the far-distance solutions are included in the appendix.

### 3.1 CO(1–0) emission towards HESS J1702–420

Overall, emission in the CO(1–0) lines is detected overlapping HESS J1702–420 along the line-of-sight over many kinematic velocity intervals. We present the average  $^{12}\text{CO}(1–0)$  and  $^{13}\text{CO}(1–0)$  emission spectra within the RMS elliptical extent of HESS J1702–420, as described in Aharonian et al. (2008), in Figure 2. This region is indicated by the dashed ellipse in the top-left panel of Figure 3.

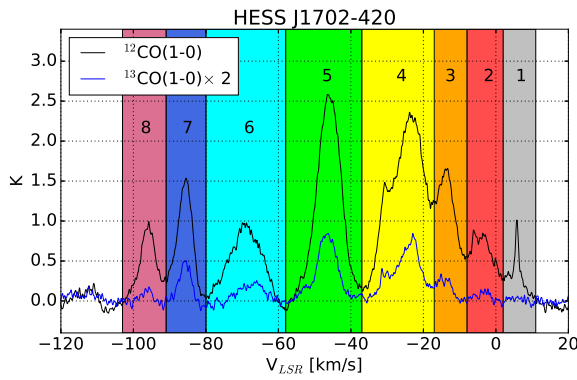


**Figure 2.** Average  $^{12}\text{CO}(1–0)$  and  $^{13}\text{CO}(1–0)$  emission spectra (black and blue respectively) within the elliptical extent of HESS J1702–420 as described in Aharonian et al. (2008) (indicated by the dashed black ellipse in Figure 3). The  $^{13}\text{CO}(1–0)$  spectrum has been scaled by a factor of 2 for clarity. The coloured rectangles indicate the velocity intervals for each of the ‘components’ of CO(1–0) emission, as described in text.

From the spectra, we see that there are multiple features in which there is significant CO(1–0) emission between  $\sim -91$  and  $+11 \text{ km s}^{-1}$ . We divide this velocity space into eight ‘components’, each indicated by a colour rectangle in Figure 2. For each of these components, we generate an integrated emission map over the corresponding velocity range. Figure 3 displays a mosaic of the  $^{12}\text{CO}(1–0)$  integrated images, while the  $^{13}\text{CO}(1–0)$  images are displayed in Figure A1, located in the appendix. A position-velocity (in longitude) image of the  $^{12}\text{CO}(1–0)$  emission in the region indicated by the solid magenta rectangle in Figure 3 is shown in Figure 4, with the estimated velocity positions of the Galactic spiral arms along the line-of-sight labelled. These locations were estimated using the 4-arm model of the Galaxy from Vallée (2014) and the Galactic rotation curve from Brand & Blitz (1993).

The integrated  $^{12}\text{CO}(1–0)$  image for component 1 ( $v_{\text{LSR}} = 2$  to  $11 \text{ km s}^{-1}$ ) shows a minor amount of emission overlapping HESS J1702–420. A vertical feature of more intense emission appears to the immediate Galactic North-west of the TeV source, which is also present in the  $^{13}\text{CO}(1–0)$ . We note that the dominant  $^{12}\text{CO}(1–0)$  emission in this component is very narrow ( $\Delta v_{\text{FWHM}} \sim 2 \text{ km s}^{-1}$ ), and is seen at positive kinematic velocities. Along this line of sight, there is only one solution to the Galactic rotation curve,  $\sim 17.5 \text{ kpc}$ . However, the narrowness of the emission feature implies the gas is not located at this extreme distance, and it is more likely to be local cloud located nearby in the local spur or somewhere between the Sun and the Sagittarius spiral arm. Since the Sagittarius spiral arm is located  $\sim 0.5 \text{ kpc}$  away along the line of sight (Vallée 2014), we adopt a general approximate distance equal to half this distance,  $\sim 250 \text{ pc}$ , for the gas within this component.

Component 2 ( $v_{\text{LSR}} = -8$  to  $2 \text{ km s}^{-1}$ ) has no CO(1–0) emission that overlaps the TeV peak, though there appears to be some overlap towards the Galactic East and West sides of the source. There may be a subtle hint of a ring-like feature in the Galactic East side, seen in the  $^{12}\text{CO}(1–0)$ . The more intense emission seen in left side of the ‘ring’ also appears in the  $^{13}\text{CO}(1–0)$ . The gas traced here may be part of the Sagittarius I or Scutum II spiral arms.

In component 3 ( $v_{\text{LSR}} = -17$  to  $-8 \text{ km s}^{-1}$ ),  $^{12}\text{CO}(1–0)$  emission is seen overlapping most of HESS J1702–420. In particular, more intense emission is seen to the Galactic West of the TeV peak.  $^{13}\text{CO}(1–0)$  emission seen in this component is also located to the Galactic West, though it appears mostly beyond the extent of the TeV source.

In the distribution of  $^{12}\text{CO}(1–0)$  towards HESS J1702–420 seen in component 4 ( $v_{\text{LSR}} = -37$  to  $-17 \text{ km s}^{-1}$ ), there appears to be an irregular shaped region of diminished emission to the Galactic East of the TeV peak which the  $\gamma$ -ray contours appear to somewhat follow. The  $^{13}\text{CO}(1–0)$  overlapping the source is also diminished, and the  $\gamma$ -ray contours appears to ‘sit’ in a cavity. A region of more intense emission in both  $^{12}\text{CO}(1–0)$  and  $^{13}\text{CO}(1–0)$  is seen to the Galactic South-west of the source. Component 4 may be located within the Scutum I or Norma II spiral arms, and the spectra of component 4 (Figure 2) shows signs of being composed of more than one unresolved blended features. As an approximation, we have considered them part of the same component.

Component 5 ( $v_{\text{LSR}} = -58$  to  $-37 \text{ km s}^{-1}$ ), likely in the Norma I spiral arm, has  $^{12}\text{CO}(1–0)$  and  $^{13}\text{CO}(1–0)$  emission which overlaps most of the TeV source. An interesting elongated raindrop-shaped region of more intense  $^{12}\text{CO}(1–0)$  emission is seen coming in from

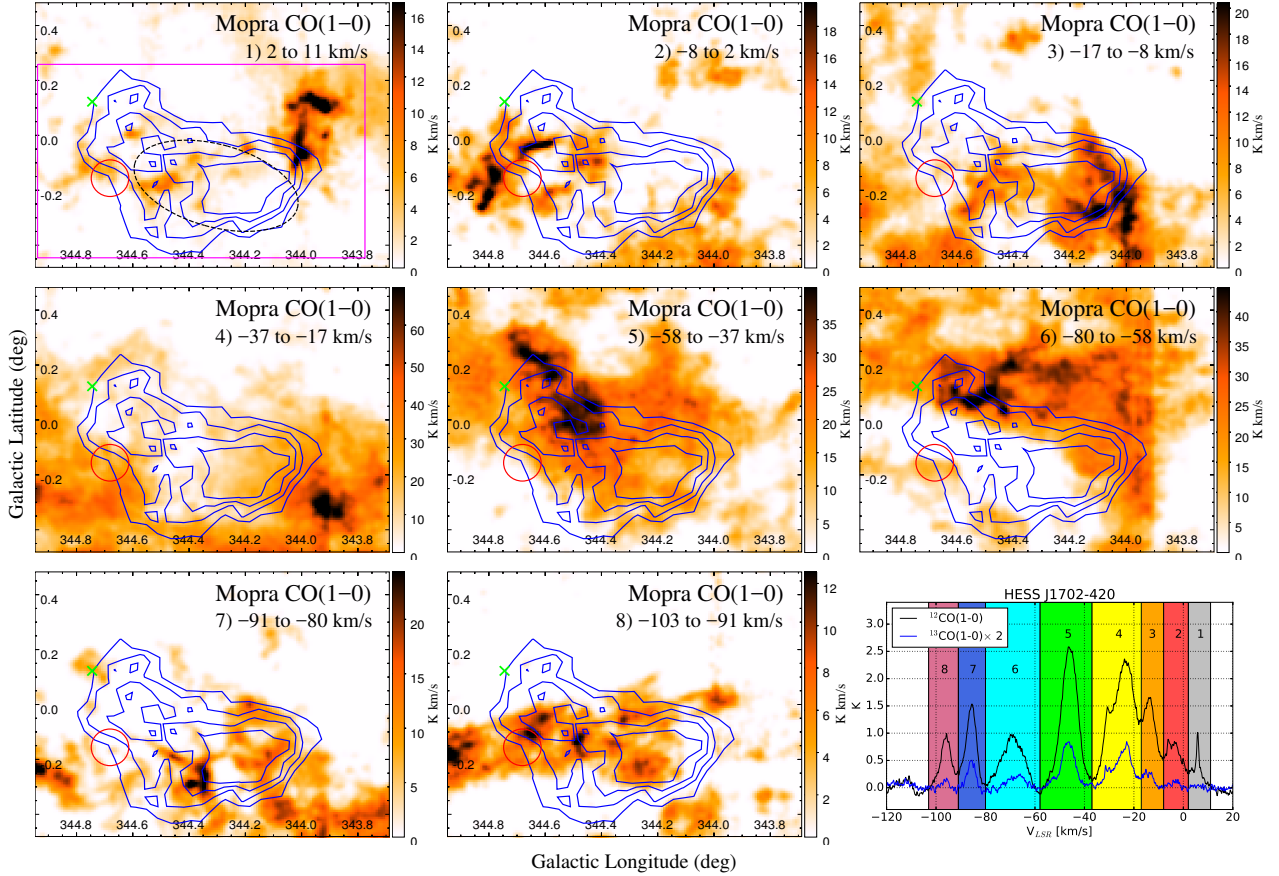


**Figure 3.** Integrated  $^{12}\text{CO}(1-0)$  emission images [ $\text{K km s}^{-1}$ ] towards HESS J1702–420 within the velocity intervals of the CO(1–0) components. The blue contours show the HESS significance at  $4\sigma$ ,  $5\sigma$ ,  $6\sigma$ , and  $7\sigma$  (Aharonian et al. 2008). The red circle and green X indicate the positions of SNR G344.7–0.1 and PSR J1702–4128 respectively. The elliptical extent of HESS J1702–420, as described in Aharonian et al. (2008), is indicated by the dashed black ellipse in the top-left panel. The large magenta rectangle in the top-left panel shows the region used for the position-velocity plot in Figure 4. For reference, the bottom-right panel is a duplicate of Figure 2.

the Galactic North west of HESS J1702–420, pointing towards the TeV peak. The  $^{13}\text{CO}(1-0)$  image shows more intense emission towards the ‘base’ of the raindrop within the extent of the TeV source.

In component 6 ( $v_{\text{LSR}} = -80$  to  $-58 \text{ km s}^{-1}$ ), extended emission in both  $^{12}\text{CO}(1-0)$  and  $^{13}\text{CO}(1-0)$  lines appear to overlap the Galactic North and Northwest rim of HESS J1702–420. Filamentary regions of more intense emission appear to the Galactic North of the source. Strikingly, a sharp band of non-detection seems to cut through HESS J1702–420, entering from the Galactic East side and exiting through the Galactic South-west.

There is some overlap of  $^{12}\text{CO}(1-0)$  emission towards the TeV peak seen in component 7 ( $v_{\text{LSR}} = -91$  to  $-80 \text{ km s}^{-1}$ ), though none is seen towards the tail of  $\gamma$ -ray emission which extends to the Galactic North east. A region of slightly more intense  $^{12}\text{CO}(1-0)$  emission is seen to the immediate left of the TeV peak, which is positionally coincident with and morphologically sim-

ilar to the HII region G344.366–0.262 (see Figure 1). The HII region has a measured kinematic velocity of  $v_{\text{LSR}} = -84.1 \text{ km s}^{-1}$  (Anderson et al. 2014), consistent with that of component 7. Hence it is likely that the gas traced here is associated with the HII region.

Component 8 ( $v_{\text{LSR}} = -103$  to  $-91 \text{ km s}^{-1}$ ) has a bar-like arm of  $^{12}\text{CO}(1-0)$  emission extending into HESS J1702–420 from the Galactic East, which may be part of the Perseus spiral arm. The structure does not continue to extend further to the Galactic West past the TeV emission. Minimal emission in  $^{13}\text{CO}(1-0)$  is detected in this component.

To calculate the physical parameters of the molecular gas in these components, we fit the spectral features seen in the CO(1–0) line emission with Gaussian functions. We then calculate the mass and density of the gas in the components following the methods outlined in §2.2. The Gaussian fit parameters and the calculated gas parameters are displayed in Table 1.

**Table 1** The fitted  $^{12}\text{CO}(1-0)$  line parameters and the calculated physical gas parameters for each of the components within the elliptical extent of HESS J1702–420. The line-of-sight velocity,  $v_{\text{LSR}}$ , line width (full-width-half-maximum),  $\Delta v_{\text{FWHM}}$ , and peak intensity,  $T_{\text{peak}}$ , were derived from Gaussian fits. The optical depth of the line,  $\tau_{12}$ , was calculated following §2.2.1.

Component	Distance <sup>†</sup> (kpc)	$v_{\text{LSR}}$ (km s $^{-1}$ )	$\Delta v_{\text{FWHM}}$ (km/s)	$T_{\text{peak}}$ (K)	$\tau_{12}$	$\overline{N}_{H_2}$ ( $10^{21} \text{ cm}^{-2}$ )	Mass ( $M_{\odot} \times 10^4$ )	$\bar{n}$ ( $10^2 \text{ cm}^{-3}$ )
1	0.25	5.8	2.1	0.7	2.0	0.3	0.001	1.8
2	0.5	-4.2	10.8	0.8	4.9	1.3	0.03	5.0
3	1.6	-13.4	4.5	1.2	6.7	0.8	0.2	1.0
4	2.6	-24.0	13.4	2.2	8.7	4.7	3.0	3.3
5	4.0	-46.0	7.5	2.6	8.1	3.1	4.9	1.4
6	5.1	-69.1	9.9	0.9	5.3	1.5	3.7	0.5
7	5.7	-85.8	4.9	1.5	3.2	1.2	3.7	0.4
8	6.0	-95.9	5.4	0.9	3.5	0.78	2.7	0.2

<sup>†</sup>The distance used for mass and density calculations are the near-solutions using the Galactic rotation curve presented in Brand & Blitz (1993). The exception is component 1 which has a positive kinematic velocity an adopted distance of 250 pc as mentioned in text. Calculations using the far-distance solutions can be found in Table A1.

### 3.2 HI emission towards HESS J1702–420

Extensive emission in the HI line is seen along the line-of-sight towards HESS J1702–420 at kinematic velocities between  $\sim -175$  and  $+100 \text{ km s}^{-1}$ . The average spectrum of HI emission within the elliptical extent of HESS J1702–420 (Aharanian et al. 2008) is shown in the bottom-right panel of Figure 5. The velocity intervals of the molecular gas components seen in the  $^{12}\text{CO}(1-0)$  and  $^{13}\text{CO}(1-0)$  data, as described in §3.1, are indicated by the coloured rectangles overlaid on the spectrum. We produced HI integrated emission images in the corresponding velocity ranges, which are displayed in the eight other panels of Figure 5.

There appears to be no immediately obvious correspondence between the integrated HI and CO(1–0) emission images for components 1 through 4, though enhanced HI emission is seen in filamentary regions in components 1 and 3, and in a circular region to the Galactic North-east of HESS J1702–420 in component 2.

In component 5, more intense HI emission appears in the Galactic North-east corner of the TeV source, close to the elongated raindrop-shaped feature seen in  $^{12}\text{CO}(1-0)$ . However, the more intense HI does not appear to overlap with the ‘base’ of the raindrop.

In component 6, enhanced HI emission appears with general correspondence with the filamentary structures observed in  $^{12}\text{CO}(1-0)$  to the Galactic North of HESS J1702–420. The HI also appears to be somewhat diminished towards the Galactic Southern part of the source.

Relatively intense HI emission appears in a region just to the left of the TeV peak in component 7. This

correlates with the more intense  $^{12}\text{CO}(1-0)$  emission also seen in this region.

The HI emission in component 8 follows the general distribution of the CO(1–0), being a bar-like arm that extends across HESS J1702–420. The more intense HI emission extends from the Galactic East into the TeV source peak position, much like the  $^{12}\text{CO}(1-0)$ . Unlike the  $^{12}\text{CO}(1-0)$ , however, the HI emission appears to extend all the way past the TeV source, continuing towards the Galactic West.

We calculate the physical parameters of the atomic hydrogen gas within the defined components following §2.2.2, and display them in Table 2. Note that unlike the CO(1–0) analysis, we do not fit Gaussian functions to the HI spectrum, as the ‘components’ were identified based on the individual features seen in the CO(1–0) data. Instead, we use the total integrated HI signal within the velocity intervals of the corresponding component in our calculations.

## 4 Discussion

Currently, there are no firm associations between HESS J1702–420 with any known source at other wavelengths, and as such the particular production mechanism behind the observed  $\gamma$ -rays is unknown. Using our understanding of the ISM, we now investigate possible origin scenarios behind the TeV  $\gamma$ -ray source.

### 4.1 The hadronic production scenario of TeV $\gamma$ -rays

In the hadronic scenario, highly accelerated CRs interact with ambient gas in the ISM, producing TeV  $\gamma$ -rays via p-p interactions and subsequent pion decay. In the

**Table 2** The calculated physical gas parameters for atomic hydrogen gas from HI analysis for each of the components within the elliptical extent of HESS J1702–420. The distance and velocities used for the calculations are taken from the CO(1–0) analysis in the corresponding component (see §3.1). Calculations using the far-distance solutions can be found in Table A2.

Component	Distance (kpc)	$v_{\text{LSR}}$ (km s $^{-1}$ )	$\overline{N_H}$ (10 $^{21}$ cm $^{-2}$ )	Mass (M $_{\odot} \times 10^4$ )	$\bar{n}$ (10 $^2$ cm $^{-3}$ )
1	0.25	5.8	1.6	0.004	4.3
2	0.5	−4.2	2.0	0.02	2.7
3	1.6	−13.4	1.8	0.2	0.7
4	2.6	−24.0	3.5	0.8	0.9
5	4.0	−46.0	1.9	1.1	0.3
6	5.1	−69.1	1.6	1.4	0.2
7	5.7	−85.8	1.0	1.1	0.1
8	6.0	−95.9	0.73	0.9	0.08

CO(1–0) data, we traced molecular gas features along the line-of-sight overlapping HESS J1702–420, which we divided into eight ‘components’, as described in §3. Target material for CRs can be both molecular and atomic gas, and it is instructive to consider the distribution of the total column density,  $N_H$ , within each component. First, we smooth our CO(1–0) data up to the beam size of the HI data. We then multiply the integrated CO(1–0) and HI intensity maps by the appropriate X-factors (as in §2.2) to obtain maps of  $N_{\text{H}_2}$  and  $N_{\text{HI}}$  respectively. Finally, we sum these maps following  $N_H = N_{\text{HI}} + 2N_{\text{H}_2}$  to obtain total column density maps for each component. These images are displayed in Figure 6. We find that, in general, the total column density maps follow the distribution of the CO(1–0) traced H<sub>2</sub> gas.

Some potentially interesting morphological correspondences are seen between the total column density maps and the TeV emission from HESS J1702–420. The material that is present maybe acting as target material for CRs, assuming the presence of some nearby accelerator.

We consider the expected flux of  $\gamma$ -rays produced when gas of mass  $M_{\odot}$  is bombarded by CRs in the context of the material within each of our components. Recasting Equation (10) from Aharonian (1991) for the  $\Gamma = 2.1$  spectrum of HESS J1702–420 using a pivot energy of 1 TeV, we acquire the relationship:

$$F(\geq E_{\gamma}) = 4.15 \times 10^{-13} E_{\gamma}^{-1.1} \left( \frac{M_5}{d^2} \right) k_{CR} \text{ cm}^{-2} \text{ s}^{-1} \quad (2)$$

which gives the expected  $\gamma$ -ray flux above energy  $E_{\gamma}$  as a function of  $M_5$ , the mass of the target material in units of 10 $^5$  M $_{\odot}$ ,  $d$ , the distance to the target material in kpc, and  $k_{CR}$ , the CR enhancement value compared with that observed on Earth.

The  $\gamma$ -ray flux of HESS J1702–420 is given as  $F(> 200 \text{ GeV}) = 15.9 \times 10^{-12} \text{ cm}^{-2} \text{ s}^{-1}$  (Aharonian et al. 2006b). Using Equation 2, we are able to calculate the value of  $k_{CR}$  necessary in each component, given the mass of gas contained within. We take the total amount of gas in the components as the sum of the molecular gas traced by CO(1–0) (§3.1) and atomic gas traced by HI (§3.2). We find that in all of the components, the atomic gas makes up a sizeable fraction ( $\gtrsim 25\%$ ) of the total gas mass. The mass values, along with  $k_{CR}$  values for each component are displayed in Table 3. We note that the  $k_{CR}$  values are effectively independent of the assumed distance to the gas components, as the distance terms in Equation 2 cancel out those used in the mass calculations.

The calculated  $k_{CR}$  values for each of the components are of the order  $\sim 100$ . These values are achievable given the presence of a nearby (within a few 10s of pc) and young ( $\lesssim 10^3$  yr) impulsive CR accelerator (Aharonian & Atoyan 1996).

In the case where the TeV  $\gamma$ -ray flux is produced hadronically, the total CR energy budget can be expressed as  $W_p = L_{\gamma} \tau_{pp}$ . Here,  $L_{\gamma}$  is the  $\gamma$ -ray luminosity, and  $\tau_{pp}$  is the cooling time of CR protons via proton-proton collisions which is given by:  $\tau_{pp} \approx 6 \times 10^7 (n/1 \text{ cm}^{-3})^{-1}$  yr (Aharonian & Atoyan 1996), where  $n$  is the target gas number density.

We have estimated the average number density,  $\bar{n}$ , within our gas components (Tables 1, 2, A1 and A2), and calculate the  $\gamma$ -ray luminosity for HESS J1702–420 above 200 GeV for both the near and far-distance solutions. From here, the values of  $W_p$  for each component were calculated, and are displayed in Table 4. In the case of the near-distance assumption, the  $W_p$  value for each component appears to be a fraction of the canonical energy injected into CRs by a SNR ( $\sim 10^{50}$  erg), and it may be plausible that an SNR powers the TeV  $\gamma$ -ray flux seen from HESS J1702–420. For the far-distance

**Table 3** The calculated CR enhancement values,  $k_{CR}$ , for each gas component as described in §3 within the extent of HESS J1702–420. Molecular gas masses and atomic gas masses come from  $^{12}\text{CO}(1-0)$  and HI analyses respectively assuming the near-distance solutions (see Tables 1 and 2). Both molecular and atomic gas is considered for the total average density,  $\bar{n}$ . The values of  $k_{CR}$  are independent of assumed distance, as discussed in text.

Component	$v_{\text{LSR}}$ ( $\text{km s}^{-1}$ )	Distance (kpc)	Molecular mass ( $\text{M}_{\odot}$ )	Atomic mass ( $\text{M}_{\odot}$ )	Total mass ( $\text{M}_{\odot}$ )	$\bar{n}$ ( $10^2 \text{ cm}^{-3}$ )	$k_{CR}$
1	2 to 11	0.25	10	40	50	6.1	810
2	−8 to 2	0.5	300	200	500	8.3	320
3	−17 to −8	1.6	2,000	2,000	4,000	2.0	420
4	−37 to −17	2.6	30,000	8,000	38,000	4.2	120
5	−58 to −37	4.0	49,000	11,000	60,000	1.7	170
6	−80 to −58	5.1	37,000	14,000	51,000	0.7	330
7	−91 to −80	5.7	37,000	11,000	48,000	0.5	441
8	−103 to −91	6.0	27,000	9,000	36,000	0.3	650

assumptions, several of the components have  $W_p$  values slightly greater than the canonical amount, which may suggest a more energetic supernova event than standard, or a higher efficiency in accelerating CRs. The age of the potential SNR also will play an important role. Younger SNRs, within a few 1000 years old, tend to have  $W_p$  values  $< 10^{49}$  erg, as many of the CRs are in the early stages of acceleration and are still confined to the SNR. More evolved SNRs, with several tens of thousands of years worth of CR acceleration and escape, may be required for  $W_p$  to reach values  $\geq 10^{49}$  erg (see e.g. Fukui et al. 2012; Yoshiike et al. 2013; Fukuda et al. 2014). Far-distance assumptions would also imply a much larger TeV source, with estimated diameters of  $> 100$  pc based on the angular size of HESS J1702–420. Such large sizes may be problematic in scenarios based on a single young accelerator, as accelerated particles may not have had enough time to travel over those distances.

For the case of HESS J1702–420, we now consider G344.7–0.1, the only known SNR towards the TeV source.

#### 4.1.1 SNR G344.7–0.1

The distance to the SNR G344.7–0.1, as mentioned in §1, is not well understood. However, the small angular size and the high absorption column density from X-ray observations (Combi et al. 2010; Giacani et al. 2011; Yamaguchi et al. 2012) suggests that G344.7–0.1 is located at a large distance on the opposite side of the Galaxy (Yamaguchi et al. 2012). To constrain the distance to this SNR, we extract the average  $^{12}\text{CO}(1-0)$  and HI spectra within the extent of G344.7–0.1. Following §2.2, we calculate the total column density  $N_{\text{H}}$ , and are able to find the total cumulative  $N_{\text{H}}$  as a function of kinematic velocity  $v_{\text{LSR}}$ . We assume that all the gas traced was located at the near-distance.

**Table 4** Calculated values for the total CR energy budget,  $W_p$ , in each gas component assuming a pure hadronic scenario for HESS J1702–420 for both near and far-distance solutions to the Galactic rotation curve.

Component	$W_p$ (erg)	
	Near	Far
1	$3.9 \times 10^{50}$	$3.9 \times 10^{50}$
2	$3.8 \times 10^{45}$	$1.1 \times 10^{50}$
3	$1.6 \times 10^{47}$	$1.4 \times 10^{50}$
4	$2.0 \times 10^{47}$	$3.0 \times 10^{49}$
5	$1.2 \times 10^{48}$	$3.2 \times 10^{49}$
6	$4.7 \times 10^{48}$	$5.4 \times 10^{49}$
7	$8.3 \times 10^{48}$	$4.9 \times 10^{49}$
8	$1.5 \times 10^{49}$	$1.4 \times 10^{50}$

We plot the total cumulative  $N_{\text{H}}$  against  $v_{\text{LSR}}$  towards G344.7–0.1 in Figure 7, as well as the cumulative  $N_{\text{H}_2}$  and  $N_{\text{H}}$  calculated from  $^{12}\text{CO}(1-0)$  and HI emission respectively. The modelled absorption column density from X-ray observations from Combi et al. (2010), Giacani et al. (2011) and Yamaguchi et al. (2012) were mutually consistent, with values  $N_{\text{H}} \sim (4.3 - 5.4) \times 10^{22} \text{ cm}^{-2}$ , and are indicated by the shaded rectangle in Figure 7.

We find that the total cumulative  $N_{\text{H}}$  does not reach the modelled values, even up to the velocity corresponding to the tangent point ( $v_{\text{LSR}} \sim -150 \text{ km s}^{-1}$  for the tangent point at  $\sim 8$  kpc using the rotation model from Brand & Blitz 1993). This may be due to several reasons. The total cumulative  $N_{\text{H}}$  strongly depends on the value of the X-factors used to convert brightness temperature to column density. In particular, the CO X-factor,  $X_{\text{CO}(1-0)}$ , has uncertainties of  $\sim 30\%$  across the disk of

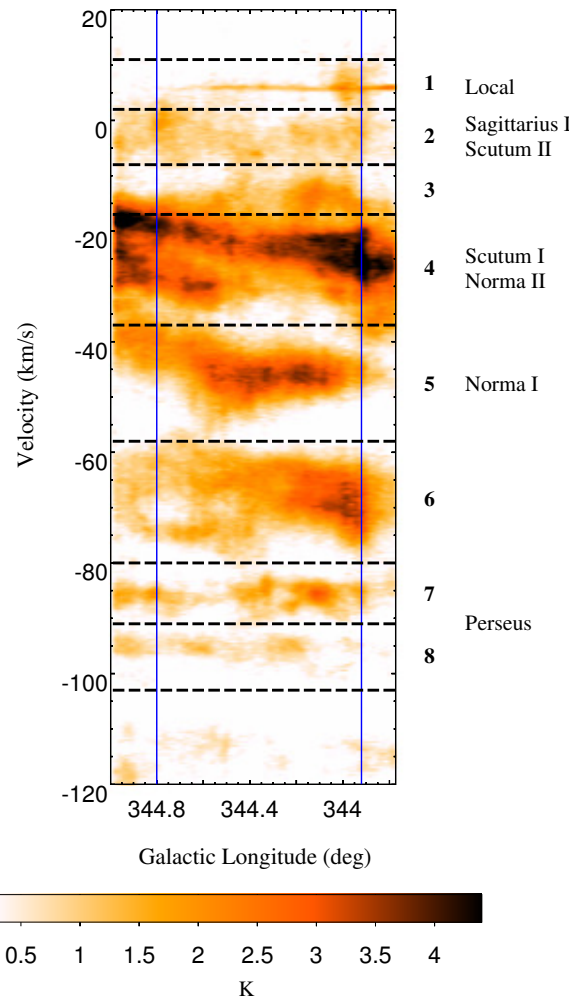


**Figure 4.** Position-velocity image of  $^{12}\text{CO}(1-0)$  emission [K] in Galactic longitude towards HESS J1702–420 in the region indicated in Figure 3. The dashed horizontal lines and the numbers in boldface indicate the corresponding velocity intervals of the gas components and described in §3.1. Vertical blue lines indicate the longitudinal extent of HESS J1702–420 at  $4\sigma$  significance (Aharonian et al. 2008). Estimated locations of Galactic spiral arms along the line-of-sight have been labelled, based on the model presented in Vallée (2014) as mentioned in text. In cases where the line of sight intersects a spiral arm more than once, the labels ‘I’ and ‘II’ indicates the closer and further intersections respectively.

the Galaxy (Bolatto et al. 2013), which in this case may have caused an underestimation of total column density. Additionally, we are assuming the case of optically thin HI, and as mentioned in §2.2.2 this may lead to an underestimation of the total HI column density by up to a factor of 2 (Fukui et al. 2012). Even so, the fact that the X-ray derived  $N_{\text{H}}$  values are larger than our calculated total cumulative  $N_{\text{H}}$  suggests that the dis-

tance to G344.7–0.1 is  $\gtrsim 8$  kpc, at least further than the tangent point along this line-of-sight. We find no evidence to suggest that the SNR is located any closer than 14 kpc as estimated by Dubner et al. (1993), and agree with Yamaguchi et al. (2012) who noted that the distance estimate of 6.3 kpc from Giacani et al. (2011) is too low.

We consider now a scenario in which CRs accelerated by the SNR are diffusing through the intervening ISM towards the TeV peak of HESS J1702–420. The diffusion time can be given by  $\tau_{\text{diff}} = d^2/(6D(E))$ , where  $d$  is the diffusion distance and  $D(E)$  is the diffusion coefficient at energy  $E$  (Ginzburg & Syrovatskii 1964). To calculate  $D(E)$ , we use the magnetic field strength within the intervening ISM calculated from derived gas densities. As described above, G344.7–0.1 is likely located further than the tangent point along the line of sight. Thus, we take the gas densities obtained from our gas analyses assuming the far distances as presented in Tables A1 and A2. Under this assumption, the gas density  $\bar{n} < 10^2 \text{ cm}^{-3}$  for every component, and following Crutcher et al. (2010), the magnetic field strength was taken to be  $10 \mu\text{G}$ .

We then use Equation 2 from Gabici et al. (2007) to calculate  $D(E)$ , assuming the suppression factor  $\chi = 0.1$  used in other studies of the dense ISM towards the TeV  $\gamma$ -ray sources associated with the SNR W28 (Giuliani et al. 2010; Gabici et al. 2010; Li & Chen 2012). Note that a somewhat slow diffusion case was required to keep particles from escaping too quickly. We consider CRs of energy  $E_{\text{CR}} = 2 \text{ TeV}$ , which would produce  $\gamma$ -rays of energy  $\sim 200 \text{ GeV}$  via p-p interactions which is near the detectability threshold of HESS.

Based on the estimated distance of 14 kpc to G344.7–0.1 (Dubner et al. 1993), the separation between G344.7–0.1 and the TeV peak of HESS J1702–420 is  $d \sim 120 \text{ pc}$ , and the corresponding diffusion time is calculated to be  $\tau_{\text{diff}} \sim 100 \text{ kyr}$ . The radius of G344.7–0.1 at the distance of 14 kpc is  $\sim 16 \text{ pc}$ . Employing the model of a SNR in Sedov phase from Chevalier (1974), the age of the remnant would be  $\sim 38 \text{ kyr}$ .

We further consider the limiting case in which G344.7–0.1 is located at the distance of the tangent point along the line of sight ( $\sim 8$  kpc). Under this assumption, the diffusion distance  $d \sim 70 \text{ pc}$ , and  $\tau_{\text{diff}}$  is calculated to be  $\sim 34 \text{ kyr}$ . The SNR would have a radius of  $\sim 9 \text{ pc}$  and an estimated age of 6.3 kyr.

In both cases, we find that  $\tau_{\text{diff}}$  is much greater than the SNR age. Thus it is unlikely that CRs produced by G344.7–0.1 would have been able to diffuse far enough to produce the TeV  $\gamma$ -rays observed from HESS J1702–420.

Aharonian et al. (2008) concluded that the SNR G344.7–0.1 was not associated with HESS J1702–420, based on its small angular size, the large distance esti-

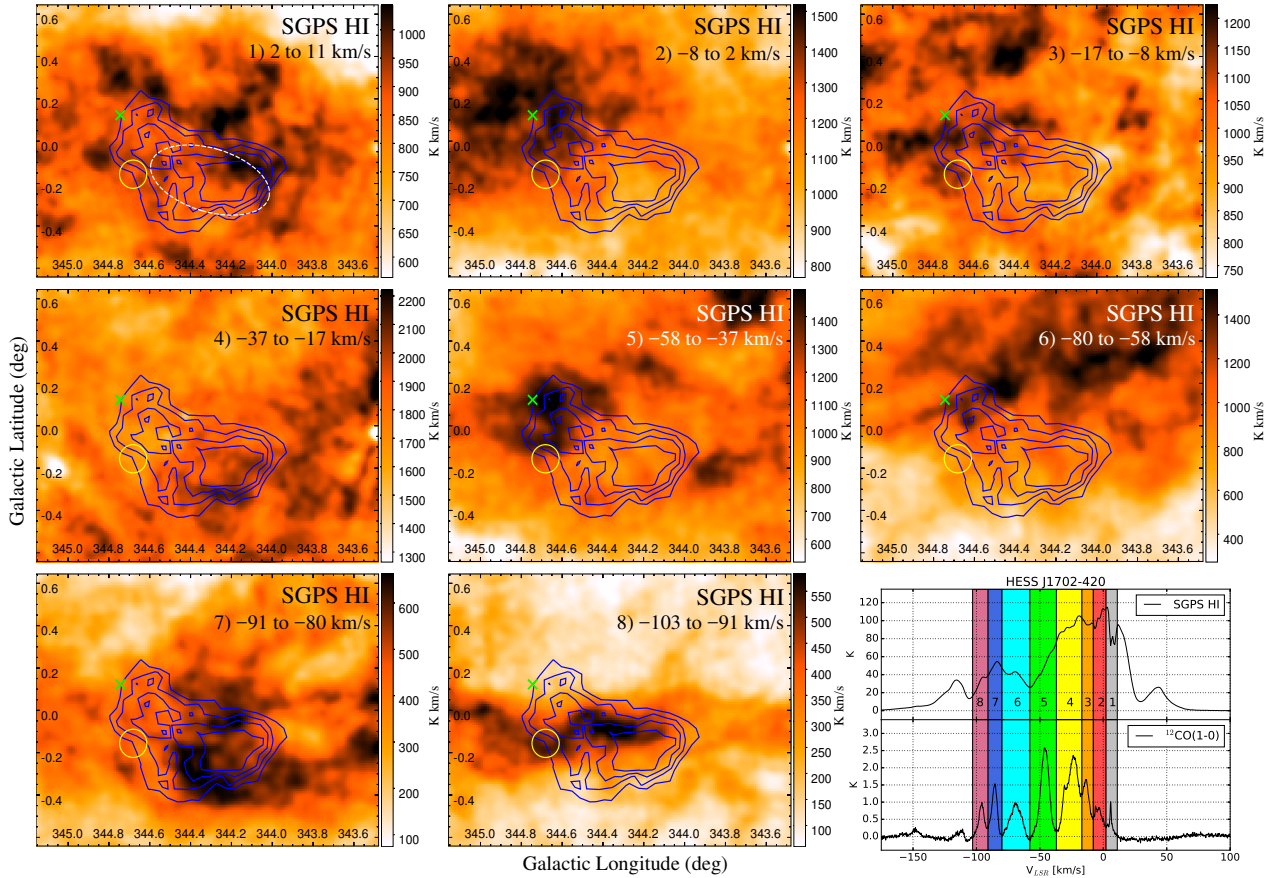


**Figure 5.** Integrated HI emission images [ $\text{K km s}^{-1}$ ] from SGPS data towards HESS J1702–420 within the velocity intervals indicated. The blue contours show the HESS significance at  $4\sigma$ ,  $5\sigma$ ,  $6\sigma$ , and  $7\sigma$  (Aharonian et al. 2008). The yellow circle and green X indicate the positions of SNR G344.7–0.1 and PSR J1702–4128 respectively. The elliptical extent of HESS J1702–420, as described in Aharonian et al. (2008), is indicated by the dashed white ellipse in the top-left panel. The average HI and  $^{12}\text{CO}(1-0)$  emission spectra within this elliptical extent is displayed in the bottom-right panel. The coloured rectangles indicate the components seen in CO(1–0) emission as described in text.

mate and separation from the TeV emission peak. We did not find evidence to suggest that the SNR is located closer than previously assumed, and find that it is unlikely that CRs generated by the SNR have diffused far enough to generate the  $\gamma$ -rays from the TeV source. Hence, we find no evidence to support an association between HESS J1702–420 and SNR G344.7–0.1.

#### 4.1.2 Unknown accelerator towards HESS J1702–420

While the only known SNR towards HESS J1702–420, G344.7–0.1, is unlikely to be behind the TeV  $\gamma$ -ray emission, some other, as-of-yet unidentified accelerator may be producing CRs that are interacting with the local ISM. Figure 6 shows the total column density of the interstellar gas towards HESS J1702–420 in the major components identified along the line of sight. In §4.1 we found that the required CR enhancement rate  $k_{\text{CR}}$

for each component was of the order  $\sim 100$ , indicating that a local (within a few 10s of pc) accelerator such as a SNR would be sufficient for the TeV  $\gamma$ -rays to be produced hadronically (Aharonian & Atoyan 1996).

There may exist some potentially interesting correspondence between the distribution of ISM material and the TeV  $\gamma$ -ray emission. Looking at the total column density for component 5 in Figure 6, we see that the TeV contours appear to overlap relatively well with an ISM cloud structure, and it may be plausible that the TeV  $\gamma$ -rays are produced by accelerated CRs interacting with the available target material. The density of this overlapping cloud is fairly uniform, with the exception of a denser, tear-drop shaped region towards the upper regions of the tail of the TeV emission to the Galactic North-east of the source. The emission from the TeV peak of HESS J1702–420 may be produced by CRs from a potential accelerator located near that posi-

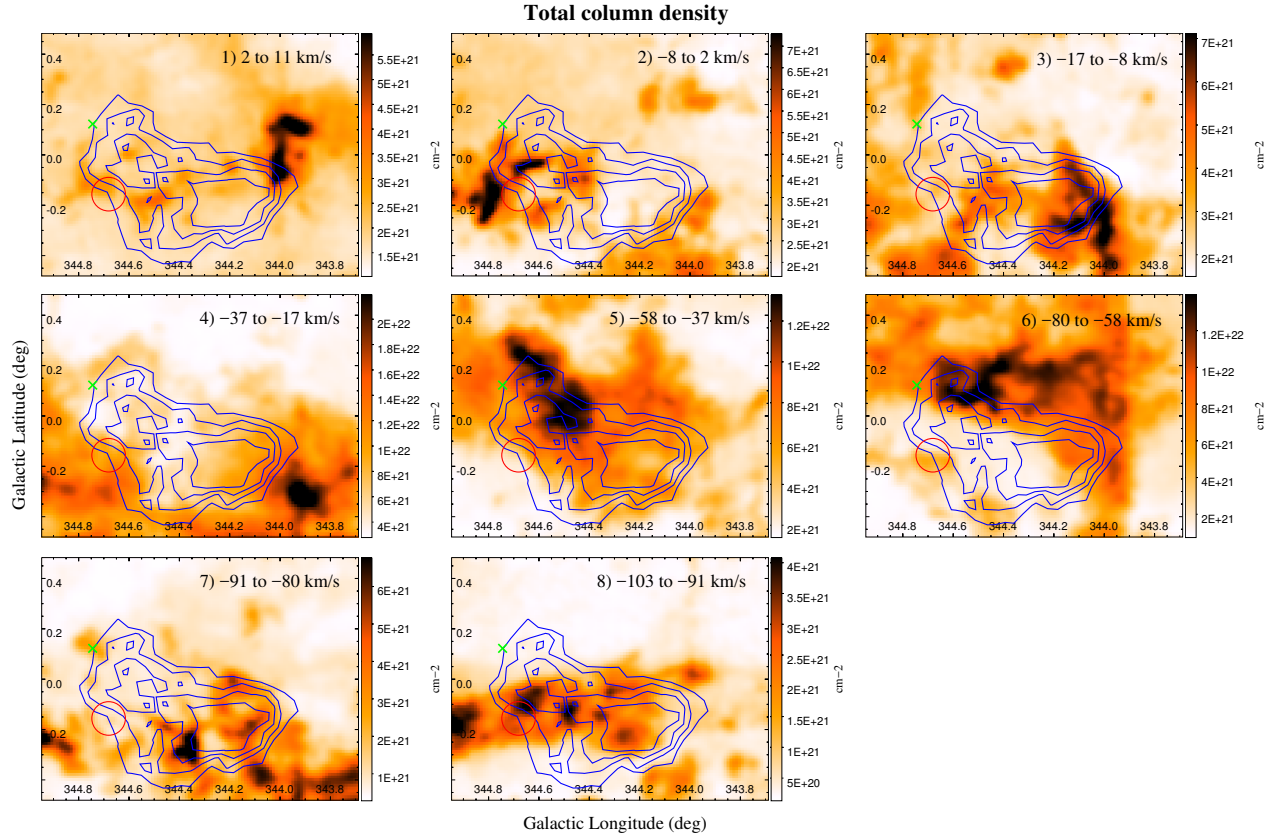


**Figure 6.** Total column density maps [ $\text{cm}^{-2}$ ] towards HESS J1702–420 within the velocity intervals indicated. The blue contours show the HESS significance at  $4\sigma$ ,  $5\sigma$ ,  $6\sigma$ , and  $7\sigma$  (Aharonian et al. 2008). The red circle and green X indicate the positions of SNR G344.7–0.1 and PSR J1702–4128 respectively.

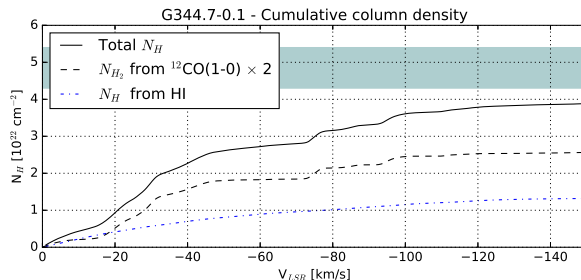


**Figure 7.** Total cumulative hydrogen column density  $N_H$  as a function of  $v_{\text{LSR}}$  (solid line) towards SNR G344.7–0.1. The dashed and dot-dashed lines show the cumulative molecular and atomic hydrogen column densities calculated from  $^{12}\text{CO}(1-0)$  and HI respectively. The shaded region indicates the modelled values of  $N_H$  required from X-ray observations (Combi et al. 2010; Giacani et al. 2011; Yamaguchi et al. 2012).

We can also consider a continuous accelerator scenario, which may involve massive stars and their clusters accelerating CRs via their stellar winds. As mentioned in §3.1, the HII region G344.366–0.262 is seen near the TeV peak of HESS J1702–420. This region may indicate massive star formation, and contains a young stellar object (YSO) 2MASS J17031902–4201452 (Cutri et al. 2003). The HII region is positionally coincident and consistent in velocity ( $v_{\text{LSR}} \sim -84 \text{ km s}^{-1}$ , with corresponding distance  $\sim 5.7 \text{ kpc}$ ) with the gas traced in component 7. It may be possible that CRs accelerated by massive stars are interacting with the ambient ISM to produce the observed TeV  $\gamma$ -rays (Voelk & Forman 1982), though the correspondence between the TeV emission and gas does not appear very pronounced. This situation in which an unidentified TeV source overlaps smaller HII regions is also seen in the case of HESS J1626–490 (Eger et al. 2011).

tion. CRs diffusing away from this accelerator may then be interacting with the material present to the Galactic North-east, forming the extended tail of TeV emission.

## 4.2 The leptonic production scenario of TeV $\gamma$ -rays

For a leptonic scenario, the dominant production of TeV  $\gamma$ -rays comes from the upscattering of background photons by high energy CR electrons with multi-TeV energies via the inverse-Compton effect. In the case of HESS J1702–420, the leptonic scenario involves PSR J1702–4128, the only known pulsar towards the TeV source. The pulsar is located at the edge of HESS J1702–420 and has a fairly large ( $\sim 0.5^\circ$ ) angular separation from the position of the TeV peak. This implies that any high energy electrons produced by PSR J1702–4128 and its PWN would have needed to diffuse through the intervening ISM before generating the  $\gamma$ -ray emission.

The dispersion distance to PSR J1702–4128 is estimated to be 5.2 kpc (Kramer et al. 2003). The corresponding kinematic velocity for the distance estimate is  $\sim -70 \text{ km s}^{-1}$ , which places the pulsar within gas component 6 ( $v_{\text{LSR}} = -80$  to  $-58 \text{ km s}^{-1}$ ) as described in §3. At this distance, the separation between the pulsar and the TeV peak of HESS J1702–420 is  $\sim 50$  pc.

When considering the morphology of the gas in component 6, thought to be located at the distance of the pulsar, we see a general anti-correlation between the total column density (see Figure 6) and the TeV emission of HESS J1702–420. Interestingly, there exists a density void in the bottom regions of the TeV source. A region of greater density lies above this void. Consider a situation where the supernova event which produced PSR J1702–4128 occurred near the center of the TeV emission. The void may have been formed by the stellar winds of the high mass progenitor star. PSR J1702–4128 may have received some kick velocity to the Galactic North-east, leading to its current position. At the estimated distance of  $\sim 5.2$  kpc, PSR J1702–4128 would have travelled  $\sim 25$  pc in this scenario. With an estimated age of  $\sim 55$  kyr (Kramer et al. 2003), its kick velocity would be  $\sim 450 \text{ km s}^{-1}$ , fairly typical of pulsar kick velocities (Hansen & Phinney 1997).

We consider the case where electrons generated by PSR J1702–4128 are diffusing through the gas within component 6 towards the TeV peak of HESS J1702–420 over a distance  $d = 50$  pc. We calculate the diffusion time  $\tau_{\text{diff}}$  following the formalism presented in §4.1.1. To calculate  $D(E)$ , we used the magnetic field strength within the intervening ISM in component 6. Given that the average density  $\bar{n}$  for component 6 was  $\sim 70 \text{ cm}^{-3}$ , the magnetic field strength was taken to be  $10 \mu\text{G}$  following Crutcher et al. (2010). We consider electrons of energy  $E_e = 5 \text{ TeV}$ , which would produce  $\gamma$ -rays of energy  $\sim 200 \text{ GeV}$  via the inverse-Compton effect which is near the detectability threshold of HESS. In this case, the diffusion time  $\tau_{\text{diff}}$  is calculated to be  $\sim 11$  kyr.

The synchrotron cooling time of CR electrons is given by  $\tau_{\text{sync}} \approx (b_s \gamma_e)^{-1} \text{ s}$ , where  $b_s = 1.3 \times 10^{-15} (B/\text{mG})^2 \text{ s}^{-1}$ , and  $\gamma_e$  is the Lorentz factor of the electron. We find that  $\tau_{\text{sync}} \sim 25$  kyr. Given that  $\tau_{\text{diff}} < \tau_{\text{sync}}$ , it may be possible that accelerated electrons from PSR J1702–4128 and its PWN are able to diffuse through the intervening ISM without losing all their energy to synchrotron losses en-route.

The inverse-Compton cooling time, given by  $\tau_{\text{IC}} = 3 \times 10^8 (U_{\text{rad}} E)^{-1}$ , is  $\sim 240$  kyr for 5 TeV electrons, given the typical radiation density of the cosmic microwave background (CMB)  $U_{\text{rad}} = 0.25 \text{ eV cm}^{-3}$ . This implies that the extent of inverse-Compton emission is limited by the age of PSR J1702–4128, estimated to be  $\sim 55$  kyr (Kramer et al. 2003). However, depending on the time history of the pulsar period, encapsulated by the braking index, this age may be overestimated, bringing it closer to the diffusion time  $\tau_{\text{diff}} \sim 11$  kyr.

The TeV luminosity of HESS J1702–420 would require a  $\sim 70\%$  conversion efficiency of the pulsar spin-down power, a value that is much higher than that seen in other, firmly identified TeV PWN (Abdalla et al. 2017, A&A in press). The problem may be mitigated somewhat if we consider the possibility that the spin-down power of the pulsar is underestimated, and the age overestimated, if the estimated braking index,  $n$ , is different from the standard value of  $n = 3$ . Actual values of  $n$  have been confidently measured in the range of  $2 < n < 3$  (Livingstone et al. 2005, and references therein). If the true value of  $n$  for PSR J1702–4128 is closer to 2, the age of the pulsar may be overestimated and the past spin-down power underestimated by a factor of  $\sim 2$  (Gaensler & Slane 2006). If it is the case that the pulsar spin-down power was much greater in the past, relic electrons from the earlier history of the pulsar may now be contributing to the production of TeV  $\gamma$ -rays (e.g. see discussion in Aharonian et al. 2006a).

While the gas morphology does not discount the idea that HESS J1702–420 is powered by PSR J1702–4128 and the associated PWN, this scenario has several potential issues that disfavour it. The large separation between the pulsar and TeV peak would imply a rather asymmetric PWN (Aharonian et al. 2008), which is not seen in X-ray observations towards PSR J1702–4128 (Chang et al. 2008). Additionally, the TeV  $\gamma$ -ray spectrum of HESS J1702–420 is described by a power law  $dN/dE = N_0 E^{-\Gamma}$ , with a relatively hard photon index of  $\Gamma = 2.1$  and maximum detected  $\gamma$ -ray energy of  $\sim 30 \text{ TeV}$  (Aharonian et al. 2008). Due to severe synchrotron losses, it is typically difficult to accelerate a population of electrons to energies capable of producing hard and broad  $\gamma$ -ray spectra with energies which extend into tens of TeV (Hinton & Hofmann 2009). Hence, this leptonic scenario for HESS J1702–420 can be considered somewhat unlikely.

## 5 Conclusions

We have studied the ISM towards the unidentified and dark TeV  $\gamma$ -ray source HESS J1702–420 using CO(1–0) data from the Mopra Southern Galactic Plane Survey and archival HI data from SGPS.

The CO(1–0) data revealed several components of emission along the line of sight which overlapped the TeV source. Motivated by these molecular gas components, we looked at the HI emission within the same velocity intervals. From the CO(1–0) and HI data, we were able to estimate the physical parameters of the molecular and atomic hydrogen respectively in the ISM.

For the scenario in which the TeV  $\gamma$ -rays were produced by hadronic processes, we found that the total gas mass and densities present in our gas components (except component 1) implied CR enhancement rates of  $\lesssim 500$  and total CR energy budgets  $W_p$  of  $\sim 10^{45}$  to  $10^{49}$  erg. This suggested a hadronic origin scenario was plausible for HESS J1702–420 given a local CR accelerator.

We investigated scenarios involving the known potential counterparts; the SNR G344.7–0.1, and the PSR J1702–4128, both located near the outskirts of HESS J1702–420. Comparing the total cumulative column density towards G344.7–0.1, calculated from CO(1–0) and HI data, with modelled column densities from X-ray observations in previous works, we found that the SNR is likely to be located at least further than the Galactic tangent point ( $\sim 8$  kpc along this line of sight). We found no structures in the ISM that appeared to correspond with G344.7–0.1, and found that it is unlikely that CRs accelerated by the SNR have been able to diffuse far enough towards HESS J1702–420 to generate the TeV  $\gamma$ -ray emission. This suggested that G344.7–0.1 is an unlikely candidate for association.

However, there were some potentially interesting correspondences seen between the distribution of ISM and the TeV  $\gamma$ -ray emission, particularly in the case of the gas traced in component 5. We speculated on a scenario in which an as-of-yet undetected accelerator was producing CRs which are interacting with the favourably distributed target material. Based on the available target material in this component, we found that a CR accelerator, such as a young SNR, would be able to produce the TeV  $\gamma$ -rays seen from HESS J1702–420.

We considered the leptonic scenario involving PSR J1702–4128, located near the Galactic North-east edge of HESS J1702–420. The void in the gas seen at the estimated distance to the pulsar near the center of the TeV source. This could have been formed by the SNR potentially linked with PSR J1702–4128, with the pulsar receiving some kick velocity to reach its current position. The scenario where highly energetic electrons from PSR J1702–4128 are diffusing through the intervening ISM towards the center of

HESS J1702–420 was considered. Based on the density of the gas from our ISM study, we found that the electrons may have diffused far enough to reach the TeV peak of HESS J1702–420. However, while the gas morphology suggest that this scenario is plausible, the lack of an asymmetric PWN seen in X-rays, the hard TeV  $\gamma$ -ray spectrum extending to tens of TeV, and the abnormally high ( $\sim 70\%$ ) spin-down power conversion efficiency disfavoured such a scenario.

Future observations with next-generation  $\gamma$ -ray telescopes, such as the Cherenkov Telescope array, will have increased angular resolutions approaching that of the CO(1–0) data used in this study. These observations will reveal fine detail in the  $\gamma$ -ray emission, enabling more intricate morphological comparisons with the ISM, and a better understanding of this mysterious TeV  $\gamma$ -ray source.

## 6 ACKNOWLEDGEMENTS

The Mopra radio telescope is part of the Australia Telescope National Facility. Operations support was provided by the University of New South Wales and the University of Adelaide. The UNSW Digital Filter Bank used for the observations with Mopra was provided with financial support from the Australian Research Council (ARC), UNSW, Sydney and Monash universities. We also acknowledge ARC support through grants DP120101585 and LE160100094. J.C.L. acknowledges support through the provision of Australian Government Research Training Program Scholarship. C.B. acknowledges support from the #TeamMopra kickstarter contributors, listed at [www.mopra.org](http://www.mopra.org).

## REFERENCES

- Abdalla H., et al., 2017, A&A, in press
- Acero F., et al., 2015, ApJS, 218, 23
- Aharonian F. A., 1991, Ap&SS, 180, 305
- Aharonian F. A., Atoyan A. M., 1996, A&A, 309, 917
- Aharonian F., et al., 2005, Science, 307, 1938
- Aharonian F., et al., 2006a, A&A, 460, 365
- Aharonian F., et al., 2006b, ApJ, 636, 777
- Aharonian F., Akhperjanian A. G., Barres de Almeida U., et al., 2008, A&A, 477, 353
- Anderson L. D., Bania T. M., Balser D. S., Cunningham V., Wenger T. V., Johnstone B. M., Armentrout W. P., 2014, ApJS, 212, 1
- Bolatto A. D., Wolfire M., Leroy A. K., 2013, ARA&A, 51, 207
- Braiding C., et al., 2015, PASA, 32, e020
- Brand J., Blitz L., 1993, A&A, 275, 67
- Burton M. G., et al., 2013, PASA, 30, e044
- Chang C., Konopelko A., Cui W., 2008, ApJ, 682, 1177
- Chevalier R. A., 1974, ApJ, 188, 501
- Churchwell E., et al., 2009, PASP, 121, 213

- Combi J. A., et al., 2010, *A&A*, **522**, A50
- Crutcher R. M., Wandelt B., Heiles C., Falgarone E., Troland T. H., 2010, *ApJ*, **725**, 466
- Cutri R. M., et al., 2003, VizieR Online Data Catalog, **2246**
- Dickey J. M., Lockman F. J., 1990, *ARA&A*, **28**, 215
- Donath A., Brun F., Chaves R. C. G., Deil C., Marandon V., Terrier R., 2017, *AIP Conference Proceedings*, **1792**, 040001
- Dubner G. M., Moffett D. A., Goss W. M., Winkler P. F., 1993, *AJ*, **105**, 2251
- Eger P., Rowell G., Kawamura A., Fukui Y., Rolland L., Stegmann C., 2011, *A&A*, **526**, A82
- Fujinaga T., et al., 2011, *PASJ*, **63**, S857
- Fukuda T., Yoshiike S., Sano H., Torii K., Yamamoto H., Acero F., Fukui Y., 2014, *ApJ*, **788**, 94
- Fukui Y., et al., 2012, *ApJ*, **746**, 82
- Gabici S., Aharonian F. A., Blasi P., 2007, *Ap&SS*, **309**, 365
- Gabici S., Casanova S., Aharonian F. A., Rowell G., 2010, in Boissier S., Heydari-Malayeri M., Samadi R., Valls-Gabaud D., eds, SF2A-2010: Proceedings of the Annual meeting of the French Society of Astronomy and Astrophysics. p. 313
- Gaensler B. M., Slane P. O., 2006, *ARA&A*, **44**, 17
- Gallant Y. A., 2007, *Ap&SS*, **309**, 197
- Giacani E., Smith M. J. S., Dubner G., Loiseau N., 2011, *A&A*, **531**, A138
- Ginzburg V. L., Syrovatskii S. I., 1964, The Origin of Cosmic Rays
- Giuliani A., et al., 2010, *A&A*, **516**, L11
- Green D. A., 2014, Bulletin of the Astronomical Society of India, **42**, 47
- Hansen B. M. S., Phinney E. S., 1997, *MNRAS*, **291**, 569
- Henkel C., Wilson T. L., Bieging J., 1982, *A&A*, **109**, 344
- Hinton J. A., Hofmann W., 2009, *ARA&A*, **47**, 523
- Kramer M., et al., 2003, *MNRAS*, **342**, 1299
- Lau J. C., et al., 2017, *MNRAS*, **464**, 3757
- Li H., Chen Y., 2012, *MNRAS*, **421**, 935
- Livingstone M. A., Kaspi V. M., Gavril F. P., 2005, *ApJ*, **633**, 1095
- Manchester R. N., Hobbs G. B., Teoh A., Hobbs M., 2005, *AJ*, **129**, 1993
- McClure-Griffiths N. M., Dickey J. M., Gaensler B. M., Green A. J., Havercorn M., Strasser S., 2005, *ApJS*, **158**, 178
- Strong A. W., Moskalenko I. V., Reimer O., Digel S., Diehl R., 2004, *A&A*, **422**, L47
- Vallée J. P., 2014, *AJ*, **148**, 5
- Voelk H. J., Forman M., 1982, *ApJ*, **253**, 188
- Whiteoak J. B. Z., Green A. J., 1996, *A&AS*, **118**, 329
- Yamaguchi H., Tanaka M., Maeda K., Slane P. O., Fosster A., Smith R. K., Katsuda S., Yoshii R., 2012, *ApJ*, **749**, 137
- Yamauchi S., Ueno M., Koyama K., Bamba A., 2005, *PASJ*, **57**, 459
- Yoshiike S., et al., 2013, *ApJ*, **768**, 179

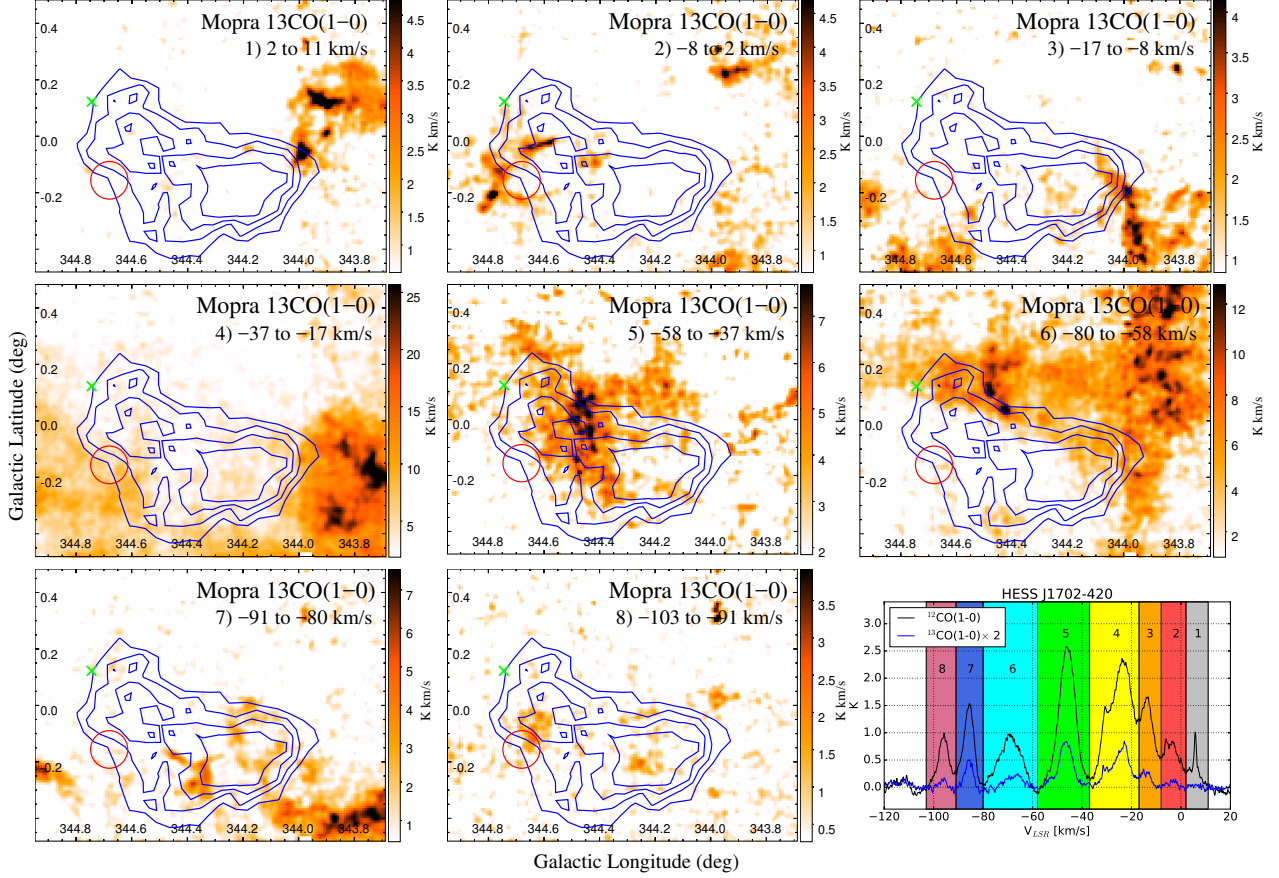


**Figure A1.** Integrated  $^{13}\text{CO}(1-0)$  emission images [ $\text{K km s}^{-1}$ ] towards HESS J1702–420 within the velocity intervals indicated. The blue contours show the HESS significance at  $4\sigma$ ,  $5\sigma$ ,  $6\sigma$ , and  $7\sigma$  (Aharonian et al. 2008). The red circle and green X indicate the positions of SNR G344.7–0.1 and PSR J1702–4128 respectively. The panel in the bottom right displays the average  $^{12}\text{CO}(1-0)$  and  $^{13}\text{CO}(1-0)$  emission spectrum (black and blue respectively) within the elliptical extent of HESS J1702–420 as described in Aharonian et al. (2008). The  $^{13}\text{CO}(1-0)$  is scaled by a factor of 2 for clarity.

**Table A1** The fitted  $^{12}\text{CO}(1-0)$  line parameters and the calculated physical gas parameters for each of the components within the elliptical extent of HESS J1702–420, as described in §3.1. The far-distance solution to the Galactic rotation curve has been assumed. The line-of-sight velocity,  $v_{\text{LSR}}$ , line width (full-width-half-maximum),  $\Delta v_{\text{FWHM}}$ , and peak intensity,  $T_{\text{peak}}$ , were derived from Gaussian fits. The optical depth of the line,  $\tau_{12}$ , was calculated following §2.2.1.

Component	Distance (kpc)	$v_{\text{LSR}}$ ( $\text{km s}^{-1}$ )	$\Delta v_{\text{FWHM}}$ (km/s)	$T_{\text{peak}}$ (K)	$\tau_{12}$	$\overline{N}_{\text{H}_2}$ ( $10^{21} \text{ cm}^{-2}$ )	Mass ( $M_{\odot} \times 10^4$ )	$\overline{n}$ ( $10^2 \text{ cm}^{-3}$ )
1	0.25	5.8	2.1	0.7	2.0	0.3	0.001	1.8
2	15.9	-4.2	10.8	0.8	4.9	1.3	32.2	0.2
3	14.8	-13.4	4.5	1.2	6.7	0.8	17.5	0.1
4	13.8	-24.0	13.4	2.2	8.7	4.7	85.8	0.6
5	12.3	-46.0	7.5	2.6	8.1	3.1	46.0	0.5
6	11.3	-69.1	9.9	0.9	5.3	1.5	18.5	0.2
7	10.7	-85.8	4.9	1.5	3.2	1.2	13.1	0.2
8	10.4	-95.9	5.4	0.9	3.5	0.78	8.1	0.1

**Table A2** The calculated physical gas parameters for atomic hydrogen gas from H $\alpha$  analysis for each of the components within the elliptical extent of HESS J1702–420, as described in §3.1. The far-distance solution to the Galactic rotation curve has been assumed.

Component	Distance (kpc)	$v_{\text{LSR}}$ (km s $^{-1}$ )	$\overline{N_H}$ (10 $^{21}$ cm $^{-2}$ )	Mass (M $_{\odot}$ × 10 $^4$ )	$\bar{n}$ (10 cm $^{-3}$ )
1	0.25	5.8	1.6	0.004	4.3
2	15.9	−4.2	2.0	17.6	0.8
3	14.8	−13.4	1.8	13.3	0.8
4	13.8	−24.0	3.5	22.9	1.7
5	12.3	−46.0	1.9	9.9	1.0
6	11.3	−69.1	1.6	7.1	0.9
7	10.7	−85.8	1.0	4.1	0.6
8	10.4	−95.9	0.73	2.7	0.5

# Chapter 6

## Conclusions and Future Work

The work that has been presented in this thesis comprises of investigations into the interstellar medium (ISM) towards dark Galactic TeV gamma-ray sources, with an aim to better understand the nature of these mysterious astrophysical phenomena. This work has made use of data from ground-based radio telescopes, utilising various molecular and atomic spectral lines to gain insight into the physical properties of the interstellar gas. Using this knowledge, it was possible to explore the possible origin scenarios for each of the sources by constraining the hadronic and leptonic contributions to the gamma-ray fluxes, as well as by investigating the plausibility of nearby counterparts that were seen at other wavelengths.

In total, five TeV gamma-ray sources were studied:

- **HESS J1640–465** and **HESS J1641–463**: a pair of TeV gamma-ray sources coincident with two supernova remnants (SNR) and connected by a complex of HII regions. HESS J1641–463 was particularly interesting as it is a strong PeVatron candidate, only appearing at higher energies with a hard gamma-ray spectrum with no sign of a cut-off. The investigation of the ISM presented in this thesis revealed molecular gas overlapping the TeV sources at their estimated distances, with particularly dense gas bridging the two sources. It was found that the TeV gamma-rays could have been produced by the cosmic-rays (CRs) accelerated by the SNRs interacting with the local gas. However the older SNR that is coincident with HESS J1641–463 may not have been able to generate the parent population of CRs required to produce the observed gamma-ray spectrum. Instead, the scenario in which the SNR coincident with HESS J1640–465 was acting as a PeVatron was investigated, with accelerated cosmic rays diffusively propagating across the dense gas bridge to reach HESS J1641–463. This scenario was found to be plausible, given the distribution of the ISM, and readily explains the hardness of gamma-ray spectrum observed from HESS J1641–463.

- **HESS J1614–518:** a mysterious dark TeV gamma-ray source with no immediately obvious counterparts seen in other wavelengths. In the investigation of the ISM conducted in this thesis, a peculiar ring of dense gas was found located towards the centre of the source. It was shown that a scenario involving CRs accelerated by an undetected SNR, possibly associated with two X-ray sources within the TeV source, could be producing the observed gamma-rays in an hadronic interaction scenario. Alternatively, a scenario in which the CRs were produced by the stellar winds from the young stellar cluster Pismis 22 was also found to explain the TeV flux. Both scenarios were consistent with the presence of the dense gas ring, and it may well be the case that the TeV emission from HESS J1614–518 is due to a hadronic process.
- **HESS J1616–508:** a TeV gamma-ray source with no firm association with any other counterpart. Several interesting high-energy phenomena are seen towards this source, including two SNRs and three pulsars. Investigation of the ISM towards HESS J1616–508 revealed many overlapping components of molecular gas along the line of sight, including a dense loop of gas which cut through the centre of the source. In light of this distribution of gas, an investigation into all of the known counterpart candidates was presented in this thesis. None of these, however, returned strong evidence to link them with the TeV emission. In light of this, an unknown accelerator interacting with morphologically conspicuous and spatially matching gas overlapping HESS J1616–508 was speculated on. It was found that an undetected SNR, whose progenitor star which may have shaped the structure of the gas, would readily be able to supply the CRs required to produce the TeV gamma-rays.
- **HESS J1702–420:** a dark TeV gamma-ray source that is considered a Pe-Vatron candidate. Two potential counterparts, a SNR and a pulsar, are seen towards the outskirts of this poorly understood source. The investigation of the ISM presented in this thesis found potentially interesting morphological correspondences between the TeV emission and gas. Given the distribution of the ISM, it was found unlikely that potential CRs accelerated by the SNR were responsible for the TeV emission. A leptonic scenario involving the pulsar could not be ruled out by the ISM study, though the required energetics and nature of the TeV gamma-ray emission disfavoured such a case. Additional scenarios involving CRs from stellar winds from massive stars and undetected accelerators were also investigated and found to be plausible given their possible interaction with favourably positioned gas.

---

Many more dark Galactic TeV gamma-ray sources exist, and investigations into the distribution of local ISM are important in the efforts to unravel these enigmas. In this spirit, future work will involve the continued exploration of the ISM towards the TeV gamma-ray sources in our Galaxy using radio observations of spectral lines and analyses similar to those employed in this thesis.

The work that has been conducted here will form a strong basis for comparisons with next-generation gamma-ray telescopes. These instruments, such as the upcoming Cherenkov Telescope Array (CTA, CTA website 2017), will have arcminute angular resolutions which approach that of the spectral line data used in the studies of the ISM presented in this thesis, as well as increased energy resolution and sensitivities compared with that of current systems. This will allow for more intricate comparisons between the fine details of the gamma-ray emission from Galactic TeV sources and the ISM, which will play an important role in distinguishing between the hadronic and leptonic contributions to the TeV emission, furthering our understanding into these mysterious phenomena.

## CHAPTER 6. CONCLUSIONS AND FUTURE WORK

# Appendix A

## Cosmic-ray Acceleration

A discussion of how charged particles are accelerated via 2nd and 1st order Fermi acceleration was presented in §1.3.3.1 and §1.3.3.2 respectively. Additional details and derivations of the values and equations used in the discussion are presented in this appendix. The material presented here is primarily adapted from Protheroe & Clay (2004).

### A.1 2nd Order Fermi Acceleration

In 2nd order Fermi acceleration, charged particles are thought to interact with the turbulent magnetic fields inside interstellar gas clouds. The elastic collisions experienced by the charged particles within the clouds may impart additional energy to the particle.

In §1.3.3.1, it was shown that the fractional change in the energy of a charged particle between entering and exiting the interstellar medium cloud is given by:

$$\begin{aligned} \frac{\Delta E}{E} &\equiv \frac{E_2 - E_1}{E_1} \\ &= \frac{1 - \beta_{\text{cloud}} \cos \theta_1 + \beta_{\text{cloud}} \cos \theta'_2 - \beta_{\text{cloud}}^2 \cos \theta_1 \cos \theta'_2}{1 - \beta_{\text{cloud}}^2} - 1 \end{aligned} \quad (\text{A.1})$$

where  $E_1$  and  $E_2$  are the energies of the particle when it enters and exits the cloud respectively,  $\theta_1$  is the angle in the lab frame at which the particle enters the cloud with respect to the velocity  $V_{\text{cloud}}$  of the cloud,  $\theta'_2$  is the exit angle of the particle in the cloud frame, and  $\beta_{\text{cloud}} = V_{\text{cloud}}/c$ . This situation is illustrated in Figure 1.4.

From here, in order to find the average energy change for a large population of charged particles,  $\langle \Delta E/E \rangle$ , we require the average values of  $\cos \theta_1$  and  $\cos \theta'_2$ . Inside the interstellar medium cloud, we assume that the CR scatters multiple times off of

## APPENDIX A. COSMIC-RAY ACCELERATION

---

the internal magnetic fields such that its final exit direction is completely randomised. As such,  $\langle \cos \theta'_2 \rangle = 0$ .

We can obtain  $\langle \cos \theta_1 \rangle$  by considering the collision rates between CRs and the cloud. Consider the case with a population of CRs, travelling with some velocity  $v$ , at an angle  $\theta_1$  relative to the cloud's velocity  $V_{\text{cloud}}$ , with a number density of  $n_{\text{CR}}$ . This is illustrated in Figure A.1.

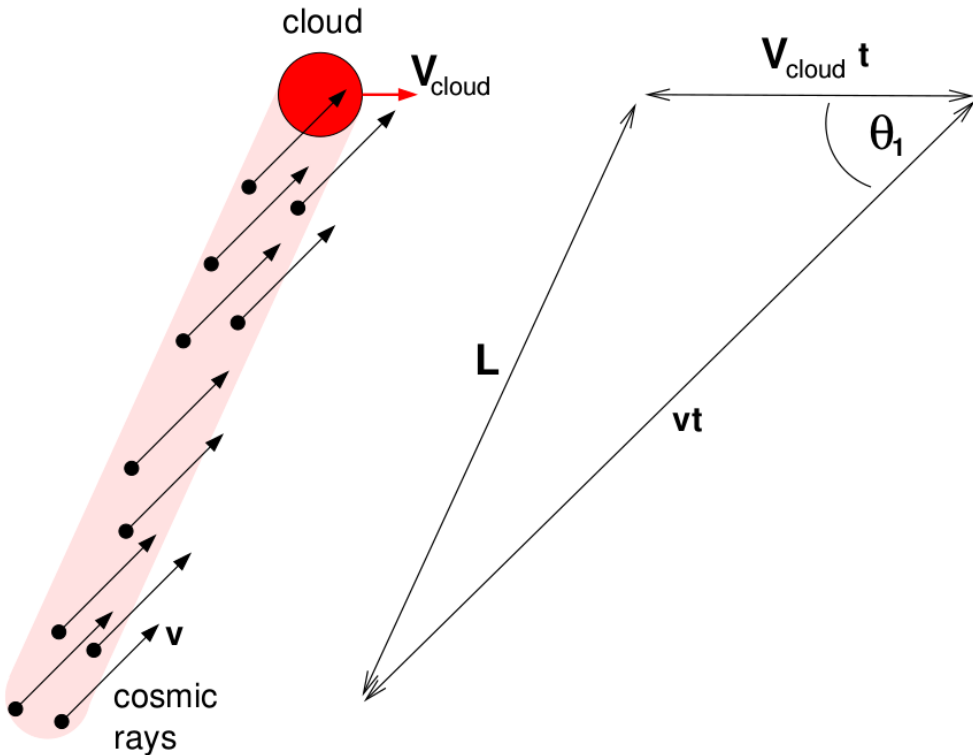


Figure A.1: A population of CRs with velocity  $v$  moving at an angle  $\theta_1$  relative to the cloud velocity  $V_{\text{cloud}}$ . The CRs in the shaded volume of length  $L$  will collide with the cloud in some time interval  $t$ . Image is adapted from Protheroe & Clay (2004).

From Figure A.1, the value of  $L$  can be expressed via the cosine rule as:

$$L = t \sqrt{v^2 + V_{\text{cloud}}^2 - 2V_{\text{cloud}}v \cos \theta_1} \quad (\text{A.2})$$

In the typical case where the CR particle speed is much larger than that of the cloud ( $v \gg V_{\text{cloud}}$ ), Equation A.2 simplifies to:

$$L \approx (v - V_{\text{cloud}} \cos \theta_1)t \quad (\text{A.3})$$

The collision rate of CRs, with number density  $n_{\text{CR}}$ , and the cloud is then:

$$L = \frac{n_{\text{CR}} L \sigma}{t} = n_{\text{CR}} (v - V_{\text{cloud}} \cos \theta_1) \sigma \quad (\text{A.4})$$

where  $\sigma$  is the cross-sectional area of the cloud. CRs are relativistic particles and travel close to the speed of light. Taking  $v \rightarrow c$ , and letting  $V_{\text{cloud}} = \beta_{\text{cloud}} c$ , the collision probability,  $P_{\text{coll}}$ , is:

$$P_{\text{coll}} \propto (1 - \beta_{\text{cloud}} \cos \theta_1) \quad (-1 < \cos \theta_1 < 1) \quad (\text{A.5})$$

To find the average value of a variable  $x$  in a continuous function  $f(x)$ , we use  $\langle x \rangle = \int x f(x) dx / \int f(x) dx$ . Hence the average value of  $\cos \theta_1$  can be found by:

$$\begin{aligned} \langle \cos \theta_1 \rangle &= \frac{\int \cos \theta_1 P_{\text{coll}} d(\cos \theta_1)}{\int P_{\text{coll}} d(\cos \theta_1)} \\ &= \frac{\int \cos \theta_1 (1 - \beta_{\text{cloud}} \cos \theta_1) d(\cos \theta_1)}{\int (1 - \beta_{\text{cloud}} \cos \theta_1) d(\cos \theta_1)} \end{aligned} \quad (\text{A.6})$$

Hence, for  $(-1 < \cos \theta_1 < 1)$ , this simplifies to:

$$\langle \cos \theta_1 \rangle = -\frac{\beta_{\text{cloud}}}{3} \quad (\text{A.7})$$

Now we can insert  $\langle \cos \theta'_2 \rangle = 0$  and Equation A.7 into Equation 1.13 which yields:

$$\frac{\langle \Delta E \rangle}{E} \approx \frac{4}{3} \beta_{\text{cloud}}^2 \quad (\text{A.8})$$

Thus, the average change in energy is positive and a population of CRs will be, on average, accelerated in a process that is proportional to  $\beta_{\text{cloud}}^2$ .

## A.2 1st Order Fermi Acceleration

In 1st order Fermi acceleration (see §1.3.3.2), charged particles undergo multiple scatterings off the turbulent magnetic fields in head-on collisions either side of some shock front. Each time the particle crosses the shock front, it has energy imparted upon it, resulting in a rapid increase in the particle energy. This scenario is illustrated in Figure 1.5.

To find the resulting energy spectrum of CRs produced by 1st order Fermi acceleration, we need to consider the probability of a CR crossing the shock multiple times,

## APPENDIX A. COSMIC-RAY ACCELERATION

---

and consequently receiving multiple successive boosts in energy, before escaping. The probability of a CR not returning to the shock and escaping downstream is given by:

$$P_{\text{escape}} = \frac{R_{\text{loss}}}{R_{\text{cross}}} \quad (\text{A.9})$$

where  $R_{\text{loss}}$  is the rate at which CRs are lost downstream and  $R_{\text{cross}}$  is the rate at which CRs cross from upstream to downstream.  $R_{\text{loss}}$  is simply the number density of the CRs,  $n_{\text{CR}}$ , multiplied by the flow speed:

$$R_{\text{loss}} = n_{\text{CR}} \frac{V_s}{R} \quad (\text{m}^{-2} \text{s}^{-1}) \quad (\text{A.10})$$

$R_{\text{cross}}$  can be found by integrating  $R_{u \rightarrow d}$  (Equation 1.15) over the solid angle in the direction forward of the shock:

$$\begin{aligned} R_{\text{cross}} &= \frac{1}{4\pi} \int_{-1}^0 R_{u \rightarrow d}(\theta_1) 2\pi d(\cos \theta_1) \\ &= \frac{1}{4\pi} \int_{-1}^0 (-n_{\text{CR}} v \cos \theta_1) 2\pi d(\cos \theta_1) \\ &= \frac{1}{4} n_{\text{CR}} v \quad (\text{m}^{-2} \text{s}^{-1}) \end{aligned} \quad (\text{A.11})$$

where  $v$  is the CR velocity. The probability of escape, (Equation A.9) and the probability of return,  $P_{\text{return}}$ , can now be given as:

$$\begin{aligned} P_{\text{escape}} &= \frac{4}{R} \frac{V_s}{v} \\ P_{\text{return}} &= 1 - P_{\text{escape}} \\ &= 1 - \frac{4}{R} \frac{V_s}{v} \end{aligned} \quad (\text{A.12})$$

From here, the probability of a CR crossing the shock at least  $k$  times is:

$$P(> K) = [P_{\text{return}}]^k = \left[ 1 - \frac{4}{R} \frac{V_s}{v} \right]^k \quad (\text{A.13})$$

The energy of the CR, with initial energy  $E_0$ , would then be:

$$E = E_0 \left( 1 + \frac{\Delta E}{E} \right)^k \quad (\text{A.14})$$

The integral of the energy spectrum of a population of particles which cross the shock

$k$  times,  $Q(> k)$ , is proportional to the probability of said population crossing the shock  $k$  times:

$$Q(> k) \propto \left[ 1 - \frac{4}{R} \frac{V_s}{v} \right]^k \quad (\text{A.15})$$

The value of  $k$  can be expressed in terms of  $E$  by rearranging Equation A.14:

$$k = \frac{\ln(E/E_0)}{\ln(1 + \Delta E/E)} \quad (\text{A.16})$$

It can then be shown, allowing  $A$  be some constant, that:

$$\begin{aligned} \ln[Q(> k)] &= A + k \ln(P_{\text{return}}) \\ \therefore \ln[Q(> E)] &= A + \frac{\ln(P_{\text{return}})}{\ln(1 + \Delta E/E)} (\ln E - \ln E_0) \end{aligned} \quad (\text{A.17})$$

From here, a constant  $\Gamma$  is defined such that:

$$\begin{aligned} \Gamma &= \frac{-\ln(P_{\text{return}})}{\ln(1 + \Delta E/E)} \\ &= \frac{-\ln\left(1 - \frac{4V_s}{Rv}\right)}{\ln\left[1 + \frac{4}{3}\left(\frac{R-1}{R}\right)\frac{V_s}{c}\right]} \end{aligned} \quad (\text{A.18})$$

Equation A.18 can be simplified by considering that, for  $x \ll 1$ ,  $\ln(1+x) \simeq x$ . Since  $V_s \ll c$ , the expression for  $\Gamma$  becomes:

$$\Gamma \simeq \frac{P_{\text{escape}}}{\Delta E/E} = \frac{\frac{4V_s}{Rv}}{\frac{4}{3}\left(\frac{R-1}{R}\right)\frac{V_s}{c}} \quad (\text{A.19})$$

As  $v \rightarrow c$ ,  $\Gamma \simeq \frac{3}{R-1}$ . Equation A.17 can be now written in terms of  $\Gamma$  as:

$$\begin{aligned} \ln[Q(> E)] &= A - \Gamma[\ln(E) - \ln(E_0)] \\ &= B - \Gamma \ln(E) \end{aligned} \quad (\text{A.20})$$

where  $A$  and  $B = A + \Gamma \ln(E_0)$  are constants. Thus,  $Q$  is given by:

$$\begin{aligned} Q(> E) &= \exp(B - \Gamma \ln(E)) \\ \Rightarrow Q(> E) &\propto E^\Gamma \end{aligned} \quad (\text{A.21})$$

---

## APPENDIX A. COSMIC-RAY ACCELERATION

Hence, the CR spectra from 1st order Fermi acceleration is acquired:

$$\begin{aligned} Q(> E) &\propto E^{-\frac{3}{R-1}} && \text{(integral form)} \\ Q(E) &\propto E^{-\frac{R+2}{R-1}} && \text{(differential form)} \end{aligned} \tag{A.22}$$

# Bibliography

- Abraham J., Abreu P., Aglietta M., Ahn E. J., Allard D., Allen J., Alvarez-Muñiz J., Ambrosio M., Anchordoqui L., Andringa S., et al. 2010, Physics Letters B, 685, 239
- Abramowski A., Acero F., Aharonian F., et al., 2012, Astronomy and Astrophysics, 537, A114
- Abreu P., Aglietta M., Ahn E. J., Allard D., Allekotte I., Allen J., Alvarez Castillo J., Alvarez-Muñiz J., Ambrosio M., Aminaei A., et al. 2010, Astroparticle Physics, 34, 314
- Aharonian F., Akhperjanian A. G., Aye K.-M., et al., 2005a, Science, 307, 1938
- Aharonian F., Akhperjanian A. G., Aye K.-M., et al., 2005b, Astronomy and Astrophysics, 442, 1
- Aharonian F., Akhperjanian A. G., Barres de Almeida U., et al., 2008, Astronomy and Astrophysics, 490, 685
- Aharonian F., Akhperjanian A. G., Bazer-Bachi A. R., et al., 2006a, Nature, 439, 695
- Aharonian F., Akhperjanian A. G., Bazer-Bachi A. R., et al., 2006b, Astronomy and Astrophysics, 457, 899
- Aharonian F., Akhperjanian A. G., Bazer-Bachi A. R., et al., 2006c, The Astrophysical Journal, 636, 777
- Aharonian F., Akhperjanian A. G., Bazer-Bachi A. R., et al., 2007, Astronomy and Astrophysics, 467, 1075
- Aharonian F., Akhperjanian A. G., Bazer-Bachi A. R., et al., 2008, Astronomy and Astrophysics, 481, 401
- Aharonian F. A., 2004, Very high energy cosmic gamma radiation : a crucial window on the extreme Universe. World Scientific Publishing Co

## BIBLIOGRAPHY

---

- Aharonian F. A., Atoyan A. M., 1996, *Astronomy and Astrophysics*, 309, 917
- Aharonian F. A., Atoyan A. M., Kifune T., 1997, *Monthly Notices of the Royal Astronomical Society*, 291, 162
- Allan H. R., 1971, Eds JG Wilson, SG Wouthuysen, Amsterdam: North-Holland, 171
- Anderson L. D., Bania T. M., 2009, *The Astrophysical Journal*, 690, 706
- Baade W., Zwicky F., 1934, *Proceedings of the National Academy of Science*, 20, 259
- Beck R., 2008, in Aharonian F. A., Hofmann W., Rieger F., eds, American Institute of Physics Conference Series Vol. 1085 of American Institute of Physics Conference Series, Galactic and Extragalactic Magnetic Fields. pp 83–96
- Blandford R., Eichler D., 1987, *Physics Reports*, 154, 1
- Blumenthal G. R., Gould R. J., 1970, *Reviews of Modern Physics*, 42, 237
- Blümmer J., Engel R., Hörandel J. R., 2009, *Progress in Particle and Nuclear Physics*, 63, 293
- Bolatto A. D., Wolfire M., Leroy A. K., 2013, *Annual Review of Astronomy and Astrophysics*, 51, 207
- Brand J., Blitz L., 1993, *Astronomy and Astrophysics*, 275, 67
- Burton M. G., Ashley M. C. B., Braiding C., Freeman M., Kulesa C., Wolfire M. G., Hollenbach D. J., Rowell G., Lau J., 2015, *The Astrophysical Journal*, 811, 13
- Burton M. G., Braiding C., Glueck C., Goldsmith P., Hawkes J., Hollenbach D. J., Kulesa C., Martin C. L., Pineda J. L., Rowell G., Simon R., Stark A. A., Stutzki J., Tothill N. J. H., Urquhart J. S., Walker C., Walsh A. J., Wolfire M., 2013, *Publications of the Astronomical Society of Australia*, 30, e044
- Crutcher R. M., Wandelt B., Heiles C., Falgarone E., Troland T. H., 2010, *The Astrophysical Journal*, 725, 466
- CTA website, 2017, <https://www.cta-observatory.org>
- de Wilt P., Rowell G., Walsh A. J., Burton M., Rathborne J., Fukui Y., Kawamura A., Aharonian F., 2017, *Monthly Notices of the Royal Astronomical Society*, 468, 2093

## BIBLIOGRAPHY

---

- Deil C., Brun F., Carrigan S., Chaves R., Donath A., Gast H., Marandon V., Terrier R., 2015, in 34th International Cosmic Ray Conference (ICRC2015) Vol. 34 of International Cosmic Ray Conference, The H.E.S.S. Galactic plane survey. p. 773
- Dickey J. M., Lockman F. J., 1990, Annual review of astronomy and astrophysics, 28, 215
- Donath A., Brun F., Chaves R. C. G., Deil C., Marandon V., Terrier R., 2017, AIP Conference Proceedings, 1792, 040001
- Fermi E., 1949, Phys. Rev., 75, 1169
- Fukui Y., Sano H., Sato J., Torii K., Horachi H., Hayakawa T., McClure-Griffiths N. M., Rowell G., Inoue T., Inutsuka S., Kawamura A., Yamamoto H., Okuda T., Mizuno N., Onishi T., Mizuno A., Ogawa H., 2012, The Astrophysical Journal, 746, 82
- Gabici S., Aharonian F. A., 2007, The Astrophysical Journal, 665, L131
- Gabici S., Aharonian F. A., Casanova S., 2009, Monthly Notices of the Royal Astronomical Society, 396, 1629
- Garden R. P., Hayashi M., Hasegawa T., Gatley I., Kaifu N., 1991, The Astrophysical Journal, 374, 540
- Ginzburg V. L., Syrovatskii S. I., 1964, The Origin of Cosmic Rays
- Goldsmith P. F., Langer W. D., 1999, The Astrophysical Journal, 517, 209
- Greisen K., 1966, Physical Review Letters, 16, 748
- Gusdorf A., Cabrit S., Flower D. R., Pineau Des Forets G., 2008, Astronomy and Astrophysics, 482, 809
- Habart E., Walmsley M., Verstraete L., Cazaux S., Maiolino R., Cox P., Boulanger F., Pineau des Forets G., 2005, Space Science Reviews, 119, 71
- HEAT website, 2017, <http://soral.as.arizona.edu/heat/>
- Heitler W., 1954, The quantum theory of radiation, 3rd ed. edn. Clarendon Press Oxford
- Henkel C., Wilson T. L., Bieging J., 1982, Astronomy and Astrophysics, 109, 344
- Hess V., 1912, Physikalische Zeitschrift, 13, 1084

## BIBLIOGRAPHY

---

HESS Collaboration 2016, *Nature*, 531, 476

HESS website, 2017, <https://www.mpi-hd.mpg.de/hfm/HESS>

Heyer M., Dame T. M., 2015, *Annual Review of Astronomy and Astrophysics*, 53, 583

Irvine W. M., Goldsmith P. F., Hjalmarson A., 1987, in Hollenbach D. J., Thronson Jr. H. A., eds, *Interstellar Processes* Vol. 134 of *Astrophysics and Space Science Library*, Chemical abundances in molecular clouds. pp 561–609

Kerr F. J., Lynden-Bell D., 1986, *Monthly Notices of the Royal Astronomical Society*, 221, 1023

Ladd N., Purcell C., Wong T., Robertson S., 2005, *Publications of the Astronomical Society of Australia*, 22, 62

Lau J. C., Rowell G., Voisin F., Braiding C., Burton M., Fukui Y., Pointon S., Ashley M., Jordan C., Walsh A., 2017, *Publications of the Astronomical Society of Australia*, 34, e064

Marcowith A., Lemoine M., Pelletier G., 2006, *Astronomy and Astrophysics*, 453, 193

Moderski R., Sikora M., Coppi P. S., Aharonian F., 2005, *Monthly Notices of the Royal Astronomical Society*, 363, 954

Mopra CSIRO website, 2017, <https://www.csiro.au/en/Research/Facilities/ATNF/Mopra-radio-telescope>

Nicholas B. P., Rowell G., Burton M. G., Walsh A. J., Fukui Y., Kawamura A., Maxted N. I., 2012, *Monthly Notices of the Royal Astronomical Society*, 419, 251

Planck Collaboration Ade P. A. R., Aghanim N., Arnaud M., Ashdown M., Aumont J., Baccigalupi C., Balbi A., Banday A. J., Barreiro R. B., et al. 2011, *Astronomy and Astrophysics*, 536, A19

Protheroe R. J., Clay R. W., 2004, *Publications of the Astronomical Society of Australia*, 21, 1

Renaud M., Hoppe S., Komin N., Moulin E., Marandon V., Clapson A.-C., 2008, in American Institute of Physics Conference Series Vol. 1085 of *American Institute of Physics Conference Series*, Pulsar Wind Nebula candidates recently discovered by H.E.S.S.. pp 285–288

---

## BIBLIOGRAPHY

- Rieger F. M., de Oña-Wilhelmi E., Aharonian F. A., 2013, *Frontiers of Physics*, 8, 714
- Roman-Duval J., Jackson J. M., Heyer M., Rathborne J., Simon R., 2010, *The Astrophysical Journal*, 723, 492
- Romero G. E., 2008, in Aharonian F. A., Hofmann W., Rieger F., eds, American Institute of Physics Conference Series Vol. 1085 of American Institute of Physics Conference Series, Gamma rays from star-forming regions. pp 97–103
- Rybicki G. B., Lightman A. P., 1979, Radiative processes in astrophysics
- Safi-Harb S., 2017, in 6th International Symposium on High Energy Gamma-Ray Astronomy Vol. 1792 of American Institute of Physics Conference Series, Gamma2016: Highlights and summary of galactic science. p. 020015
- Strong A. W., Mattox J. R., 1996, *Astronomy and Astrophysics*, 308, L21
- Strong A. W., Moskalenko I. V., Reimer O., Digel S., Diehl R., 2004, *Astronomy and Astrophysics*, 422, L47
- Tafalla M., Myers P. C., Caselli P., Walmsley C. M., 2004, *Astronomy and Astrophysics*, 416, 191
- Townes C., Schawlow A., 1955, *Microwave spectroscopy. International series in pure and applied physics*, McGraw-Hill
- Urquhart J. S., Hoare M. G., Purcell C. R., Brooks K. J., Voronkov M. A., Indermuehle B. T., Burton M. G., Tothill N. F. H., Edwards P. G., 2010, *Publications of the Astronomical Society of Australia*, 27, 321
- Vallée J. P., 2014, *The Astrophysical Journal*, 148, 5
- van Dishoeck E. F., Black J. H., 1988, *The Astrophysical Journal*, 334, 771
- Voisin F., Rowell G., Burton M. G., Walsh A., Fukui Y., Aharonian F., 2016, *Monthly Notices of the Royal Astronomical Society*, 458, 2813
- Völk H. J., Bernlöhr K., 2009, *Experimental Astronomy*, 25, 173
- Voronkov M. A., Caswell J. L., Ellingsen S. P., Green J. A., Breen S. L., 2014, *Monthly Notices of the Royal Astronomical Society*, 439, 2584
- Wakely S. P., Horan D., 2008, *International Cosmic Ray Conference*, 3, 1341

## BIBLIOGRAPHY

---

Weekes T. C., Cawley M. F., Fegan D. J., Gibbs K. G., Hillas A. M., Kowk P. W., Lamb R. C., Lewis D. A., Macomb D., Porter N. A., Reynolds P. T., Vacanti G., 1989, The Astrophysical Journal, 342, 379

Wilson T. L., Rohlfs K., Hüttemeister S., 2009, Tools of Radio Astronomy. Springer-Verlag

Zatsepin G. T., Kuz'min V. A., 1966, Soviet Journal of Experimental and Theoretical Physics Letters, 4, 78